Physics of Atomic Nuclei, Vol. 64, No. 6, 2001, pp. 1001–1004. From Yadernaya Fizika, Vol. 64, No. 6, 2001, pp. 1077–1080.
Original English Text Copyright © 2001 by Casten.

Evolution of Structure in Exotic Nuclei*

R. F. Casten**

Wright Nuclear Structure Laboratory, Yale University, New Haven, USA

Received September 11, 2000

Abstract—Nuclear structure in exotic nuclei is likely to be quite different than in the nuclei we have been able to access near the valley of stability. With the development of advanced radioactive-beam facilities, we will, for the first time, have access to long isotopic chains of nuclei. A key facet of exotic nuclei therefore will be the study of the evolution of structure with N, Z, and A to an extent never before imagined. Yet, the beam intensities will be very low (relative to stable beams); hence, we will need to extract more physics from less data. We will discuss several aspects of structural evolution and its elucidation in exotic nuclei. *© 2001 MAIK "Nauka/Interperiodica".*

1. INTRODUCTION

Nuclear structure in exotic nuclei is likely to be quite different than in the nuclei we have been able to access near the valley of stability. New orbits will be occupied; nuclei near the drip lines will be loosely bound, exhibiting spatially extended topologies; the unbound continuum will play an important role; the outer reaches of neutron-rich nuclei will contain regions of dilute, essentially pure neutron matter; residual interactions such as pairing and the pn interactions will differ significantly from what we are accustomed to; magic numbers are likely to be significantly altered.

With the development of advanced radioactive-beam facilities, we will, for the first time, have access to long isotopic chains of nuclei. One of the most enticing aspects of the study of exotic nuclei will therefore be the mapping of structure in new nuclear regions far from stability. Primarily, this will focus on neutron-rich nuclei, where all the facets listed in the previous paragraph come into play.

In early studies of neutron-rich nuclei, emphasis must be on obtaining the first, basic information on these nuclei. The relevant experimental techniques will be long-familiar ones—β decay and Coulomb excitation, to name just two—carried out with vastly better instruments than in their heyday 30–40 years ago, when nuclear physicists were mapping out the stable nuclei, and with techniques such as inverse kinematics that are dictated by the particular nature of radioactive-beam experiments.

It is the purpose of this paper to discuss and illustrate some of the characteristics of structural evolution in nuclei and some of the interpretative techniques to extract the most physics from sparse data.

2. STRUCTURAL EVOLUTION

It is well known that nuclei soften as valence nucleons are added beyond magic numbers and that, for a given number of valence nucleons, a more equal distribution between protons and neutrons aids in the development of collectivity and deformation. Indeed, this is the idea behind the N_pN_n scheme. A general, highly schematic, overview of structural evolution across a pair of proton/neutron major shells is shown in Fig. 1.

Magic nuclei are characterized by rather high excitation energies for low-lying states and by an abundance of negative-parity states among the first few excited states. Singly magic nuclei typically have level systems like that shown in the second panel of Fig. 1, with $R_{4/2} \equiv E(4_1^+)/E(2_1^+) < 2$ and decreas-

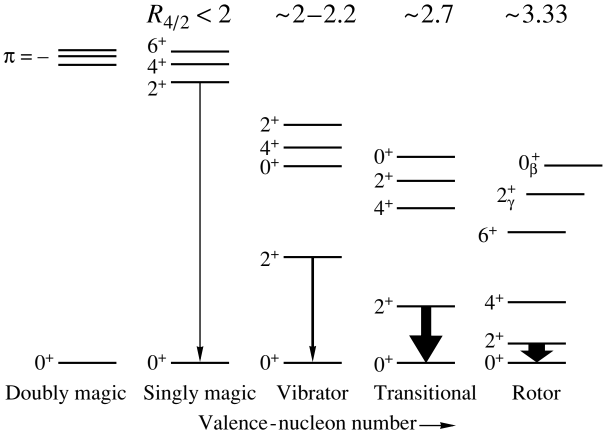

Fig. 1. Schematic view of the evolution of structure from magic nuclei to midshell.

---

*This article was submitted by the author in English.

**e-mail: `rick@riviera.physics.yale.edu`

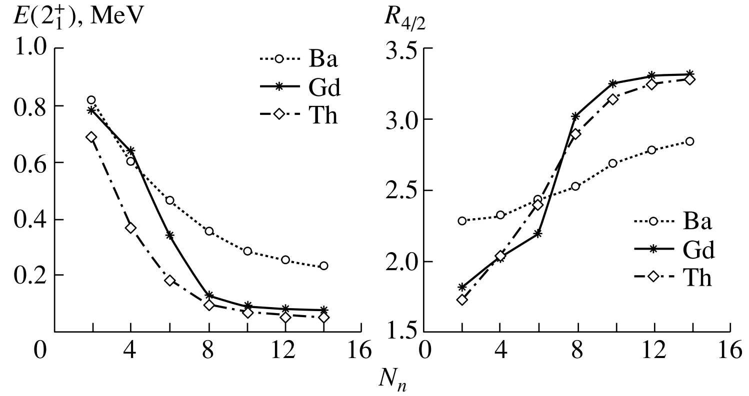

Fig. 2. Empirical phenomenology of Gd, Ba ($N < 82$), and Th nuclei illustrating three distinct morphological trends.

ing spacings between successive states. This is characteristic of an $|j^n J\rangle$ configuration and the seniority two levels extend up to $J_{\max} = 2j - 1$.

With both valence protons and neutrons, vibrations about spherical shapes appear, characterized by $R_{4/2}$ values near 2.0. With more valence nucleons, a transitional region develops—whose character is highly region-dependent—but which leads, by one trajectory or another, through $R_{4/2}$ values approaching and exceeding 3.0, at which point a permanent static deformation, and accompanying rotational behavior, with $R_{4/2} \to 3.33$, ensues.

Throughout such an evolutionary scenario, $E(2_1^+)$ drops and the yrast $B(E2)$ values grow substantially.

Such a generic picture, however, masks specific trajectories within an evolutionary sequence. Three such trajectories, discussed in [1], are shown in Fig. 2, where we have specifically selected three elements, Gd, Ba ($N < 82$), and Th, to illustrate the ideas below.

A key point here is that, throughout the history of nuclear physics, we have had several benchmark structural paradigms, such as those in Fig. 1—magic nuclei, vibrators, rotors—that represent limiting cases of structural evolution. However, we have never had paradigms for structural change, but yet most nuclei are in regions of structural change. Moreover, such regions usually involve competing degrees of freedom and have, historically, been the most difficult to treat. Figure 2 is an initial effort to provide a classification scheme for such transitional regions, presented primarily in the hope that it will spur more formal theoretical study.

Figure 2 shows $E(2_1^+)$ and $R_{4/2}$ for three isotopic chains. Normally, as in the first part of this section, these two observables are considered to reflect similar aspects of the equilibrium structure. Figure 2, however, shows that they, in fact, reflect somewhat different physics and that this is useful in classifying different structural morphologies.

The Gd transition region is known to be rapid (almost as fast as that near $A = 100$) and has been recently described, based upon extensive new data, in terms of a critical phase transition, involving a crossing of spherical and deformed configurations [2]. Both $E(2_1^+)$ and $R_{4/2}$ change very rapidly near $N = 90$.

In Th, a gradual onset of deformation occurs. $E(2_1^+)$ decreases rather gradually, reflecting this evolution. However, surprisingly, $R_{4/2}$ increases almost as abruptly as in Gd.

The explanation centers on understanding the physics behind the ratio $R_{4/2}$. Rotational energies go as $(\hbar/2I)J(J+1)$. Hence, in first order, as soon as nuclei become deformed, the moment of inertia cancels out in the ratio $R_{4/2}$. $R_{4/2} = 3.33$ for deformed nuclei regardless of the deformation. Thus, $R_{4/2}$ is like a binary indicator of the spherical or deformed character of a nucleus: hence the rapid rise in $R_{4/2}$ in Th as soon as stable deformation sets in. $E(2_1^+)$, in contrast, is proportional to $1/\beta$ (in first order) and hence decreases systematically as the deformation grows.

The third trajectory in Fig. 2 reflects a new degree of freedom, axial asymmetry. The rotor value, $R_{4/2} = 3.33$, applies only for axially symmetric nuclei. For nuclei with large axial asymmetry, $R_{4/2}$ is substantially lower ($\sim$2.5 for $\gamma \sim 30°$). Hence, in the Ba nuclei, which evolve from spherical through highly axially asymmetric shapes toward symmetric rotor shapes, $R_{4/2}$ increases gradually and, likewise, $E(2_1^+)$ drops smoothly and slowly.

More formal developments of models for transitional nuclei are urgently needed as opportunities for the study of new mass regions with exotic nuclei emerge in the coming years. Hopefully, the discussion above will encourage such work.

3. THE Ni AND Sn NUCLEI

Two particularly attractive opportunities for interesting structural evolution that can address fundamental questions relating to shell structure are the Ni and Sn nuclei. The Ni isotopes are unique: from the proton drip line to very neutron-rich nuclei, these isotopes cross four magic numbers (20, 28, 40, 50) and span five major shells (8–20, 20–28, 28–40, 40–50, >50).

One of the major issues in exotic nuclei is the robustness of magicity. We know that major subshell gaps such as $Z = 40$ and 64 are fragile and recent studies [3] of ^{32}Mg have shown that even the major-shell gap $N = 20$ can dissolve in proton deficient nuclei. Therefore, of high interest in Ni is the status of the magic numbers at the limits of accessibility.

In Sn, recent data [4] reveal a fascinating facet of the evolution of structure that is related to a very general phenomenon recently noted in two-particle and two-hole nuclei. The Sn systematics is shown in Fig. 3*a*. ^{132}Sn shows the characteristics of a doubly magic nucleus. Most of the Sn nuclei show nearly constant excited-state energies typical of the generalized seniority scheme. $E(2_1^+) \sim 1200$ across the entire $N = 50$–82 shell. It is a striking departure in this systematics, therefore, that $E(2_1^+)$ in ^{134}Sn drops to 725 keV. More importantly, $R_{4/2}(^{134}\mathrm{Sn}) = 1.45$, whereas $R_{4/2}(^{130}\mathrm{Sn}) = 1.63$. Is there a simple explanation of this behavior? Before addressing that issue, we note that this phenomenon in Sn is not isolated. In fact, it applies to virtually *all* two-particle ($2p$) and two-hole ($2h$) nuclei. One (of many) examples is shown in Fig. 3*b*. It has not been easy to understand these data. Yet, the fact that it has now been found in Sn changes the situation. Sn, being singly magic, is very simple to calculate in the shell model: one needs to treat only two-valence nucleons occupying a small set of orbits. If we can understand the data in Sn (in a transparent way), we can perhaps get an understanding of a much more general phenomenon.

This point highlights one of the most appealing subjects of exotic nuclei. The opportunity is not to study hundreds of new nuclei, but the possibility to access selected nuclei with special properties. Often, as in this case, the key is to choose nuclei that magnify particular interactions or isolate particular effects in systems that are easy to understand.

Mias [4] has carried out shell-model calculations for ^{130,134}Sn and reproduced the essential results above, in particular, the larger $R_{4/2}$ ($2h$) value. From an analysis of the resulting wave functions, the underlying physics becomes clear. At the end of major shells, the shell-model orbit j values are generally low (e.g., $d_{3/2}$), while, at the start of a shell, higher j values are encountered. Hence, above a magic number, n particles in a $|j^n\rangle$ configuration, interacting with a short-range attractive residual interaction, give a sequence of 0^+, 2^+, 4^+, 6^+ states, with successively smaller spacings, and, hence, an $R_{4/2}$ ratio that is well below 2.0. Below a magic number, though, a 4^+ level cannot be formed from, say, two particles in a $d_{3/2}$ orbit. The 4_1^+ level therefore requires elevation of a particle in such an orbit to another orbit, requiring extra energy and leading to a larger $R_{4/2}$ value.

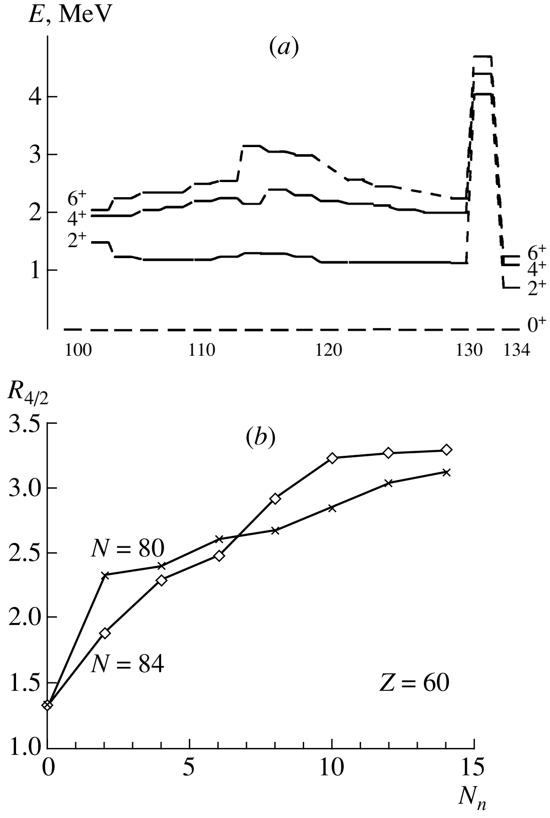

Fig. 3. (*a*) Systematics of the lowest states of the Sn nuclei. (*b*) Systematics of $R_{4/2}$ ratios for $Z = 60$, showing the general result that $R^{2h}_{4/2} > R^{2p}_{4/2}$ (figure courtesy of N.V. Zamfir).

The fact that there is such a simple explanation of the Sn systematics and that the same phenomenon, $R^{2h}_{4/2} > R^{2p}_{4/2}$, appears in essentially all nonmagic nuclei where the data are known suggests that similar underlying physics is at work, although it would have been much more difficult, and, doubtless, ambiguous, to have first tackled the problem in nuclei with open shells of both protons and neutrons.

4. CONCLUSION

In the paragraphs above, we have shown a couple of examples of structural evolution, first in collective nuclei and then in singly magic nuclei, discussing the underlying physics, with emphasis on the systematic opportunities provided by beams of exotic nuclei.

ACKNOWLEDGMENTS

I am grateful to G. Mias for permission to quote the results of his shell-model calculations for Sn and to N.V. Zamfir for innumerable discussions and for help in preparation of the figures.

This work was supported by the US DOE under grant no. DE-FG02-91ER-40609.

REFERENCES

1. R. F. Casten *et al.,* Phys. Lett. B **481**, 1 (2000).
2. F. Iachello, N. V. Zamfir, and R. F. Casten, Phys. Rev. Lett. **81**, 1191 (1998).
3. T. Motobayashi *et al.,* Phys. Lett. B **346**, 9 (1995).
4. G. Mias, Senior Project (Yale Univ., 2000); G. Mias *et al.,* to be published.

Physics of Atomic Nuclei, Vol. 64, No. 6, 2001, pp. 1005–1010. From Yadernaya Fizika, Vol. 64, No. 6, 2001, pp. 1081–1086.
Original English Text Copyright © 2001 by Rohoziński, Pomorski, Próchniak, Zając, Droste, Srebrny.

Collective States of Transitional Nuclei*

S. G. Rohoziński**, **K. Pomorski**[1)], **L. Próchniak**[1)],
K. Zając[1)], **Ch. Droste**[2)], and **J. Srebrny**[2)]

Institute of Theoretical Physics, Warsaw University, Poland

Received September 11, 2000

Abstract—The “quadrupole plus pairing” collective model is constructed for the microscopic description of low-lying collective states of even–even transitional nuclei. Inclusion of the model to the core–quasiparticle coupling model in order to describe odd nuclei is realized. An approximation scheme suitable for investigation of the quadrupole excitations is demonstrated. Exemplary results of microscopic calculations for the Ru isotopes are shown. © *2001 MAIK “Nauka/Interperiodica”*.

1. INTRODUCTION

The aim of the research presented here is a microscopic description of low-lying collective excitations in transitional nuclei. Nowadays, the nuclear many-body problem is treated mainly in an independent-quasiparticle approximation. Different approaches, i.e., different interactions and different methods, are used to define the quasiparticles and the mean field.[3)] However, all of them deal with the notion of intrinsic system. To describe rotational bands in well-deformed nuclei, it is sufficient to project somehow intrinsic states onto a good angular momentum or to rotate the intrinsic system. This is not the case for transitional nuclei in which rotational motion is coupled to vibrations. On the other hand, correlations of quasiparticles taken into account within various versions of the random-phase approximation (RPA) lead just to vibrational states. Again, the rotation–vibration coupling important for transitional nuclei is not taken into account. In principle, a version of the interacting-boson model (IBM) could explain collective states in transitional nuclei as such types of models give states of a definite angular momentum and are able to include rotation–vibration coupling. Unfortunately, reliable methods of calculating parameters of the IBM Hamiltonians from a microscopic many-body theory are not known, and the IBM remains a purely phenomenological model as yet.

At the moment, the best method of description of the collective states of transitional nuclei seems to be the generator-coordinate method (GCM) leading to an integral eigenvalue problem provided all variables adequate for the orientation and vibrations of the nucleus are used as generator coordinates. The Gaussian overlap approximation (GOA) to the GCM leads to a differential eigenvalue problem [2] for a general Bohr Hamiltonian (GBH) [3]. A classical counterpart of GBH can be obtained from a microscopic theory also by means of the cranking method or the adiabatic time-dependent approximation to a microscopic Hamiltonian [4, 5]. However, then a requantization procedure should be applied to such a Hamiltonian in order to obtain its quantum form. Nowadays, one has reliable methods of calculation of parameters of the GBH from a particular microscopic Hamiltonian. The description of collective states *via* GBH has, however, its shortcoming: this is an adiabatic approach, and coupling to other, say, quasiparticle degrees of freedom is neglected. This is why it can be appropriate for even–even nuclei only.

The GBH has already been used for a long time to describe the quadrupole collective states of transitional nuclei from different regions of masses (e.g., [4, 6]). The Bohr deformation parameters, β and γ, and the Euler angles defining an orientation of the intrinsic system have been used as the dynamical variables. The approach, when treated as phenomenological with parameters of the Hamiltonian fitted to experimental data, has been quite successful (cf., e.g., [7]). However, when the collective Hamiltonian (potential and inertial functions) was calculated microscopically, the results obtained, especially for energy levels, were not compatible with the corresponding experimental quantities [6]. It has turned out that the calculated inertia is too small, giving overly high

---

*This article was submitted by the authors in English.

[1)] Institute of Physics, Maria Curie-Skłodowska University, Lublin, Poland.

[2)] Institute of Experimental Physics, Warsaw University, Poland.

[3)] E.g., [1] can be consulted for a review of different approaches to the theory of nuclear structure mentioned here and below throughout the Introduction.

**e-mail: `Stanislaw-G.Rohozinski@fuw.edu.pl` excitation energies. This conclusion seems to be independent of a microscopic model used so far. A strong sensitivity of calculated inertial functions to pairing correlations is observed in all cases, which suggests that the pairing vibrations [8] can strongly affect the quadrupole excitations (cf. [9]). In fact, it seems to be a natural effect. The schematic microscopic model of the nuclear structure takes into account the quadrupole and pairing two-body interactions. So, this is natural to treat mean values of the corresponding single quasiparticle potentials on an equal footing and use them as collective dynamical variables. This is why we have proposed the "quadrupole plus pairing" collective model [10].

In Section 2.1 the GBH in an extended "quadrupole plus pairing" collective space is constructed. It is shown in Section 2.2 how to describe collective states of even–odd and odd–even transitional nuclei within a core–quasiparticle coupling model using results of the GBH. An approximation scheme for solving the eigenvalue problem of the GBH suitable for description of the quadrupole excitations is explained in Section 3. Exemplary results of calculations for isotopes of ruthenium are demonstrated in Section 4. Finally, conclusions coming from the present research are drawn in Section 5.

2. THE "QUADRUPOLE PLUS PAIRING" COLLECTIVE MODEL

2.1. Even–Even Nuclei: The General Bohr Hamiltonian

Let the space of collective variables of the model be formed by the set of the nine following quantities:

β, γ, the Bohr deformation parameters (describing the nuclear shape or the quadrupole moment in the intrinsic frame);

ϕ, θ, ψ, the Euler angles (describing the orientation of the intrinsic frame);

Δ^p, Δ^n, the proton and neutron energy gaps (describing the proton and neutron pairing correlations);

Φ^p, Φ^n, the proton and neutron gauge angles (describing rotations in the proton and neutron gauge spaces or transfer of the proton and neutron pairs).

Thus, the collective motion described by the model has nine degrees of freedom. We do not introduce here any quantities connected with the correlation of proton–neutron pairs as we do not take into account the proton–neutron pairing forces. Those can play a role for the $Z \approx N$ systems, i.e., either lighter or exotic ones which are beyond the scope of the present research.

The classical collective Hamiltonian can be written as

$$\mathcal{H}_{\text{quad-pair}} = \frac{1}{2}\left[B_{\beta\beta}\dot{\beta}^2 + 2B_{\beta\gamma}\dot{\beta}\beta\dot{\gamma} + B_{\gamma\gamma}\beta^2\dot{\gamma}^2\right] \tag{1}$$

$$+ \frac{1}{2}\sum_{k=1}^{3} I_k^2(\dot{\phi}, \dot{\theta}, \dot{\psi})/\mathcal{J}_k$$

$$+ V_{\text{def}} + \sum_{t=p,n}\left\{\frac{1}{2}\left[B_{\Delta^t\Delta^t}(\dot{\Delta}^t)^2 + \mathcal{J}_{\Phi^t}(\dot{\Phi}^t)^2\right]\right.$$

$$+ V_{\text{pair}}^{(t)} + \lambda^{(t)}\mathcal{J}_{\Phi^t}\dot{\Phi}^t$$

$$\left. + B_{\beta\Delta^t}\dot{\beta}\dot{\Delta}^t + B_{\gamma\Delta^t}\beta\dot{\gamma}\dot{\Delta}^t\right\}.$$

It does not contain mixed terms of type $\dot{\Delta}^p\dot{\Delta}^n$ as the proton and the neutron pairing are not coupled to each other. Also, it is not invariant under time reversal because of terms linear in $\dot{\Phi}^t$, meaning that the direction of rotation in the proton or neutron gauge spaces (i.e., adding or subtracting nucleon pairs) is not the same thing. The Hamiltonian in the form (1) is obtained by means of the cranking method. It has to be quantized by the Pauli–Podolsky prescription. The GCM gives a quantum Hamiltonian immediately. The structure of the quantum collective Hamiltonian obtained by either method is the following:

$$\hat{\mathcal{H}}_{\text{quad-pair}} \tag{2}$$

$$= \hat{\mathcal{T}}_{\text{vib}}(\beta, \gamma; \Delta^n, \Delta^p) + V_{\text{def}}(\beta, \gamma, \Delta^n, \Delta^p)$$

$$+ \hat{\mathcal{H}}_{\text{rot}}(\phi, \theta, \psi; \beta, \gamma, \Delta^n, \Delta^p)$$

$$+ \sum_{t=p,n}\left[\hat{\mathcal{T}}_{\text{pair}}^{(t)}(\Delta^t, \Phi^t; \beta, \gamma)\right.$$

$$\left. + V_{\text{pair}}^{(t)}(\beta, \gamma, \Delta^t) + \hat{\mathcal{T}}_{\text{quad-pair}}^{(t)}(\beta, \gamma, \Delta^t)\right].$$

The particular terms of the Hamiltonian in (2) are either the second or the first order differential operators in their arguments given in front of semicolon; the term $\hat{\mathcal{T}}_{\text{quad-pair}}^{(t)}$ is the second order differential operator in all of its arguments. We do not give here an evident form of all these terms which is more or less obvious. The entire Hamiltonian is determined by the following 19 functions of β, γ, Δ^p, and Δ^n for a given Z, N (cf. (1)):

$V_{\text{def}}, V_{\text{pair}}^{(p)}, V_{\text{pair}}^{(n)}$, the deformation and pairing potentials;

$B_{\beta\beta}, B_{\beta\gamma}, B_{\gamma\gamma}$, the quadrupole vibrational inertial functions (mass parameters);

$\mathcal{J}_1, \mathcal{J}_2, \mathcal{J}_3$, the quadrupole moments of inertia;

$B_{\Delta^t\Delta^t}$ for $t = p, n$, the pairing vibrational inertial functions;

$B_{\beta\Delta^t}, B_{\gamma\Delta^t}$ for $t = p, n$, the quadrupole–pairing mixed vibrational inertial functions;

$\mathcal{J}_{\Phi^t}$ for $t = p, n$, the pairing moments of inertia;

$\lambda^{(t)}$ for $t = p, n$, the chemical potentials.

All above functions can be calculated from a given microscopic model. We do not give here prescriptions how to do it. References [2, 4, 5, 10, 11] can be consulted in this respect. It remains to construct other collective operators like, e.g., electric and magnetic multipole operators. This can also be done from the microscopic theory.

Collective states of a given nucleus can be found by solving the common eigenvalue problem for the following set of operators:

$\hat{\mathcal{H}}_{\mathrm{quad-pair}}$, the collective Hamiltonian;

$\hat{I}^2$, $\hat{I}_z$, the total angular momentum and its projection onto a lab axis z;

$\hat{\mathcal{N}}_t = -i\partial/\partial\Phi_t$ for $t = p, n$, the particle number excess operators. In other words the following set of equations should be solved:

$$\hat{\mathcal{H}}_{\mathrm{quad-pair}}|IM, n_{\mathrm{p}}, n_{\mathrm{n}}; Z, N\rangle \tag{3}$$

$$= E_{In_{\mathrm{p}},n_{\mathrm{n}}}(Z,N)|IM, n_{\mathrm{p}}, n_{\mathrm{n}}; Z, N\rangle,$$

$$\hat{I}^2|IM, n_{\mathrm{p}}, n_{\mathrm{n}}; Z, N\rangle = I(I+1)\hbar^2|IM, n_{\mathrm{p}}, n_{\mathrm{n}}; Z, N\rangle,$$

$$\hat{I}_z|IM, n_{\mathrm{p}}, n_{\mathrm{n}}; Z, N\rangle = M\hbar|IM, n_{\mathrm{p}}, n_{\mathrm{n}}; Z, N\rangle,$$

$$\hat{\mathcal{N}}_p|IM, n_{\mathrm{p}}, n_{\mathrm{n}}; Z, N\rangle = 2n_{\mathrm{p}}|IM, n_{\mathrm{p}}, n_{\mathrm{n}}; Z, N\rangle,$$

$$\hat{\mathcal{N}}_n|IM, n_{\mathrm{p}}, n_{\mathrm{n}}; Z, N\rangle = 2n_{\mathrm{n}}|IM, n_{\mathrm{p}}, n_{\mathrm{n}}; Z, N\rangle.$$

For the nucleus of given Z and N, the excitation energies $E_I(Z,N) = E_{I00}(Z,N) - E_{000}(Z,N)$ and the states $|IM; Z, N\rangle \equiv |IM, 0, 0; Z, N\rangle$ with the pair excess numbers $n_{\mathrm{p}}, n_{\mathrm{n}} = 0$ are relevant. However, those of either $n_{\mathrm{p}} = 1$ or $n_{\mathrm{n}} = 1$ will be important for the odd–even or the even–odd nuclei, respectively.

2.2. Odd Nuclei: The Core–Quasiparticle Coupling Model

Having even–even nuclei described, one can use them as cores and try to describe collective states in odd nuclei within the Core–Quasiparticle Coupling Model (CQCM) [12]. The collective excitations of an odd nucleus are understood as collective excitations of the even–even cores coupled to the single-particle excitations of the odd particle. The quadrupole–quadrupole interaction between the core and the particle is assumed. Here the description of an even–odd nucleus with given Z (even) and N (odd) is demonstrated. The case of an odd–even nucleus can be repeated in a similar way. The nucleus in question is treated as the system of either the lighter collective core, $(Z, N-1)$, and the neutron or the heavier collective core, $(Z, N+1)$, and the neutron hole. This way, the neutron quasiparticle is defined.

The following information about the cores is further needed:

excitation energies,

$$E_I(Z, N \mp 1);$$

reduced matrix elements of the mass quadrupole operator,

$$Q_{I'I}(Z, N \mp 1) = \langle I'; Z, N \mp 1 \parallel Q_2 \parallel I; Z, N \mp 1\rangle;$$

the neutron pair transfer matrix elements,

$$\Delta^n_{I'I}(Z, N \mp 1) = \delta_{I'I}\delta_{M'M}\langle IM, 0, \pm 1; Z, N \mp 1|\Delta^n e^{\pm 2i\Phi^n}|IM, 0, 0; Z, N \mp 1\rangle.$$

All the above quantities one has when solving the eigenvalue problem (3) of the previous section.

Needful information about the neutron comprises the following quantities:

the neutron single-particle energies, e^n_j, from a vicinity of the Fermi level μ^n;

reduced single-particle quadrupole matrix elements, $q^n_{jj'} = \langle n, j \parallel r^2 Y_2 \parallel n, j'\rangle$.

The two quantities, the neutron Fermi level μ^n and the quadrupole–quadrupole coupling constant κ, can, in principle, be deduced from considerations on the equilibrium deformation but are usually treated as fitting parameters.

The core–quasiparticle state with spin J and energy $E_J(Z,N)$ of the even–odd nucleus has the form

$$|JK; Z, N\rangle = \sum_{j,I}\Big\{ u^n_J(j,I)\left[a^\dagger_{nj}|I; Z, N-1\rangle\right]_{JK} \tag{4}$$

$$+ v^n_J(j,I)\left[\tilde{a}_{nj}|I; Z, N+1\rangle\right]_{JK}\Big\}.$$

The standard CQCM equations for the spectroscopic factors $u^n_J(j,I)$ and $v^n_J(j,I)$ read

$$\left(E_J(Z,N) - E_I(Z,N-1) - (e^n_j - \mu^n)\right) u^n_J(j,I)$$

$$= -\frac{\kappa}{2}\sum_{j',I'}(-1)^{j'+I'+J}\begin{Bmatrix} j & j' & 2 \\ I' & I & J \end{Bmatrix} \tag{5}$$

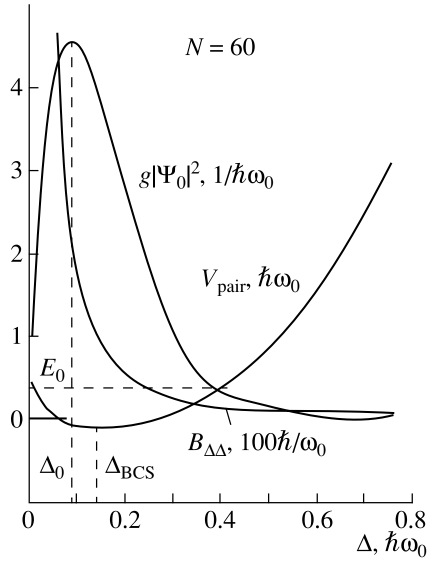

Fig. 1. Zero-point pairing vibration of neutrons in ^{104}Ru at deformation $\beta = 0.2$, $\gamma = 20°$. The equilibrium value of the energy gap is $\Delta_{\rm BCS} \approx 0.14\hbar\omega_0$, whereas the most probable value is $\Delta_0 \approx 0.09\hbar\omega_0$. The oscillator frequency is $\hbar\omega_0 \approx 41/A^{1/3}$ MeV.

$$\times\, q^n_{jj'} Q_{I'I}(Z, N-1) u^n_J(j', I') + \sum_{j',I'} \Delta^n_{I'I}(Z, N-1)\delta_{j'j} v^n_J(j', I'),$$

$$\left(E_J(Z,N) - E_I(Z, N+1) + (e^n_j - \mu^n)\right) v^n_J(j, I) = \frac{\kappa}{2}\sum_{j',I'}(-1)^{j'+I'+J}\left\{\begin{matrix} j & j' & 2 \\ I' & I & J\end{matrix}\right\} \tag{6}$$

$$\times\, q^n_{jj'} Q_{I'I}(Z, N+1) v^n_J(j', I') + \sum_{j',I'} \Delta^n_{I'I}(Z, N+1)\delta_{j'j} u^n_J(j', I').$$

The core-polarization effect, which might be important, is neglected in the above equations.

3. AN APPROXIMATION SCHEME

So far, the exact solutions of the eigenvalue problem (3) are not available. Construction of a code for full diagonalization is in progress. To investigate the quadrupole collective states of transitional nuclei, an approximation scheme is invented. It goes in the following steps:

1. The quadrupole—pairing coupling in kinetic energy is neglected; i.e., the last term in Hamiltonian (2) is set to $\hat{\mathcal{T}}^{(t)}_{\rm quad-pair}(\beta, \gamma, \Delta^t) = 0$ for $t = p, n$.

2. The zero-point pairing vibrations of neutrons and protons for given β and γ are found by solving the partial eigenvalue problem

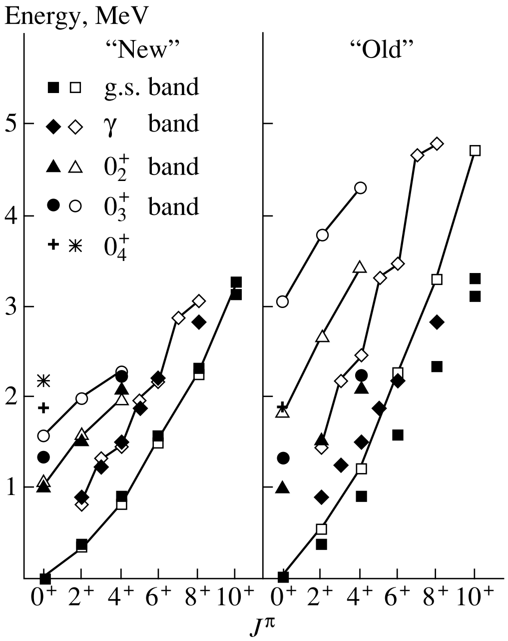

Fig. 2. Experimental [13, 14] (closed points) and theoretical (open points connected by straight lines) energy levels in ^{104}Ru versus angular momentum J^π. The theoretical levels are calculated with ("new") and without ("old") the effect of zero-point pairing vibration taken into account.

$$\hat{\mathcal{H}}^{(t)}_{\rm pair}(\Delta^t; \beta, \gamma)\Psi_0(\Delta^t; \beta, \gamma) = E^{(t)}_0(\beta, \gamma)\Psi_0(\Delta^t; \beta, \gamma), \tag{7}$$

$$\hat{N}_t(\Phi^t)\Psi_0(\Delta^t; \beta, \gamma) = 0,$$

where

$$\hat{\mathcal{H}}^{(t)}_{\rm pair}(\Delta^t; \beta, \gamma) = \hat{\mathcal{T}}^{(t)}_{\rm pair}(\Delta^t; \beta, \gamma) + V^{(t)}_{\rm pair}(\Delta^t, \beta, \gamma) \tag{8}$$

and the collective pairing kinetic energy in the subspace belonging to eigenvalues $2n_p = 0$ and $2n_n = 0$ of the particle number excess operators reads

$$\hat{\mathcal{T}}^{(t)}_{\rm pair} = -\frac{\hbar^2}{2\sqrt{g(\Delta^t)}}\frac{\partial}{\partial\Delta^t}\frac{\sqrt{g(\Delta^t)}}{B_{\Delta^t\Delta^t}(\Delta^t)}\frac{\partial}{\partial\Delta^t}; \tag{9}$$

here, $g(\Delta^t, \beta, \gamma)$ is a normalization weight.

3. The most probable neutron or proton energy gap $\Delta^t_0(\beta, \gamma)$ is found, i.e., the value of Δ^t for which $g|\Psi_0|^2$ takes a maximum at given β and γ (see Fig. 1).

4. The eigenvalue problem is solved for the following quadrupole part of the GBH (2) with the energy gaps replaced with their most probable values for given deformations:

$$\begin{aligned}\hat{\mathcal{H}}_{\rm coll} = {} & \hat{\mathcal{T}}_{\rm vib}(\beta, \gamma; \Delta^n_0(\beta, \gamma), \Delta^p_0(\beta, \gamma)) \\ & + V_{\rm coll}(\beta, \gamma, \Delta^n_0(\beta, \gamma), \Delta^p_0(\beta, \gamma)) \\ & + \hat{\mathcal{H}}_{\rm rot}(\phi, \theta, \psi; \beta, \gamma, \Delta^n_0(\beta, \gamma), \Delta^p_0(\beta, \gamma)),\end{aligned} \tag{10}$$

where

$$V_{\text{coll}} = V_{\text{def}} + E_0^{(n)} + E_0^{(p)} \tag{11}$$

and the vibrational and rotational quadrupole kinetic energies are

$$\hat{\mathcal{T}}_{\text{vib}} = -\frac{\hbar^2}{2\sqrt{wr}}\left\{\frac{1}{\beta^4}\left[\partial_\beta\left(\beta^4\sqrt{\frac{r}{w}}B_{\gamma\gamma}\partial_\beta\right) - \partial_\beta\left(\beta^3\sqrt{\frac{r}{w}}B_{\beta\gamma}\partial_\gamma\right)\right]\right.$$
$$\left.+\frac{1}{\beta\sin 3\gamma}\left[\frac{1}{\beta}\partial_\gamma\left(\sqrt{\frac{r}{w}}\sin 3\gamma B_{\beta\beta}\right)\partial_\gamma - \partial_\gamma\left(\sqrt{\frac{r}{w}}\sin 3\gamma B_{\beta\gamma}\partial_\beta\right)\right]\right\} \tag{12}$$

and

$$\hat{\mathcal{H}}_{\text{rot}} = \frac{1}{2}\sum_{k=1}^{3}\hat{I}_k^2/\mathcal{J}_k, \tag{13}$$

respectively. The operators $\hat{I}_1$, $\hat{I}_2$, and $\hat{I}_3$ are the intrinsic angular momenta being the first-order differential operators in the Euler angles; here, the volume element is $d\tau = \beta^4\sqrt{wr}|\sin 3\gamma|d\beta d\gamma\sin\theta d\theta d\phi d\psi$, where $w = B_{\beta\beta}B_{\gamma\gamma} - B_{\beta\gamma}^2$ and $r = \mathcal{J}_1\mathcal{J}_2\mathcal{J}_3/(4\beta^6 \times \sin^2 3\gamma)$.

The above approximation scheme allows for investigation of the quadrupole excitations of a given nucleus which are affected by the zero-point pairing vibrations. The pairing excitations themselves are omitted.

4. RESULTS FOR Ru ISOTOPES

To illustrate the approach presented in the previous sections, some results of calculations within the present approximation scheme for even–even neutron-rich isotopes of ruthenium ($^{104-114}$Ru, $Z = 44$, $N = 60$–70) are shown here. The Nilsson deformed mean field and state-independent pairing forces were used for the microscopic description of the nuclei in question. To construct the collective Hamiltonian, we used the microscopic–macroscopic method for deformation potential, cranking method for mass parameters, and the GCM + GOA for pairing. There were no free parameters fitted to data in the calculation. Apart from earlier data [13, 14], we have at our disposal still unpublished data taken from multiple Coulomb excitations (COULEX) of ^{104}Ru [15], the heaviest stable isotope of ruthenium. The COULEX data contain not only energy levels but also a comprehensive set of $E2$ matrix elements so important for verification of collective models. Unfortunately, COULEX of heavier, unstable Ru isotopes cannot be observed. These nuclei are investigated mainly by means of γ spectroscopy of fission fragments [16, 17]. We have also at our disposal by courtesy of Urban [18] unpublished data for even–odd isotopes ^{109}Ru and ^{111}Ru. Calculations for these

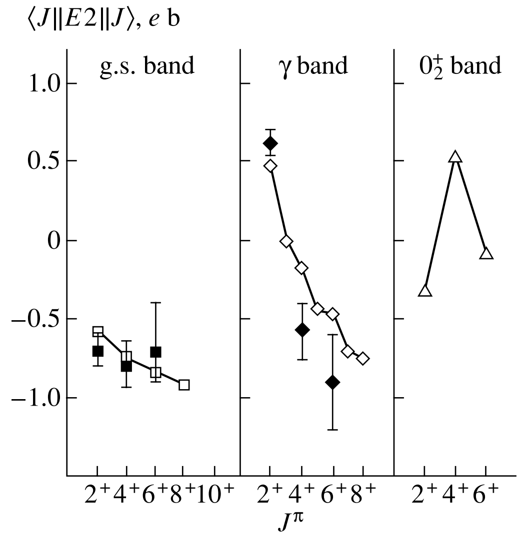

Fig. 3. Experimental [13–15] (closed points) and calculated (open points connected by straight lines) diagonal reduced matrix elements of the quadrupole electric operator in excited states of ^{104}Ru.

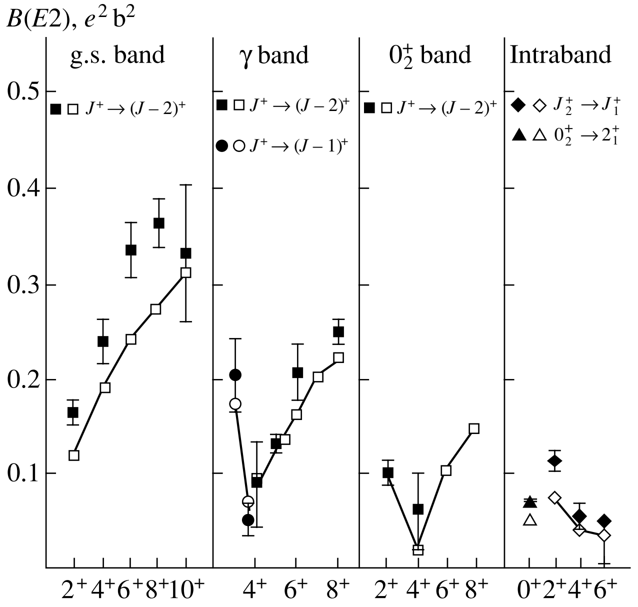

Fig. 4. Experimental [13–15] (closed points) and calculated (open points connected by straight lines) reduced $E2$ transition probabilities in ^{104}Ru.

odd isotopes using the results for the corresponding even–even cores ^{108}Ru, ^{110}Ru, and ^{112}Ru are in progress.

Figure 2 shows how important the effect of zero-point pairing vibrations on the quadrupole excitation energies in ^{104}Ru really is. The present ("new") calculation gives energies in excellent agreement with experimental values, whereas that with the original Bohr Hamiltonian ("old") overestimates them a lot. The same effect is observed for other even–even Ru isotopes. Figures 3 and 4 show the results of the present calculation of diagonal reduced $E2$ matrix elements and reduced $E2$ transition probabilities, respectively, again for ^{104}Ru. The agreement with experimental data is really very good, as good as for microscopic calculations without free parameters.

5. CONCLUSIONS

The collective "quadrupole plus pairing" model based on the schematic microscopic model has been constructed to describe low-lying collective excitations of even–even transitional nuclei. In order to investigate the quadrupole collective states, an approximation scheme has been proposed which consists in taking into account an effect of the zero-point pairing vibrations on the quadrupole part of the collective Hamiltonian. Such an approach to the quadrupole excitations has been successfully applied to the description of collective properties of even–even transitional nuclei from various mass regions, namely, isotopes of Te, Xe, Ba, Ce, Nd, and Sm from the neutron-deficient region $50 < Z, N < 82$ [10]; isotopes of Ru and Pd from the neutron-rich region $28 < Z < 50$, $50 < N < 82$ [19]; and isotopes of Gd and Er from the rare-earth region [20]. In all cases, an essential role of zero-point pairing vibrations was found. Including this effect has allowed us to obtain very good results for neutron-rich and rare-earth nuclei and much improvement of results for neutron-deficient ones. In all calculations, no free parameters were used to fit results to experimental data. It has been shown how the present collective model can be inserted to core–quasiparticle coupling model in order to describe collective properties of odd nuclei.

In conclusion, we may say that the low-lying collective excitations of transitional nuclei seem to be of the "quadrupole plus pairing" rather than pure quadrupole nature. However, we are still not sure if only these two types of degrees of freedom really account for the lowest collective excitations of all heavy nuclei.

ACKNOWLEDGMENTS

The contribution of one of us (S.G.R.) to this research was supported in part by the Polish Committee for Scientific Research (KBN) under contract no. 2 P03B 040 14. The present paper is an introduction to a new project, partial support of which by the KBN is acknowledged in advance.

REFERENCES

1. P. Ring and P. Schuck, *The Nuclear Many-Body Problem* (Springer-Verlag, Berlin, 1980).
2. A. Góźdź, K. Pomorski, M. Brack, and E. Werner, Nucl. Phys. A **442**, 50 (1985).
3. K. Kumar and M. Baranger, Nucl. Phys. A **92**, 608 (1967).
4. M. Baranger and K. Kumar, Nucl. Phys. A **122**, 241 (1968).
5. T. Kaniowska, A. Sobiczewski, K. Pomorski, and S. G. Rohoziński, Nucl. Phys. A **274**, 151 (1976).
6. S. G. Rohoziński, J. Dobaczewski, B. Nerlo-Pomorska, *et al.*, Nucl. Phys. A **292**, 66 (1977).
7. D. Troltenier, J. P. Draayer, B. R. S. Babu, *et al.*, Nucl. Phys. A **601**, 56 (1996).
8. D. R. Bès, R. A. Broglia, R. P. J. Perazzo, and K. Kumar, Nucl. Phys. A **143**, 1 (1970).
9. S. Piłat and K. Pomorski, Nucl. Phys. A **554**, 413 (1993).
10. L. Próchniak, K. Zając, K. Pomorski, S. G. Rohoziński, and J. Srebrny, Nucl. Phys. A **648**, 181 (1999).
11. A. Góźdź and K. Pomorski, Nucl. Phys. A **451**, 1 (1986).
12. F. Dönau and U. Hagemann, Z. Phys. A **293**, 31 (1979).
13. J. Srebrny, D. Cline, C. Y. Wu, *et al.*, in *Proceedings of International Conference on Extreme States in Nuclear Systems, Dresden, 1980*, Report No. 404, ZfK (Rossendorf, 1980), p. 72.
14. J. Stachel, P. Hill, N. Kaffrell, *et al.*, Nucl. Phys. A **419**, 589 (1984).
15. J. Srebrny, T. Czosnyka, D. Cline, *et al.*, (to be published).
16. J. A. Shannon, W. R. Philips, J. L. Durrel, *et al.*, Phys. Lett. B **336**, 136 (1994).
17. Q. H. Lu, K. Butler-Moore, S. J. Zhu, *et al.*, Phys. Rev. C **52**, 1348 (1995).
18. W. Urban, private communication.
19. K. Zając, L. Próchniak, K. Pomorski, *et al.*, Nucl. Phys. A **653**, 71 (1999).
20. K. Zając, L. Próchniak, K. Pomorski, *et al.*, Acta Phys. Pol. B **31**, 459 (2000).

Physics of Atomic Nuclei, Vol. 64, No. 6, 2001, pp. 1011–1014. From Yadernaya Fizika, Vol. 64, No. 6, 2001, pp. 1087–1090.
Original English Text Copyright © 2001 by Börner, Jentschel.

High-Resolution Gamma-Ray Spectroscopy*

H. G. Börner** and **M. Jentschel**

Institut Laue–Langevin, Grenoble, France

Received September 11, 2000

Abstract—To obtain the highest possible resolution in a measurement has always been one of the major challenges for experimental physicists because increased resolution generally results in progress. At the Institut Laue–Langevin, gamma rays emitted after neutron capture can be recorded with parts-per-million resolution. This is achieved by diffracting the gamma rays on highly perfect Si or Ge crystals. Precise measurement of the Bragg angles and the crystal lattice spacings permits the determination of wavelengths or energies. This outstanding resolving power allows the measurement of extremely small Doppler effects caused by the emission of primary gamma rays. These so-called gamma-ray-induced Doppler broadening measurements have given rise to applications in both nuclear and condensed matter physics. *© 2001 MAIK "Nauka/Interperiodica".*

1. INTRODUCTION

Nuclei display many diverse modes of excitation. The observed behavior of nuclear systems can be interpreted in terms of the competition between the motion of individual particles and the collective motion of many nucleons. It is evident that it has always been a central challenge in nuclear physics to understand the interplay between these concepts. This is related to the nature of the nucleus as a many-body quantal object and to the role of the Pauli principle in this fermionic system. Despite years of studies, both experimental and theoretical, we do not yet fully understand collective excitations. Many different models are needed to describe the many features observed. The interplay between the different degrees of freedom in a nucleus can be ideally probed by investigating the gamma transitions involved in its de-excitation. The most crucial information is thereby obtained from absolute transition rates which can be deduced from the knowledge of the state lifetimes, which provide a very sensitive test of different theoretical approaches. We will in the following describe briefly the main characteristics of the Gamma Ray Induced Doppler broadening (GRID) technique, optimized at the Institut Laue–Langevin, and discuss some of its applications to the measurements of multiphonon states in several nuclei.

2. THE GRID TECHNIQUE

It is well known that the Doppler effect can be used to determine short lifetimes of excited nuclear states. In the Doppler shift attenuation (DSA) technique, one uses accelerated ion beams impinging on a sample. The reaction products then recoil with a velocity that is typically several percent of the speed of light. The Doppler shift of gamma rays emitted by the recoiling nuclei is in the keV region and can easily be measured with semiconductor detectors.

In thermal neutron capture, the product nucleus is excited by the neutron binding energy of approximately 10 MeV. In contrast to the DSA technique, the contribution of the reaction mechanism to the recoil is negligible due to the low average incident energy of thermal neutrons (~25 meV). The capture state will typically decay by the emission of gamma rays since the compound nuclear system is below the particle emission threshold. Each emitted gamma ray induces a recoil in the nucleus of its origin with velocity v given by $v/c = E/Mc^2$, where c is the velocity of light, E is the gamma-ray energy, and M is the mass of the nucleus. These velocities are on the order of 10^{-4} to 10^{-6} of the velocity of light—up to 4 orders of magnitude smaller than those observed in DSA. Consequently the Doppler shifts of secondary gamma rays, emitted after gamma-ray-induced recoil, are extremely small. They can be detected with ppm resolution crystal spectrometers like those available at the Institut Laue–Langevin [1, 2]. Because there is no preferred direction for the emission of primary gamma rays, the secondary gamma rays will show a Doppler broadening rather than a Doppler shift. The obtained lineshape depends—besides the magnitude of the original recoil—on two time scales: the lifetime τ of the nuclear level that is depopulated by the measured gamma ray and the slowing-down time for the recoiling atom to thermalize. The corresponding

---

*This article was submitted by the authors in English.

**e-mail: `borner@ill.fr`

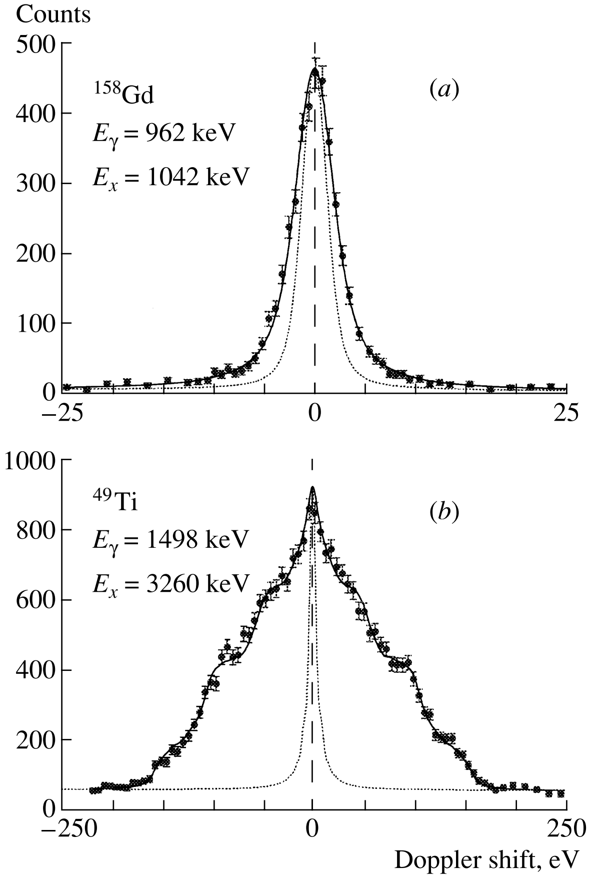

Fig. 1. Two examples for Doppler-broadened lineshapes: (*a*) the lineshape obtained for the lifetime study of a level in ^{158}Gd, (*b*) the lineshape obtained for the study of interatomic potentials using TiO_2 single crystals. The dotted curves show the instrumental resolution function (about 3 ppm for ^{158}Gd). The solid curves are fits to the data that incorporate Doppler broadening due to the finite lifetimes (∼500 fs for the ^{158}Gd level, ∼15 fs for the ^{49}Ti level). Mind the different scales for the abscissa: the Doppler shift for ^{49}Ti is large compared to ^{158}Gd because (i) ^{49}Ti is lighter; (ii) the recoil in ^{49}Ti is mainly due to primary feeding, whereas it is mainly due to cascade feeding in ^{158}Gd; and (iii) the lifetime of the ^{49}Ti level is much shorter (less slowing down) than the one chosen for ^{158}Gd. The line shape of the upper profile shows structure due to the fact that an oriented single crystal was used. In the case of Gd the target consisted of powder material.

technique is called GRID, and more details of the basic principles may be found elsewhere [3, 4]. When the nucleus has deexcited after neutron capture, it may find itself either in a stable ground state or decay further—generally by beta decay or K capture. Also, such subsequent decay modes induce recoils which can be studied in high resolution gamma spectroscopy. At low recoil velocities, the slowing-down time is quite short and this limits the determination of lifetimes to below about 10 ps. However, there is in principle no lower limit as below about 1 fs one can measure experimentally the natural width Γ [eV] $\simeq 6.6\times10^{-16}/\tau$ [s] of the corresponding transitions. The slowing down of the recoiling atoms has first been described within the so-called mean-free-path approach [3], but it has also been studied in detail by using molecular dynamics simulations [5]. This has proven to be especially powerful when applied to the measurement of Doppler profiles of gamma rays emitted by atoms from oriented single crystals [6, 7]. Due to the regular arrangement of atoms in a single crystal, the rate of slowing down depends on the recoil direction (channeling and/or blocking caused by the surrounding atoms). In the Doppler profiles, fine structure appears (Fig. 1) which depends on the orientation of the crystals with respect to the spectrometer. The GRID method can be applied to all nuclei which can be reached by thermal neutron capture. In exceptional cases, nuclei with up to two neutrons beyond stability have been studied. Due to the extreme resolving power, natural target materials can be used.

3. TWO-PHONON STATES IN DEFORMED NUCLEI

The existence of two-phonon states in deformed nuclei has been of considerable debate for more than 30 years. It was therefore an important fundamental result in 1991 when an experiment at the ILL [8] using the GRID technique found a state in ^{168}Er which could be associated with a $K^\pi = 4^+$ two-phonon γ-vibrational mode ($4^+\gamma\gamma$). This measurement of enhanced $E2$ transitions from the levels at 2055 keV and 2169 keV, the 4^+ and 5^+ states of the $K^\pi = 4^+$ band, respectively, immediately had both far-reaching theoretical and experimental consequences. These results reinvigorated the experimental searches for multiphonon vibrational excitations in nuclei. It led to searches for multiphonon states in other nuclei. Interesting aspects of vibrational motion were uncovered, including varying degrees of anharmonicities for the single and double-phonon vibrational excitations. Nevertheless the discussion continues and centers now on the magnitude of the two-phonon component in the wave function needed to reproduce the enhanced $E2$ rate. Certain models predict that states with properties of $K^\pi = 4^+$ states should be widespread in the well-deformed rare-earth region. V.G. Soloviev, with the quasiparticle-phonon nuclear model (QPNM) [9], however, predicted that $K^\pi = 4^+$ states should exist only in a few cases such as ^{164}Dy, ^{166}Er, and ^{168}Er. The predictions concerning $K^\pi = 0^+$ two-phonon γ vibrations ($0^+\gamma\gamma$) are even more controversial. Some models predict that they should lie at excitation energies similar to the two-phonon $4^+\gamma\gamma$ excitation, while others claim that the first excited $K^\pi = 0^+$ band in nuclei is the $0^+\gamma\gamma$ vibration. Experimental work at ILL with respect to studies of multiphonon vibrational excitations is going in three general directions. One is a systematic search and measurement of $K^\pi = 4^+$ bands in deformed nuclei in order to identify the collective $4^+\gamma\gamma$ modes. Secondly, there are searches for two-phonon $0^+\gamma\gamma$ modes and, thirdly, searches for $0^+\beta\beta$ modes.

3.1. $K^\pi = 4^+$ States

^{164}Dy was one of the first nuclei after ^{168}Er where at ILL the search for two-phonon γ-vibrational states continued (meantime Garrett *et al.* [10] had found evidence for the existence of both, the $K^\pi = 0^+$ and 4^+ two γ vibrations in ^{166}Er). As mentioned above, ^{164}Dy is one of the three candidates proposed by QPNM calculations. A candidate for a $K^\pi = 4^+$ double γ vibration was identified at 2173 keV [11]. The measurements involved the use of crystal spectroscopy, coincidence data, and electron spectroscopy. The lifetime for this level was then determined via the GRID method, and it was found that this state exhibits some degree of collective enhancement in its decay. Figure 2 shows the corresponding part of the level scheme. The collective enhancement suggests a two-phonon γ-vibrational component in its wave function, although the present data does not determine if it is the dominant component. At variance to that, an investigation of the lifetimes of the first $K^\pi = 4^+$ band in the neighboring ^{162}Dy isotope [12] does not indicate that this configuration would be a good candidate for a two-phonon $\gamma\gamma$ vibration.

3.2. $K^\pi = 0^+$ States

The nature of excited $K^\pi = 0^+$ bands still remain even more enigmatic. The difficulty lies in the many ways that a $K^\pi = 0^+$ band can be made but also in the lack of measured lifetimes for $K^\pi = 0^+$ bands. Consequently the lifetimes of several of the 2^+ states of the first excited $K^\pi = 0^+$ bands were investigated in—amongst others—^{164}Dy, ^{168}Er , and ^{156,158}Gd.

For ^{168}Er, it was found that the absolute transition probabilities of the decay of this 2^+ state to the γ band are moderately collective [13]. This could suggest an admixture of a double γ vibration in the wave function of the state and rule out a pure β-vibrational mode. For ^{164}Dy, however, it was concluded [13] that the theoretical overestimation of the β to γ transition rate points towards a less collective structure of the first excited $K^\pi = 0^+$ band than in ^{168}Er and lends support to the interpretation of the band as mainly a quasiparticle excitation.

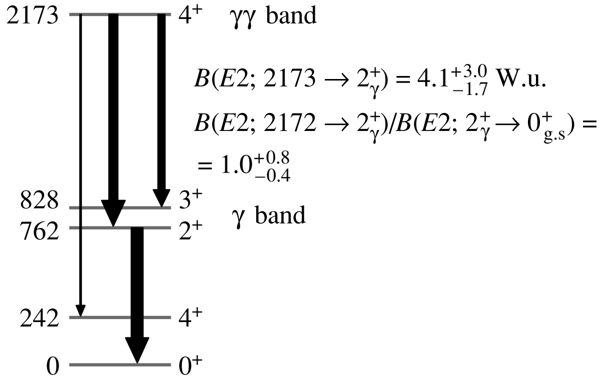

Fig. 2. Partial level scheme of ^{164}Dy [11] (energy in keV). $B(E2)$ values were deduced from the known and measured lifetimes of the 2^+ state of the γ band and the 2173 keV state, respectively.

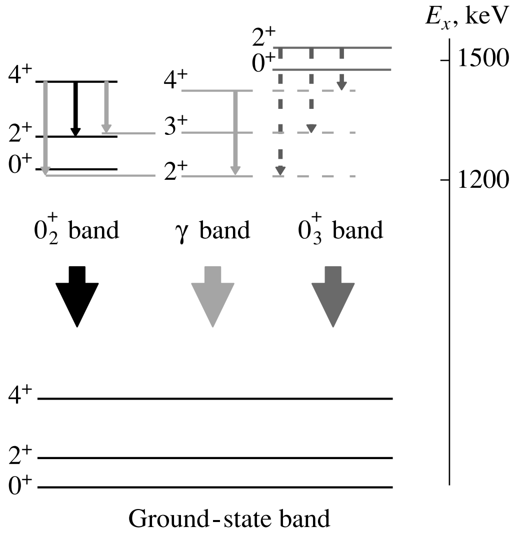

Fig. 3. Schematic representation of a partial level scheme for ^{158}Gd. The dashed transitions were shown to be misplaced in the level scheme.

High-resolution studies in ^{158}Gd [14] also yielded new absolute $B(E2)$ values associated with $K^\pi = 0^+$ excitations. Strong $B(E2)$ values from the 0^+_2 band to the nearby γ band were confirmed, but it was shown that these can be explained by an existing [15] four-band mixing calculation. Another result concerned the potentially large and collective $K^\pi = 0^+$ to γ transitions from the $K^\pi = 0^+_3$ band at 1452 keV. However, precise energy measurements of the transitions and levels involved showed that previously assigned gamma-ray lines from the 2^+ level of this second excited 0^+ band were incorrectly placed

(Fig. 3). This removed the existing evidence for multiphonon character for this band as well.

In ^{156}Gd, the first $K^{\pi} = 0^{+}$ band is below the single-phonon γ-vibrational excitation. Transitions from this first excited $K^{\pi} = 0^{+}$ band to the ground state in ^{156}Gd appear to be collective, and this band was interpreted as the β band [16]. It was also found [16] that the 0_4^+ band at 1715 keV is strongly connected to the γ band. In this case, this establishes possible evidence for this configuration being a candidate for a $K^{\pi} = 0^{+}$ $\gamma\gamma$-vibrational band.

In summary, ultraprecise energies and absolute $B(E2)$ values associated with $K^{\pi} = 0^{+}$ and $K^{\pi} = 4^{+}$ excitations in a number of rare-earth nuclei, measured with the GRID technique, reveal significant information relating to the possible existence or absence of two-phonon vibrational excitations in deformed nuclei. However, so far no unique signature concerning such states seems to emerge. Further systematic studies are certainly needed.

REFERENCES

1. M. S. Dewey *et al.,* Nucl. Instrum. Methods Phys. Res. A **284**, 151 (1989).
2. E. G. Kessler *et al.,* submitted to Nucl. Instrum. Methods Phys. Res.
3. H. G. Börner and J. Jolie, J. Phys. G **19**, 217 (1993).
4. H. G. Börner *et al.,* Phys. Lett. B **215**, 45 (1988).
5. J. Keinonen *et al.,* Phys. Rev. Lett. **67**, 3692 (1991).
6. M. Jentschel *et al.,* Nucl. Instrum. Methods Phys. Res. B **115**, 446 (1996).
7. N. Stritt *et al.,* Phys. Rev. B **59**, 6762 (1999).
8. H. G. Börner *et al.,* Phys. Rev. Lett. **66**, 691 (1991).
9. V. G. Soloviev *et al.,* J. Phys. G **20**, 113 (1994).
10. P. E. Garrett *et al.,* Phys. Rev. Lett. **78**, 4545 (1997).
11. F. Corminboeuf *et al.,* Phys. Rev. C **56**, R1201 (1997).
12. A. Aprahamian *et al.,* to be published.
13. H. Lehmann *et al.,* Phys. Rev. C **57**, 569 (1998).
14. H. G. Börner *et al.,* Phys. Rev. C **59**, 2432 (1999).
15. R. C. Greenwood *et al.,* Nucl. Phys. A **304**, 327 (1978).
16. R. de Haan *et al.,* to be published.

Physics of Atomic Nuclei, Vol. 64, No. 6, 2001, pp. 1015–1019. From Yadernaya Fizika, Vol. 64, No. 6, 2001, pp. 1091–1095.
Original English Text Copyright © 2001 by Warner.

The Role of Isospin on the $N = Z$ Line[*]

D. D. Warner[**]
CLRC Daresbury Laboratory, UK

Received September 11, 2000

Abstract—The role played by isospin in nuclear structure phenomena encountered on the $N = Z$ line is discussed. New results on Coulomb energy differences (CED) at high spin for odd-A nuclei in the $f_{7/2}$ shell are presented and interpreted in the framework of a simple Cranked Shell Model treatment involving an exact numerical diagonalisation. Results for the CED between the $A = 46$ even–even mirror pairs are also discussed. The CED between the $T = 1$ states in $N = Z$ odd–odd nuclei and their isobaric analogues are suggested as a possible probe of np pairing on the $N = Z$ line. First results from a numerical diagonalization of IBM-4 are cited. © *2001 MAIK "Nauka/Interperiodica".*

1. INTRODUCTION

Nuclei along the $N = Z$ line display several unique characteristics which arise from two principal sources. Firstly, the coincidence of neutron and proton Fermi surfaces ensures maximum spatial overlap between the neutron and proton wave functions, so that, as the number of valence nucleons increases with increasing mass, strong collective effects develop. Secondly, the charge independence of the nuclear force gives rise to a neutron–proton exchange symmetry which can be represented by the isospin quantum number and which manifests itself in a number of structural features observable only on, or very near, the $N = Z$ line. Examples include $SU(4)$ symmetry, which is good for only the lightest of nuclei and rapidly gets worse as the spin–orbital force increases; mirror symmetry, which is currently being studied to higher spins than ever before; and np pairing correlations. Finally, breaking of the isospin symmetry itself is expected to occur most strongly for the heaviest masses on the $N = Z$ line.

Clearly collective effects on the $N = Z$ line can be expected to become most apparent as we go up in mass and enter regions of larger valence space. However, only in recent years has experimental sensitivity been sufficient to begin to probe some of the relevant questions. Thus, for example, $A = 51$ is the current mass limit for the high-spin mirror studies [1], while ^{76}Sr [2] probably now represents the limit of spectroscopy for $N = Z$ nuclei, meaning the heaviest nucleus in which more than the first one or two yrast states have been identified. It is obviously not possible to explore all of these features in this talk, which will therefore concentrate on mirror nuclei at high spin, where new data have become available, and on a few aspects of np pairing.

2. MIRROR NUCLEI AT HIGH SPIN

Until very recently, the most recent results on this topic were those for the ^{49}Cr/^{49}Mn mirror pair [3] which extend to the band terminating spin of $31/2^-$ in each case and reveal a collective structure with the standard backbend/alignment taking place around $J^\pi = 17/2^-$. Similar data have been obtained for the $A = 47$ pair also [4]. Very recently, however, a new study [1] by the same collaboration has revealed the complete yrast structure up to band termination of the $A = 51$ mirror pair ^{51}Fe/^{51}Mn. In this case, the maximum spin state achievable within the $f_{7/2}$ shell is $27/2^-$, and the results were obtained using the combination of the GAMMASPHERE gamma-ray detector array and the fragment mass analyzer (FMA) at the ATLAS facility of Argonne National Laboratory. The deduced level schemes are shown in Fig. 1. Nothing was known about the excited states of the neutron-deficient partner ^{51}Fe prior to this investigation.

The Coulomb energy differences (CED) between states for the $A = 49$ and 51 mirror pairs are shown in Fig. 2 as a function of angular momentum. The degree of collectivity is greater for the mid shell pair with $A = 49$ than for $A = 51$. This is evident both from the observed level structures and from the smoother behavior of the CEDs in the former case. Nevertheless, the data for both pairs reveal a sudden change at $J^\pi = 17/2^-$, analogous to the behavior of the rotational alignment. The basic origin of this phenomenon has been understood for some time [5]; for $A = 49$, the

---

[*] This article was submitted by the author in English.
[**] e-mail: `d.warner@dl.ac.uk`

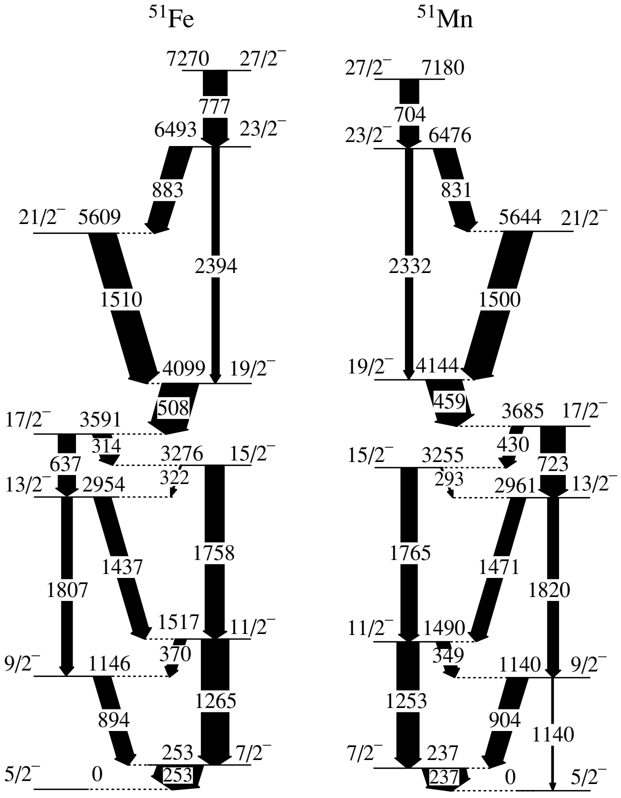

Fig. 1. The level schemes of the $A = 51$ mirror pair [1] (energy in keV).

blocking of the odd proton in Mn causes the two neutrons to align first and vice versa for Cr. The Coulomb energy in Cr therefore decreases because of the decrease in spatial overlap of the two aligning protons, with a consequent increase in the CED of Fig. 2. Similarly, for $A = 51$, the protons align in Fe and hence the difference Fe–Mn decreases. However, in the interpretation of the earlier data [5, 6], which did not extend to such high spin, it was thought that the CED would saturate at higher spin, in common with the two-proton alignment. Instead, the new data show an unexpected return of the CED towards zero after the first bandcrossing.

These new features can be understood [7] and put on a more quantitative footing in the framework of a cranked shell model calculation. The Hamiltonian consists of a cranked deformed one-body term and a scalar two-body term which is taken as the delta interaction

$$H' = h_{\text{def}} - g\delta(\mathbf{r}_1 - \mathbf{r}_2) - \omega J_x. \tag{1}$$

Here, h_{def} is the quadrupole deformed mean field,

$$h_{\text{def}} = -4\kappa\sqrt{\frac{4\pi}{5}}\sum_i Y_{20}(\hat{r}_i), \tag{2}$$

and κ is the deformation energy, which is related to the usual deformation parameter β by

$$\kappa \simeq 0.16\hbar\omega_0(N + 3/2)\beta, \tag{3}$$

where $\hbar\omega_0$ is the harmonic oscillator frequency of the deformed potential and N the quantum number of the major shell. $G = g\int |R_{nl}(r)|^4 r^2 dr$ is used as the energy unit.

The Hamiltonian has been diagonalized numerically for particles in the $f_{7/2}$ shell with $\kappa = 1.5$ MeV, which approximately corresponds to the observed deformation in the $f_{7/2}$ region. The two-proton Coulomb matrix elements have been calculated using empirical values from the binding energy differences given by $V_{\text{C}}(J) = 2BE(^{42}\text{Sc}; J) - BE(^{42}\text{Ca}; J) - BE(^{42}\text{Ti}; J)$. As pointed out in [5], use of these values should incorporate a first-order treatment of the omitted correction terms [8] known to be necessary for a full description of absolute Coulomb energies. The current study uses differences in excited states and thus concentrates on the changes induced by the changing collective structure.

The results for the CED between both odd–even and even–even mirror partners are plotted in Fig. 3 against the rotational frequency, the latter being given in units of the pairing strength G, which takes a value of $\simeq$1 MeV in this region. It is to be noted that in the absence of an explicit neutron–proton interaction it is necessary to perform the calculations for protons only. Thus, for example, the CED between the $A = 49$ systems of five protons + four neutrons $(5p + 4n)$ and $4p + 5n$ are shown as $5p$–$4p$, while $A = 51$ is $6p$–$5p$.

It is clear that the calculations reproduce both the observed rise and subsequent fall of the CED in each case. The results can be understood by considering the behavior of the concomitant alignment shown in Fig. 4, remembering that, at any crossing representing an alignment of protons, the Coulomb energy will drop due to the transition from the paired $(J = M = 0)$ state to the two-particle aligned $(J = M_x = 6)$ state. Thus, taking the $5p$–$4p$ case as an example, the differences in the Coulomb energy of the two mirror nuclei will show a rise at the frequency at which the crossing begins in the four-particle case, followed by a fall as the alignment in the $5p$ nucleus sets in. In the $6p$–$5p$ case, the result is the inverse.

A similar argument can be adopted for pairs of even–even mirror nuclei in the $f_{7/2}$ shell, and the results for the $4p$–$2p$ case are plotted on the right of Fig. 3. These CED correspond to the mirror pair ^{46}Cr and ^{46}Ti. The calculated values in this case are again constant at low rotational frequency but then show an increase at around $\hbar\omega = 0.65G$. This corresponds to the first crossing in the $2p$ nucleus.

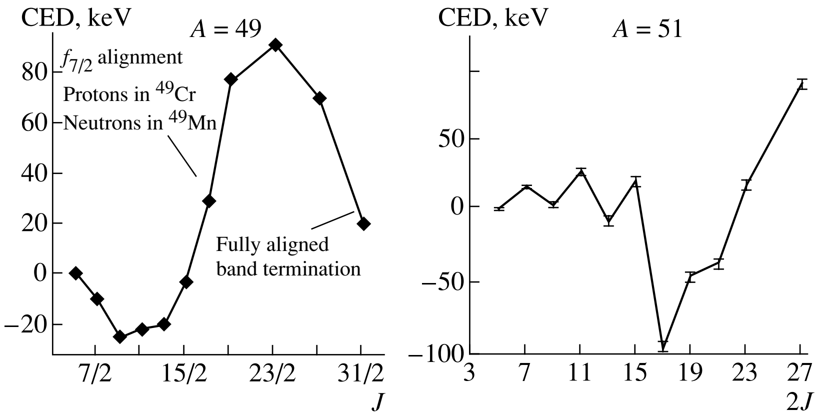

Fig. 2. The measured CED for the $A = 49$ and 51 pairs of mirror nuclei [1, 3].

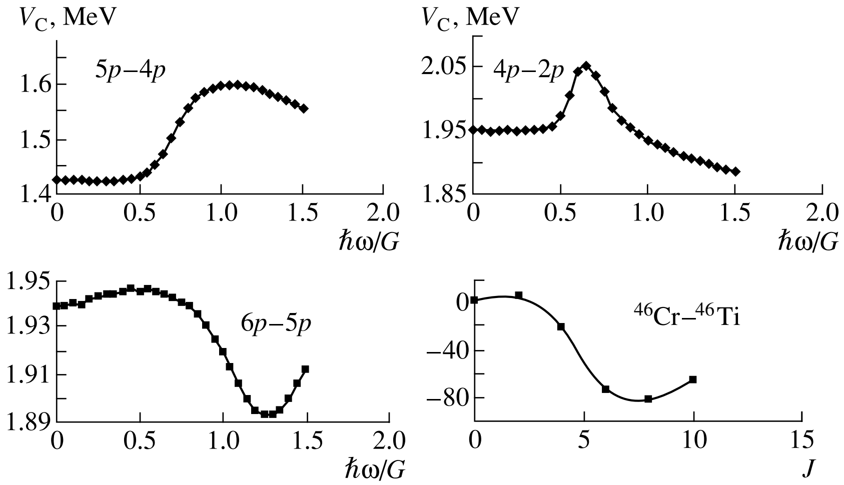

Fig. 3. Predicted CED [7] for (left) the odd mass pairs of mirror nuclei and (right) the even mass $A = 46$ pair (upper) compared with recent results (lower) [9].

Since the first crossing in the $4p$ nucleus occurs at a somewhat later frequency, we observe that the initial increase is cut off prematurely by the onset of the $4p$ alignment. If the first bandcrossings in the $2p$ and the $4p$ case had occurred at the same rotational frequency, then we would not have predicted any increase at all in the calculated CED, while, if their order was inverted, we would predict an effect of the opposite sign. In fact, Fig. 3 shows that very preliminary data [9] for the yrast states of the $T_z = -1$ nucleus ^{46}Cr obtained at the GAMMASPHERE+FMA facility at ANL seem to indicate that the sign of the CED effect is indeed opposite to expectations. The reason for this is currently not clear, but could also arise because the schematic calculations of Figs. 3 and 4 were performed at a single value of the deformation which may not be appropriate for the less collective $A = 46$ nuclei.

There is one other set of CED which can be considered, namely, those involving the $T = 1$ isobaric analogue states in the odd–odd $N = Z$ nucleus. For the $A = 46$ example cited above, this would imply the $T = 1$ states in ^{46}V. A theoretical treatment would necessitate explicit inclusion of isospin and hence np modes in the formalism, and such a framework is not yet available, but the first experimental information of this type has recently been obtained. More specifically, results from a recent study [10] which populated the $T = 1$ states of ^{46}V allow the first glimpse of the CED between ^{46}V and ^{46}Ti, shown in Fig. 5.

The figure shows a rapid increase in the CED up to the $J^\pi = 6^+$ state. CSM calculations indicate that it is the protons which align first in ^{46}Ti, which would give rise to an increase in the CED plotted. Hence, in ^{46}V, the alignment must stem from neutron–neutron or neutron–proton pairs. In fact, the pair structure in the two nuclei can be deduced from the algebraic treatment of the isospin in the IBM-3 model [11], yielding the results shown in the table for the three types of boson in the model basis. There is a sur-

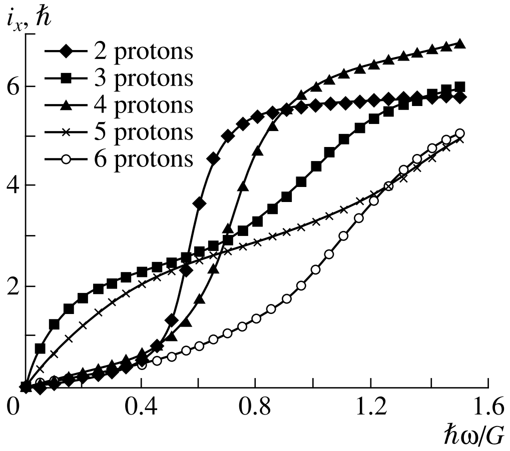

Fig. 4. The aligned proton angular momentum (i_x) as a function of rotational frequency for various proton numbers in the $f_{7/2}$ shell [7].

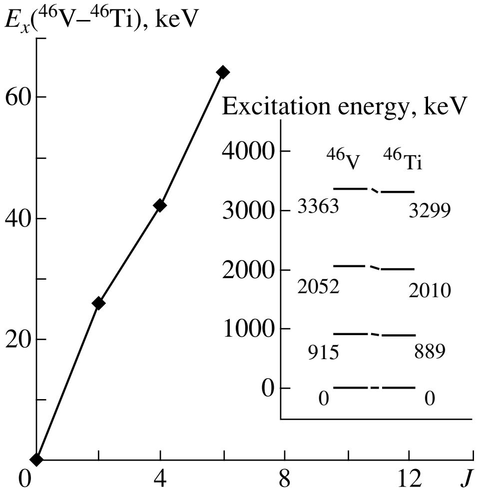

Fig. 5. Measured CED for the isobaric analog $T = 1$ states in ^{46}V and ^{46}Ti [10].

prisingly large increase in the number of np pairs in going to the self-conjugate system, suggesting that they must dominate the alignment process in ^{46}V and that study of the CED involving such systems may offer an insight into the spatial correlations associated with np pairs as a function of rotational frequency.

3. NEUTRON–PROTON PAIRING

The first results on the $T = 1$ isobaric analogs for $A = 46$ can be viewed in the context of the overall behavior of the ground states of odd–odd $N = Z$ nuclei, which shows a steady decrease in the energy separation of the $T = 1$ and $T = 0$ states as mass increases along the $N = Z$ line until, above $A = 40$, the ground state becomes $T = 1$. This lowering of the $T = 1$ states is accompanied by a gradual reduction in the contribution of $T = 0$ pairs in the ground state [12]. This feature is probably linked to the change from ls to jj coupling as the strength of the spin–orbit interaction increases, which results in a steady erosion in the purity of the $L = 0$, $S = 1$ wave function of the $T = 0$ pair, rendering it less attractive relative to its $T = 1$ competitor. The switch to $T = 1$ ground states favors the study of CED involving the odd–odd nuclei; unfortunately, however, it is the $T = 0$ states which appear to be favored in the feeding when these nuclei are created in heavy-ion fusion evaporation reactions.

From a theoretical point of view, many approaches are currently being developed to deal with the problem of heavy $N = Z$ nuclei. Examples include variational approximations, like BCS or HFB, direct diagonalization of the shell model or the use of Monte Carlo techniques. The Interacting Boson Model of Arima and Iachello [13] has achieved an impressive level of success in the description of collective features in medium-heavy nuclei, and, recently, a first step has been made [14] towards the use of the isospin invariant version of the model, IBM-4, to analyze the structure of $N = Z$ nuclei at the beginning of the 28–50 shell. The microscopic foundations of such a numerical boson calculation have been studied by calculating, where possible, the Hamiltonian from a realistic shell model interaction using a mapping procedure that relies on the existence of approximate fermionic symmetries.

The first test of the IBM-4 Hamiltonian thus de-

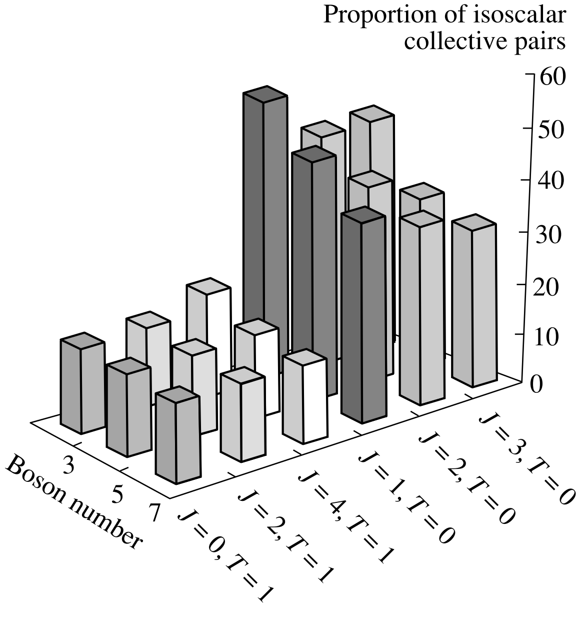

Fig. 6. Pair structure of lowest states of odd–odd, $N = Z$ nuclei beyond ^{58}Cu [14].

Values of the boson (pair) number for $A = 46$, $T = 1$ from IBM-3

	Ti ($Z = 22$)	V ($Z = 23$)
N_p	4/5	2/5
N_n	9/5	2/5
N_{np}	2/5	11/5

rived was made on the recently studied levels of the odd–odd, $N = Z$ nucleus ^{62}Ga. Both shell model and IBM-4 predict a 0^+ ($T = 1$) ground state and a 1^+ ($T = 0$) first-excited state. Note that this represents an inversion with respect to the order in ^{58}Cu, which agrees with the data. Given that no free parameter is introduced in the IBM-4 calculation, the agreement for the $T = 0$ levels can be called remarkable and a near one-to-one correspondence with shell model levels can be established. Further calculations have been made [14] for the next two odd–odd $N = Z$ nuclei, ^{66}As and ^{70}Br, where shell model calculations have not yet been possible and, in the latter case, no data yet exist on the low-lying level structure.

Another application of this formalism is that a quantitative indication of the pair structure of nuclear states can be readily obtained by computing boson-number expectation values in the IBM-4 eigenstates. This is illustrated in Fig. 6, where the proportion of isoscalar bosons of the total number of bosons is plotted for various states in the three odd–odd $N = Z$ nuclei studied. The first important feature to note is the *mixture* of $T = 1$ and $T = 0$ pairs in the lowest states with, for example, the $T = 1$, 0^+ ground state containing 10–20% of $T = 0$ bosons; this is an unavoidable consequence of isospin invariance. The correlation between the energy separation of $T = 0$ and 1 states and the dominance of one pairing mode over another has been pointed out before [12]; here the separation is around 1 MeV, and it seems clear that this is already sufficient to signal that the $T = 1$ collective pair structure is significantly more attractive than for $T = 0$.

REFERENCES

1. M. A. Bentley *et al.,* submitted to Phys. Rev. C.
2. C. J. Lister, private communication.
3. C. D. O'Leary *et al.,* Phys. Rev. Lett. **79**, 4349 (1997).
4. M. A. Bentley *et al.,* Phys. Lett. B **437**, 243 (1998).
5. J. A. Sheikh, P. van Isacker, D. D. Warner, and J. A. Cameron, Phys. Lett. B **252**, 314 (1990).
6. J. A. Cameron *et al.,* Phys. Lett. B **319**, 58 (1993).
7. J. A. Sheikh, D. D. Warner, and P. van Isacker, Phys. Lett. B **443**, 16 (1998).
8. N. Auerbach, Phys. Rep. **98**, 273 (1983).
9. P. E. Garrett *et al.,* to be published.
10. C. D. O'Leary *et al.,* Phys. Lett. B **459**, 73 (1999).
11. J. E. Garcia-Ramos and P. van Isacker, Ann. Phys. (N.Y.) **274**, 45 (1999).
12. P. van Isacker and D. D. Warner, Phys. Rev. Lett. **78**, 3266 (1997).
13. A. Arima and F. Iachello, Phys. Rev. Lett. **35**, 1069 (1975).
14. O. Juillet, P. van Isacker, and D. D. Warner, to be published.

Physics of Atomic Nuclei, Vol. 64, No. 6, 2001, pp. 1020–1026. From Yadernaya Fizika, Vol. 64, No. 6, 2001, pp. 1096–1102.
Original English Text Copyright © 2001 by Voronov.

Double Giant Resonances in Nuclei[*]

V. V. Voronov[**]

Joint Institute for Nuclear Research, Dubna, Moscow oblast, 141980 Russia

Received November 9, 2000

Abstract—A brief review of the results of microscopic calculations aimed at describing the characteristics of double giant dipole resonances (DGDR) is presented. Special attention is paid to a systematic microscopic study of the anharmonic properties of DGDRs for nuclei with mass numbers $40 \leq A \leq 208$. It is found that the corrections of the energy centroid of a DGDR from its harmonic limit are negative, have a value on the order of a few hundred keV, and follow an A^{-1} dependence. *© 2001 MAIK "Nauka/Interperiodica".*

1. INTRODUCTION

The concept of the RPA phonons is a usual way to treat collective excitations in many-body systems. The best method to examine its validity in actual physical systems is to study deviations from the harmonic picture for multiphonon excitations. The anharmonicity of such excitations appears owing to the corrections associated with the Pauli exclusion principle [1–3]. Many examples of anharmonical behavior are well known from the low-excitation-energy part of nuclear spectra.

The discovery of the double giant dipole resonance (DGDR) in nuclei [4–8]—that is, the giant dipole resonance (GDR) built on top of another GDR—and the observation of small deviations from the harmonic picture of the excitation energy and spreading width, combined with the large deviations of the associated Coulomb excitation cross sections measured in relativistic heavy-ion collisions [7], require better understanding of the role that anharmonicities play in the spectrum of the DGDR.

Anharmonicities can affect electromagnetic DGDR cross sections in several ways. For example, the energy shifts of the DGDR states from the harmonic values can have a pronounced effect on the electromagnetic cross section because of the exponential dependence of these quantities on the Q value of the process [9]. In addition, anharmonicities lead to changes in $E1$-transition matrix elements and finally give rise to many paths, other than the (harmonic) two-step one, to excite a DGDR in electromagnetic processes.

Various aspects of the influence of anharmonicities on the electromagnetic DGDR cross sections were considered in [9–19], but no clear picture of the DGDR anharmonicity problem emerged. In particular, there is no consensus on the mass-number dependence of the energy shifts from the harmonic values. The first systematic calculation of the spectrum of a DGDR in a complete one- and two-phonon basis (the effect of three-phonon states on anharmonicity is small [14]) for nuclei with mass number A spanning the whole mass table was performed in [20]. Here, we will discuss the results of microscopic studies of DGDR anharmonicity.

2. BASIC FORMULAS AND NUMERICAL DETAILS

The Hamiltonian of the quasiparticle–phonon model (QPM) used in describing the system contains, in addition to a mean-field term, which determines the single-particle motion of protons and neutrons, a monopole pairing interaction and a separable multipole–multipole force, whose strengths are adjusted in such a way as to reproduce the odd–even mass differences and the spectrum of low-lying vibrations and of giant resonances, respectively [3].

To study the anharmonic properties of two-phonon excited states with a total spin J and its projection M, one can describe them by the wave function

$$|\Psi^{\nu}_{JM}\rangle = \left\{ \sum_i R_i(J\nu) Q^+_{Ji} \right. \tag{1}$$

$$\left. + \sum_{\lambda_1 i_1 \leq \lambda_2 i_2} P^{\lambda_2 i_2}_{\lambda_1 i_1}(J\nu) \frac{[Q^+_{\lambda_1 \mu_1 i_1} Q^+_{\lambda_2 \mu_2 i_2}]_{JM}}{\sqrt{1+\delta_{\lambda_1 i_1, \lambda_2 i_2}}} \right\} |\rangle_{\rm ph} ,$$

which is a superposition of different one- and two-phonon configurations, with $|\rangle_{\rm ph}$ being the phonon

---

[*] This article was submitted by the author in English.

[**] e-mail: `voronov@thsun1.jinr.ru`

vacuum. The coupling of two-phonon states to three-phonon states, which was considered in [14], leads to the fragmentation of the strength of two-phonon states. In (1), use has been made of the notation

$$[Q^+_{\lambda_1\mu_1 i_1} Q^+_{\lambda_2\mu_2 i_2}]_{JM} = \sum_{\mu_1\mu_2} C^{JM}_{\lambda_1\mu_1\lambda_2\mu_2} Q^+_{\lambda_1\mu_1 i_1} Q^+_{\lambda_2\mu_2 i_2},$$

where C is a Clebsch–Gordan coefficient.

In our approach, phonons possess the internal fermion structure. The phonon creation operator $Q^+_{\lambda\mu i}$ of multipole order λ, projection μ, and order number i is a linear combination of two quasiparticle creation (α^+_{jm}) and annihilation (α_{jm}) operators with shell quantum numbers $j \equiv (n, l, j)$ and m,

$$Q^+_{\lambda\mu i} = \frac{1}{2}\sum_{\tau}^{n,p}\sum_{jj'}\Big\{\psi^{\lambda i}_{jj'}[\alpha^+_j \alpha^+_{j'}]_{\lambda\mu} - (-1)^{\lambda-\mu}\varphi^{\lambda i}_{jj'}[\alpha_{j'}\alpha_j]_{\lambda-\mu}\Big\}. \qquad (2)$$

The energy spectrum of one-phonon states $\omega_{\lambda i}$ is obtained by solving quasiparticle-RPA equations. These equations also yield the values of the forward $(\psi^{\lambda i}_{jj'})$ and backward $(\varphi^{\lambda i}_{jj'})$ amplitudes in Eq. (2). In the case of a separable form of a residual interaction with a radial form factor $f_\lambda(r)$, they are

$$\binom{\psi}{\varphi}^{\lambda i}_{jj'}(\tau) = \frac{1}{\sqrt{2\mathcal{Y}^{\lambda i}_\tau}} \frac{f^\lambda_{jj'}(\tau)(u_j v_{j'} + v_j u_{j'})}{\varepsilon_j + \varepsilon_{j'} \mp \omega_{\lambda i}},$$

where $f^\lambda_{jj'} = \langle j'||f_\lambda(r)||j\rangle$; u_j and v_j are the coefficients of the Bogolyubov transformation from particle (a_{jm}) to quasiparticle operators, $a^+_{jm} = u_j\alpha^+_{jm} + (-1)^{j-m}v_j\alpha_{j-m}$; and ε_j is a quasiparticle energy and $\mathcal{Y}_\tau$ are normalization coefficients (see, e.g., [3] for an explicit form). The quasiparticle spectrum and the coefficients u_j and v_j are obtained by solving BCS equations.

To obtain the spectrum $E_\nu(J)$ of the states in (1) and their structure—i.e., the coefficients R and P—it is necessary to diagonalize the matrices

$$\left|\left|\langle\Psi^{\nu'}_J|H|\Psi^\nu_J\rangle - E\langle\Psi^{\nu'}_J|\Psi^\nu_J\rangle\right|\right|_{[\nu\times\nu']} = \left\|\begin{matrix}\langle[Q_{\lambda_4 i_4}Q_{\lambda_3 i_3}]_J|H|[Q^+_{\lambda_1 i_1}Q^+_{\lambda_2 i_2}]_J\rangle & U^{\lambda_1 i_1}_{\lambda_2 i_2}(Ji) \\ U^{\lambda_4 i_4}_{\lambda_3 i_3}(Ji) & \omega_{Ji} - E\end{matrix}\right\| = 0 \qquad (3)$$

for a definite value of J.

The QPM Hamiltonian can be written in terms of quasiparticle and phonon operators as

$$H = \sum_{jm}\varepsilon_j\alpha^+_{jm}\alpha_{jm} - \frac{1}{4}\sum_{\lambda\mu i i'}\sum_{\tau}^{n,z}\frac{X^{\lambda i}_\tau + X^{\lambda i'}_\tau}{\sqrt{\mathcal{Y}^{\lambda i}_\tau \mathcal{Y}^{\lambda i'}_\tau}} Q^+_{\lambda\mu i}Q_{\lambda\mu i'} + H_{\text{int}}, \qquad (4)$$

where

$$X^{\lambda i}_\tau = \frac{1}{2\lambda+1}\sum_{jj'}^{\tau}\frac{[f^\lambda_{jj'}(\tau)(u_j v_{j'} + v_j u_{j'})]^2(\varepsilon_j + \varepsilon_{j'})}{(\varepsilon_j + \varepsilon_{j'})^2 - \omega^2_{\lambda i}}$$

and H_{int} is the term responsible for the interaction between quasiparticles and phonons. The coefficients in the second term of (4) are such that the model Hamiltonian in the form (4) is diagonal in the space of one-phonon configurations [21, 22]. Thus, no double counting of quasiparticle operators is due to the fact that they appear twice in the first and second terms because the phonons themselves possess the internal fermion structure [2].

The matrix element of the interaction between two-phonon configurations has the form

$$\begin{aligned}\sum_{\text{all }\mu}\langle[Q_{\lambda_4\mu_4 i_4}Q_{\lambda_3\mu_3 i_3}]_{JM}|H|[Q^+_{\lambda_1\mu_1 i_1}Q^+_{\lambda_2\mu_2 i_2}]_{JM}\rangle &= (\omega_{\lambda_1 i_1} + \omega_{\lambda_2 i_2}) \\ &\times\left\{\delta_{\lambda_1 i_1,\lambda_3 i_3}\delta_{\lambda_2 i_2,\lambda_4 i_4} + K^{\lambda_4 i_4\lambda_3 i_3}_{\lambda_1 i_1\lambda_2 i_2}(J)\right\} \\ &- \frac{1}{4}\sum_{i\tau}\left[\frac{X^{\lambda_3 i_3}_\tau + X^{\lambda_3 i}_\tau}{\sqrt{\mathcal{Y}^{\lambda_3 i_3}_\tau\mathcal{Y}^{\lambda_3 i}_\tau}}K^{\lambda_4 i_4\lambda_3 i}_{\lambda_1 i_1\lambda_2 i_2}(J) + \frac{X^{\lambda_4 i_4}_\tau + X^{\lambda_4 i}_\tau}{\sqrt{\mathcal{Y}^{\lambda_4 i_4}_\tau\mathcal{Y}^{\lambda_4 i}_\tau}}K^{\lambda_4 i\lambda_3 i_3}_{\lambda_1 i_1\lambda_2 i_2}(J)\right. \\ &\left. + \sum_{\substack{\lambda_5 i_5\\ \lambda_6 i_6}}\frac{X^{\lambda_5 i_5}_\tau + X^{\lambda_5 i}_\tau}{\sqrt{\mathcal{Y}^{\lambda_5 i_5}_\tau\mathcal{Y}^{\lambda_5 i}_\tau}}K^{\lambda_4 i_4\lambda_3 i_3}_{\lambda_5 i_5\lambda_6 i_6}(J)K^{\lambda_6 i_6\lambda_5 i}_{\lambda_1 i_1\lambda_2 i_2}(J)\right]\frac{1}{\sqrt{(1+\delta_{\lambda_1 i_1,\lambda_2 i_2})(1+\delta_{\lambda_3 i_3,\lambda_4 i_4})}},\end{aligned} \qquad (5)$$

where the coefficients K^J are complex functions of phonon amplitudes ψ and φ in (2) and are given by

$$K^{\lambda_4 i_4 \lambda_3 i_3}_{\lambda_1 i_1 \lambda_2 i_2}(J) = \sum_{\substack{j_1 j_2 \\ j_3 j_4}} (-1)^{j_2+j_4} \hat{\lambda}_1 \hat{\lambda}_2 \hat{\lambda}_3 \hat{\lambda}_4 \left[(-1)^{\lambda_2+\lambda_4} \begin{Bmatrix} j_1 & j_2 & \lambda_4 \\ j_4 & j_3 & \lambda_3 \\ \lambda_1 & \lambda_2 & J \end{Bmatrix} \left(\psi^{\lambda_3 i_3}_{j_3 j_4} \, \psi^{\lambda_1 i_1}_{j_1 j_4} \, \psi^{\lambda_2 i_2}_{j_3 j_2} \, \psi^{\lambda_4 i_4}_{j_1 j_2} \right. \right. \tag{6}$$

$$\left. - \varphi^{\lambda_3 i_3}_{j_3 j_4} \, \varphi^{\lambda_1 i_1}_{j_1 j_4} \, \varphi^{\lambda_2 i_2}_{j_3 j_2} \, \varphi^{\lambda_4 i_4}_{j_1 j_2} \right) - (-1)^{\lambda_1+\lambda_2} \begin{Bmatrix} \lambda_1 & \lambda_2 & J \\ j_2 & j_4 & j_3 \end{Bmatrix} \begin{Bmatrix} \lambda_3 & \lambda_4 & J \\ j_2 & j_4 & j_1 \end{Bmatrix}$$

$$\left. \times \left(\varphi^{\lambda_3 i_3}_{j_1 j_4} \, \varphi^{\lambda_1 i_1}_{j_4 j_3} \, \psi^{\lambda_2 i_2}_{j_2 j_3} \, \psi^{\lambda_4 i_4}_{j_1 j_2} - \psi^{\lambda_3 i_3}_{j_1 j_4} \, \psi^{\lambda_1 i_1}_{j_4 j_3} \, \varphi^{\lambda_2 i_2}_{j_2 j_3} \, \varphi^{\lambda_4 i_4}_{j_1 j_2} \right) \right]$$

with $\hat{\lambda}_i = \sqrt{2\lambda_i + 1}$. The terms in K^J that are proportional to $\psi^2\varphi^2$ and to φ^4 do not exceed 1 to 2% of the leading term ψ^4 for low-lying collective phonons and are negligibly small for phonons associated with giant resonances.

For photons of natural parity, a matrix element of the interaction between one- and two-phonon configurations is given by

$$U^{\lambda_1 i_1}_{\lambda_2 i_2}(\lambda i) \tag{7}$$

$$= \sum_{\text{all } \mu} \langle [Q_{\lambda \mu i} | H | [Q^+_{\lambda_1 \mu_1 i_1} Q^+_{\lambda_2 \mu_2 i_2}]_{JM} \rangle$$

$$= (-1)^{\lambda_1+\lambda_2-\lambda} \hat{\lambda}_1 \hat{\lambda}_2$$

$$\times \sum_{\tau}^{n,p} \sum_{j_1 j_2 j_3} \left[\frac{f^{\lambda}_{j_1 j_2} v^{(-)}_{j_1 j_2}}{\sqrt{\mathcal{Y}^{\lambda i}_{\tau}}} \begin{Bmatrix} \lambda_1 & \lambda_2 & \lambda \\ j_2 & j_1 & j_3 \end{Bmatrix} \right.$$

$$\times \left(\psi^{\lambda_1 i_1}_{j_3 j_1} \, \varphi^{\lambda_2 i_2}_{j_2 j_3} + \psi^{\lambda_2 i_2}_{j_2 j_3} \, \varphi^{\lambda_1 i_1}_{j_3 j_1} \right)$$

$$+ \frac{f^{\lambda_1}_{j_1 j_2} v^{(-)}_{j_1 j_2}}{\sqrt{\mathcal{Y}^{\lambda_1 i_1}_{\tau}}} \begin{Bmatrix} \lambda_1 & \lambda_2 & \lambda \\ j_3 & j_2 & j_1 \end{Bmatrix}$$

$$\times \left(\varphi^{\lambda i}_{j_2 j_3} \, \varphi^{\lambda_2 i_2}_{j_3 j_1} + \psi^{\lambda i}_{j_2 j_3} \, \psi^{\lambda_2 i_2}_{j_3 j_1} \right)$$

$$+ \frac{f^{\lambda_2}_{j_1 j_2} v^{(-)}_{j_1 j_2}}{\sqrt{\mathcal{Y}^{\lambda_2 i_2}_{\tau}}} \begin{Bmatrix} \lambda_1 & \lambda_2 & \lambda \\ j_1 & j_3 & j_2 \end{Bmatrix}$$

$$\left. \times \left(\psi^{\lambda i}_{j_3 j_1} \, \psi^{\lambda_1 i_1}_{j_2 j_3} + \varphi^{\lambda i}_{j_3 j_1} \, \varphi^{\lambda_1 i_1}_{j_2 j_3} \right) \right],$$

where $v^{(-)}_{j_1 j_2} = u_{j_1} u_{j_2} - v_{j_1} v_{j_2}$.

The diagrams corresponding to the various terms in (5) and (7) are shown in Fig. 1. The wavy lines correspond to the RPA phonons, and the straight lines with arrows represent fermions. In addition to these diagrams, there are also diagrams that can be generated by inverting the direction of the phonon lines in the diagrams presented in Fig. 1 (for details, see [2, 3, 23]). A direct diagonalization of the QPM Hamiltonian enables one to take into account the contribution of all possible diagrams that are responsible for anharmonical corrections.

The orthogonality relation between pure two-phonon configurations has the form

$$\sum_{\text{all } \mu} \langle [Q_{\lambda_4 \mu_4 i_4} Q_{\lambda_3 \mu_3 i_3}]_{JM} \mid [Q^+_{\lambda_1 \mu_1 i_1} Q^+_{\lambda_2 \mu_2 i_2}]_{JM} \rangle \tag{8}$$

$$= \delta_{\lambda_1 i_1, \lambda_3 i_3} \delta_{\lambda_2 i_2, \lambda_4 i_4}$$

$$+ \frac{K^{\lambda_4 i_4 \lambda_3 i_3}_{\lambda_1 i_1 \lambda_2 i_2}(J)}{\sqrt{(1 + \delta_{\lambda_1 i_1, \lambda_2 i_2})(1 + \delta_{\lambda_3 i_3, \lambda_4 i_4})}}.$$

Equations (5), (7), and (8) were obtained by applying the exact commutation relations between phonon operators—i.e., by taking into account their internal fermion structure.

In order to eliminate the energy dependence in a two-step process of the DGDR excitation in relativistic heavy-ion collisions—this dependence also modifies the energy centroid of the DGDR with respect to a double energy of the single GDR—we have calculated, for DGDR excitation, the energy-independent quantity

$$B_{\nu}([E1 \times E1]_J) \tag{9}$$

$$= \left| \sum_i \langle \Psi^{\nu}_J | E1 | \Psi^i_{1^-} \rangle \langle \Psi^i_{1^-} | E1 | \Psi_{\text{g.s.}} \rangle \right|^2$$

$$= \frac{2J+1}{3} \left| 2 \sum_{i_1 \le i_2} P^{1^- i_2}_{1^- i_1}(J\nu) \frac{M_{i_1}(E1) M_{i_2}(E1)}{\sqrt{1 + \delta_{i_1, i_2}}} \right|^2,$$

where $M_i(E1)$ is the reduced transition probability of the $E1$ excitation of the ith one-phonon 1^- configuration from the ground state. The intermediate

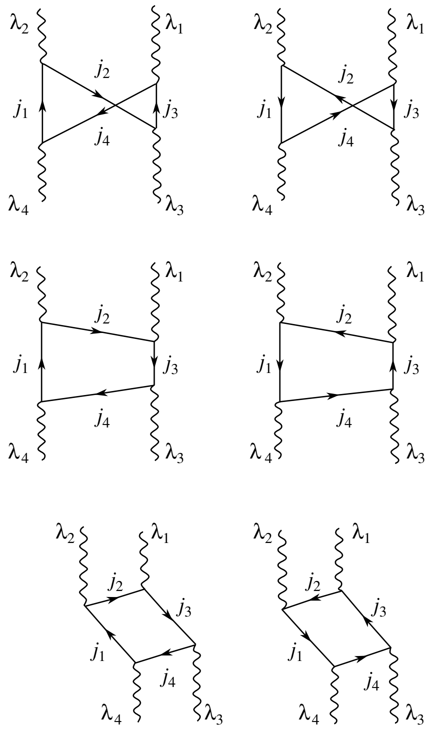

Fig. 1. Diagrams contributing to the anharmonicity shift of the DGDR.

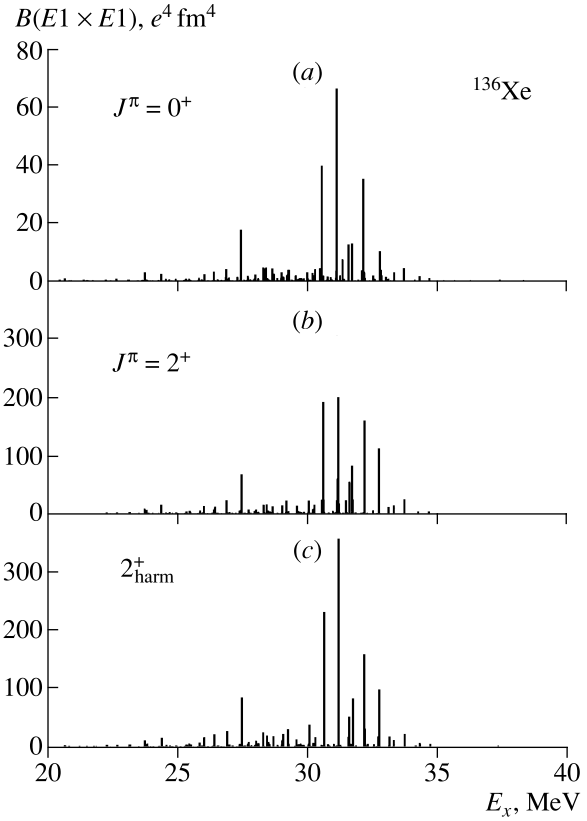

Fig. 2. Energy distributions of the $B(E1 \times E1)$ values associated with the excitation of the (a) 0^+ and (b) 2^+ components of the DGDR in ^{136}Xe, along with the same quantity for the (c) 2^+ component in the harmonic limit. Scales are chosen to be in proportion to $2J + 1$.

states $\Psi^i_{1^-}$ belonging to the GDR are described in the one-phonon approximation. The results will be compared with the harmonic picture of nuclear excitation in which $P^{\lambda_2 i_2}_{\lambda_1 i_1}(J\nu) = \delta_{\lambda_1 i_1 \lambda_2 i_2, 1^- i_1 1^- i_2}$ and the excitation energy of the two-phonon configuration $[1^- i_1 \times 1^- i_2]_J$ is exactly equal to $(\omega_{1^- i_1} + \omega_{1^- i_2})$.

Natural-parity phonons of multipole order λ from 0 to 4 were used in the calculations. All one-phonon configurations up to the excitation energy of 50 MeV were included in the first term of the wave function (1). The basis of two-phonon configurations was slightly truncated to make calculations possible as follows: all collective and weakly collective phonons that contribute to the energy-weighted sum rule (EWSR) with more than 0.2% for dipole phonons and 1.0% for other multipolarities were taken into account.

3. RESULTS

The calculations have been performed for nuclei from various mass regions. Figure 2 shows the quantities $B_\nu([E1 \times E1]_J)$ for various (two-phonon) states ν (eigenstates of the total Hamiltonian with angular momentum and parity 0^+ and 2^+) of the nucleus ^{136}Xe.

The results of our calculations are listed in the table. Presented in the second column of the table is the exhaustion of TRK EWSR by electric dipole phonons included in the model space. In the third column, the exhaustion of the DGDR sum rule $S_2^{(1)}$ introduced in [24] is given for the sum of 0^+ and 2^+ components of the DGDR in our calculations. This quantity is

$$S_2^{(1)} = 4 S_1^{(0)} S_1^{(1)} ,$$

where $S_1^{(1)}$ is the TRK sum rule for the GDR. For

$$S_1^{(0)} = \sum_i \left| \langle 1_i^- | E1 | \mathrm{g.s.} \rangle \right|^2 ,$$

we used the value from our calculation of GDR excitation in the one-phonon approximation. A small difference between the exhaustion of the EWSR for the DGDR and the GDR is due to the fact that the ground state is considered as a phonon vacuum in the present approach and that ground-state correlations, which arise from the interaction between multiphonon configurations, are not taken into account. In the last two columns of the table, the values of the anharmonicity shift of the DGDR energy centroid

$$E_c(J) = \frac{\sum_\nu B_\nu([E1 \times E1]_J) E_\nu(J)}{\sum_\nu B_\nu([E1 \times E1]_J)}$$

Percentage of the EWSR exhausted by the GDR and DGDR of nuclei and values of the anharmonicity shift $\Delta E_c(J^\pi)$ of the energy centroid for the $J^\pi = 0^+$ and 2^+ components of the DGDR from its harmonic limit

Nuclei	EWSR, %		$\Delta E_c(J^\pi)$, keV	
	GDR	DGDR	$J^\pi = 0^+$	$J^\pi = 2^+$
^{40}Ca	104	103	−643	−740
^{58}Ni	104	103	−476	−495
^{86}Kr	106	105	−309	−271
^{120}Sn	106	105	−199	−194
^{136}Xe	103	102	−203	−179
^{208}Pb	94	94	−108	−158

with respect to the energy centroid of the DGDR in the harmonic approximation—i.e., the double value of the energy centroid of the GDR—are presented individually for the 0^+ and 2^+ components of the DGDR.

Corrections associated with the Pauli exclusion principle are responsible for this energy shift [2]. Excluding four-quasiparticle configurations, which violate the Pauli exclusion principle, reduces somewhat the collectivity of two-phonon configurations. Thus, from general arguments, we should expect a positive sign of the shift for two-phonon states formed by two isoscalar phonons and a negative sign when we are dealing with isovector phonons, as in the case of the DGDR.

According to the predictions of various approaches for the A dependence of the anharmonicity shifts, their value follows the A^{-1} [1, 18] or $A^{-5/3}$ [16] dependence. The results of the present calculations follow the A^{-1} dependence very well, although both doubly magic and semimagic nuclei have been included in the consideration. Weighing equally the 0^+ and 2^+ components of the DGDR, we obtain a $|\Delta E| \sim A^{-\alpha}$ dependence with $\alpha = 1.08 \pm 0.06$ from a χ^2 analysis of the results in the table. To better appreciate the results, one should point out that the present calculations of the shift have been performed without free parameters. The strength of the isovector dipole residual interaction, the most important parameter for this calculation, was fixed on the basis of a fit to the energy of the GDR centroid in each nucleus known from experiment or systematics.

Let us compare the results of the present calculation for the anharmonicity energy shifts with the results of our previous calculations that took into account an additional coupling to three-phonon configurations [14]. Figures 3*b* and 3*c* show the quantity $B(E1) \times B(E1)$ (9), which is associated with the Coulomb excitation of the $J^\pi = 0^+$ and $J^\pi = 2^+$ components of the DGDR. The quantity $B(E1)$ associated with the Coulomb excitation of the GDR is shown in Fig. 3*a*. The calculated excitation functions displayed in Figs. 3*b* and 3*c* yield the following values for the centroid and the width of the DGDR in ^{136}Xe: $\langle E_{0^+}\rangle = 30.68$ MeV and $\Gamma_{0^+} = 6.82$ MeV for the 0^+ component of the DGDR and $\langle E_{0^+}\rangle = 30.71$ MeV and $\Gamma_{2^+} = 6.84$ MeV for the 2^+ component. These values are to be compared with $\langle E_{1^-}\rangle = 15.40$ MeV and $\Gamma_{1^-} = 4.72$ MeV for the single GDR in this nucleus from our calculation. In this case, the anharmonicity shifts $\Delta E_c(J^\pi) = E_{\mathrm{DGDR}} - 2E_{\mathrm{GDR}}$ are about −100 keV; they are underestimated in relation to the present calculation. The calculated widths are quite close to the predictions of the harmonic model, $\Gamma_{\mathrm{DGDR}} = \sqrt{2}\Gamma_{\mathrm{GDR}}$. The last ones are in good agreement with experimental data [7] too. Large-scale calculations taking into account the coupling of the DGDR to one- and three-phonon terms can reproduce very well the integrated characteristics of the DGDR in many nuclei [8].

Comparing the results of the present calculation of the DGDR properties with the previous ones [14], we should note the following. The main idea of the calculation in [14] was to describe the width of the DGDR; for this reason, the three-phonon term was added to the wave function (1), but we had to truncate very strongly the basis of the two-phonon configurations in order to make numerical calculations possible. Thus, only the most important two-phonon configurations of the type $[1^-_i \otimes 1^-_{i'}]$ have been included in the model space. Also, the internal fermion structure of phonons was taken into account only for the one- and two-phonon configurations, while the three-phonon ones were treated as those that are constructed of bosons. For this reason, the shift of the DGDR centroid in [14] was underestimated, and 0^+ and 2^+ components of the DGDR were virtually degenerate. In the present calculation, the model space of two-phonon configurations is rather complete and the $B([E1 \times E1]_J)$ strength distribution over two components of the DGDR is different. It is presented in Fig. 2*a* for 0^+ and in Fig. 2*b* for 2^+ components of the DGDR in ^{136}Xe along with the strength distribution in the harmonic limit in Fig. 2*c*.

Although the calculations discussed above have been done with a separable residual interaction, a comparison with other calculations performed for some doubly magic nuclei within different approaches and with the Skyrme [25] or Migdal [12] forces supports the A^{-1} dependence.

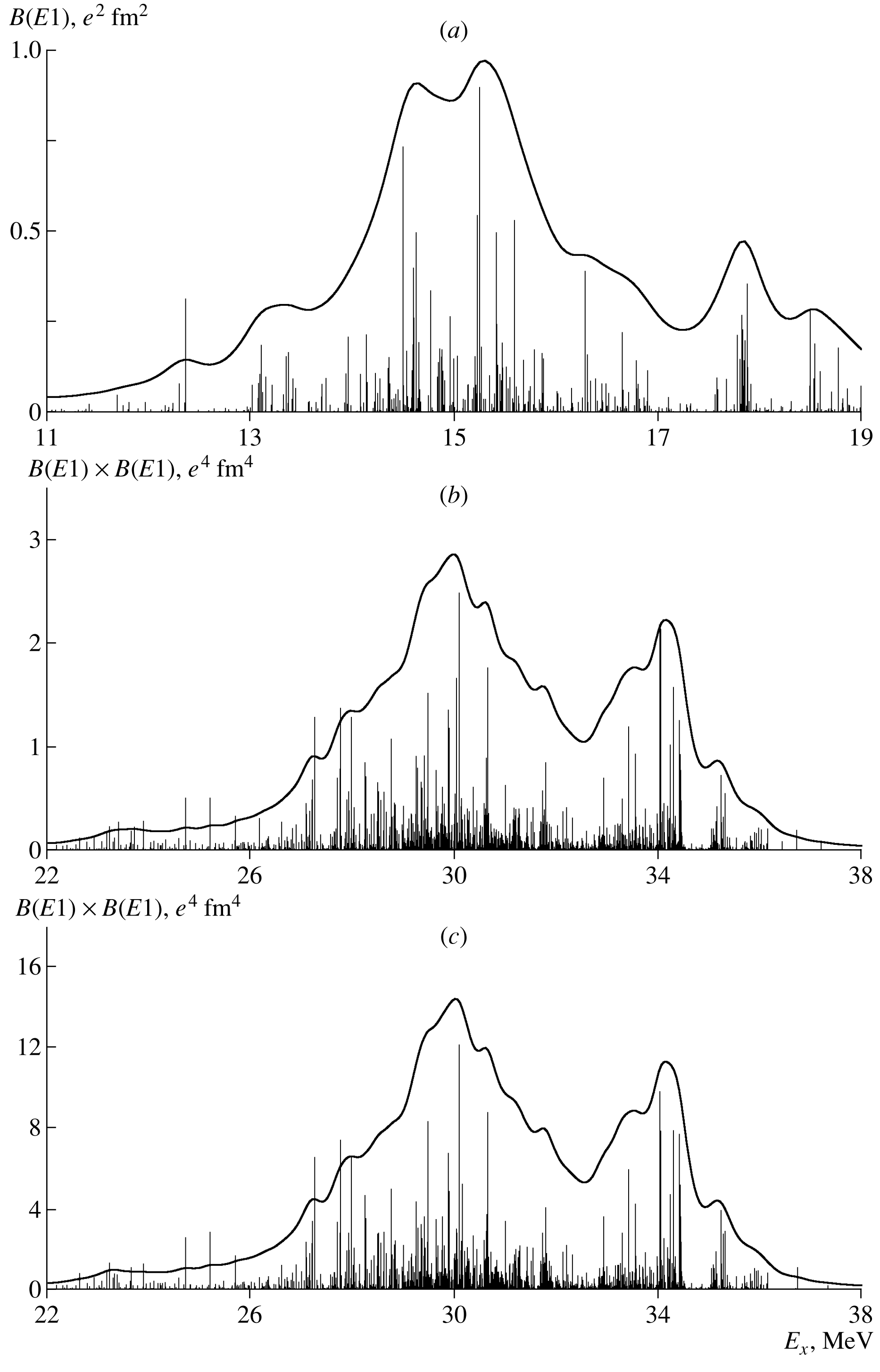

Fig. 3. Fragmentation of the most collective (*a*) one-phonon 1^- and two-phonon $[1^- \otimes 1^-]$ configurations with (*b*) $J^\pi = 0^+$ and (*c*) $J^\pi = 2^+$. The results are presented with a smearing parameter $\Delta = 0.5$ MeV.

4. CONCLUSION

On the basis of the present and other microscopic calculations, one can conclude that the integrated characteristics of the double giant resonances can be described very well and that the deviation of the energy centroid of the DGDR from the harmonic limit as a function of the mass number A displays a behavior typical of that associated with the global properties characterizing the system, like the energy centroid of the GDR.

ACKNOWLEDGMENTS

I would like to thank my colleagues P.F. Bortignon, R.A. Broglia, and V.Yu. Ponomarev for fruitful collaboration and A.P. Severyukhin for help.

REFERENCES

1. A. Bohr and B. R. Mottelson, *Nuclear Structure*, vol. 2: *Nuclear Deformations* (Benjamin, New York, 1975; Mir, Moscow, 1977).
2. V. V. Voronov and V. G. Soloviev, Teor. Mat. Fiz. **57**, 75 (1983).
3. V. G. Soloviev, *Theory of Atomic Nuclei: Quasiparticles and Phonons* (Institute of Physics, Bristol, 1992).
4. S. Mordechai and C. F. Moore, Int. J. Mod. Phys. E **3**, 39 (1994).
5. H. Emling, Prog. Part. Nucl. Phys. **33**, 729 (1994).
6. P. Chomaz and N. Frascaria, Phys. Rep. **252**, 275 (1995).
7. T. Aumann, P. F. Bortignon, and H. Emling, Annu. Rev. Nucl. Part. Sci. **48**, 351 (1998).
8. C. A. Bertulani and V. Yu. Ponomarev, Phys. Rep. **321**, 139 (1999).
9. A. Winther and K. Adler, Nucl. Phys. A **319**, 518 (1979).
10. F. Catara, Ph. Chomaz, and N. Van Giai, Phys. Lett. B **233**, 6 (1989).
11. V. Yu. Ponomarev *et al.,* Phys. Rev. Lett. **72**, 1168 (1994).
12. S. Nishizaki and J. Wambach, Phys. Rev. C **57**, 1515 (1998).
13. C. Volpe *et al.,* Nucl. Phys. A **589**, 521 (1995); **647**, 246 (1999).
14. V. Yu. Ponomarev, P. F. Bortignon, R. A. Broglia, and V. V. Voronov, Z. Phys. A **356**, 251 (1996).
15. P. F. Bortignon and C. H. Dasso, Phys. Rev. C **56**, 574 (1997).
16. G. F. Bertsch and H. Feldmeier, Phys. Rev. C **56**, 839 (1997).
17. E. G. Lanza, M. V. Andrcs, F. Catara, *et al.,* Nucl. Phys. A **613**, 445 (1997).
18. I. Hamamoto, Phys. Rev. C **60**, 054320 (1999).
19. G. F. Bertsch, P. F. Bortignon, and K. Hagino, Nucl. Phys. A **657**, 59 (1999).
20. V. Yu. Ponomarev, P. F. Bortignon, R. A. Broglia, and V. V. Voronov, Phys. Rev. Lett. **85**, 1400 (2000).
21. A. I. Vdovin and V. G. Soloviev, Fiz. Élem. Chastits At. Yadra **14**, 237 (1983) [Sov. J. Part. Nucl. **14**, 99 (1983)].
22. V. V. Voronov and V. G. Soloviev, Fiz. Élem. Chastits At. Yadra **14**, 1380 (1983) [Sov. J. Part. Nucl. **14**, 583 (1983)].
23. P. F. Bortignon, A. Bracco, and R. A. Broglia, *Giant Resonances. Nuclear Structure at Finite Temperature* (Harwood Academy, New York, 1998).
24. H. Kurasawa and T. Suzuki, Nucl. Phys. A **597**, 374 (1996).
25. M. Tohyama, nucl-th/0003034.

Physics of Atomic Nuclei, Vol. 64, No. 6, 2001, pp. 1027–1029. From Yadernaya Fizika, Vol. 64, No. 6, 2001, pp. 1103–1104.
Original English Text Copyright © 2001 by Bortignon.

Nuclear Structure at Finite Temperature: A Review*

P. F. Bortignon**

Dipartimento di Fisica, Università degli Studi, and INFN, Milano, Italy

Received September 11, 2000

Abstract—Information on nuclear structure at finite temperature is obtained from the physics of the level density, of the rotational damping, and of the giant dipole resonance thermally excited on a compound nucleus at very large excitation energy (and angular momentum). The current understanding in terms of mean-field theories and beyond is reviewed. The coupling to doorway states and the coupling to many-particle–many-hole states in the random-matrix-theory limit are discussed. Emphasis will be on the close relation between the single-particle damping and the damping of collective vibrations. The coherence between the particle and the hole strongly suppresses the vibrational damping, in particular, the temperature dependence. © *2001 MAIK "Nauka/Interperiodica"*.

Experimental information on nuclear structure properties at finite temperature T up to few MeV is obtained from the study of the nuclear level densities, and in the last decades from the physics of the rotational damping and of the giant dipole resonance (GDR) thermally excited on compound nucleus states at very large excitation energy and angular momentum [1, 2]. The contributions of A. Schiller, S. Leoni, and F. Camera at this conference discuss very recent, exciting experimental achievements in these fields. In what follows, I will shortly review some recent theoretical developments.

There is no need to stress the role of the level density $\rho(E_x)$ at the excitation energy E_x, being important for theoretical estimates of any nuclear reaction rates. In particular, this is true for nucleosynthesis calculations, with the s and r processes determined by the competition between neutron capture and beta decay.

Conventional calculations of ρ are based on the Fermi gas model, in which all many-body effects, but those associated with fermion statistics, are neglected, in particular, the small-amplitude quantal as well as the large-amplitude thermal fluctuations associated with the surface collective vibrations. Along with the Fermi gas formula, popular is the backshifted Bethe formula (BBF), where the ground state energy is backshifted by an amount Δ adjusted for each nucleus together with the level density parameter a to obtain

$$\rho(E_x) \propto \exp\left(2\sqrt{a(E_x-\Delta)}\right). \qquad (1)$$

Powerful methods to take the effects of the fluctuations into account have been developed making use of the functional-integral techniques. Assuming a nuclear Hamiltonian which contains, at most, two-body terms and making use of the Hubbard–Stratonovich transformation, the partition function Z (from which ρ is obtained) is written as a functional integral over auxiliary one-body fluctuating fields $\sigma(\tau)$. Different approximations have been used to evaluate this integral, as the static path approximation (SPA) and the SPA + RPA, with the RPA carried out not only around the mean field σ_0, but also in configurations away from it. Thus, increases of the level density of orders of magnitude are obtained compared to the mean-field values, especially at low excitation energy [3]. More recently, the integral has been evaluated exactly (up to statistical errors) by Monte Carlo methods as in the shell-model Monte Carlo approach (SMMC) [4, 5]. With the aid of Hamiltonians that include correctly the dominating collective components of realistic effective interactions in terms of monopole pairing and isoscalar multipole–multipole terms [6], impressive agreement with the empirical values is obtained for a and Δ (the SMMC level densities are fitted to the BBF). This is so for E_x up to 20 MeV and in nuclei of mass A up to ^{162}Dy [7–9].

In heavier nuclei and at higher excitation energy, the T dependence of the level-density parameter a can be obtained from the behavior of the effective mass m^* [10],

$$\frac{m^*}{m} = \frac{m_k}{m}\frac{m_\omega}{m}, \qquad (2)$$

for which we have $a \propto m^*$. The k mass m_k/m is connected to the nonlocality of the mean field and is rather constant with T, while the ω mass

---

[*] This article was submitted by the author in English.

[**] e-mail: `pierfrancesco.bortignon@mi.infn.it`

m_ω/m, connected to the frequency dependence of the real part of the single-particle (hole) self-energy $\Sigma_{\rm sp}(\omega, T)$, drops from the $T = 0$ value of about 1.5 (at the Fermi energy) to unity for temperature of about the frequency of the collective surface vibrations to which single-particle motion is coupled [11, 12] in the doorway-state coupling model. Thus, a is expected to drop to the Fermi gas value, in qualitative agreement with the existing, still limited, experimental evidences. The extension of this approach is in progress for the deformed nuclei. Results at zero temperature are just published in [13].

The imaginary part of $\Sigma_{\rm sp}(\omega, T)$ gives the spreading width $\Gamma^\downarrow$ of single-particle (hole) states. The coupling to doorway $2p$–$1h$ ($2h$–$1p$) states containing a collective surface vibration produces a linear dependence on energy $\omega - \epsilon_{\rm F}$ and temperature [14, 15] as

$$\Gamma_j^\downarrow = \alpha(\omega - \epsilon_{\rm F}) + \beta T\,, \tag{3}$$

where α and β are of the order of 1 for $\omega \approx \epsilon_{\rm F}$ and of order of 4 and 0.2 respectively for $(\omega - \epsilon_{\rm F}) \approx 8$ MeV as in the GDR [16]. While α compares well with the empirical values [17] (testifying to the success of the doorway coupling model), no direct comparison is possible for β.

The spreading width $\Gamma_{\rm GR}^\downarrow$ of the GR is not simply related to the single-particle (hole) spreading widths because of the interference between the amplitudes describing the decay of the single-particle and single-hole states in the doorway states [18]. These terms (vertex corrections) ensure the coherence of the collective motion and the fulfillment of the conservation laws (Ward identities). In particular, they strongly reduce (because of cancellation effects) the weak $\beta \approx 0.2$ temperature dependence of the spreading width $\Gamma_j^\downarrow$, making the spreading width $\Gamma_{\rm GR}^\downarrow$ in this doorway coupling model very much temperature-independent [14, 16, 19]. At zero temperature, the resulting values have been shown to be in agreement with the data for a variety of GR modes and nuclei [1]. Recently [20], a careful analysis of the contribution to $\Gamma_{\rm GR}^\downarrow$ of the collision-integral type of terms (in which the GR is coupled to $2p$–$2h$ uncorrelated states via effective interactions) has shown that this contribution is indeed small, of the order of 25–30% of $\Gamma_{\rm GR}^\downarrow$, when calculated employing a realistic microscopic in-medium cross section. Much larger and much faster growing (as T^2) values were claimed in the past. The authors of [20] concluded that “there is plenty of room for coherent damping mechanism due to coupling of the dipole mode with surface fluctuations.” Thus, the experimental growth of the total $\Gamma_{\rm GDR}$ with T and angular momentum is explained in terms of large-amplitude fluctuations of shape and orientation [21–23]. Problems remain in a more punctual comparison with the strength functions extracted from the experimental spectra and with the total GDR strength at very high excitation energy.

The success of the doorway coupling approach is justified by the smooth properties of the coupling to the chaotic background of many-particle–many-hole states in the compound nucleus (CN), which will not alter the main features of the strength functions obtained in the doorway coupling. In the random matrix theory limit, we write for the interaction matrix elements V_n between the GR and the background states

$$(V_n) = 0,\ \ (V_n V_m) = \delta_{nm} v^2/N, \tag{4}$$

where v is the typical mixing matrix element between the resonance and simple intrinsic states and N is the number of significant components of the complicated CN states. Then, we obtained

$$\Gamma^\downarrow = 2\pi v^2 \rho/N \sim v^2/a, \tag{5}$$

where $a \sim ND$ is the fragmentation energy interval (D the mean level spacing). All exponentially growing quantities are eliminated due to the random properties with $(1/\sqrt{N})$ scaling of the coupling [24–26].

ACKNOWLEDGMENTS

I would like to thank R.A. Broglia, P. Donati, and N. Giovanardi for the fruitful collaboration on the subjects above over many years.

REFERENCES

1. P. F. Bortignon, A. Bracco, and R. A. Broglia, *Giant Resonances. Nuclear Structure at Finite Temperature* (Harwood Academy, New York, 1998).
2. *Proceedings of the Topical Conference on Giant Resonances, 1998,* Ed. by A. Bracco and P. F. Bortignon; Nucl. Phys. A **649** (1999).
3. P. Arve *et al.,* Ann. Phys. (N.Y.) **183**, 309 (1988); G. Puddu, P. F. Bortignon, and R. A. Broglia, Ann. Phys. (N.Y.) **206**, 409 (1991).
4. G. H. Lang *et al.,* Phys. Rev. C **48**, 1518 (1993).
5. S. E. Koonin, D. J. Dean, and K. Langanke, Phys. Rep. **278**, 1 (1997).
6. Y. Alhassid *et al.,* Phys. Rev. Lett. **77**, 1444 (1996).
7. H. Nakata and Y. Alhassid, Phys. Rev. Lett. **79**, 2939 (1997).
8. J. A. White *et al.,* Phys. Rev. C **61**, 034303 (2000).
9. Y. Alhassid *et al.,* Phys. Rev. Lett. **84**, 4313 (2000).
10. C. Mahaux, P. F. Bortignon, R. A. Broglia, and C. H. Dasso, Phys. Rep. **120**, 1 (1985).
11. P. F. Bortignon and C. H. Dasso, Phys. Lett. B **189**, 381 (1987).
12. P. Donati *et al.,* Phys. Rev. Lett. **72**, 2835 (1994).

13. P. Donati *et al.,* Phys. Rev. Lett. **84**, 4317 (2000).
14. P. F. Bortignon *et al.,* Nucl. Phys. A **460**, 149 (1986).
15. N. Giovanardi *et al.,* Ann. Phys. (N.Y.) (in press).
16. P. Donati, N. Giovanardi, P. F. Bortignon, and R. A. Broglia, Phys. Lett. B **383**, 15 (1996).
17. C. Mahaux and R. Sartor, Adv. Nucl. Phys. **20**, 1 (1991).
18. G. F. Bertsch, P. F. Bortignon, and R. A. Broglia, Rev. Mod. Phys. **55**, 287 (1983).
19. N. Giovanardi *et al.,* Nucl. Phys. A **641**, 95 (1998).
20. O. Yilmaz *et al.,* Phys. Lett. B **472**, 258 (2000).
21. W. E. Ormand, P. F. Bortignon, R. A. Broglia, and A. Bracco, Nucl. Phys. A **614**, 217 (1997).
22. M. Mattiuzzi *et al.,* Nucl. Phys. A **612**, 262 (1997).
23. D. Kusnezov, Y. Alhassid, and K. Snover, Phys. Rev. Lett. **81**, 542 (1998).
24. V. Zelevinsky, Annu. Rev. Nucl. Part. Sci. **46**, 237 (1996).
25. V. Zelevinsky, Nucl. Phys. A **649**, 403c (1999).
26. B. Lauritzen, P. F. Bortignon, R. A. Broglia, and V. G. Zelevinsky, Phys. Rev. Lett. **74**, 5190 (1995).

Physics of Atomic Nuclei, Vol. 64, No. 6, 2001, pp. 1030–1032. From Yadernaya Fizika, Vol. 64, No. 6, 2001, pp. 1105–1107.
Original English Text Copyright © 2001 by Kvasil, Lo Iudice, Nesterenko, Macková.

Coupling of Giant Resonances via Residual Interactions*

J. Kvasil**, N. Lo Iudice[1)], V. O. Nesterenko[2)], and A. Macková

Particle and Nuclear Physics Institute, Charles University, Praha, Czech Republic

Received September 11, 2000

Abstract—The coupling between $E2$ and $M1$ modes in deformed ^{154}Sm is investigated within the novel averaging RPA approach with the factorized residual interaction. The calculations show that the $E2$ giant resonance is not noticeably affected by the coupling. At the same time, the $M1$ response demonstrates a new structure (high-energy branch of the scissors mode) at 24–25 MeV. © *2001 MAIK "Nauka/Interperiodica".*

Deformed nuclei, as compared with spherical ones, demonstrate strong fragmentation of the strength of giant resonances. The deformation results in a considerable broadening or even splitting of the resonances. This effect has already been well studied in numerous publications (see, e.g., [1]). Much less attention has been paid to other consequence of the deformation, the mixing of electric and magnetic excitations of a given parity. This effect is rather fragile and, in principle, needs a careful microscopic analysis and considerable computational effort.

The residual two-body interaction can be decomposed into a series of separable multipole, spin–multipole, etc., terms (see, e.g., [2, 3]). In deformed nuclei, the moments λ of such terms cannot be associated with the moment of a nuclear state. As a result, the nuclear state with quantum numbers K^π can be affected by any electric and magnetic residual interactions $\lambda\mu$ with the same parity and $\mu = K$. In the present paper, we will analyze the remarkable example of the coupling of $E2$ and $M1$ modes in deformed ^{154}Sm. The main question to be addressed is how much this effect influences $E2$ and $M1$ giant resonances. As compared to other studies of this problem (see, e.g., [4, 5]), we will use the novel specific technique [6] which allows one to avoid the solution of the complex RPA equations describing the coupling electric and magnetic modes. This simplification is especially important if one deals with giant resonances in deformed nuclei which are known to embrace a huge configuration space. Besides, the experiment provides only averaged properties of giant resonances, and, therefore, in any case, we do not need information about every RPA root.

For the analysis mentioned above, the Lorentzian averaging technique [6–8] was used to determine the $E2$ and $M1$ strength functions. This technique is described in detail in [6], where it is applied to the Hamiltonian with separable multipole and spin–multipole residual interactions. The electromagnetic operators, as well as the fields of the residual interaction, are presented within the signature formalism which is especially suitable for fast rotating nuclei. In the framework of this approach, the RPA axial symmetrical Hamiltonian can be decomposed into the mutually commuting terms, $H_K\binom{r}{\pi}$,

$$H_{\rm RPA} = \langle {\rm RPA}|{\rm H}|{\rm RPA}\rangle + \sum_{r=+1}\sum_{\pi=+1}\sum_{K\geq 0} H_K\binom{r}{\pi}, \tag{1}$$

where each term $H_K\binom{r}{\pi}$ contains the multipole $M_{\lambda K} \sim r^\lambda Y_{\lambda K}$ and spin–multipole $T_{l\lambda K} \sim r^l[\sigma \otimes Y_l]_{\lambda K}$ operators with given parity π, signature r, and projection K (the projection of the angular moment to the symmetry axis). In the case of the $E2$ and $M1$ resonances, we may restrict ourselves to the following terms of the Hamiltonian (see [6]): $H_{K=0}\binom{r=+1}{\pi=+1}$ (pairing, M_{20}, and T_{010} terms) and $H_{K=1}\binom{r=+1}{\pi=+1}$ (T_{011} and M_{21} terms).

The RPA equations for the collective vibrations of electric and magnetic type are solved independently for each part, $H\binom{r}{\pi}$, of the Hamiltonian (1). They can be written [6] as a system of algebraic equations for unknowns $R_i^{(\nu)}$

$$\sum_{j=1}^{2n} D_{ij} R_j^{(\nu)} = 0, \qquad D_{ij} = D_{ji}, \tag{2}$$

---

[*] This article was submitted by the authors in English.

[1)] Dipartimento di Scienze Fisiche, Università di Napoli Federico II, Italy.

[2)] Bogoliubov Laboratory of Theoretical Physics, JINR, Dubna, Russia.

[**] e-mail: `kvasil@hp02.troja.mff.cuni.cz`

where the matrix D_{ij} contains quasiparticle matrix elements of the single-particle operators involved to the $H_K\binom{r}{\pi}$. In (2), n is the number of the single-particle multipole and spin–multipole operators included in the $H_K\binom{r}{\pi}$ and the index ν numerates the solutions of Eq. (2) (see [6] for details). The solutions $R_j^{(\nu)}$ determine the contributions of two-quasiparticle components j to the phonons ν (for each set of K, r, π). The Lorentz averaging technique allows one to determine the strength function for the reduced transition probability without the time-consuming procedure of the solution of the RPA equations (2) for each phonon state. The expression for the strength function (as a function of the excitation energy E) is [6]

$$\begin{aligned} &S(XL\mu, gr \longrightarrow K^\pi) \qquad (3)\\ &= \sum_\nu B(XL\mu, gr \longrightarrow \nu)\rho(E-E_\nu)\\ &= \frac{2}{\pi}\mathrm{Im}\frac{\det[\hat{B}(z)]}{\det[\hat{D}(z)]}\Bigg|_{z=E+i\Delta/2} + \frac{\Delta}{2\pi}\sum_{ij}(p_{i\bar{j}}^{X\lambda\mu})^2\\ &\times\left[\frac{1}{(\varepsilon_{i\bar{j}}-E)^2+\Delta^2/4} - \frac{1}{(\varepsilon_{i\bar{j}}+E)^2+\Delta^2/4}\right]. \end{aligned}$$

Here, $B(XL\mu, gr \longrightarrow \nu)$ is the reduced probability of the electromagnetic transition $XL\mu$ between the ground state and the phonon state ν with quantum numbers K^π $(K=\mu)$, E_ν is the excitation energy of the one-phonon state ν, the matrices $\hat{B}(z)$ and $\hat{D}(z)$ are defined in [6], $\varepsilon_{i\bar{j}}$ is the energy of the two-quasiparticle state $i\bar{j}$, and $p_{i\bar{j}}^{X\lambda\mu}$ is the corresponding single-particle matrix element of the $X\lambda\mu$ transition. Further, $\rho(E-E_\nu) = \Delta/[2\pi((E-E_\nu)^2+(\Delta/2)^2)]$ is the Lorentz function with the averaging parameter Δ (here $\Delta = 1$ MeV). The first term of the right-hand side of (3) represents the contribution of the residual interaction, while the second term gives the contribution of the unperturbed system. The sum of the strength functions (3) over all projections K $(K \geq 0)$ gives the total strength function $S(XL)$.

Numerical calculations have been performed for the spherical nucleus ^{144}Sm and deformed one ^{154}Sm. We started with the spherical Nilsson average field with its standard parametrization given in [9]. Using the Hartree–Fock–Bogolyubov method, we obtained neutron and proton quasiparticle fields (deformed one for ^{154}Sm; see [6] for details). The parameters of the nn and pp monopole pairing were taken from [10]. The strength constants, $\kappa_2[\tau=0] = 9.2 \times 10^4$ MeV fm^{-4} and $\kappa_2[\tau=1] = -2.6 \times 10^3$ MeV fm^{-4}, of the isoscalar and isovector quadrupole residual interaction, respectively, were taken in accordance with [11]. To restore the rotational invariance of the RPA Hamiltonian, the constant $\kappa_2[\tau=0]$ was slightly varied in order to get the zero energy for the first RPA solution. The isoscalar and isovector strength constants of the spin residual interaction, $\kappa_{01}[\tau=0] = -2.26$ MeV and $\kappa_{01}[\tau=1] = -3.26$ MeV, were chosen following the prescription [12] and available experimental data for the $M1$ giant resonance. Gyromagnetic factors $g_s(n) = -2.7$, $g_l(n) = 0$, $g_s(p) = 3.9$, and $g_l(p) = 1$ were used. Spin and orbital contributions to the $M1$ response were calculated with $g_l(n) = g_l(p) = 0$ and $g_s(n) = g_s(p) = 0$, respectively.

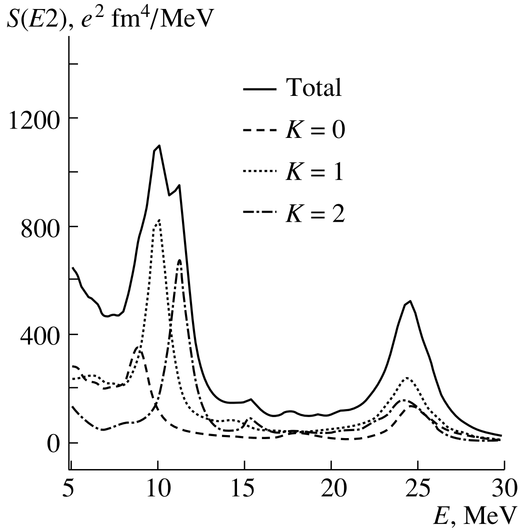

Fig. 1. $E2$ strength function in deformed ^{154}Sm.

The numerical results are exhibited in Figs. 1 and 2. Our calculations show that the coupling between $E2$ and $M1$ resonances does not influence noticeably the $E2$ resonance (this resonance is presented in Fig. 1). So, the analysis presented below will concern only the $M1$ resonance. In Figs. 2*a* and 2*b*, this resonance and its orbital and spin components are compared in spherical ^{144}Sm and deformed ^{154}Sm. Unlike the spherical case, the orbital component in ^{154}Sm dominates in the low-energy region. This component represents the well-known scissors mode [13] which exists only in deformed systems. In the energy region of the main peak, 5–10 MeV, the spin component dominates in both spherical and deformed nuclei. Due to the deformation splitting, the resonance in ^{154}Sm is much wider than in ^{144}Sm (compare Figs. 2*a* and 2*c*).

The most interesting effect is that the $M1$ mode in ^{154}Sm has the distinctive high-energy bump at 24–25 MeV. As is seen from Fig. 2*b*, this bump is of the orbital character. It has no counterpart in the spherical ^{144}Sm. Figure 2*c* shows that the bump takes place only in the $K = 1$ branch of the $M1$ response.

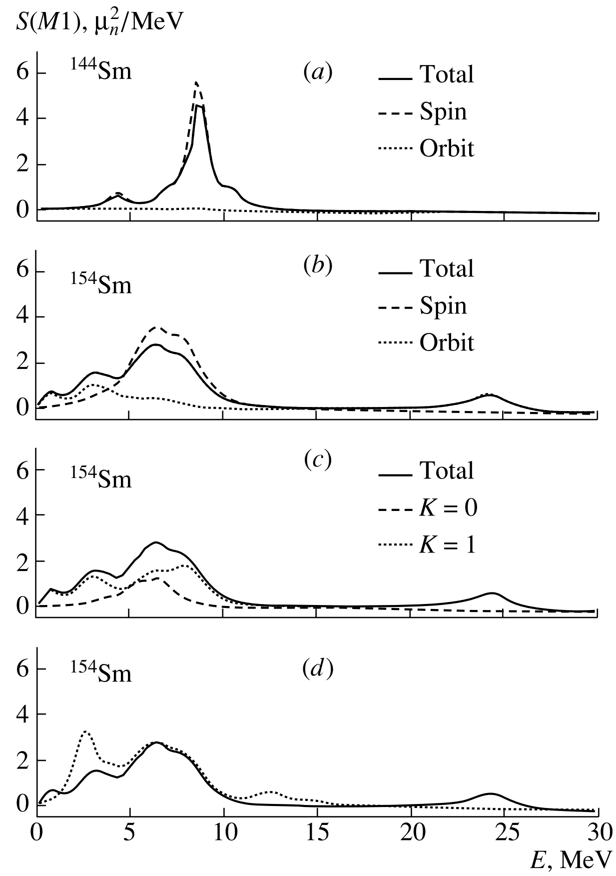

Fig. 2. $M1$ strength function in spherical (a) ^{144}Sm and (b–d) deformed ^{154}Sm. The parts of the figure represent (a and b) complete strength function and its orbital and spin components; (c) complete strength function and contributions of projections with $K = 0, 1$; (d) results obtained with the spin residual interaction only (dotted curve) and with the coupling between the spin and quadrupole interactions (solid curve). See the text for details.

The origin of the bump is explained in Fig. 2d, where two versions of the calculations are presented: with the spin residual interaction only ($T_{01\mu}$ terms) and with the coupling between the spin and quadrupole interactions ($T_{01\mu}$ and $M_{2\mu}$ terms). It is seen that just the coupling of the spin and quadrupole modes results in the high-energy resonance at 24–25 MeV. This treatment is confirmed by the remarkable correlation between this resonance and the isovector $E2$ resonance presented in Fig. 1. Both the resonances are placed at the same energy. In fact, the $M1$ bump at 24–25 MeV represents the high-energy branch of the orbital scissors mode. This result agrees with the previous schematic and microscopic RPA calculations (see [14] and references therein).

The correlation between the scissors mode and $E2$ excitations can be motivated by the close connection between the operator of the scissors mode, l_x (x projection of the single-particle angular momentum), and the operator r^2Y_{21} of the $E2$ mode. For example, in the configuration space of the harmonic anisotropic oscillator, there is a link between the corresponding particle–hole matrix elements

$$\langle p|l_x|h\rangle \propto b(\omega_0)\langle p|r^2Y_{21}|h\rangle, \qquad (4)$$

where $b(\omega_0) = 2\omega_0$ and $\delta\omega_0$ for the $\Delta N = 0$ and $\Delta N = 2$ transitions, respectively; N is a principal shell quantum number; δ is the parameter of the quadrupole deformation; and ω_0 is the oscillator frequency. So, the scissor excitations have to be essentially influenced by the residual quadrupole interaction.

In summary, the novel averaging technique has been used for the RPA study of the coupling of $E2$ and $M1$ modes in deformed ^{154}Sm. The interplay of the modes results in the remarkable high-energy (24–25 MeV) bump in the $M1$ response. Our analysis shows that the bump represents the high-energy branch of the scissors mode.

ACKNOWLEDGMENTS

The work was partly supported by RFBR grant no. 00-0217194 (V.O.N.) and by a Czech Republic grant no. 202/99/1718 (J.K. and A.M.).

REFERENCES

1. J. Speth and J. Wambach, in *Electric and Magnetic Resonances in Nuclei,* Ed. by J. Speth (World Scientific, Singapore, 1991), p. 1.
2. V. G. Soloviev, A. V. Sushkov, and N. Yu. Shirikova, Phys. Rev. C **56**, 2528 (1997).
3. V. G. Soloviev, *Theory of Complex Nuclei* (Pergamon, Oxford, 1976).
4. N. Lo Iudice and A. Richter, Phys. Lett. B **228**, 291 (1989).
5. R. Nojarov, A. Faessler, and M. Dilfender, Phys. Rev. C **51**, 2449 (1995).
6. J. Kvasil, N. Lo Iudice, V. O. Nesterenko, and M. Kopal, Phys. Rev. C **58**, 209 (1998).
7. L. A. Malov, V. O. Nesterenko, and V. G. Soloviev, Teor. Mat. Fiz. **32**, 134 (1977).
8. J. Kvasil and R. G. Nazmitdinov, Fiz. Élem. Chastits At. Yadra **17**, 613 (1986) [Sov. J. Part. Nucl. **17**, 265 (1986)].
9. K. Jain, P. C. Sood, R. K. Sheline, and A. K. Jain, Rev. Mod. Phys. **62**, 393 (1990).
10. P. Möller and P. Nix, http://t2.lanl.gov.
11. A. Bohr and B. R. Mottelson, *Nuclear Structure* (Benjamin, New York, 1974; Mir, Moscow, 1977), Vol. II.
12. B. Castel and I. Hamamoto, Phys. Lett. B **65**, 27 (1976).
13. N. Lo Iudice and F. Palumbo, Phys. Rev. Lett. **41**, 1532 (1978).
14. N. Lo Iudice, Phys. Rev. C **57**, 1246 (1998).

Physics of Atomic Nuclei, Vol. 64, No. 6, 2001, pp. 1033–1038. From Yadernaya Fizika, Vol. 64, No. 6, 2001, pp. 1108–1113.
Original English Text Copyright © 2001 by Lo Iudice.

Interplay between Orbital and Spin Motion in Heavy Nuclei[*]

N. Lo Iudice[**]

Dipartimento di Scienze Fisiche and INFN Sezione di Napoli,
Università di Napoli Federico II, Italy

Received September 11, 2000

Abstract—We investigate the role of orbital and spin motion in shaping the structure of the magnetic dipole and quadrupole spectra in spherical as well as in deformed heavy nuclei. © *2001 MAIK "Nauka/Interperiodica".*

1. INTRODUCTION

Most of the investigations on magnetic excitations were associated in the past with spin excitations only. More specifically, they were devoted to the quenching of the spin magnetic dipole and quadrupole transitions, a problem not completely solved yet [1]. In the past twenty years, however, the interest toward orbital excitations has literally exploded after the discovery of the low-lying $M1$ excitations, known as scissors mode [2], in ee' scattering [3]. Such a mode arises from a rotational oscillation of protons against neutrons and represents a unique example of orbital magnetic excitation. Systematic experimental and theoretical investigations have proved its existence in all deformed nuclei and unveiled its peculiar properties. It is well established by now that the mode is fragmented into several closely packed $M1$ transitions, mainly promoted by the convection current, with a summed $M1$ strength growing quadratically with nuclear deformation [4–7]. This law represents the most spectacular signature of the mode.

A fallout of the experiments stimulated by the discovery of the mode was the detection of spin excitations over an energy range of 4 to 12 MeV [8, 9]. Theoretical investigations have shown that the existence of the low-lying scissors mode is a consequence of the separation of the orbital from spin excitations. Such a splitting is promoted mainly by the spin–spin interaction which pushes the spin excitations at high energies, well above the domain of the orbital transitions.

Another peculiarity of the scissors mode is its strict correlation with deformation. According to the geometric two-rotor model [2] and consistent with all the other theoretical approaches, the scissors mode should exist in deformed nuclei only. As we shall discuss in the present paper, this is true if the mode is to be excited from the ground state. Nothing forbids, however, building a scissors mode on excited states with nonvanishing quadrupole moments in spherical nuclei. It has been shown in fact that these states can be constructed [10] and correspond to the so called mixed-symmetry states of the proton–neutron interacting boson model (IBM-2), observed in very recent experiments [11, 12].

The interference between orbital and spin motion is of crucial importance in the case of magnetic quadrupole transitions. The existence of the so-called twist mode [13] relies on the possibility of separating the spin from the orbital $M2$ excitations. Since such a separation cannot be obtained experimentally, one can get only indirect evidence of the existence of this mode through a combination of experimental measurements and theoretical analyses. Indeed, in a recent ee' experiment on ^{90}Zr, it has been shown that the contribution of the twist mode is essential in order to reproduce the experimental data [14].

In the present paper, we will discuss briefly the scissors mode and the spin excitations in deformed nuclei and try to clarify how spin and orbital motions interfere so as to generate the observed pattern of the $M1$ spectra at low and intermediate energies. We will then discuss the mechanism responsible for the excitation of the scissors mode in spherical nuclei. We finally discuss the possible outcome of this interference between orbital and spin motion in the $M2$ channel and provide the conditions for the separation of the orbital from the spin excitations and consequent identification of the twist mode.

2. SCISSORS MODE AND SPIN EXCITATIONS IN DEFORMED NUCLEI

In order to illustrate the excitation mechanism of the scissors mode, we decompose the full shell model

---

[*] This article was submitted by the author in English.

[**] e-mail: `loiudice@na.infn.it`

$M1$ operator into a rotational, a spin, and a scissors piece. The latter one, responsible for the excitation of the scissors mode, has the form

$$\mathbf{M}_{\rm sc}(M1) = \left(\frac{3}{16\pi}\right)^{1/2} \mathbf{S}(g_p - g_n)\mu_N \qquad (1)$$

$$= \left(\frac{3}{16\pi}\right)^{1/2} (\mathbf{J}^{(p)} - \mathbf{J}^{(n)})(g_p - g_n)\mu_N.$$

In axially deformed nuclei, the operator $\mathbf{S} = \mathbf{J}^{(p)} - \mathbf{J}^{(n)}$ generates a rotation of protons versus neutrons around an axis lying in the equatorial plane and, through such a relative rotational displacement, arouses a restoring force. The net result is a proton–neutron rotational oscillation, which in the two-rotor model (TRM) [2] is described by a two-dimensional harmonic oscillator in the angles ϑ_k between the proton and neutron symmetry axes and their conjugate variables $S_k = id/d\vartheta_k$ $(k = 1, 2)$. The scissors mode corresponds to the first excited eigenstate of intrinsic excitation energy $\omega = \sqrt{C_\vartheta/\Im_{\rm sc}}$, where $\Im_{\rm sc}$ and C_ϑ are, respectively, the mass parameter and the restoring force constant of the Hamiltonian. The state carries the $M1$ strength

$$B_{\rm sc}(M1)\uparrow = \frac{3}{16\pi}\, \Im_{\rm sc}\, \omega g_r^2\, \mu_N^2. \qquad (2)$$

This formula, of general validity, has the virtue of relating the properties of the mode to those of the nuclear mass parameter. In particular, the behavior of the moment of inertia versus deformation yields a summed $M1$ strength quadratic in the deformation parameters in agreement with experiments [15].

A largely model-independent study of the collective properties of the mode can be carried out by exploiting the energy weighted sum rule $M1$, which relates the energy weighted sum of the $M1$ strengths to the $E2$ transition probabilities [16, 17]. These being known experimentally, it has been possible to carry out an empirical analysis [17] which shows that the sum rule is almost exhausted only once the contribution of another mode of scissors nature at high energy is included. Indeed, such a mode is predicted in schematic RPA. The same study shows that the sum rule yields the deformation law for both low- and high-energy modes if the energy of the low-energy mode depends weakly on deformation. This is confirmed explicitly in schematic RPA [18].

Although successful in accounting for many of the properties of the mode, RPA calculations could not reproduce the energy distribution of the $M1$ strength. Such a failure has induced us to go beyond the harmonic approximation by computing the $M1$ spectra in the QPNM which accounts for the coupling between one and two RPA phonon states [19]. In the QPNM [20], one expresses a Hamiltonian of general separable form, acting on both particle–hole and particle–particle channels, in terms of quasiparticle operators and RPA phonons. An elaborated procedure yields a new Hamiltonian of the quasiparticle–phonon form. This transformed Hamiltonian is then put into diagonal form by using the variational principle with a trial wave function

$$\Psi_\nu(K^\pi = 1^+) \qquad (3)$$

$$\sim \left\{ \sum_v C_v^{(\nu)} Q_v^\dagger + \sum_{v_1, v_2} D_{v_1 v_2} Q_{v_1}^\dagger Q_{v_2}^\dagger \right\} \Psi_0.$$

The starting QPNM Hamiltonian is composed of a one-body deformed Woods–Saxon potential and a two-body interaction of separable form acting in the particle–hole and the particle–particle channels. The interaction is responsible for the separation of the orbital from the spin transitions. The observation of the scissors mode, in fact, results from the combined effect of the spin–spin interaction which pushes the low-lying spin excitation up in energy and the other components which tend to make more compact the orbital peaks.

A systematic analysis shows that the fragmentation induced by the coupling between one and two RPA phonons, although modest, improves the agreement between computed and measured spectra. Also the summed $M1$ strength is of the same order as the one observed experimentally. The coupling does not alter the nature of the transitions, which, in the range 2–4 MeV, remain of orbital nature. A modest spin admixture, however, affects considerably the intensity of the transition because of the constructive interference between orbital and spin motion. We have also tested the scissors nature of the transitions and found for the overlap with the scissors state $\sum_n |\langle K^\pi = 1^+, n|\psi_{\rm sc}\rangle|^2 \simeq 0.4$. Most of the other percentage goes to the high-lying states describing the high-energy scissors mode.

As pointed out already, the systematic experimental study of the scissors mode has lead to the discovery of spin excitations in rare-earth and actinide nuclei through pp' scattering [8, 9]. These $M1$ peaks fall in the energy range 4–12 MeV and, in some nuclei like ^{154}Sm, form a spectrum with two distinct bumps (Fig. 1). It has not been established yet if these two peaks correspond to distinct proton and neutron excitations [21] or to isovector and isoscalar excitations [22]. On the experimental side, highly sensitive NRF experiments using a EUROBALL cluster module have found [23] that the $\gamma\gamma'$ spectrum is in qualitative agreement with the strength distribution derived from pp'. Nevertheless, nonnegligible discrepancies between the two spectra are noticeable. Contrary to the pp' experiment, the $\gamma\gamma'$ strength falls very rapidly to zero above 6 MeV. Moreover, the $\gamma\gamma'$ spectrum displays a nonnegligible strength, not seen in pp', in the 4–5 MeV region. It is reasonable to relate the above discrepancies to the different characteristics of the two experimental techniques. It might well be that the orbital amplitudes, not seen in pp', interfere destructively with the spin amplitudes, thereby generating the observed deep minimum. It is also reasonable to believe that the unexpected dipole strength at 4–5 MeV is a signal for the occurrence of either orbital $M1$ or $E1$ transitions. In order to shed some light on these puzzling problems, we performed an RPA calculation using a Hamiltonian of general separable form [24]. As shown in Fig. 1, the computed spectrum has two main peaks, in qualitative agreement with pp' experiments. A detailed analysis indicates that the high-lying peak is mainly due to neutron spin excitations, while most of the peaks at lower energy are to be ascribed to proton spin and orbital transitions. It is also true that the high-energy spin excitations are mainly of isovector nature, while the ones at lower energy are mostly isoscalar. In any case, the spectrum is quite sensitive to the shell structure. As shown in Fig. 1, the spectrum is basically due to spin excitations. Though generally small, the orbital amplitudes interfere with the spin ones over the full energy range, thereby affecting considerably the shape of the spectrum. The orbital $M1$ strength is actually dominant in the range 4–6, suggesting that the strength seen in this region in $\gamma\gamma'$ scattering is due to orbital (but not scissors-like) excitations. The deep minimum above 6 MeV, consistent with the new $\gamma\gamma'$ results [23], is also to be noticed.

On the grounds of these results, we would be tempted to conclude that the orbital motion may account for the discrepancies between pp' and $\gamma\gamma'$ experiments. On the other hand, strong and serious discrepancies exist between computed and experimental spectra. While its sum is of the same magnitude as the measured one, the RPA $M1$ strength is not as fragmented as required by the experiments. Conclusive statements about the nature of the spectrum may come only by calculations in an enlarged space which include four quasiparticle configurations or, in the QPNM scheme, two RPA phonons.

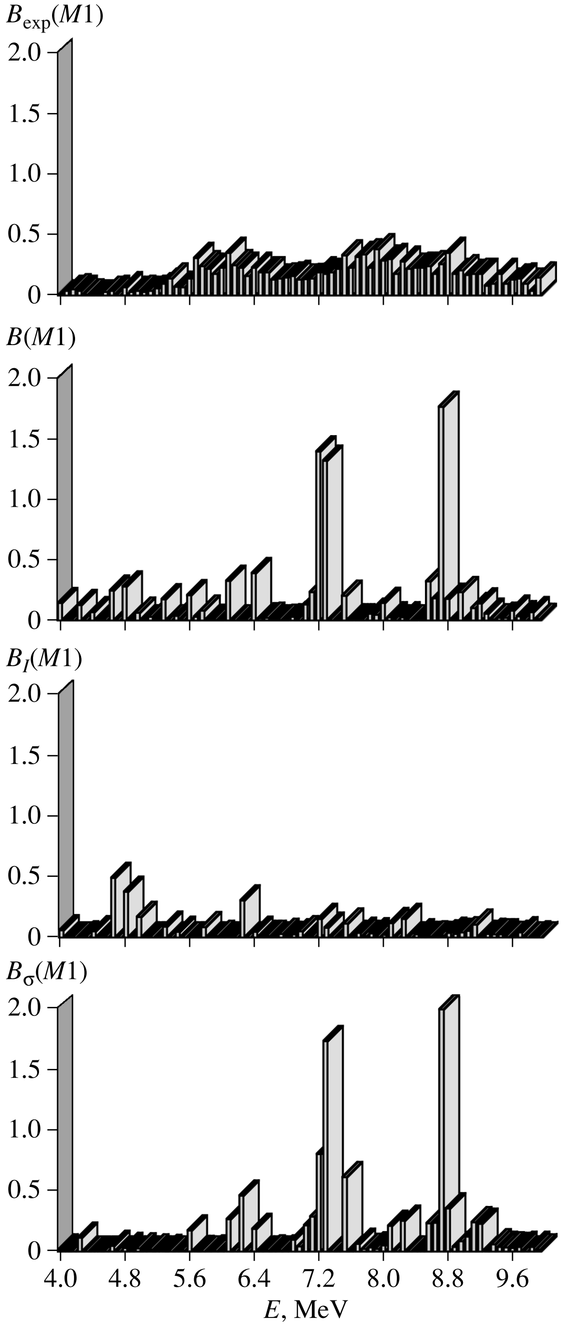

Fig. 1. Experimental versus computed total, orbital, and spin $M1$ spectra in ^{154}Sm. The $M1$ strength is summed in bins of 80 keV.

3. SCISSORS MODE IN SPHERICAL NUCLEI

In the language of the proton–neutron interacting boson model (IBM-2) [25], the scissors mode is known as a mixed-symmetry state with respect to proton–neutron boson exchange. For several years, the scissors was the only mixed-symmetry state detected experimentally out of the many predicted in IBM-2. New mixed-symmetry states have been identified in a recent experiment on ^{94}Mo [11, 12]. This experiment has not only identified several mixed-symmetry states, but has produced an almost exhaustive mass of information on low-lying levels and absolute transition strengths. All these new data have been analyzed using the IBM-2. More specifically, they have defined symmetric and mixed-symmetry states as

$$|\psi_{\rm sym}\rangle \propto (Q_s)^n|0\rangle = (Q_p + Q_n)^n|0\rangle, \qquad (4)$$
$$|\psi_{\rm ms}\rangle \propto Q_{\rm ms}(Q_s)^{n-1}|0\rangle = (Q_p - Q_n)(Q_s)^{n-1}|0\rangle.$$

Namely, the mixed symmetry state is obtained from a symmetric one by replacing one symmetric quadrupole operator $Q_s = Q_p + Q_n$ with the antisymmetric one $Q_{\rm ms} = Q_p - Q_n$. According to this scheme, one should get (i) strong $E2$ transitions between states of the same symmetry and (ii) strong $M1$ transitions between mixed-symmetry and symmetric partners. Such a simple picture describes quite accurately the experimental data.

In a recent paper [10], we have carried out a fully microscopic study of these new experimental data within the QPM [20] discussed in the previous section. We have found that the QPM states have a simple structure which leads to regularities in the systematic of the $E2$- and $M1$-transition strengths and enforces the consistency with experiments as well as with the IBM scheme. More specifically, we have got a set of F-spin symmetric states connected among themselves through strong $E2$ transitions and a set of mixed-symmetry and scissors-like states coupled to the symmetric ones through strong $M1$ transitions. All these predictions are supported by the experimental data.

We have, on the other hand, pointed out that there is not a clear cut distinction between mixed-symmetry and scissors states. Such a state can in fact be constructed by the following procedure:

$$\begin{aligned} |\psi_{\rm sc}\rangle &\propto S_\mu(Q_s)^{n-1}|0\rangle \qquad (5)\\ &= (J^p_\mu - J^n_\mu)(Q_s)^{n-1}|0\rangle \\ &\propto Q_{\rm ms}(Q_s)^{n-1}|0\rangle \propto |\psi_{\rm ms}\rangle. \end{aligned}$$

Namely, the scissors operator turns a symmetric into a mixed-symmetry state. There is no way of distinguishing the two kinds of states. Both kinds of states have the same signature, a strong $M1$ coupling with the symmetric states and strong $E2$ transitions among themselves. We have also shown that, acting on excited states of spin J, the scissors operator creates several states with spins $J, J-1, J+1$ generating three branches of the same scissors mode.

4. $M2$ ORBITAL AND SPIN EXCITATIONS

The knowledge about spin and orbital motion in nuclei can be further enriched by the study of magnetic quadrupole ($M2$) transitions. Indeed, the spin components of the $M2$ operator induce relative displacements between spin-up and spin-down nucleons giving rise to spin–dipole excitations. Its orbital part correlates the relative displacement of the protons with their magnetic orbits generating the so-called twist mode. Such a mode, predicted for spherical nuclei in a fluid-dynamics model [13], can be viewed as arising from a mutual rotation among different layers of the nuclear fluid around the z axis by an angle proportional to the z coordinate. Since no restoring force would be generated by such a rotation in an ideal fluid, the observation of such a mode would indicate that the nucleus behaves as an elastic medium rather than a perfect Fermi liquid.

Experimentally, electron scattering is specially suitable for a clean and complete study of $M2$ transitions. These experiments, however, do not distinguish between orbital and spin motion. One therefore has to rely also on theoretical analyses. A quite important and promising advance toward the understanding of the nature of the $M2$ transitions and the identification and characterization of the twist mode has been made recently by the Darmstadt group [14]. In a high-resolution electron-scattering experiment in ^{40}Ca and ^{90}Zr supported by a theoretical microscopic analysis, they found that the orbital contribution is appreciable and necessary for the reproduction of the experimental data. This would therefore be the first indirect evidence of the existence of the twist mode.

Since the possibility of detecting the twist mode relies on the separation of the orbital from the spin–dipole excitations, it is therefore of interest to check if deformation may favor the splitting by inducing a selective fragmentation of the orbital and the spin $M2$ strengths. There is another aspect which links $M2$ transitions to deformation. The $M2$ transitions are the magnetic counterpart of the electric dipole excitations. We might therefore hope to observe a K splitting of the $M2$ resonance similar to the $E1$ case.

We have carried out a study of the $M2$ transitions in proton–neutron quasiparticle RPA using a separable potential of general form which includes dipole and spin–dipole fields [26]. We have computed the strength distributions by means of a strength function technique developed for proton–neutron RPA in the signature formalism [27]. This technique avoids lengthy diagonalizations and therefore allows us to cover the full energy range of the $M2$ transitions. Due to the simple structure of the interaction, it was also possible to test the sensitivity of spin–dipole and orbital $M2$ spectra to the strength of the interaction. This latter issue is quite relevant to the possible identification of the twist mode, which relies on the separation between the two different excitation modes. We did not include explicitly the $2p$–$2h$ configurations. We accounted for the spreading of the strength only effectively through the width used in the calculation of the strength function.

We explored the sensitivity of the $M2$ spectrum to the spin–dipole interaction by computing the strength function for ^{154}Sm using different values of the spin–dipole coupling constant. We found that the unperturbed strength function exhibits a single peak which results from the constructive interference between the orbital and the spin–dipole amplitudes. The corresponding strengths are almost equally fragmented and spread over the same energy range around a common centroid. As we turn on the interaction, the orbital strength is practically unaffected. The spin–dipole strength, instead, gets more fragmented and is shifted at higher energy. For the current values of the coupling constant, the $M2$ strength function splits into two separate peaks, one at low energy around 7 MeV and another at high energy around 16 MeV (Fig. 2). The first is almost entirely of orbital nature; the second, much broader, is entirely due to spin–dipole excitations. The complete overlap between orbital and spin–dipole strength in the unperturbed case proves that the splitting has little to do with deformation. Indeed we get a similar result also for ^{144}Sm (Fig. 2, upper panel). Deformation has the only effect of inducing more fragmentation. In fact, the peaks are broader in the deformed ^{154}Sm. The results obtained are compatible with the available experimental data. We best reproduce the electron scattering data in ^{90}Zr [14] for a value of the strength constant which generates two distinct bumps, one mainly of orbital and the other of spin–dipole nature. This differs from the results of the theoretical analysis carried out in [14], where orbital and spin–dipole strengths overlap.

The effects of deformation become manifest if we carry out a fine-tuned analysis of the $M2$ spectrum in ^{154}Sm. The low-lying, mainly orbital, bump can be unfolded into three peaks generated, respectively, by $K^\pi = 0^-$ (low-lying peak), $K^\pi = 1^-$ (middle peak), and $K^\pi = 2^-$ (upper peak) transitions (Fig. 3). This fine-tuned splitting of the $M2$ resonance reflects the close correspondence between electric dipole and magnetic quadrupole transitions. Indeed, the $K^\pi = 0^-$ and $K^\pi = 2^-$ magnetic quadrupole excitations are the counterpart of the $K^\pi = 0^-$ and $K^\pi = 1^-$ electric modes, while the $K^\pi = 1^-$ magnetic excitations involving dipole oscillations perpendicular to the direction of the angular momentum along the symmetry axis as well as in the equatorial plane are an intruder which falls in between the other two cases and fill partially the gap between the $K^\pi = 0^-$ and $K^\pi = 2^-$ peaks. Because of the $K^\pi = 1^-$ intruders, the splitting of the low-lying, mainly orbital, $M2$ resonance is not too pronounced and may be observed only in a high-resolution experiment. No K splitting is observed in the region of the spin excitations. This might be due to shell effects, like the coexistence of spin-flip–dipole with spin–dipole excitations in the same energy domain.

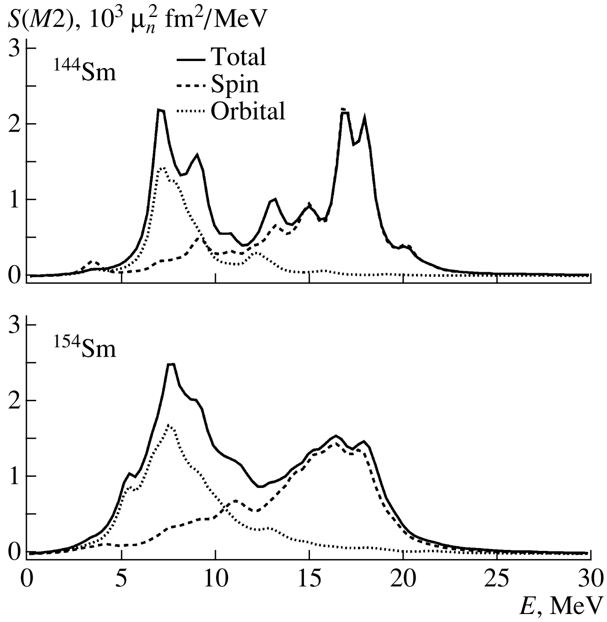

Fig. 2. The orbital, spin, and total RPA $M2$ strength functions in ^{154}Sm and ^{144}Sm.

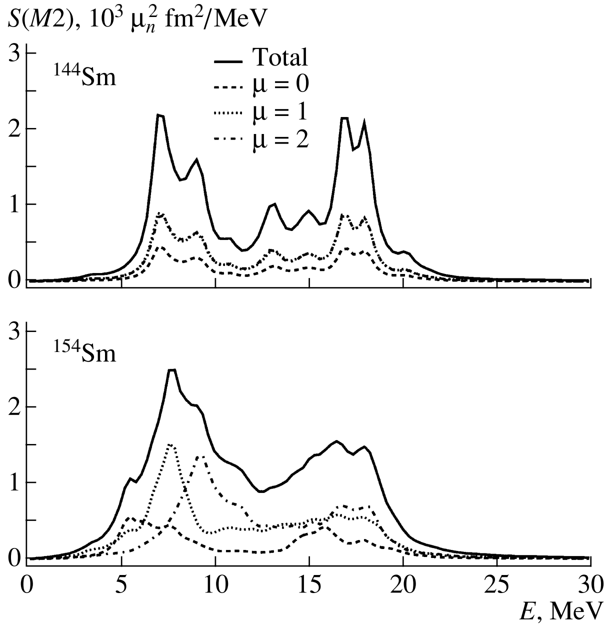

Fig. 3. The unfolding of the RPA $M2$ strength function in ^{154}Sm into its K^π components.

5. CONCLUSION

The survey has shown that the collective features of the low-lying $M1$ excitations, chiefly the quadratic deformation law, are described fairly well in phenomenological as well as schematic models. In particular, formulas extrapolated from schematic RPA give a satisfactory systematic not only of the $M1$ strength but also of the energy centroids.

A fairly good description of the fragmentation of the mode is given within the QPNM which includes anharmonicities by coupling one and two RPA phonon configurations. The same scheme has been shown to be necessary for explaining the fragmentation of the $M1$-spin strength. We have also shown that the destructive interference between orbital and spin motion plays an important role in shaping these spectra.

We have shown how scissors states can be built on excited states in spherical nuclei. These are nothing but the mixed-symmetry states observed in a recent experiment. A QPM calculation, crucial for the description of these excitations, has predicted an energy and transition scheme fully consistent with IBM-2 and experiments.

In all these excitations, the subtle interference between orbital and spin transition amplitudes plays a crucial role. Indeed, the identification of the scissors mode has relied on its separation from the spin excitations. We have discussed the mechanism which achieves such a splitting.

The interplay between orbital and spin motion is even more crucial in the case of $M2$ transitions. We may in fact hope to observe the twist mode only if the spin–dipole strength is pushed up in energy. We have shown when this is the case. Also interesting is the role of deformation which may be responsible for a possible K splitting of the $M2$ resonance similar to the $E1$ case.

Finally, it might be worth mentioning that an $M1$ mode, which is the analog of the nuclear scissors mode, was predicted in a schematic model [28] and supported recently by more realistic microscopic calculations [29]. Unlike the other excitations, such a mode has the virtue of falling at much lower energy than the overwhelming plasmon resonance. It might therefore have some chances of being detected.

REFERENCES

1. A. Richter, Prog. Part. Nucl. Phys. **34**, 261 (1995).
2. N. Lo Iudice and F. Palumbo, Phys. Rev. Lett. **41**, 1532 (1978).
3. D. Bohle *et al.,* Phys. Lett. B **137**, 27 (1984).
4. W. Ziegler *et al.,* Phys. Rev. Lett. **65**, 2515 (1990).
5. C. Rangacharyulu *et al.,* Phys. Rev. C **43**, R949 (1991).
6. J. Margraf *et al.,* Phys. Rev. C **47**, 1474 (1993).
7. N. Pietralla *et al.,* Phys. Rev. C **52**, R2317 (1995).
8. D. Frekers *et al.,* Phys. Lett. B **244**, 178 (1990).
9. A. Richter, Nucl. Phys. A **553**, 417c (1993).
10. N. Lo Iudice and Ch. Stoyanov, Phys. Rev. C **62**, 047302 (2000).
11. N. Pietralla *et al.,* Phys. Rev. Lett. **83**, 1303 (1999).
12. N. Pietralla *et al.,* Phys. Rev. Lett. **84**, 3775 (2000).
13. G. Holzwarth and G. Eckart, Z. Phys. A **283**, 219 (1977).
14. P. von Neumann-Cosel *et al.,* Phys. Rev. Lett. **82**, 1105 (2000).
15. N. Lo Iudice and A. Richter, Phys. Lett. B **304**, 193 (1993).
16. L. Zamick and D. C. Zheng, Phys. Rev. C **46**, 2106 (1992).
17. N. Lo Iudice, Phys. Rev. C **58**, 1246 (1998).
18. N. Pietralla *et al.,* Phys. Rev. C **58**, 184 (1998).
19. V. G. Soloviev *et al.*, Nucl. Phys. A **600**, 155 (1996).
20. V. G. Soloviev, *Theory of Atomic Nuclei: Quasiparticles and Phonons* (Institute of Physics, Bristol, 1992).
21. C. De Coster and K. Heyde, Phys. Rev. Lett. **66**, 2456 (1991).
22. D. Zawischa, M. Macfarlane, and J. Speth, Phys. Rev. C **42**, 1461 (1990).
23. P. von Neumann-Cosel, Prog. Part. Nucl. Phys. **38**, 213 (1997).
24. V. G. Soloviev *et al.*, J. Phys. G **25**, 1023 (1999).
25. A. E. L. Dieperink, Prog. Part. Nucl. Phys. **9**, 121 (1983).
26. J. Kvasil *et al.,* submitted for publication.
27. J. Kvasil *et al.,* Phys. Rev. C **58**, 209 (1998).
28. E. Lipparini and S. Stringari, Phys. Rev. Lett. **63**, 570 (1989).
29. V. O. Nesterenko *et al.,* Phys. Rev. Lett. **83**, 57 (1999).

Physics of Atomic Nuclei, Vol. 64, No. 6, 2001, pp. 1039–1043. From Yadernaya Fizika, Vol. 64, No. 6, 2001, pp. 1114–1118.

Gamma Decay of the Giant Dipole Resonance and Feeding of Superdeformed States in ^{143}Eu*

F. Camera**

Dipartimento di Fisica and INFN, Università degli Studi, Milano, Italy

Received September 11, 2000

Abstract—The γ decay of the giant dipole resonance (GDR) built on excited nuclear states has been measured in coincidence with the low-energy γ discrete transitions for the nucleus ^{143}Eu. The reaction used was ^{110}Pd(^{37}Cl, $4n$)^{143}Eu at a beam energy of 165 MeV. The EUROBALL spectrometer (for the measurement of discrete γ transitions) coupled with the HECTOR array (for high-energy γ-ray detection) has been used. The high-energy γ-ray spectrum in coincidence with superdeformed (SD) discrete transitions of ^{143}Eu shows an "excess" between 9–12 MeV if compared with the one associated to cascades which do not pass through the SD configurations. Such an "excess" is in the energy region where one expects the low-energy component of the GDR strength function built on a SD state. The measured intensity can be reproduced by the statistical model assuming that the superdeformation survives only few MeV above the yrast line. A similar and consistent scenario has also been obtained by comparing the high-energy γ-ray spectra of ^{143}Eu in coincidence with its spherical (which is fed by the SD configuration) and its triaxial configuration (which is bypassed by the decay of the SD states). © *2001 MAIK "Nauka/Interperiodica"*.

1. INTRODUCTION

The γ decay of the giant dipole resonance (GDR) built on excited nuclei has been extensively used to probe the properties of hot and rotating nuclei. In fact, the sensitivity of the GDR strength function to nuclear deformation allows one to study the nuclear shape and its temperature/spin induced dependence by the measurement of the dipole response.

In recent years, with the availability of powerful detector arrays, it has been possible to perform exclusive measurements where the GDR properties have been measured, for example, as a function of excitation energy [1], angular momentum [2], or by choosing specific evaporation residues [3].

An interesting and still open question concerns the population and decay of superdeformed (SD) structures in cold rotating nuclei, and, in particular, the $E1$ cooling, which is expected to play an important role in the feeding mechanism of SD configurations [4, 5].

The feeding of SD structures has been a long standing problem since the time of the discovery of the first SD band [6, 7]. In fact, it was experimentally observed that SD bands are populated with an intensity which is approximately one order of magnitude larger than that of normally deformed (ND) configurations at high spins (Fig. 1). A possible explanation relies on the $E1$ statistical cooling [4, 5]. Namely, the $E1$ transition probability at $E_\gamma \approx 9$–11 MeV for the GDR decay built on SD configurations is expected to be several times larger than that of ND states due to both the shape of the GDR strength function and the level density of SD states. In particular, for the GDR in a SD nucleus, one-third of the total energy-weighted sum rule (EWSR) strength (corresponding to the dipole oscillation along the nuclear symmetry axis of a collective SD prolate nucleus) is shifted from ≈15 to ≈10 MeV, an energy close to the neutron binding energy favoring, consequently, the γ decay of the GDR into a SD state.

A good candidate for such kind of study is the nucleus ^{143}Eu. In fact, at high spin, it presents both a strong discrete SD band (1% of the total) and an intense $E2$ quasicontinuum of excited SD bands [8]. At low spin, instead, a quasispherical (ND) and triaxially deformed (TD) shapes [9–12] coexist. Both the SD yrast band and the SD quasicontinuum follow decay routes that end up only in spherical low-spin states (ND). Therefore, one should see the γ decay of the GDR built on SD states by comparing the high-energy γ-ray spectra gated by either discrete SD transitions (if possible), or low-spin ND transitions, or by low-spin TD transitions.

In an experiment [13] previously performed by coupling the NORDBALL (which consisted of 17 HpGe detectors and a multiplicity filter) with the HECTOR arrays (for the detection of high energy

---

*This article was submitted by the author in English.

**e-mail: `camera@mi.infn.it`

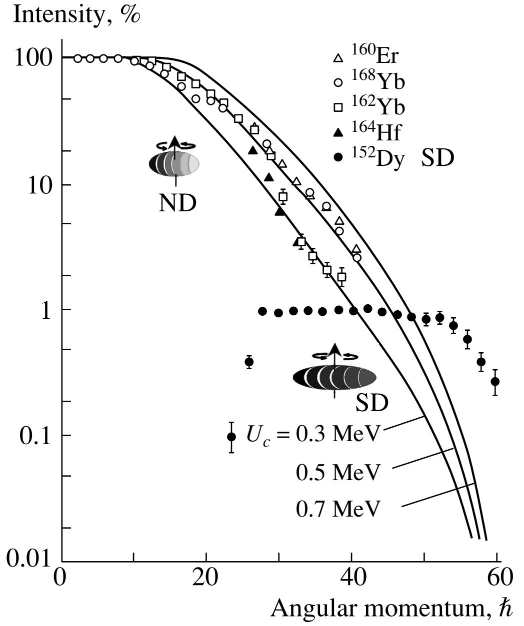

Fig. 1. Discrete line intensities normalized to the intensity of the $2^+ \rightarrow 0^+$ ground-state transitions versus spin for some well-deformed nuclei and for a SD band (from [4]).

γ rays), indirect evidence of the GDR built on SD states in ^{143}Eu has been obtained by comparing the high-energy spectrum in coincidence with ND discrete transitions with the one in coincidence with TD transitions. In that experiment, an excess of γ rays centered around 10 MeV was observed and interpreted as the low-energy component of the SD GDR. However, the statistics were rather poor, pointing to the necessity for a new and better experiment.

In this paper, we discuss the results of a new experiment on ^{143}Eu searching for evidence of a GDR built on SD states. The measurement has been made using the EUROBALL spectrometer coupled with the HECTOR array. The experimental apparatus is several times more powerful than that used in [13], so that it has been possible to gate directly on discrete SD transitions.

2. THE EXPERIMENT

The experiment was performed at the Legnaro National INFN laboratories in Italy using EUROBALL (which consists of 15 Cluster and 26 Clover HpGe detectors) coupled with 8 Large BaF$_2$ crystals from the HECTOR array. High-energy γ rays (5–30 MeV) detected in the BaF$_2$ crystals have been measured in coincidence with low-energy discrete transitions detected in Cluster and Clover Germanium detectors. Four small BaF$_2$ crystals placed at 5 cm from the target provided the time reference for time-of-flight measurements used to discriminate neutrons. The FERA based electronics of the BaF$_2$ was coupled with EUROBALL VXI electronics.

The reaction used was ^{110}Pd(^{37}Cl, $4n$)^{143}Eu at a beam energy of 165 MeV. The ^{110}Pd target was 97.3% pure and 950 μg/cm^2 thick with an Au backing of 15 mg/cm^2. The chosen bombarding energy represents a good compromise for the good population of the SD band and for $E1$ emission of the final residual nucleus around the yrast line. The compound nucleus ^{147}Eu was formed at an excitation energy of 79 MeV. The maximum angular momentum is predicted to be $62\hbar$ by the Swiatecki model [14] and $68\hbar$ by the model of Winther [15].

The absolute experimental full-energy peak efficiency for high-energy γ rays in the BaF$_2$ detectors was approximately 1%, while, for low-energy transitions in EUROBALL, it was approximately 8%. The gain of each BaF$_2$ detector was monitored continuously by a LED source, and small shifts have been corrected by an off-line analysis. The calibration of HpGe detectors has been performed using ^{60}Co and ^{152}Eu sources, while the BaF$_2$ detectors have been calibrated by using the 15.1-MeV γ rays produced in the reaction $^{11}\mathrm{B} + \mathrm{D} = {}^{12}\mathrm{C}^* + n$.

3. RESULTS

As described in [13], the idea followed in the past to seek a GDR built on SD states is based on the comparison of the high-energy spectrum gated by ND low-spin transitions (known to be populated by the SD configurations) with that gated by TD low-spin transitions (known not to be populated by SD transitions). In this case, as we did not have a multiplicity filter, we have made an additional gate on the first excited states of ^{143}Eu to isolate the $4n$-decay channel.

The comparison of the measured ND-gated and TD-gated high-energy spectra is shown in the left panel of Fig. 2. In the right panel, the ratio of the two spectra is shown. As was measured in [13], an excess of yield centered around 10–11 MeV is also clearly evident here. The intensity of the excess is comparable with that previously measured, confirming that superdeformation survives only few MeV above the yrast line, as the statistical model calculations of Fig. 2 show.

In the calculations, we denote with $Y_{\mathrm{ND}}(E_\gamma)$ the γ yield corresponding to the ND nucleus and with $Y_{\mathrm{SD}}(E_\gamma)$ that corresponding to the SD nucleus case. The $Y_{\mathrm{ND}}(E_\gamma)$ yield was obtained under the assumption that the GDR strength function has the shape of a single Lorentzian centered at 15 MeV and with

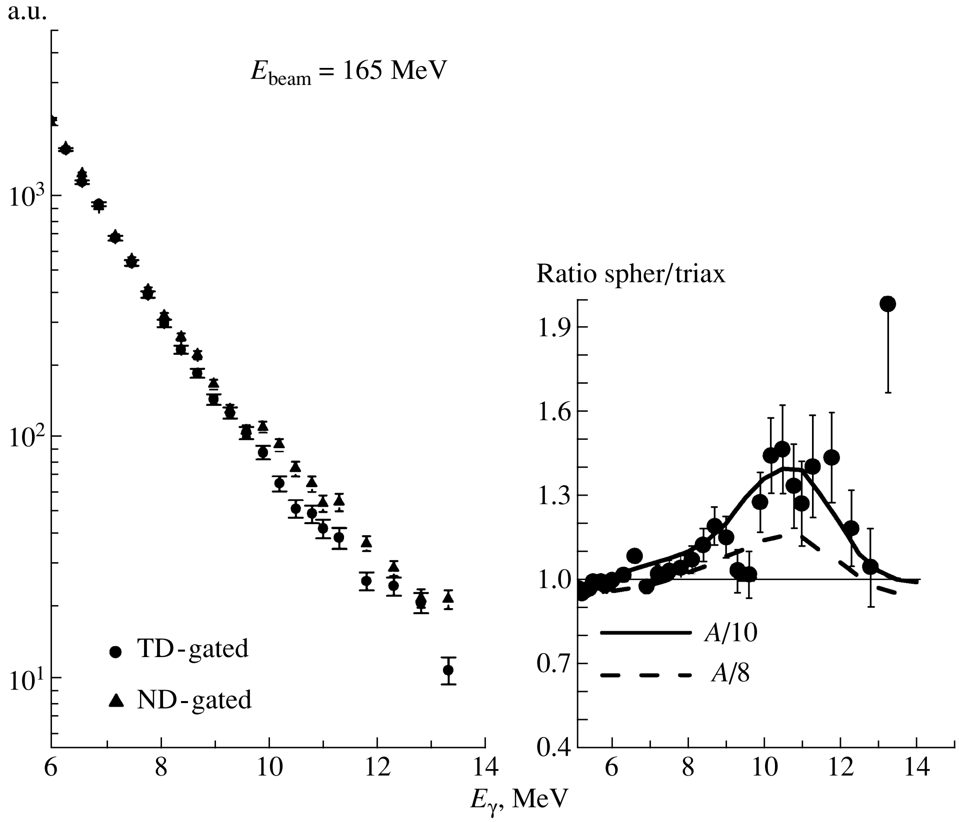

Fig. 2. Left panel: The spectrum shown with closed triangles is double-gated by spherical transitions (populated by the SD decay); the other (closed circles) is double-gated by the low-energy transitions of the triaxial configuration. Right panel: The points show the ratio spectrum obtained by dividing the two spectra shown in the left panel. The corresponding calculated values using the statistical model (as described in the text) are shown with the curves: the dashed curve was calculated using $a = A/8$ MeV^{-1} for the level density parameter of all states, while the solid curve was obtained using the value $a = A/10$ MeV^{-1} for the SD states and $a = A/8$ MeV^{-1} for the ND states.

a width varying, with increasing excitation energy, from 5 to 8 MeV. Instead, the $Y_{\text{SD}}(E_\gamma)$ yield was obtained by means of a procedure similar to that adopted for the $Y_{\text{ND}}(E_\gamma)$ yield but by using a two-Lorentzian GDR strength function of SD type and a different value of the level density in the region with angular momentum $40\hbar < I < 55\hbar$ and energy U above the yrast in the interval $0 < U < 15$ MeV. The GDR strength function that was used for this region of the phase space has $E_{1\text{GDR}} = 10.5$ MeV, $\Gamma_{1\text{GDR}} = 3$ MeV with 33% of EWSR strength and $E_{2\text{GDR}} = 17$ MeV, $\Gamma_{2\text{GDR}} = 6.5$ MeV, with 66% of EWSR strength. For the density of SD states, we have assumed two different values: $a = A/8$ MeV^{-1} and $a = A/10$ MeV^{-1}.

The experimental ratio in the left part of Fig. 2 can be reproduced assuming that for 40–55$\hbar$ and up to 15 MeV above the yrast 40% of the cascades which end in the ND part pass through a SD configuration [8]. In particular, the expression

$$Y_{\text{ratio}}(E_\gamma) = \frac{0.4Y_{\text{SD}}(E_\gamma) + 0.6Y_{\text{ND}}(E_\gamma)}{Y_{\text{ND}}(E_\gamma)} \qquad (1)$$

was used. The dashed curve in Fig. 2 corresponds to the $Y_{\text{ratio}}(E_\gamma)$ obtained using a level density coefficient $a = A/8$ MeV^{-1} in the SD region, while the solid curve corresponds to $a = A/10$ MeV^{-1}. The results agree with the data of [13].

The high statistics and the good quality of the data have allowed us to extract the high-energy γ-ray spectrum in coincidence with the discrete SD transitions. This spectrum is shown in the left panel of Fig. 3, compared with the high-energy spectrum (solid line) gated by TD transitions. Again, an excess of γ rays at 10–11 MeV is clearly visible.

In the right panel of Fig. 3, the intensity population of the discrete SD band (closed squares) has been plotted relative to the energy of the coincident high-energy γ rays. The 917-keV transition from the first excited state over the $11/2^-$ isomeric state of ^{143}Eu

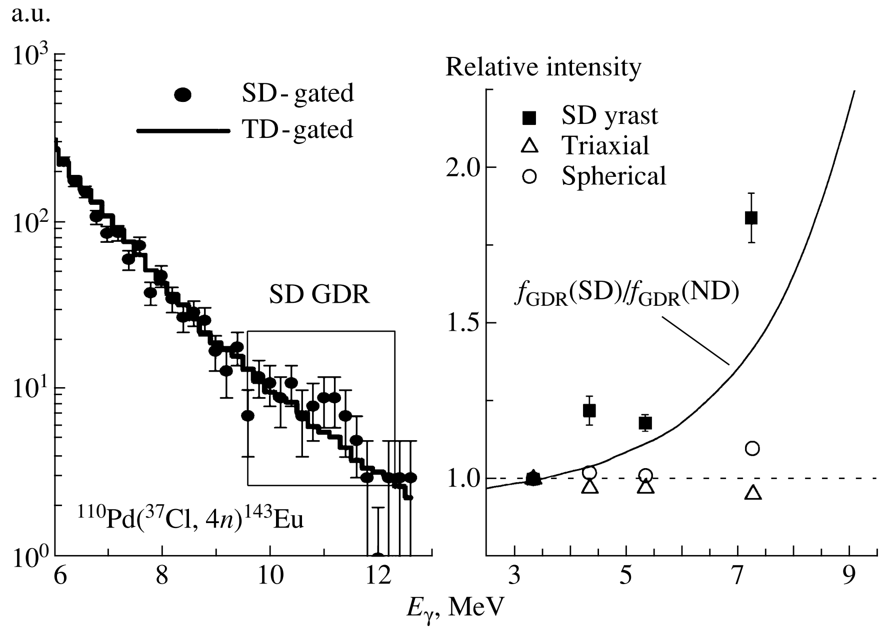

Fig. 3. Left panel: Comparison of high-energy γ-ray spectrum double-gated by the lines of the SD yrast band (closed circles) with the spectrum gated by lines of the triaxial configuration. Right panel: Intensity of the SD yrast band (squares) and of TD and low-lying ND transitions as a function of the energy of the gating transition relative to the value measured at $E_\gamma = 3$ MeV. The solid curve, which represents a lower limit for feeding by γ decay from the GDR built of a SD nucleus, was obtained as a ratio of the SD and ND GDR strength functions.

has been used as a reference. Other experimental points corresponding to transitions of the spherical shape and of the triaxial shape obtained with the same procedure used for the SD yrast lines are shown in the same figure for comparison.

While in the case of transitions of the ND and TD configurations a constant behavior is found, with a value of ≈ 1, a rather pronounced increase with γ-ray energy is instead measured in the case of the transitions of the SD yrast band. If this increase is due to the fact that the $E1$ feeding of the SD band originates from a residual nucleus in an excited state consisting of a dipole vibration on the SD structure, this should follow the low-energy tail of the GDR strength function. This simple estimate, shown with the solid curve, represents the lowest limit expected for the situation in which the gating high-energy transition has a SD nature and is feeding directly the SD band. The larger measured values could reflect both level density effects as well as the fact that the high-energy gating transitions do not all end necessarily on the SD yrast states.

4. CONCLUSIONS

The recent experimental data discussed here show evidence of a GDR built on SD states and that superdeformation exists only few MeV over the yrast line in the high-spin region. Such results confirm the indications of [13].

The experimental fact that the intensity of the discrete SD band increases by a factor of ≈ 2 when one gates with high-energy γ rays clearly shows that SD configurations are preferably populated by $E1$ cooling, namely, by the decay of the SD GDR.

ACKNOWLEDGMENTS

This work is based on an experiment performed by a large collaboration with the EUROBALL array. In particular, I thank the participation of A. Bracco, S. Leoni, G. Benzoni, S. Frattini, B. Million, and N. Blasi from University of Milano and INFN sez. of Milano; M. Kmiecik, A. Maj, J. Styczen, and M. Zieblinski from the Niewodnizanski Institute of Nuclear Physics—Krakow; M. Bergstrom and B. Herskind from the Niels Bohr Institute; A. Algora, A. Gadea, and R. Isocrate from Laboratori Nazionali di Legnaro; J. Nyberg and A. Axelsson from the Department of Radiation Sciences, Uppsala University; G. Lo Bianco from the University of Camerino; and M. Castoldi and A. Zucchiatti from INFN sez. of Genova.

REFERENCES

1. E. Ramakrishnan *et al.,* Phys. Rev. Lett. **76**, 2025 (1996).

2. M. Mattiuzzi *et al.,* Nucl. Phys. A **612**, 262 (1997).
3. F. Camera *et al.,* Phys. Rev. C **60**, 014306 (1999).
4. K. Shiffer *et al.,* Z. Phys. A **332**, 17 (1989).
5. B. Herskind *et al.,* Phys. Rev. Lett. **59**, 2416 (1987).
6. P. J. Twin *et al.,* Phys. Rev. Lett. **57**, 811 (1986); M. A. Bentley *et al.,* Phys. Rev. Lett. **59**, 2141 (1987).
7. B. Haas *et al.,* Phys. Rev. Lett. **60**, 503 (1988).
8. S. Leoni *et al.,* Phys. Rev. Lett. **76**, 3281 (1996).
9. M. Piiparinen *et al.,* Phys. Rev. C **52**, R1 (1995).
10. M. Piiparinen *et al.,* Nucl. Phys. A **605**, 191 (1996).
11. A. Atac *et al.,* Phys. Rev. Lett. **70**, 1069 (1993).
12. A. Atac *et al.,* Z. Phys. A **355**, 343 (1996).
13. F. Camera *et al.,* Eur. Phys. J. A **2**, 1 (1998).
14. W. J. Swiatecki, Phys. Scr. **24**, 113 (1981).
15. A. Winther, Nucl. Phys. A **594**, 203 (1995).

Physics of Atomic Nuclei, Vol. 64, No. 6, 2001, pp. 1044–1047. From Yadernaya Fizika, Vol. 64, No. 6, 2001, pp. 1119–1122.

Compression Modes in Nuclei: RPA and QRPA Predictions with Skyrme Interactions*

G. Colò, **N. Van Giai**[1)], **P. F. Bortignon**, and **M. R. Quaglia**[2)]

Dipartimento di Fisica, Università degli Studi, and INFN, Milano, Italy

Received September 11, 2000

Abstract—Isoscalar monopole and dipole resonances in ^{90}Zr, ^{116}Sn, ^{144}Sm, and ^{208}Pb are studied within the framework of self-consistent HF–RPA or HF–BCS plus quasiparticle RPA. A comparison with recent experimental data obtained at Texas A&M University, as well as the problems related to the determination of the nuclear incompressibility K_∞, is discussed. © *2001 MAIK "Nauka/Interperiodica".*

The isoscalar giant monopole resonance (ISGMR), the so-called "breathing mode" of the nucleus associated with the operator

$$\hat{M} = \sum_{i=1}^{A} r_i^2, \qquad (1)$$

has been intensively studied for more than two decades, especially with the aim to extract from it information on the nuclear matter incompressibility K_∞. Recently, new experimental measurements performed at the Texas A&M University cyclotron are claimed to provide a better determination of the ISGMR properties than ever obtained before for ^{90}Zr, ^{116}Sn, ^{144}Sm, and ^{208}Pb [1]. The uncertainty on the mean energy of the ISGMR (defined as $E_0 \equiv m_1/m_0$, where the moments m_k of the strength distribution are $m_k = \sum_n |\langle n|\hat{M}|0\rangle|^2 (E_n - E_{\rm g.s})^k$) is now believed to be of the order of 100–300 keV. We will discuss in the first part of this contribution the problems which persist, despite this remarkable experimental achievement, in the determination of K_∞. The second part will be devoted to another, more elusive, compressional mode of the nucleus, namely, the isoscalar giant dipole resonance (ISGDR).

It has been discussed by a number of authors [2] that the extraction of K_∞ done by means of the definition of a finite nucleus incompressibility (through the equation $E_0(\mathrm{ISGMR}) = \sqrt{\hbar^2 A K_A / m \langle r^2 \rangle}$) and of its extrapolation for $A \to \infty$ through a liquid drop-type formula is unreliable because of the many assumptions one has to use in this procedure. A more transparent way of determining K_∞ consists in performing self-consistent calculations of the ISGMR which are based on different parametrizations of the effective nucleon–nucleon interaction. The value of K_∞ associated with the effective force which reproduces the experimental values of the mean energy of the ISGMR should be chosen as the correct value. The obvious difficulty arises that, since mean energies obtained from calculations normally do not match exactly the experimental finding, the value of K_∞ should be determined by interpolation.

We report calculations of the ISGMR done using effective Skyrme interactions, within self-consistent Hartree–Fock (HF) plus random-phase approximation (RPA) in the case of ^{208}Pb, and Hartree–Fock–BCS (HF–BCS) plus quasiparticle RPA (QRPA) for the other, non-double-magic, nuclei. The parametrizations used are SkP [3], SGII [4], SKM* [5], SLy4 [6], and SkI2 [7] (they span a range of values of K_∞ from 200 to 250 MeV). The HF mean field is first calculated in coordinate space, and then the single-particle spectrum of occupied and unoccupied states is built by diagonalizing the mean field on a harmonic oscillator basis. Details of RPA calculations can be found in [8]. The dimension of the 1-particle–1-hole ($1p$–$1h$) space is fixed by requiring the exhaustion of the RPA m_1 sum rule. In the HF–BCS calculations, constant pairing gaps Δ are introduced according to the usual 12 MeV/$\sqrt{A}$ parametrization. The QRPA matrix equations are solved with a procedure which parallels what has been said for RPA, with the two quasiparticle configurations replacing the $1p$–$1h$ ones. The method is the same as that of [9].

---

[*] This article was submitted by the authors in English.

[1)] Groupe de Physique Theorique, Institut de Physique Nucléaire, Orsay, France.

[2)] Dipartimento di Fisica Teorica, Università degli Studi, and INFN, Torino, Italy.

[**] e-mail: `gianluca.colo@mi.infn.it`

The results, expressed in terms of E_0(ISGMR) vs. K_∞, are shown in Fig. 1. The symbols correspond to the RPA mean energies associated with the different Skyrme force sets, whereas the continuous lines are drawn to guide the eyes. For each nucleus, it is possible to draw a horizontal line at the experimental mean energy, and this line intersects the line shown in the figure for a value of $K_\infty^{(\mathrm{exp})}$ which should be rather constant for the four nuclei. Using as experimental mean energies the values 17.9, 15.3, and 14.2 MeV for ^{90}Zr, ^{144}Sm, and ^{208}Pb, values of K_∞ between 205 and 212 MeV are obtained. This is not shown on the figure for the sake of clarity. Using the experimental energy for ^{116}Sn (16 MeV) would give a value of K_∞ slightly outside the mentioned range.

A quite similar procedure has been applied in [1], by using the results of RPA calculations based on the finite-range Gogny interaction [10]. The result for the nuclear incompressibility is in this case 231 MeV. Apparently, therefore, different nonrelativistic models predict different values of K_∞. However, in our calculation, the treatment of some components of the particle—hole residual interaction is not fully consistent. Indeed, we neglect the two-body spin—orbit and Coulomb matrix elements. Work along this line is in progress. We conclude by mentioning that self-consistent calculations based on relativistic mean field theory [11] provide values for K_∞ which range between 250 and 270 MeV.

Equally related to the nuclear incompressibility is the ISGDR. This resonance is in fact associated with the operator

$$\hat{D} = \sum_{i=1}^{A} r_i^3 Y_{1\mu}(\hat{r}_i) \tag{2}$$

and corresponds to a nonisotropic compression of the system. Although some first indications about the energy location of this mode date back to the beginning of the eighties, as reviewed in [12], only very recently convincing evidence about its properties has come from 0° angle measurements of 240-MeV inelastically scattered α particles at Texas A&M University. The ISGDR strength has been extracted using a multipole decomposition technique. The values of the centroid energy E_0 (defined as in the case of the ISGDR) are 26.3(4), 24.3(3), 23.0(3), and 20.3(2) MeV, respectively, in ^{90}Zr, ^{116}Sn, ^{144}Sm, and ^{208}Pb.

We have done a systematic study of the ISGDR theoretical strength distributions [13], whose results are summarized in the following. The method of calculation is the same as outlined above for the ISGMR. We just recall here that in the ISGDR case one has to face the problem of the spurious state associated with the center-of-mass motion which carries the same quantum numbers $J^\pi = 1^-$. In our case, the spurious strength is subtracted from the results using a projection technique described in detail in [13].

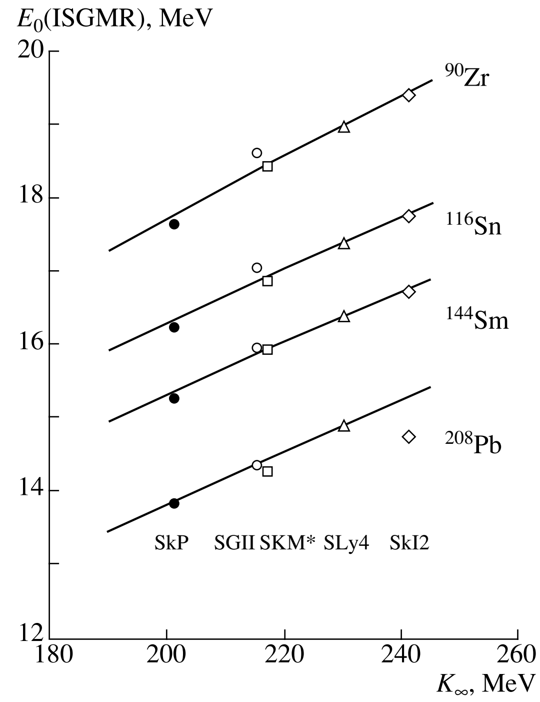

Fig. 1. ISGMR mean energies E_0 as a function of K_∞. The lines are a guide to the eye. See the text for a discussion.

The difference between the strength distributions before and after the projection of the spurious strength is shown in the top-left corner of Fig. 2 for the typical case of ^{208}Pb with the force SGII. The strengths are essentially the same in the energy range which will be denoted "giant resonance (GR) region." At lower energies, omitting the projection procedure can lead to a serious overestimation of the ISGDR strength. It is clear nevertheless from Fig. 2 that a nonnegligible amount of nonspurious strength is present in the energy range which will be called "low-energy region." This low-lying strength is due to 1-$\hbar\omega$ excitations, which of course can contain strength associated with the $\hat{D}$ operator.

In Fig. 2, we also show center-of-mass corrected strength distributions for the other nuclei calculated with a typical interaction, namely SGII. The general features are (i) a large fraction of the strength lies in the GR region and (ii) a nonnegligible amount of strength is in the low-energy region. The latter region contains about 20% of the ISGDR energy-weighted sum rule. These features are common to the results obtained with the other interactions. A more

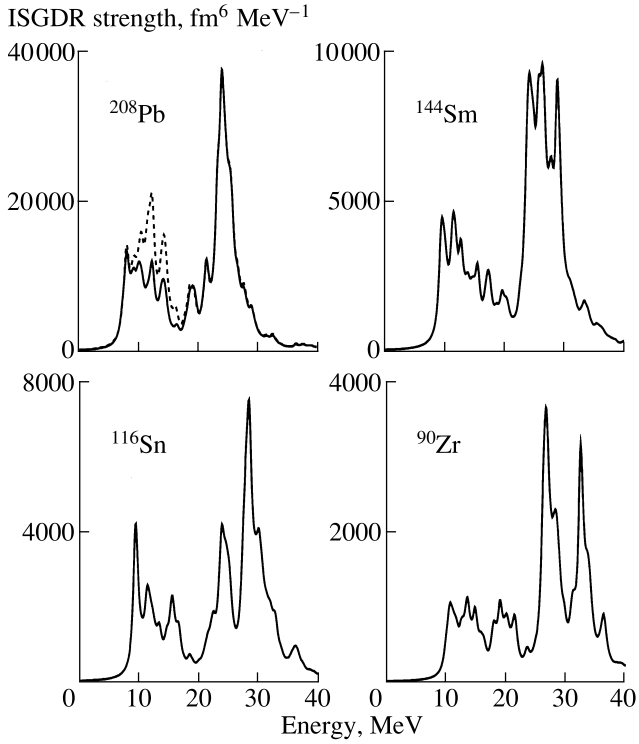

Fig. 2. ISGDR strength distributions calculated with the interaction SGII and corrected for center-of-mass effects. In the case of ^{208}Pb the dashed curve corresponds to a calculation without proper subtraction of the spurious center-of-mass state (see text).

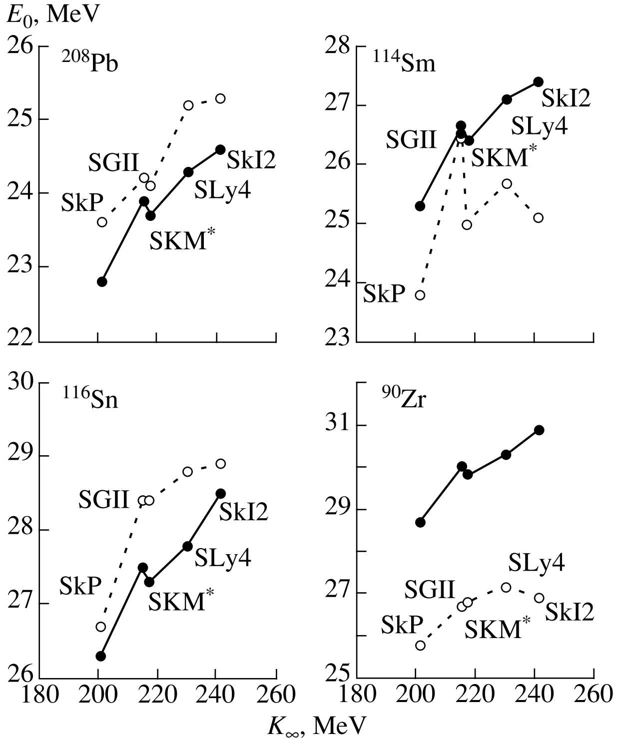

Fig. 3. Centroid energies E_0 (closed circles) and peak energies (open circles) of the GR region in the isoscalar dipole case, determined by using different Skyrme interactions and plotted as a function of K_∞. The solid and dashed lines are drawn as a guide to the eye.

detailed analysis in terms of the moments m_0 and m_1 is reported in [13].

In comparison with the existing data, there is a main issue to be faced, namely, the large discrepancy between predicted and measured GR energies, much larger than in all other GR cases. The calculations predict a sizeable amount of strength at low energy, and this seems now to be experimentally confirmed [14]. This strength does not seem to have a genuine compressional nature because its energy position does not depend on K_∞ (see also [15]).

In Fig. 3, we show the predicted peak and centroid energies of the GR region for various nuclei as a function of K_∞. The experimental values of E_0 for the GR region quoted above would be outside the figure, except for ^{90}Zr. The discrepancy appears very severe in Pb and Sn. In what follows, we concentrate on Pb because it is the nucleus where the HF + RPA model should work better.

Earlier RPA calculations [16] performed with the finite range Gogny interaction already found that the ISGDR energy was in the range of 26 MeV, in qualitative agreement with the present results. One might expect that effects beyond RPA, like the coupling to $2p$–$2h$ excitations, would somewhat lower the centroid energy. However, the calculations of [17] find a downward shift of less than 1 MeV. The ISGDR has also been calculated in the relativistic RPA approach [11] in ^{208}Pb and ^{144}Sm, and it is found that, for effective Lagrangian parametrizations corresponding to K_∞ in the range 200–270 MeV, the energy of the ISGDR is of the order of 25 MeV. Thus, the question of understanding the observed values of E_0 is still open.

In conclusion, self-consistent RPA and QRPA calculations have been done for the nuclei analyzed recently at Texas A&M University. In the case of the ISGMR, the results are in reasonable agreement with the data for the case of some Skyrme forces. Despite this, it is difficult to extract a unique value for the nuclear incompressibility K_∞. It can be in the range 200–215 MeV for Skyrme forces, or about 230 MeV for the finite-range Gogny force, or even higher in the relativistic mean field approach. Moreover, all these calculations are to some extent consistent in predicting a larger value for the ISGDR energy than experimentally observed. This is the next puzzle to be solved.

ACKNOWLEDGMENTS

We thank D.H. Youngblood and H.L. Clark for helpful discussions about the experimental data analysis and U. Garg for discussions.

REFERENCES

1. D. Youngblood, H. L. Clark, and Y. W. Lui, Phys. Rev. Lett. **82**, 691 (1999); D. Youngblood, in *Proceedings of the International Conference on Giant Resonances, RCNP, Osaka, June 2000,* Nucl. Phys. A (in press).
2. J. P. Blaizot, Phys. Rep. **64**, 171 (1980); J. M. Pearson, Phys. Lett. B **271**, 12 (1991); S. Shlomo and D. Youngblood, Phys. Rev. C **47**, 529 (1993).
3. J. Dobaczewski, H. Flocard, and J. Treiner, Nucl. Phys. A **422**, 103 (1984).
4. Nguyen Van Giai and H. Sagawa, Phys. Lett. B **106**, 379 (1981).
5. J. Bartel, P. Quentin, M. Brack, *et al.,* Nucl. Phys. A **386**, 79 (1982).
6. E. Chabanat, P. Bonche, P. Haensel, *et al.,* Nucl. Phys. A **635**, 231 (1998).
7. P.-G. Reinhard and H. Flocard, Nucl. Phys. A **584**, 467 (1995).
8. G. Colò, Nguyen Van Giai, P. F. Bortignon, and R. A. Broglia, Phys. Rev. C **50**, 1496 (1994).
9. E. Khan and N. Van Giai, Phys. Lett. B **472**, 253 (2000).
10. J. P. Blaizot, J. F. Berger, J. Dechargé, and M. Girod, Nucl. Phys. A **591**, 435 (1995).
11. Zhong-yu Ma, N. Van Giai, A. Wandelt, D. Vretenar, and P. Ring, nucl-th/9910054; N. Van Giai, in *Proceedings of the International Conference on Giant Resonances, RCNP, Osaka, June 2000,* Nucl. Phys. A (in press).
12. U. Garg, RIKEN Rev. **23**, 65 (1999).
13. G. Colò, N. Van Giai, P. F. Bortignon, and M. R. Quaglia, Phys. Lett. B **485**, 362 (2000).
14. D. H. Youngblood, private communication; H. L. Clark, in *Proceedings of the International Conference on Giant Resonances, RCNP, Osaka, June 2000,* Nucl. Phys. A (in press).
15. D. Vretenar, A. Wandelt, and P. Ring, nucl-th/0003041.
16. J. Dechargé and L. Šips, Nucl. Phys. A **407**, 1 (1983).
17. G. Colò, Nguyen Van Giai, P. F. Bortignon, and M. R. Quaglia, RIKEN Rev. **23**, 39 (1999).

Physics of Atomic Nuclei, Vol. 64, No. 6, 2001, pp. 1048–1054. From Yadernaya Fizika, Vol. 64, No. 6, 2001, pp. 1123–1129.

Properties of the Low-Lying Levels in the Transitional Ir and Au Nuclei*

B. Roussière**, **F. Ibrahim**, **J. Libert**, **J. Sauvage**, **D. Verney**, **L. Cabaret**$^{1)}$,
J. E. Crawford$^{2)}$, **J. Genevey**$^{3)}$, **D. Hojman**, **G. Huber**$^{4)}$, **A. Knipper**$^{5)}$, **F. Le Blanc**,
J. K. P. Lee$^{2)}$, **G. Marguier**$^{6)}$, **J. Oms**, **J. Pinard**$^{1)}$, and **A. Wojtasiewicz**

Institut de Physique Nucléaire, Orsay, France
Received September 11, 2000

Abstract—We try to determine to what extent an "axial prolate rotor + 1 or 2 quasiparticle model" succeeds in describing the transitional odd and odd–odd Ir and Au nuclei. The relative location of the excited states, as well as the properties of the ground and isomeric states, particularly the magnetic and spectroscopic quadrupole moments, is compared to the predictions of the model. © *2001 MAIK "Nauka/Interperiodica"*.

1. INTRODUCTION

The structure of the low-lying states in Ir and Au is very widely discussed: these nuclei belong to a region of shape instability, and various theoretical approaches setting or not axial symmetry have been used with success to interpret specific states [1–20]. Recently, both isotope series have been studied by laser spectroscopy [21–24] providing the nuclear moments of the ground and isomeric states and the change in the mean square charge radius ($\delta\langle r_c^2\rangle$). The magnetic moment ($\mu$) gives information on the structure of the state, whereas, assuming axial symmetry, the deformation of the nucleus can be extracted from $\delta\langle r_c^2\rangle$ and Q_S. On the other hand, electron spectroscopy measurements recently performed in the odd–odd ^{182}Ir and ^{184}Au nuclei [25, 26] have brought decisive information to define the structure of the low-energy levels, especially concerning the neutron and proton configurations involved in the description of these states.

The aim of this paper is to determine to what extent an "axial prolate rotor + 1 or 2 quasiparticles" approach succeeds in describing these transitional odd and odd–odd nuclei, and particularly the recent data obtained by laser and nuclear spectroscopy. The properties of the low-lying states observed in Ir and Au are presented, and similarities between these two isotope series are underlined. The main characteristics of the model are recalled, and the predictions of the model are compared with the experimental results analyzing (i) the relative location of the excited states in the odd nuclei and (ii) the properties of the ground and isomeric states (namely, the behavior of the associated rotational bands, the values of the magnetic and spectroscopic quadrupole moments) taking as an example ^{191}Ir for the heavier odd nuclei, ^{185}Ir for the lighter odd ones, and ^{184}Ir and ^{184}Au for the odd–odd isotopes.

2. EXPERIMENTAL PROPERTIES OF Ir AND Au NUCLEI

Figure 1 shows the levels located at low energy in the odd Ir and Au nuclei and interpreted as bandheads. Three groups of levels can be defined in both isotopes series. The first one is formed by the 3/2 and 1/2 positive parity states which are very close in energy. The $3/2^+$ state arising from the $2d_{3/2}$ subshell is the ground state down to $A = 187$ in Ir and down to $A = 191$ in Au. The $1/2^+$ state arising from the $3s_{1/2}$ subshell becomes the ground state in ^{187,189}Au. The second group of states is formed by the $11/2^-$ levels originating from the $1h_{11/2}$ subshell, and the third group by the two negative parity states which are the intruder states arising from the $1h_{9/2}$ subshell; the $5/2^-$ state becomes the ground state in the $A \leq 185$ Ir and Au nuclei.

Figure 2 shows $\delta\langle r_c^2\rangle$, μ, and Q_S obtained for the Ir and Au ground and isomeric states. Great similarities

---

[*] This article was submitted by the authors in English.

$^{1)}$Laboratoire Aimé Cotton, Orsay, France.

$^{2)}$Physics Department, McGill University, Montréal, Canada.

$^{3)}$Institut des Sciences Nucléaires, Grenoble, France.

$^{4)}$Institut für Physik der Universität Mainz, Germany.

$^{5)}$Institut de Recherches Subatomiques, Strasbourg, France.

$^{6)}$Institut de Physique Nucléaire, Villeurbanne, France.

[**] e-mail: `roussier@ipno.in2p3.fr`

between the two isotope series can be noted. In both cases, there is an increase in $\delta\langle r_c^2\rangle$ at $A = 186$, and when the spin of the state has the same value in Ir and Au, the magnetic moment and the spectroscopic quadrupole moment have similar values. This is particularly true for the $3/2^+$ state.

3. THE "ROTOR + 1 OR 2 QUASIPARTICLES" MODELS

These models have been developed by Meyer *et al.* [27] and Bennour *et al.* [28]. In a first step, Hartree–Fock + BCS calculations are performed for the even–even cores using the Skyrme III force and the constant G approximation for the pairing correlations. Axial symmetry is assumed. Here, the core is constrained to the deformation found experimentally from the $\delta\langle r_c^2\rangle$ measurements in Ir and Au. This first step provides us with the single-particle wave functions.

In a second step, one or two quasiparticle states are coupled to an axial rotor with the variable moment of inertia determined from the experimental energy sequence observed in the even–even core. In this approach, the Coriolis term is calculated exactly. The particle number is not conserved, which means that two cores can be used to describe an odd nucleus and four cores to describe an odd–odd nucleus. However, using the occupation probabilities which are directly related to the location of a state above or below the Fermi level, we can determine the most suitable core to represent a given configuration. In the "rotor + 2 quasiparticles" approach, the proton–neutron residual interaction (V_{pn}) is calculated using the Skyrme III force, i.e., the same force as that used to determine the neutron and proton quasiparticle wave functions.

To describe the gold and iridium nuclei, such calculations have been performed using Hg, Pt, and Os cores.

For the odd nuclei, the magnetic and spectroscopic quadrupole moments have been calculated using the procedure described in [29]. For the odd–odd nuclei, the magnetic moments have been evaluated following the method given in [30]:

$$\mu = \frac{K}{I+1}\left[g_{K_p}K_p + g_{K_n}K_n + g_R\frac{I^2+I-K^2}{K}\right]$$

with the g_{K_p} and g_{K_n} factors extracted from the theoretical magnetic moments obtained in the "rotor + 1 quasiparticle" approach for the given neutron and proton configurations.

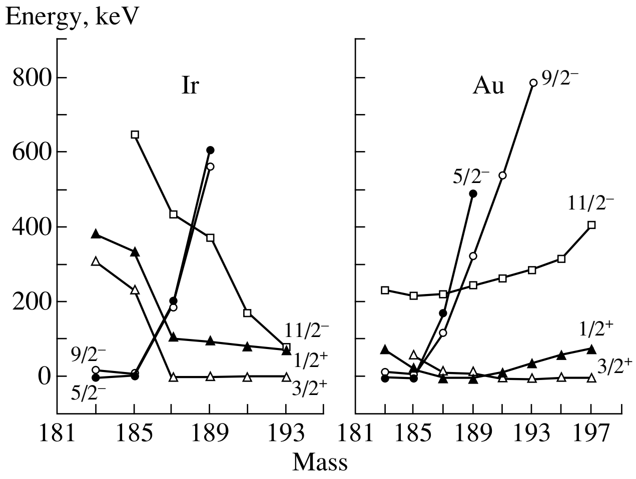

Fig. 1. Low-lying states observed in Ir and Au odd nuclei.

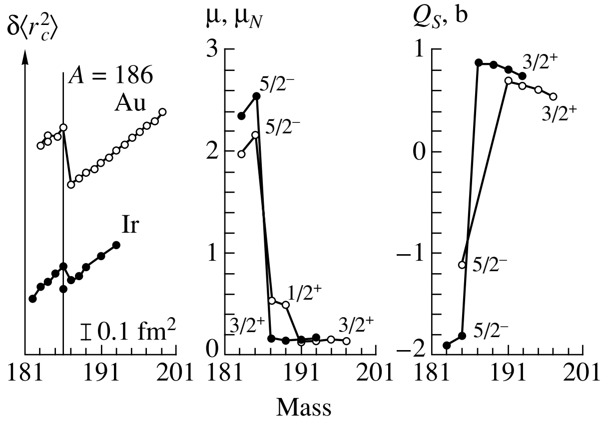

Fig. 2. $\delta\langle r_c^2\rangle$, μ, and Q_S measured in Ir (closed circles) and Au (open circles).

4. COMPARING THEORY WITH EXPERIMENT

4.1. Systematics of the Bandheads

Figure 3 shows the theoretical bandheads calculated with the "rotor + 1 quasiparticle" model using the Os and Pt cores. The theoretical states are labeled by their main component on the quasiparticle state basis using the asymptotic notation. The main differences between the results obtained with the Os and Pt cores are (i) the $5/2^+[402]$ state calculated above 500 keV with the Pt cores appears to be the ground state with the $^{182-190}$Os cores and (ii) the $9/2^-[514]$ state located above 1.4 MeV with the Pt cores is predicted to lie below 1 MeV with the Os cores. However, for both states, the occupation probabilities indicate full states, which means that, for these configurations, the Os cores describe the Re odd nuclei rather than the Ir ones. The $5/2^+[402]$ state is actually the ground state in the odd $^{179-189}$Re

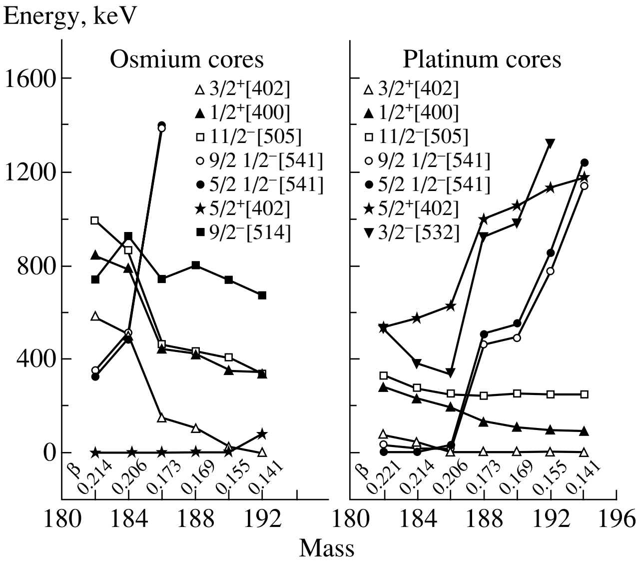

Fig. 3. Theoretical states calculated with the Os and Pt cores. Deformation β obtained from the $\delta\langle r_c^2\rangle$ measurements in Ir.

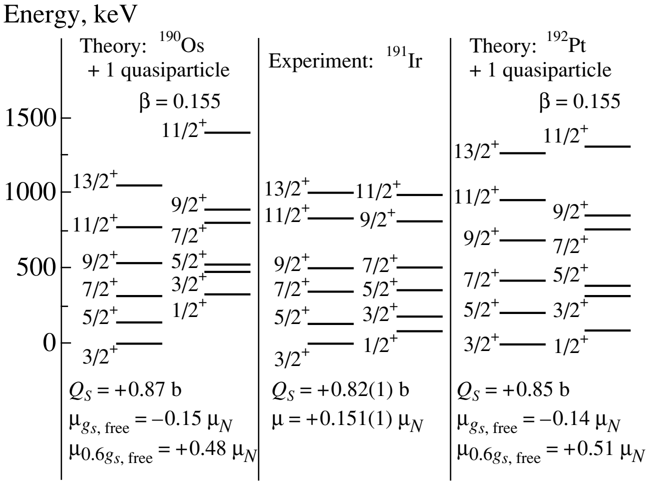

Fig. 4. $3/2^+[402]$ and $1/2^+[400]$ bands calculated with the ^{190}Os and ^{192}Pt cores compared with the experimental data in ^{191}Ir. The moments for the $3/2^+$ state are also indicated.

nuclei, and the $9/2^-[514]$ state is found at low energy ($E \leq 263$ keV) in $^{181-189}$Re [31].

The other theoretical states can be classified into two groups: the first one is formed by the $3/2^+[402]$, $1/2^+[400]$, and $11/2^-[505]$ levels with an energy decreasing when the mass of the core increases, and the second group by the $5/2^-1/2[541]$ and $9/2^-1/2[541]$ states originating from the $h_{9/2}$ subshell with an energy increasing with the mass of the core. The result is that the ground state is expected to be the $3/2^+[402]$ state in the heavier odd Ir and Au nuclei, and the $5/2^-1/2[541]$ state in the lighter odd ones. This is in agreement with the experimental data (see Fig. 1).

In the following, the $5/2^-1/2[541]$ and $9/2^-1/2[541]$ states will be labeled as originating from $h_{9/2}$. Indeed, the analysis of the wave functions describing these states shows a K mixing due to the Coriolis interaction, and this K mixing becomes stronger as the deformation increases. This point is illustrated by the wave function obtained for the $5/2^-$ state using the ^{186}Pt core constrained to various deformation values:

$$\Psi(5/2^-, \beta = 0.155)$$

$$= 80.5\%\, 5/2^-1/2[541] + 18.8\%\, 5/2^-3/2[532] + \ldots,$$

$$\Psi(5/2^-, \beta = 0.268)$$

$$= 59.5\%\, 5/2^-1/2[541] + 39.8\%\, 5/2^-3/2[532] + \ldots.$$

4.2. The $3/2^+[402]$ and $1/2^+[400]$ Bands

Experimentally, the ground state is a $3/2^+$ state in $^{187-193}$Ir and $^{191-195}$Au, and a $1/2^+$ state in ^{187,189}Au. The bands built on these two states are known and rather similar in all these nuclei. Figure 4 shows as an example the experimental data obtained in ^{191}Ir and the theoretical results obtained with the "rotor + 1 quasiparticle" model using the ^{190}Os and ^{192}Pt cores constrained to the deformation found experimentally for the ^{191}Ir ground state from the $\delta\langle r_c^2\rangle$ measurements. The band built on the $3/2^+$ state is quite well reproduced by the calculations, in particular, with the ^{190}Os core. Moreover, the experimental μ value lies between the values calculated using $g_s = g_{s,\rm free}$ and $0.6g_{s,\rm free}$, and the spectroscopic quadrupole moment is in fair agreement with the theoretical values (see Fig. 4). Thus, we can consider that the model succeeds in describing this $3/2^+$ ground state in the heavier Ir and Au nuclei. On the contrary, the experimental pattern of the band built on the $1/2^+$ state differs strongly from the predictions. Moreover, the magnetic moment measured for the $1/2^+$ state, for example in ^{189}Au, $\mu^{\rm exp}(^{189}\mathrm{Au}) = +0.494(14)\,\mu_N$, is much smaller than the values calculated for the $1/2^+[400]$ state using the ^{188}Pt core with $\beta = 0.150$: $\mu^{\rm th}_{g_{s,\rm free}} = +2.66\ \mu_N$ and $\mu^{\rm th}_{0.6g_{s,\rm free}} = +1.57\mu_N$.

4.3. The $h_{9/2}$ Structure

This structure is known and built on the ground state in the lighter Ir and Au nuclei. Figure 5 shows its pattern in ^{185}Ir, as well as the results obtained with the "rotor + 1 quasiparticle" model using the ^{184}Os and ^{186}Pt cores. The agreement between experiment and theory is quite good, in spite of some differences in the order of appearance of the levels. Table 1 shows the moments measured for the $5/2^-$ ground state in ^{185}Ir and ^{185}Au, as well as the theoretical values obtained for the various cores for deformations close to the values found experimentally from the $\delta\langle r_c^2\rangle$ measurements. With the Pt and Os cores, the wave function of the $5/2^-$ state has $K = 1/2$ as main component, but with the Hg core the wave function shows a strong $K(3/2$ and $1/2)$ mixing. This strong K mixing does not affect the values obtained for the theoretical magnetic moments but strongly increases the theoretical spectroscopic quadrupole moments (see Table 1). Therefore the change in the Q_S values between ^{185}Ir and ^{185}Au appears to be related to the change in the K mixing in the wave function describing the ground state. This K-mixing change is due to the variation of the deformation and of the Fermi level location between ^{185}Ir and ^{185}Au. Since it is quite well reproduced by the calculations, we can conclude that for this proton configuration the Coriolis effects are well accounted for by the "axial rotor + 1 quasiparticle" model.

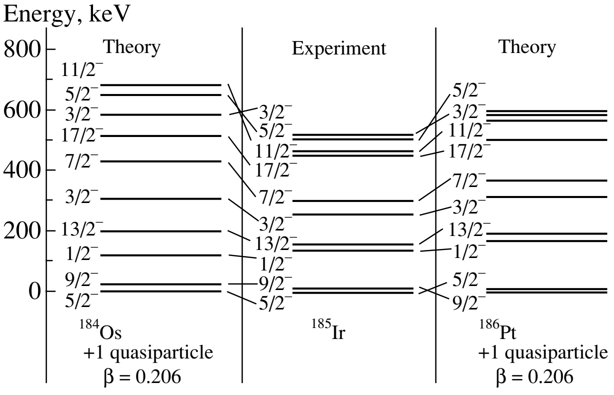

Fig. 5. The $h_{9/2}$ structure calculated with the ^{184}Os and ^{186}Pt cores compared with the experimental data in ^{185}Ir.

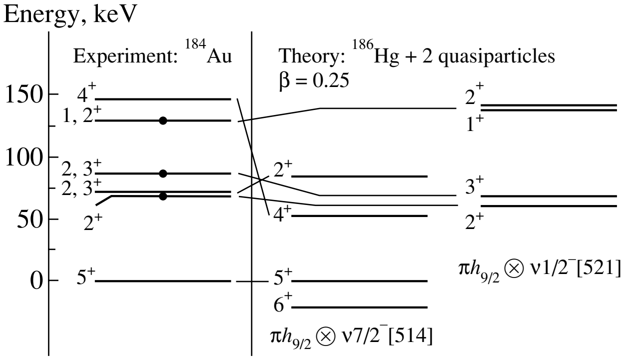

Fig. 6. The $\pi h_{9/2} \otimes \nu 7/2^-[514]$ and $\pi h_{9/2} \otimes \nu 1/2^-[521]$ configurations calculated with the ^{186}Hg core compared with the experimental data in ^{184}Au.

4.4. The $\pi h_{9/2} \otimes \nu 7/2^-[514]$ and $\pi h_{9/2} \otimes \nu 1/2^-[521]$ Configurations in ^{184}Au

From the intrinsic states observed in the neighboring odd-neutron and odd-proton nuclei, the configurations expected in ^{184}Au for the $I^\pi = 5^+$ ground state and for the $I^\pi = 2^+$ isomeric state are the following: $\pi h_{9/2} \otimes \nu 7/2^-[514]$ and $\pi h_{9/2} \otimes \nu 1/2^-[521]$ [32]. As $\pi h_{9/2}$ stands for $\pi 1/2[541]$ and/or $\pi 3/2[532]$, the possible K values are $K = 4$, 3 and/or 5, 2 for the ground state and $K = 1$, 0 and/or 2, 1 for the isomeric state.

Figure 6 represents the experimental levels which have been interpreted as members of these $\pi \otimes \nu$ configurations [32], as well as the theoretical states obtained in the frame of the "rotor + 2 quasiparticles" model using the ^{186}Hg core at the deformation found experimentally for ^{184}Au from the $\delta\langle r_c^2\rangle$ measurements. Except for the 6^+ state, each theoretical state can be associated with one experimental level. We can note that the 6^+ level has been observed experimentally but its energy location with respect to the 5^+ ground state is still unknown [33].

Table 2 shows the magnetic and spectroscopic quadrupole moments measured for the ground and isomeric states in ^{184}Au, as well as the theoretical values obtained assuming the K mixing given by the "rotor + 2 quasiparticles" calculations using the ^{186}Hg core at $\beta = 0.25$, or pure K states. The calculated μ values are not very sensitive to these various possibilities, but the experimental Q_S values indicate a pure $K = 5$ state for the ground state and a $K = 2$ component stronger than that given by the "rotor + 2 quasiparticles" calculation for the isomeric state. Such K values are obtained by coupling the $\pi 3/2[532]$ state to the $\nu 7/2^-[514]$ or $\nu 1/2^-[521]$ state. Thus, it seems that in ^{184}Au the role of the $\pi 3/2[532]$ state is underestimated by the "rotor + 2 quasiparticles" calculations, which means that the K mixing due to the Coriolis interaction is overestimated.

Table 1. Experimental moments measured for the $5/2^-$ ground state in ^{185}Ir and ^{185}Au compared with the values calculated for the $5/2^-$ state of the $h_{9/2}$ structure

Nucleus	$\mu^{\rm exp}$, μ_N $Q_S^{\rm exp}$, b	Core β_2 Main component	$\mu^{\rm th}$, μ_N a) $Q_S^{\rm th}$, b	Core β_2 Main component	$\mu^{\rm th}$, μ_N a) $Q_S^{\rm th}$, b
^{185}Ir	+2.55(7)	^{184}Os	$\mu_1 = +1.38$	^{186}Pt	$\mu_1 = +1.39$
		0.206	$\mu_2 = +2.06$	0.206	$\mu_2 = +2.10$
	−1.8(6)	85% 1/2[541]	−1.46	78.4% 1/2[541]	−1.42
^{185}Au	+2.17(7)	^{184}Pt	$\mu_1 = +1.32$	^{186}Hg	$\mu_1 = +1.31$
		0.245	$\mu_2 = +2.00$	0.242	$\mu_2 = +1.94$
	−1.1(1)	76% 1/2[541]	−1.65	65% 3/2 [532]	−1.01

a) Calculated with $g_s = g_{s,\rm free}(\mu_1)$ and $g_s = 0.6 f_{s,\rm free}(\mu_2)$.

Table 2. Experimental moments measured for the ground and isomeric states in ^{184}Au compared with the values calculated for the $\pi h_{9/2}\otimes\nu 7/2^-[514]$ and $\pi h_{9/2}\otimes\nu 1/2^-[521]$ configurations

	Experiment	Theory		
	^{184g}Au, $I^\pi = 5^+$	K mixed b)	$K = 5$	$K = 4$
$\mu[\mu_N]$ a)	+2.07(2)	+2.29	+2.36	+2.19
		+2.07	+2.21	+1.85
Q_S[b]	+4.7(3)	+3.4	+4.4	+1.8
	^{184m}Au, $I^\pi = 2^+$	K mixed c)	$K = 2$	$K = 1$
$\mu[\mu_N]$ a)	+1.44(2)	+1.10	+1.27	+0.80
		+1.21	+1.41	+1.00
Q_S[b]	+1.9(2)	+0.62	+2.2	−1.1

a) Calculated with $g_s = g_{s,\rm free}$ and $g_s = 0.6 g_{s,\rm free}$.

b) $\Psi(5^+) = 47\%(K = 5) + 31\%(K = 4) + \ldots$.

c) $\Psi(2^+) = 40\%(K = 2) + 37\%(K = 1) + \ldots$.

4.5. The $\pi h_{9/2} \otimes \nu 9/2^+$[624] Configuration in ^{184}Ir

In ^{184}Ir the 5^- ground state has been interpreted by the $\pi h_{9/2} \otimes \nu 9/2^+$[624] configuration [34]. The experimental levels identified as members of this configuration [35, 36] and the corresponding theoretical states obtained with the ^{184}Pt core are presented in Fig. 7. The agreement between experiment and theory is quite good since the same spin sequence is observed in both cases, even though the calculated energy spacings are somewhat below the observations. The wave function describing the 5^- state shows a strong mixing between the $K = 5$ and 4 components corresponding to the parallel and antiparallel coupling of the $\nu 9/2[624]$ state to the $\pi 1/2[541]$ state originating from the $\pi h_{9/2}$ subshell, and a weak $K = 3$ component due to the coupling of the same neutron state to the $\pi 3/2[532]$ state: $\Psi(5^-) = 46\%(K = 4) + 41.5\%(K = 5) + 6\%(K = 3) + \ldots$. These K percentages have been used to estimate the values of the nuclear moments presented in Table 3. The

Table 3. Experimental moments measured for the ground state in ^{184}Ir compared with the values calculated for the $\pi h_{9/2} \otimes \nu 9/2^+$[624] configuration

	Experiment	Theory			
	^{184}Ir	K mixed	$K = 5$	$K = 4$	$K = 3$
$\mu[\mu_N]$ a)	+0.69(3)	−0.92	−1.41	−0.74	+0.07
		−0.39	−0.69	−0.32	+0.719
Q_S[b]	+2.6(4)	+2.15	+3.61	+1.44	−0.24

a) The theoretical values have been calculated with $g_s = g_{s,\rm free}$ and $g_s = 0.6 g_{s,\rm free}$.

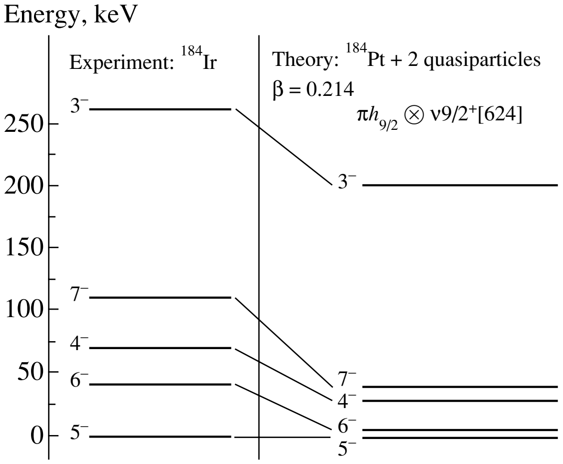

Fig. 7. The $\pi h_{9/2} \otimes \nu 9/2^+[624]$ configuration calculated with the ^{184}Pt core compared with the experimental data in ^{184}Ir.

experimental Q_S and μ values, as well as those calculated under the assumption of a pure $K = 5$, 4, or 3 state, are also shown in Table 3. In the K-mixed case, the spectroscopic quadrupole moment is in rather good agreement with the experimental value, but the magnetic moment is negative, contrary to what has been measured. It results from the μ values calculated under the assumption of a pure K state, in which case a positive value is obtained for only $K = 3$. This seems to indicate that the role of the $\pi 3/2[532]$ state is again underestimated by the "rotor + 2 quasiparticles" calculations. But in ^{184}Ir, unlike what has been observed in ^{184}Au, the wave function describing the ground state has to exhibit a K mixing in order to obtain a positive spectroscopic quadrupole moment.

5. CONCLUSIONS

The properties of the low-lying levels in the iridium and gold nuclei have been compared with the predictions of an "axial rotor + 1 or 2 quasiparticles" model assuming a prolate shape of the core and a deformation close to that extracted from the $\delta\langle r_c^2\rangle$ measurements. Since there is no adjustable parameters in the theoretical approach, we can consider that the agreement found between the theoretical and experimental results is of high quality.

Concerning the positive parity states, the properties of the $3/2^+$ ground state in the heavier Ir and Au nuclei are quite well reproduced, but some discrepancies between theory and experiment are found for the $1/2^+$ state which is the ground state in ^{187,189}Au. These positive parity states have been previously discussed in the frame of this "rotor + 1 quasiparticle" model assuming an oblate shape of the core with the deformation parameter corresponding to the minimum of the potential energy [19]. In this case, the description of the properties of the band built on the $1/2^+$ state becomes better, but that of the $3/2^+$ level, in particular, the nuclear moments, becomes worse. It remains to be seen whether the same conclusions are obtained when the calculations are constrained in deformation. On the other hand, this difficulty in reproducing the whole of the low-spin positive-parity states does not seem to be due to the axial-symmetry assumption since it has also been encountered in the recent calculations performed using the particle-triaxial-rotor model for ^{191,193}Ir [37].

On the contrary, a very good theory—experiment agreement is found for the $h_{9/2}$ structure built on the $5/2^-$ state in the lighter Ir and Au nuclei. It appears from the calculations that the more deformed the nucleus, the more important the 3/2[532] component in the wave function describing the $5/2^-$ state. As the deformation increases between ^{185}Ir and ^{185}Au, the differences observed in the experimental Q_S values are mainly due to the changes in the weight of the main components in the wave function describing the ground state.

As for the odd—odd nuclei, their properties are qualitatively well reproduced by the "rotor + 2 quasiparticles" model. The theory—experiment comparison done for ^{184}Au and ^{184}Ir indicates that the $\pi 3/2[532]$ component is favored when the $h_{9/2}$ proton is coupled to a neutron. For the configurations involving the $h_{9/2}$ structure, the K mixings due to the Coriolis interaction are better accounted for in the odd nuclei than in the odd—odd nuclei.

REFERENCES

1. C. Vieu *et al.,* Z. Phys. A **290**, 301 (1979).
2. C. Sébille-Schück *et al.,* Nucl. Phys. A **212**, 45 (1973).
3. S. André *et al.,* Nucl. Phys. A **243**, 229 (1975).
4. C. Schück *et al.,* Nucl. Phys. A **325**, 421 (1979).
5. S. André *et al.,* Nucl. Phys. A **325**, 445 (1979).
6. A. Zerrouki, Thèse 3ème cycle (Université Paris-Sud, Orsay), 1979.
7. M. A. Macias-Marques *et al.,* Nucl. Phys. A **427**, 205 (1984).
8. C. Vieu *et al.,* J. Phys. G **4**, 531, 1159 (1978).
9. A. J. Larabee *et al.,* Phys. Lett. B **169**, 21 (1986).
10. C. Bourgeois *et al.,* Nucl. Phys. A **386**, 308 (1982).
11. E. F. Zganjar *et al.,* Phys. Lett. B **58**, 159 (1975).
12. C. Bourgeois *et al.,* Nucl. Phys. A **295**, 424 (1978).
13. M. A. Deleplanque *et al.,* Nucl. Phys. A **249**, 366 (1975).
14. V. Berg *et al.,* Nucl. Phys. A **244**, 462 (1975).
15. Y. Gono *et al.,* Nucl. Phys. A **327**, 269 (1979).
16. H. Beuscher *et al.,* Z. Phys. **247**, 383 (1971).

17. Y. Gono *et al.,* Phys. Rev. Lett. **37**, 1123 (1976).
18. K. Heyde *et al.,* Phys. Rep. **102**, 291 (1983).
19. M. G. Porquet *et al.,* Nucl. Phys. A **451**, 365 (1986).
20. V. Berg *et al.,* Nucl. Phys. A **453**, 93 (1986).
21. G. Passler *et al.,* Nucl. Phys. A **580**, 173 (1994).
22. F. Le Blanc *et al.,* Phys. Rev. Lett. **79**, 2213 (1997).
23. J. Sauvage *et al.,* Hyperfine Interaction **129**, 103 (2000).
24. D. Verney *et al.,* in *Proceedings of International Conference on Experimental Nuclear Physics in Europe, Sevilla, Spain, 1999*; AIP Conf. Proc. **495**, 117 (1999).
25. B. Roussière *et al.,* Hyperfine Interaction **129**, 119 (2000).
26. B. Roussière *et al.,* Nucl. Phys. A **643**, 331 (1998).
27. M. Meyer *et al.,* Nucl. Phys. A **316**, 93 (1979).
28. L. Bennour *et al.,* Nucl. Phys. A **465**, 35 (1987).
29. J. Libert *et al.,* Phys. Rev. C **25**, 586 (1982).
30. C. Ekström and I. L. Lamm, Phys. Scr. **7**, 31 (1973).
31. R. B. Firestone, *Table of Isotopes* (Wiley, New York, 1996, 8th ed.).
32. F. Ibrahim *et al.,* Z. Phys. A **350**, 9 (1994).
33. F. Ibrahim *et al.,* Phys. Rev. C **53**, 1547 (1996).
34. E. Hagn *et al.,* Phys. Lett. B **104**, 365 (1981).
35. A. Ben Braham *et al.,* Nucl. Phys. A **482**, 553 (1988).
36. A. J. Kreiner *et al.,* Nucl. Phys. A **489**, 525 (1988).
37. E. Bezakova *et al.,* Nucl. Phys. A **669**, 241 (2000).

Physics of Atomic Nuclei, Vol. 64, No. 6, 2001, pp. 1055–1059. From Yadernaya Fizika, Vol. 64, No. 6, 2001, pp. 1130–1134.
Original English Text Copyright © 2001 by Pittel, Stoitsov.

An Improved Single-Particle Basis for Nuclear Structure Studies Far from Stability*

S. Pittel** and **M. V. Stoitsov**[1)]

Bartol Research Institute, University of Delaware, Newark, USA

Received September 11, 2000

Abstract—A new single-particle basis is proposed for use in weakly bound nuclei far from the valley of beta stability. The basis, obtained by applying a local-scaling point transformation to the states of a harmonic oscillator potential, can be tailored to have the correct asymptotic properties for weakly bound systems. We first present a test of the basis and then apply it in Hartree–Fock–Bogolyubov calculations of the even Mg isotopes, from the proton drip line to the neutron drip line. © *2001 MAIK "Nauka/Interperiodica"*.

1. INTRODUCTION

The development of experimental facilities that accelerate radioactive species will open up the possibility of exploring a wide variety of nuclei heretofore inaccessible. With these new facilities and the new detector technology that is accompanying them, it should soon be possible to study the properties of nuclei very far from the valley of beta stability. Several such facilities are already in operation, and several more advanced ones are in the planning or development stage. With these new experimental opportunities comes the need for new theoretical techniques suitable for describing the new phenomena that are expected.

Many of the theoretical techniques used in the description of nuclear structure require an appropriate single-particle basis. Most commonly used in the description of normal nuclei is the harmonic oscillator (HO) basis. This basis is particularly useful for several reasons: because of its simple analytic properties, because it provides a complete and discrete set of states, and because of its properties in numerical algorithms. But the HO basis has much less use when dealing with weakly bound nuclei far from stability, especially on the neutron-rich side. Near the neutron drip line, at least two important new pieces of physics come into play: (1) the need to include very weakly bound single-particle orbits with long tails and (2) the need to include explicitly the continuum. An HO basis, because of its Gaussian asymptotic properties, cannot accommodate this physics.

We have recently proposed [1] an alternative to the HO basis, which preserves much of its simplicity but is more suitable for the description of weakly bound nuclei. The new basis derives from the application of a local-scale transformation (LST) [2] to the single-particle states of the oscillator. Referred to as the transformed HO (THO) basis, it consists of a complete set of localized states, making it useful in basis expansion approaches, and is relatively simple to implement in numerical algorithms. Most importantly, the LST from which it derives can be tailored to yield the appropriate asymptotic properties of nuclei.

In this presentation, we review the progress that has been made in the development and application of the THO basis. We begin in Section 2 with a brief description of the basis and then in Section 3 describe a test of its usefulness [1, 3] in the context of Hartree–Fock–Bogolyubov (HFB) calculations of spherical nuclei. Such calculations can be carried out directly in coordinate space [4], thereby mitigating the need for a good single-particle basis. As we will see, the THO basis is able to reproduce the results of full coordinate-space HFB calculations for spherical nuclei far from stability. Then, in Section 4, we present the results of drip-line to drip-line HFB calculations for the even Mg isotopes [3], permitting axial deformation. Coordinate-space calculations are much more difficult for deformed nuclei for numerical reasons. As we will see, reliable configuration-space HFB calculations even for deformed nuclei are possible when using the THO basis. Finally, Section 5 contains some closing remarks.

2. THE THO BASIS

The key concept in our construction of a new basis is that of an LST of coordinates [2]. An LST

---

[*] This article was submitted by the authors in English.

[1)] Institute of Nuclear Research and Nuclear Energy, BAS, Sofia, Bulgaria.

[**] e-mail: `pittel@bartol.udel.edu`

replaces the original coordinate $\mathbf{r}$ by a new coordinate $\mathbf{r}'$, defined according to

$$\mathbf{r}' = \mathbf{f}(\mathbf{r}) = \hat{\mathbf{r}}\, f(\mathbf{r}). \tag{1}$$

The new coordinate is in the same direction as $\mathbf{r}$, but has a new magnitude that depends on a scalar function $f(\mathbf{r})$. It is further assumed that $f(\mathbf{r})$ is an increasing function of r and that $f(\mathbf{0}) = 0$.

Let us now consider an A-particle model wave function $\bar{\Psi}(\mathbf{r}_1, \mathbf{r}_2, ..., \mathbf{r}_A)$. The LST transforms it into a new A-particle wave function

$$\Psi(\mathbf{r}_1, \mathbf{r}_2, ..., \mathbf{r}_A) = D^{1/2}\bar{\Psi}(\mathbf{f}(\mathbf{r}_1),\ \mathbf{f}(\mathbf{r}_2), ..., \mathbf{f}(\mathbf{r}_A)), \tag{2}$$

where

$$D = \prod_{i=1}^{A} \frac{f^2(\mathbf{r}_i)}{r_i^2} \frac{\partial f(\mathbf{r}_i)}{\partial r_i} \tag{3}$$

is the Jacobian of the LST.

Under the assumption that the model wave function is normalized to unity,

$$\langle \bar{\Psi} | \bar{\Psi} \rangle = 1, \tag{4}$$

the LST wave function $\Psi(\mathbf{r}_1, \mathbf{r}_2, ..., \mathbf{r}_A)$ is likewise normalized to unity, regardless of the choice of f.

Let us now consider an A-particle Slater determinant,

$$\bar{\Psi}(\mathbf{r}_1, \mathbf{r}_2, ..., \mathbf{r}_A) = \frac{1}{\sqrt{A!}} \det |\bar{\psi}_i^{\mathrm{HO}}(\mathbf{r}_j)|, \tag{5}$$

built from the set of HO single-particle wave functions $\bar{\psi}_i^{\mathrm{HO}}$. Due to its unitarity, the LST takes it into another Slater determinant,

$$\Psi(\mathbf{r}_1, \mathbf{r}_2, ..., \mathbf{r}_A) = \frac{1}{\sqrt{A!}} \det |\psi_i^{\mathrm{THO}}(\mathbf{r}_j)|, \tag{6}$$

built from a new set of single-particle wave functions

$$\psi_i^{\mathrm{THO}}(\mathbf{r}) = \left[\frac{f^2(\mathbf{r})}{r^2} \frac{\partial f(\mathbf{r})}{\partial r}\right]^{1/2} \bar{\psi}_i^{\mathrm{HO}}(\mathbf{f}(\mathbf{r})). \tag{7}$$

The complete and discrete set of single-particle states, ψ_i^{THO}, derived by applying the LST to the set of HO states, is what we refer to as the transformed HO basis.

In principle, LST functions can be introduced to transform separately the three components of a three-dimensional wave function. In the applications reported here, we have permitted the transformation to affect the radial part of the oscillator wave functions only, whereby the resulting THO states have the same angular momentum properties as the original oscillator states.

The LST can in principle be chosen in any way consistent with its definitions. This gives enormous flexibility, but in fact much too much. A useful transformation is one that produces wave functions with the correct asymptotic behavior, but with as few parameters as possible.

The form of the LST function that we used in this work is

$$f(r) = \begin{cases} r\left(1 + ar^2\right)^{1/3} \ \text{for}\ r \le R \\[2ex] \sqrt{\dfrac{d_{-2}}{r^2} + \dfrac{d_{-1}}{r} + d_0 + d_1 r + d_L \ln r} \\ \text{for}\ r > R. \end{cases} \tag{8}$$

The five coefficients d_i are fixed by the requirement that the function $f(r)$ and its first, second, third, and fourth derivatives are continuous at the matching radius R. The function thus has two parameters, a and R. Since the oscillator length also determines the final THO states, the total number of parameters that define our basis is 3.

This form of the LST was obtained by considering the behavior at large and small r. At small r, nuclear densities are expected to vary weakly with r and have a central depression. A Slater determinant built from these THO wave functions produces a density at small r of the form

$$\rho(r) \approx \rho_0 + cr^2, \tag{9}$$

as desired.

More important is the behavior at large r. Asymptotically, the linear term in $f(r)$ dominates, and the THO wave functions behave like

$$\psi_i^{\mathrm{THO}}(r \to \infty) \approx \exp\left[-\frac{1}{2}kr\right], \tag{10}$$

where

$$k = \frac{d_1}{b}. \tag{11}$$

Thus, with this form of the transformation, we satisfy the requirement that the THO wave functions fall off exponentially.

With this parametrization, we determine the three parameters so as to optimize the basis for the problem of interest.

3. TEST CALCULATIONS

The principal test we carried out for our new basis was in the context of HFB calculations for weakly bound neutron-rich spherical nuclei [3]. For such nuclei, the HFB approximation can be carried out in coordinate space, where no expansion in a single-particle basis is required. How do configuration-space HFB calculations that expand both the density matrix and the pairing tensor in an optimally chosen THO basis compare with the full coordinate-space results? Can they reproduce the physics?

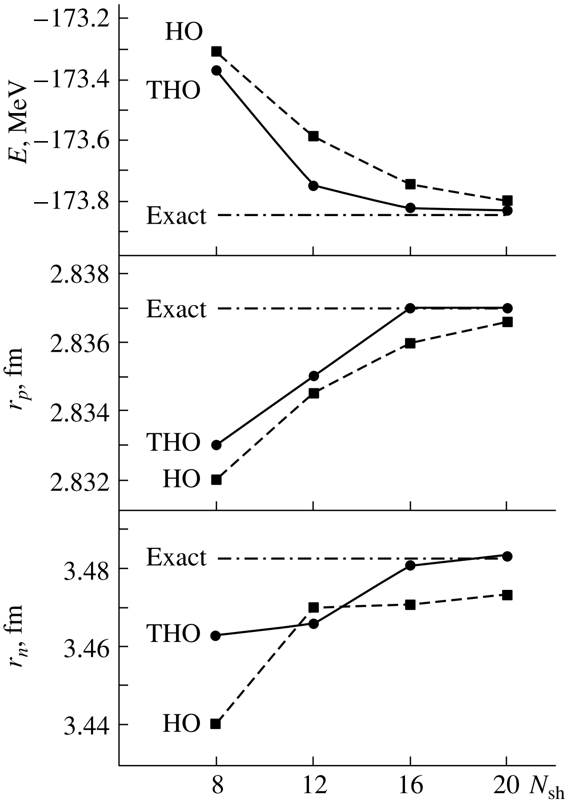

Fig. 1. Total energies E, and proton and neutron rms radii, r_p and r_n, obtained in the HFB + SLy4 calculations for ^{28}O using the HO and THO bases, as functions of the number of HO shells N_{sh}. The exact results refer to those obtained from spherical coordinate-space calculations.

These questions are addressed in Fig. 1, which show the results of calculations carried out for the very neutron-rich nucleus ^{28}O at several levels of approximation. The results labeled “exact” refer to coordinate-space HFB calculations. Also shown are the results obtained by expanding in terms of HO states and THO states. All results are presented as a function of the number of basis shells included. In the two sets of configuration-space calculations, the parameters that defined the basis were chosen variationally so as to minimize the total HFB energy. All calculations were carried out using the force SLy4. Since ^{28}O is doubly-magic, pairing correlations do not enter.

The first point to note is that an expansion in the THO basis is much better than an expansion in the HO basis. More importantly, when 20 major shells are included, the calculation in the optimized THO basis gives an excellent reproduction of the “exact” results. This is to be contrasted with the HO results, which even after 20 shells cannot reproduce the exact results very accurately.

Perhaps the key improvement is in the neutron rms radius. This is obviously a quantity that in a nucleus like ^{28}O, so close to the neutron drip line, is highly sensitive to the long tail of the last neutron’s wave function. With 20 shells, the THO calculation reproduces it very accurately, whereas the HO basis does not.

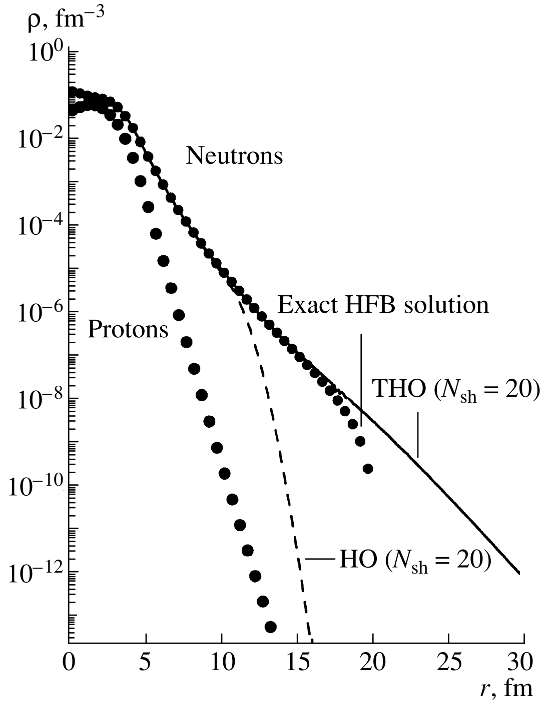

Fig. 2. Neutron densities obtained in the HFB + SLy4 calculations for ^{28}O using the HO (dashed curve) and THO (solid curve) bases. Neutron and proton densities denoted as “exact” (dots) have been obtained from spherical coordinate-space calculations in a box of 20 fm.

This latter point can be better understood from Fig. 2, where we show the calculated density distributions for the same nucleus ^{28}O. Of particular interest are the neutron distributions. The THO calculation with 20 shells reproduces the tail of the neutron density distribution very accurately. In contrast, with only 20 shells the HO calculation cannot get the tail right beyond about 10 fm. That is fine for normal nuclei, but not for very weakly bound nuclei which extend out much further. This is not to say that an oscillator basis cannot reproduce a long tail. To do so, however, would require very many major shells [1], which cannot be accommodated within existing codes.

Note, by the way, that the coordinate-space results stop at 20 fm. Coordinate-space HFB calculations are typically performed by putting the system in a large box, and in these calculations the box size was 20 fm. This artificial behavior does not enter the

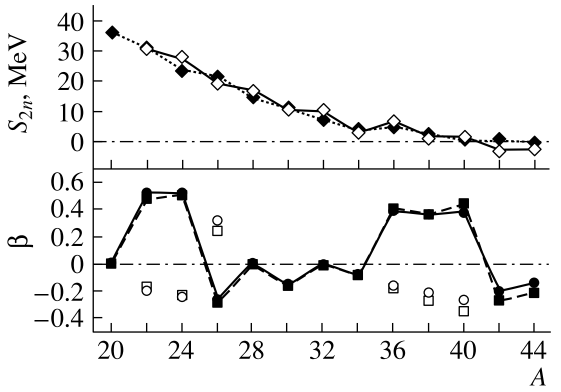

Fig. 3. Results from HFB + SLy4 calculations of the even Mg isotopes in the THO basis with 20 oscillator shells. The upper panel shows the two-neutron separation energies $S_{2n} = E(Z, N-2) - E(Z, N)$ (open symbols) and $-2\lambda_n$ (closed symbols). The lower panel shows the deformation parameters. Circles and squares refer to proton and neutron results, respectively. Closed symbols connected with lines denote values for the absolute minima in the deformation-energy curve, and open symbols to secondary minima.

configuration-space analysis, which does not require the introduction of a cutoff in r.

4. DRIP-LINE TO DRIP-LINE CALCULATIONS FOR THE EVEN Mg ISOTOPES

The success of our calculations for spherical nuclei, where they can be tested against coordinate-space results, suggests that they can also be used in deformed nuclei. In deformed nuclei, coordinate-space HFB studies are extremely difficult, because of the dramatically increased complications in going from a one-dimensional to a two-dimensional mesh.

We have now succeeded in carrying out calculations of very weakly bound deformed nuclei using the configuration-space HFB framework expanded in the THO basis. We report in Fig. 3 some of the more interesting results that emerged, referring the reader to [3] for more complete results. These calculations were carried out for all of the even Mg isotopes, from the proton drip line to the neutron drip line, using the Skyrme force SLy4 and a Volume Delta interaction in the pairing channel.

The upper panel of the figure shows the calculated results for the two-neutron separation energy S_{2n} and the related quantity $-2\lambda_n$ for the various ground state solutions. From the latter, we can readily determine λ_n, the neutron chemical potential or Fermi energy. These quantities provide direct information on the stability of the nucleus to neutron emission. In particular, a nucleus with a positive two-neutron separation energy is bound against two-neutron emission, whereas one with a negative two-neutron separation energy spontaneously decays by two-neutron emission and is formally beyond the two-neutron drip line. Analogously, a nucleus with a negative λ_n is bound against the emission of a single neutron.

The first point to note is that the heaviest even-mass Mg isotope that is bound against two-neutron decay, on the basis of having a positive two-neutron separation energy, is ^{40}Mg. The next is that both ^{42}Mg and ^{44}Mg, though unstable against two-neutron decay, have very small negative values of the chemical potential λ_n, and are thus bound against one-neutron emission.

The lower panel of Fig. 3 shows results for the quadrupole deformation parameter for the various isotopes considered. The circles correspond to the proton deformation, and the squares to the neutron deformation. Those symbols that are filled and connected by lines refer to the ground state minima; those represented by open symbols refer to the second minima. We will focus on the ground state minima.

The point to note is that for the heavier nuclei approaching ^{40}Mg—the heaviest bound against two-neutron decay—the ground state is prolate. For the next two nuclei, ^{42}Mg and ^{44}Mg, both of which are unbound against two-neutron decay but bound against one-neutron decay, the ground state is oblate. Interestingly, this change in the shape of the ground state takes place at the same point at which the nucleus becomes unstable against two-neutron emission while remaining stable against single-nucleon emission.

It is premature to take these conclusions too seriously, until we are able to explore other forces. But if they do survive, it would be quite interesting. It would indicate that there are nuclei that are stable against one-neutron emission but unstable against two-neutron emission. And perhaps most interestingly, it would suggest that under certain circumstances such nuclei might live long enough to be observed. The reason for this is related to the change in shape mentioned earlier. Since the ground state of ^{42}Mg has a different shape than that of the nucleus to which it should decay by two-neutron emission, namely, ^{40}Mg, there may be a built-in suppression of the decay. Thus, it might be possible for ^{42}Mg to live long enough to be observed, even though it is formally beyond the two-neutron drip line. More work on such an exotic possibility is clearly needed.

While this is in our view a potentially interesting conclusion and one worth thinking about and studying further, it is not the key message that we would like to transmit. The more significant message is that we are now able to carry out meaningful HFB calculations for nuclei all the way out to the drip lines, including those that are deformed. And the reason we are able to do this is because of our use of the THO basis with its improved asymptotic properties.

5. CLOSING REMARKS

In the previous two sections, we briefly summarized the tests we carried out to assess the usefulness of the THO basis and reported some results of a first application. Based on the success of these calculations, we are now in the process of carrying out other applications. On the one hand, we are carrying out a systematic study of nuclei across the periodic table in the HFB framework, with different forces and different prescriptions for pairing. For these applications, we are exploring alternative parametrizations of the transformation that are more suitable for a systematic investigation of a wide range of nuclear species. In a totally different direction, we are using the THO basis, with its improved asymptotics, in variational shell-model studies of weakly bound light nuclei. No doubt, other interesting applications of this new methodology to the study of nuclei far from stability will also be possible.

ACKNOWLEDGMENTS

The work reported here was carried out in collaboration with Jacek Dobaczewski, Witek Nazarewicz, and Peter Ring. Our part was supported by the National Science Foundation under grants nos. PHY-9600445, INT-9722810, and PHY-9970749 and by the Bulgarian National Foundation for Scientific Research under project Φ-809.

REFERENCES

1. M. V. Stoitsov, W. Nazarewicz, and S. Pittel, Phys. Rev. C **58**, 2092 (1998).
2. I. Zh. Petkov and M. V. Stoitsov, C. R. Acad. Bulg. Sci. **34**, 1651 (1981); Theor. Math. Phys. **55**, 584 (1983); Yad. Fiz. **37**, 1167 (1983) [Sov. J. Nucl. Phys. **37**, 692 (1983)].
3. M. V. Stoitsov, J. Dobaczewski, P. Ring, and S. Pittel, Phys. Rev. C **61**, 034311 (2000).
4. J. Dobaczewski, H. Flocard, and J. Treiner, Nucl. Phys. A **422**, 103 (1984).

Physics of Atomic Nuclei, Vol. 64, No. 6, 2001, pp. 1060–1063. From Yadernaya Fizika, Vol. 64, No. 6, 2001, pp. 1135–1138.
Original English Text Copyright © 2001 by Zamfir.

Octupole Correlations in the Actinides and the *spdf*-IBA Model*

N. V. Zamfir**

Wright Nuclear Structure Laboratory, Yale University, New Haven, USA;
Clark University, Worcester, USA

Received September 11, 2000

Abstract—The octupole bands in the $Z \sim 88, N \sim 134$ region, with their abundance of experimental information, offer a real challenge for different nuclear structure models. In this region, quasimolecular bands, which are thought to indicate the presence of stable octupole deformation, have been observed. The quantities most often reported are the $B(E1)/B(E2)$ branching ratios from these levels. The calculations in the framework of the *spdf* model show that the 1-pf boson limit (dipole—octupole vibrations) can describe the essential experimental features related to the octupole bands in the Rn—Th region. *© 2001 MAIK "Nauka/Interperiodica".*

1. INTRODUCTION

The nuclear octupole states, despite their almost 50 years history, are much less understood than the quadrupole collective states. The question of the existence of octupole deformation is still controversial and challenging for nuclear structure models. The difficulty arises from the fact that is no specific established phenomenological criteria for the degree of octupole collectivity. Although there are many models [1], microscopic or macroscopic, geometric or algebraic, it is not yet known definitively which nuclei are octupole-deformed, if any, and which models adequately describe the occurrence of strong octupole correlations. The recent developments in spectroscopic techniques produced qualitatively new sets of data which constitute a real challenge for different models. Extensive numerical studies are necessary to test different models in their ability to describe the essential experimental features.

2. *spdf* IBA CALCULATIONS

The Interacting Boson Model (IBA) offers a phenomenological approach by introducing bosons of a given spin which carry the corresponding multipole modes. The negative parity states are described by introducing bosons with odd values of angular momentum, $p(L=1)$ and/or $f(L=3)$, in addition to the standard $s(L=0)$ and $d(L=2)$ bosons. The *spdf* version of the IBA was introduced by Engel and Iachello [2], and the dynamical symmetries of the related group, $U(16)$, were studied by Nadjakov and Mikhailov [3a] and completely constructed and classified by Kusnezov [3b]. Although the dynamical symmetries of the *sd* IBA constituted benchmarks for the phenomenology of the quadrupole collectivity, in this case, none of the typical features of the dynamical symmetries of $U(16)$ appear to be in the data. The $Z \sim 88, N \sim 134$ nuclei, where octupole deformation is predicted by microscopic—macroscopic calculations to play a major role and where there is a wealth of experimental information, are in a quadrupole and octupole transitional region. Under these conditions, numerical calculations are needed. The model space is very large and is impractical for a systematic numerical study. Different truncations were applied, and a variety of data were successfully explained [4—8].

The aim of this work is to test the vibration-like picture ($n_p, n_f \leq 1$) in a large region of transitional nuclei ($Z = 86$—90, $N = 130$—142) in a unified way (the same Hamiltonian) and to keep the calculations as simple as possible (a minimum number of terms). The question is how much of the observed phenomena can be explained in the absence of octupole deformation. The calculations were done with the code OCTUPOLE [9] using a very simple Hamiltonian:

$$H = \epsilon_d \hat{n}_d + \epsilon_p \hat{n}_p + \epsilon_f \hat{n}_f - \kappa Q_{spdf} Q_{spdf}, \quad (1)$$

where

$$Q_{spdf} = Q_{sd} + Q_{pf} \quad (2)$$

$$= [s^\dagger \tilde{d} + d^\dagger s] - \frac{\sqrt{7}}{2}[d^\dagger \tilde{d}]^{(2)} + \frac{3\sqrt{7}}{5}[p^\dagger \tilde{f} + f^\dagger \tilde{p})]^{(2)} - \frac{9\sqrt{3}}{10}[p^\dagger \tilde{p}]^{(2)} - \frac{3\sqrt{42}}{10}[f^\dagger \tilde{f}]^{(2)}.$$

With four parameters (three boson energies ϵ_d, ϵ_p, and ϵ_f and the strength κ of the quadrupole—quadrupole interaction) having a smooth behavior

---

*This article was submitted by the author in English.

**e-mail: `zamfir@galileo.physics.yale.edu`

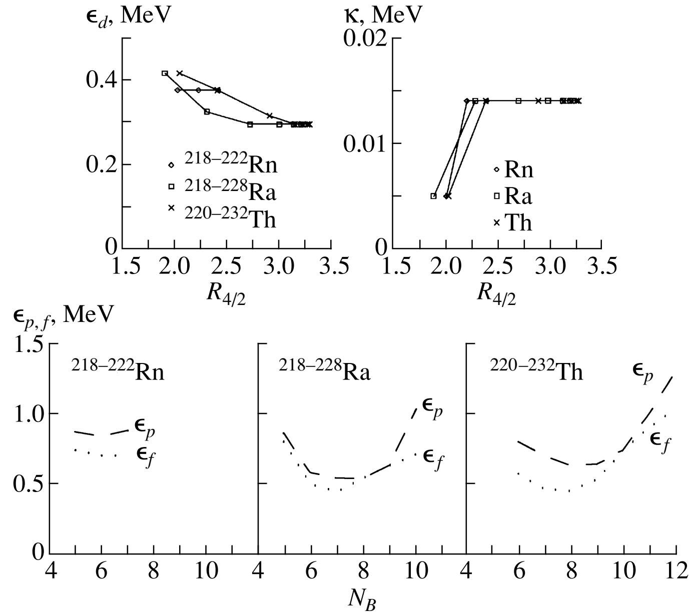

Fig. 1. The parameters of the *spdf* Hamiltonian of (1) used for Rn, Ra, and Th isotopic chains. Top: the d-boson energy (ϵ_d) and the strength of the quadrupole–quadrupole term (κ) as a function of $R_{4/2} \equiv E(4_1^+)/E(2_1^+)$ showing that for spherical nuclei ($R_{4/2} \sim 2.0$) ϵ_d is large (~0.4 MeV) and κ is small (0.005 MeV) and for transitional and quadrupole deformed nuclei ($R_{4/2} > 2.5$) ϵ_d is lower (~ 0.3 MeV) and κ is larger (0.014 MeV). Bottom: The energy of the p and f bosons ($\epsilon_{p,f}$) as a function of boson number N_B.

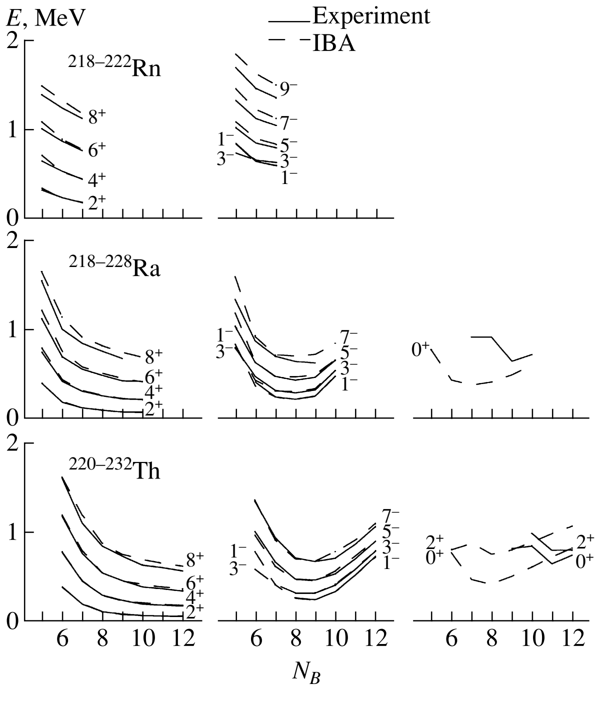

Fig. 2. Experimental (solid lines) and calculated (dashed lines) energies for the $K = 0_1^+, 0_1^-$ bands. For Ra and Th isotopes, where the band-heads for the $K = 0_2^+$ and 2_γ^+ are experimentally known in the heavier isotopes, the predictions for these bands are also shown in the panels on the right.

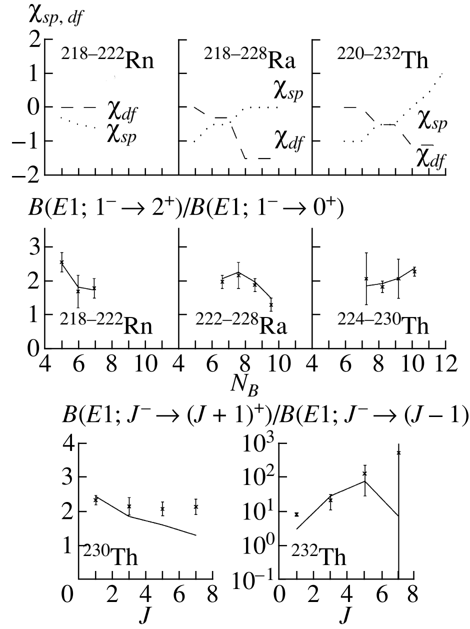

Fig. 3. Top: the parameters χ_{sp} and χ_{df} of the $T(E1)$ operator of (3) used to calculate the transition rates in the Rn, Ra, and Th isotopic chains. Middle: Experimental (symbols) and theoretical (solid lines) $B(E1)$ branching ratio from 1_1^- states in the Rn, Ra, and Th isotopes. Bottom: Similar to the middle panels, but for $J \geq 1^-$ states in ^{230,232}Th.

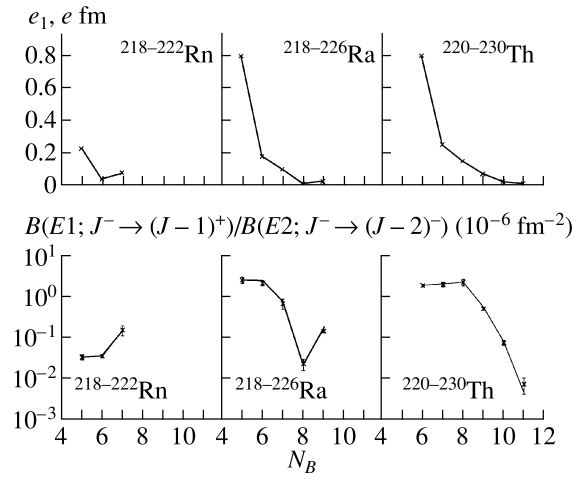

Fig. 4. Top: the effective charge, e_1, used to calculate the $E1$-transition rates. The other $E1$ parameters, χ_{sp} and χ_{df}, are presented in Fig. 3 (top). Bottom: Experimental (symbols) and theoretical (solid lines) average values for the $B(E1)/B(E2)$ ratio (a single value for e_2 was used, obtained from the fit of the known $B(E2)$ experimental values in these isotopes, $e_2 = 0.18$ e b).

across the region (Fig. 1), the energies of the alternating parity band ($K = 0_1^+$ and $K = 0_1^-$) are very nicely reproduced (Fig. 2). It is worth noting that this includes the inversion of the 1^- and 3^- states (the 1^- state is lower than 3^- in ^{218}Rn [10] and ^{218}Ra [11] and is higher in all other nuclei).

The one-body $E1$ operator is

$$T_{spdf}(E1) = e_1([p^\dagger \tilde{d} + d^\dagger \tilde{p}]^{(1)} \tag{3}$$
$$+\chi_{sp}[s^\dagger \tilde{p} + p^\dagger s]^{(1)} + \chi_{df}[d^\dagger \tilde{f} + f^\dagger \tilde{d}]^{(1)}).$$

The $E1$-branching ratios depend only on χ_{sp}, χ_{df} and are not dependent on the effective charge e_1. The parameters χ_{sp}, χ_{df} are presented in Fig. 3 (top). In Fig. 3 (middle) is shown the branching ratio $B(E1; 1_1^- \to 2_1^+)/B(E1; 1_1^- \to 0_1^+)$ for different isotopic chains, and in Fig. 3 (bottom) are presented the branching ratios $B(E1; J^- \to (J+1)^+)/B(E1; J^- \to (J-1)^+)$ as a function of spin for ^{230,232}Th. In all cases, the agreement with the data is excellent, including the large variation in magnitude of the branching ratio as a function of spin in ^{232}Th.

Another test of the model constitutes the $B(E1)/B(E2)$ ratios. For the $T(E2)$ operator, we used the sd form, namely, $T(E2) = e_2 Q_{sd}$. In Fig. 4 (bottom) are compared the experimental and theoretical average values of this ratio. This agreement was obtained with a mass-dependent effective charge, e_1, presented in Fig. 4 (top).

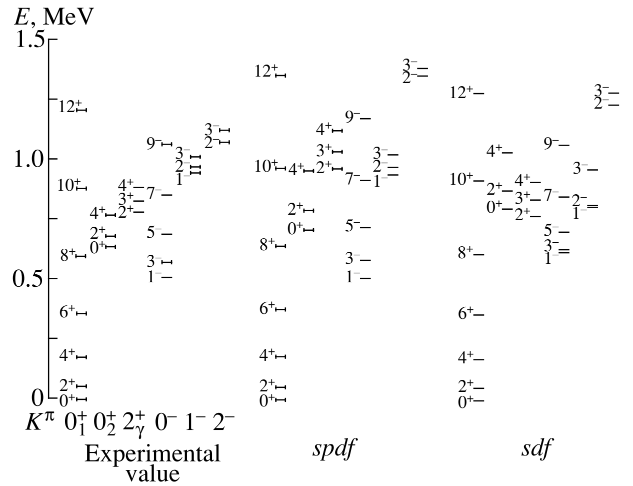

Fig. 5. Experimental values for the energies of different bands in ^{230}Th compared with *spdf* (present work) and *sdf* [12] calculations.

3. DISCUSSION

The comparisons presented in Figs. 2–4 show that calculations with 1-pf boson are able to reproduce the essential features of the alternating parity bands in the light actinides.

In order to see if the p boson is essential or not in describing the negative parity states, we show in Fig. 5 a comparison of two sets of calculations corresponding to ^{230}Th: one calculation is 1-pf boson approach described in the present work, and the

$B(E1; J_i^- \to J_{f1}^+)/B(E1; J_i^- \to J_{f2}^+)$ for octupole bands in ^{230}Th compared with calculations in the 1-pf and 1-f limits of the IBA model

K^-	J_i^-	J_{f1}^+	J_{f2}^+	Experiment	*spdf*	*sdf* [12]
0^-	1^-	2_1^+	0_1^+	2.32(14)	2.42	2.60
	3^-	4_1^+	2_1^+	2.15(24)	1.85	1.65
	5^-	6_1^+	4_1^+	2.06(19)	1.61	1.21
	7^-	8_1^+	6_1^+	2.12(24)	1.31	0.92
1^-	1^-	2_1^+	$0_{\text{g.s}}^+$	0.24(2)	0.44	0.17
	1^-	$2_{K=0_2^+}^+$	2_1^+	0.6(2)	114	2.7
	3^-	4_1^+	2_1^+	0.09(4)	0.04	0.54
2^-	2^-	$2_{K=0_2^+}^+$	2_1^+	0.28(7)	0.12	1.64
	2^-	2_γ^+	2_1^+	1.2(6)	3.8	0.9
	2^-	3_γ^+	2_γ^+	0.8(5)	0.3	0.8
	3^-	4_1^+	2_1^+	0.31(9)	0.07	0.89
	3^-	$2_{K=0_2^+}^+$	2_1^+	≃0.2	48	0.05
	3^-	2_γ^+	2_1^+	<1.1	0.01	1.8

other is only 1-f description from [12]. Although, the general pattern is similar, the *spdf* calculation describes better the position of the $K = 0_2^+$ band (lower than $K = 2_\gamma^+$). In order to see the effect on the calculated $B(E1)$ branching ratios, in the table is presented a full comparison of the two calculations with all the experimentally known $B(E1)$ branching ratios in ^{230}Th. The two calculations agree with the experimental values except those when one of the transition is to the $K = 0_2^+$ band when both sets fail to reproduce the data.

In lighter nuclei where the $K = 0_2^+$ band is known, ^{222,224}Ra and ^{226,228}Th (see Fig. 2), the 1-pf calculations with the parameters presented in Fig. 1 predict overly low 0_2^+ states. However, a slight change in the parameters improves the agreement, but the lack of data on other non-yrast states does not permit a definite answer.

4. CONCLUSION

Extensive numerical studies show that by adding only 1-pf boson to the usual *sd* space of the IBA, with smooth varying parameters, we obtained a consistent picture (except, maybe, the 0_2^+ states) over the entire nuclear region of the light actinides. In comparison with only 1-f boson, the addition of 1-p boson does not change the essential features of the agreement with the data, at least for deformed nuclei as ^{230}Th.

ACKNOWLEDGMENTS

I am grateful to Dimitri Kusnezov for collaboration in the research summarized here. Valuable discussions with R. Casten are gratefully acknowledged. Work supported by the USDOE by grants nos. DE-FG02-91ER-40609 and DE-FG02-88ER-40417.

REFERENCES

1. P. A. Butler and W. Nazarewicz, Rev. Mod. Phys. **68**, 349 (1996).
2. J. Engel and F. Iachello, Phys. Rev. Lett. **54**, 1126 (1985); Nucl. Phys. A **472**, 61 (1987).
3. (a) E. G. Nadjakov and I. N. Mikhailov, J. Phys. G **13**, 1221 (1987); (b) D. Kusnezov, J. Phys. A **22**, 4271 (1989); **23**, 5673 (1990).
4. D. Kusnezov and F. Iachello, Phys. Lett. B **209**, 420 (1988).
5. T. Otsuka and M. Sugita, Phys. Lett. B **209**, 140 (1988).
6. V. S. Lac and I. Morrison, Nucl. Phys. A **581**, 73 (1995).
7. M. Sugita, T. Otsuka, and P. von Brentano, Phys. Lett. B **389**, 642 (1996).
8. A. F. Diallo *et al.,* Ann. Phys. (N.Y.) **279**, 81 (2000).
9. D. Kusnezov, *Computer Code OCTUPOLE* (unpublished).
10. W. Kurcewicz *et al.,* Nucl. Phys. A **270**, 175 (1976).
11. M. Wieland *et al.,* Phys. Rev. C **46**, 2628 (1992).
12. P. D. Cottle and N. V. Zamfir, Phys. Rev. C **58**, 1500 (1998).

Physics of Atomic Nuclei, Vol. 64, No. 6, 2001, pp. 1064–1068. From Yadernaya Fizika, Vol. 64, No. 6, 2001, pp. 1139–1143.
Original English Text Copyright © 2001 by Sambataro.

Analysis of the $SU(3)$ Model in a Multistep Variational Approach[*]

M. Sambataro[**]

Istituto Nazionale di Fisica Nucleare, Sezione di Catania, Italy

Received September 11, 2000

Abstract—We discuss a multistep variational approach to collective excitations. The approach is developed in a boson formalism (bosons representing particle—hole excitations) and based on an iterative sequence of diagonalizations in subspaces of the full boson space. The purpose of these diagonalizations is that of searching for the best approximation of the ground state of the system. The procedure also leads us to define a set of excited states and, at the same time, of operators which generate these states as a result of their action on the ground state. We examine the cases in which these operators carry one-particle—one-hole and up to two-particle—two-hole excitations. We also explore the possibility of associating bosons to Tamm—Dancoff excitations and of describing the spectrum in terms of only a selected group of these. Tests within an exactly solvable three-level model are provided. © *2001 MAIK "Nauka/Interperiodica"*.

1. INTRODUCTION

Developing reliable microscopic approaches for the description of correlations in quantum many-body systems is a field of active research in various branches of physics. A preeminent role in this field has been traditionally played by the random phase approximation (RPA) [1]. Over the years, however, several attempts [2—16] have also been made to overcome the natural limitations of this theory related, in particular, to its lack of an internal consistency.

In a recent publication [16], with reference to the β-decay physics and working in a quasiparticle formalism, we have discussed an approach aiming at improving the quality of the standard quasiparticle RPA calculations usually made in this field. In this contribution, we present an evolution of this method which we believe to be more effective and simpler to apply in realistic cases.

The approach is developed in a boson formalism. As a preliminary step, then, a boson space will be defined where bosons identify particle—hole excitations and a mapping procedure will allow the transformation of fermion operators onto their images in this boson space. Similarly to the previous work [16], the basic point of the approach will consist in searching first for the best approximation of the ground state. Differently from the mentioned case, however, this will be achieved by means of an iterative sequence of diagonalizations in subspaces of the full boson space. As a further and important difference from the case of [16], as a result of this sequence of diagonalizations, a set of operators will also be generated which by acting on the ground state of the system will define a set of excited states. We will consider two cases: the case in which these operators carry only one-particle—one-hole ($1p$—$1h$) excitations and the case in which they include up to two-particle—two-hole ($2p$—$2h$) excitations. The comparison with exact calculations within a schematic model will allow us to judge the quality of the approximations. As a schematic model we have chosen the $SU(3)$ model [17—19].

In the second part of the contribution, we will reformulate the fermion—boson correspondence and identify bosons with properly chosen *collective* particle—hole excitations. Then, what is more interesting, we will explore the possibility of describing at least partially the spectrum of the system in terms of only a selected group of these bosons.

The article is organized as follows. In Section 2, we will describe the basic points of the procedure. In Section 3, we will provide some applications within the $SU(3)$ model. In Section 4, we will examine the case of bosons as collective particle—hole excitations. Finally, in Section 5, we will summarize the results and give some conclusions.

2. THE PROCEDURE

To simplify the notation, we will illustrate the procedure directly within the exactly solvable model which has been used for our tests. This model, the so-called $SU(3)$ model, was first discussed by Li *et al.* [17] and has been used more recently by Matsuo and Matsuyanagi [18] and Takada *et al.* [19] to test some approximation schemes. The model consists of three 2Ω-fold degenerate single-particle shells which are

---

[*] This article was submitted by the author in English.

[**] e-mail: `samba@ct.infn.it`

occupied by 2Ω particles. In the absence of interaction, then, the lowest level is completely filled, while the others are empty. This state, the Hartree–Fock (HF) state of the system, is denoted by $|0\rangle$. A single-particle state is specified by a set of quantum numbers (j, m), where j stands for the shell ($j = 0,\ 1,\ 2$) and m specifies the 2Ω substates within the shell. The creation and annihilation operators of a fermion in a state (j, m) are defined by $a^\dagger_{jm}$ and a_{jm}, respectively.

Let us consider the operators

$$K_{ij} = \sum_{m=1}^{2\Omega} a^\dagger_{im} a_{jm} \quad (i, j = 0, 1, 2). \tag{1}$$

These operators satisfy the Lie algebra of the group *SU*(3)

$$[K_{ij}, K_{kl}] = \delta_{jk} K_{il} - \delta_{il} K_{kj}. \tag{2}$$

It is assumed that the Hamiltonian of the model is written in terms of the generators K_{ij} only and contains up to two-body interactions. Its form is [19]

$$\begin{aligned} H_F = \sum_{i=1,2} \epsilon(i) K_{ii} + \sum_{i,j=1,2} V_x(i,j) K_{i0} K_{0j} \\ + \frac{1}{2} \sum_{i,j=1,2} V_v(i,j)(K_{i0}K_{j0} + K_{0j}K_{0i}) \\ + \sum_{i,j,k=1,2} V_y(i,j,k)(K_{i0}K_{jk} + K_{kj}K_{0i}), \end{aligned} \tag{3}$$

where the coefficients are real and obey the symmetry conditions $V_x(i,j) = V_x(j,i)$ and $V_v(i,j) = V_v(j,i)$. The eigenstates of H_F are constructed by diagonalizing it in the space

$$F = \left\{ |n_1 n_2\rangle = \frac{1}{\sqrt{\mathcal{N}_{n_1 n_2}}} (K_{10})^{n_1} (K_{20})^{n_2} |0\rangle \right\}_{0 \le n_1 + n_2 \le 2\Omega}, \tag{4}$$

where $\mathcal{N}_{n_1 n_2}$ are normalization factors. As in [16], we will work in a boson formalism. To begin, then, we define the boson space

$$B = \left\{ |n_1 n_2) = \frac{1}{\sqrt{n_1! n_2!}} (b^\dagger_1)^{n_1} (b^\dagger_2)^{n_2} |0) \right\}_{0 \le n_1 + n_2 \le 2\Omega}, \tag{5}$$

where the operators $b^\dagger_i$ obey standard boson commutation relations

$$[b_i, b^\dagger_j] = \delta_{ij}, \qquad [b_i, b_j] = 0, \tag{6}$$

and $|0)$ is the boson vacuum. As is evident from a glance at (4) and (5), a one-to-one correspondence exists between the states of F and B, the boson operators $b^\dagger_i$ playing the role of the excitation operators K_{i0} and the boson vacuum $|0)$ replacing the HF state $|0\rangle$. As anticipated in the Introduction, however, in Section 4 we will also examine a different correspondence and so a different meaning to attribute to these boson operators.

The mapping procedure to construct boson images of fermion operators is the same discussed in previous works [12, 16], and it is based on the requirement that corresponding matrix elements in F and B be equal. The procedure is, therefore, of Marumori-type. In correspondence with the Hamiltonian H_F (3), then, we introduce a Hermitian boson Hamiltonian H_B which we truncate at five-boson terms. This has therefore the general form

$$\begin{aligned} H_B = \alpha + \sum_i \beta_i (b^\dagger_i + \text{h.c.}) + \sum_{ij} \gamma_{ij} b^\dagger_i b_j + \sum_{i \le j} \phi_{ij} (b^\dagger_i b^\dagger_j + \text{h.c.}) \\ + \sum_{i \le j} \sum_k \epsilon_{ijk} (b^\dagger_i b^\dagger_j b_k + \text{h.c.}) + \sum_{i \le j} \sum_{k \le l} \delta_{ijkl} b^\dagger_i b^\dagger_j b_k b_l \\ + \sum_{i \le j \le k} \sum_l \rho_{ijkl} (b^\dagger_i b^\dagger_j b^\dagger_k b_l + \text{h.c.}) + \sum_{i \le j \le k} \sum_{l \le m} \tau_{ijklm} (b^\dagger_i b^\dagger_j b^\dagger_k b_l b_m + \text{h.c.}). \end{aligned} \tag{7}$$

To illustrate the iterative sequence of diagonalizations on which our approach is based, we start by introducing an arbitrary boson state $|\Psi_0^{(0)})$. We consider this as a zeroth-order approximation of the ground state, and we assume $|\Psi_0^{(0)}) = (1/\sqrt{3})(|0) + b^\dagger_1|0) + b^\dagger_2|0))$. Let us then consider the space

$$B^{(1)} \equiv \left\{ |\Psi_0^{(0)}), b^\dagger_i |\Psi_0^{(0)}), b_i |\Psi_0^{(0)}) \right\}_{i=1,2} \tag{8}$$

and diagonalize H_B in this space. $B^{(1)}$ is, in general, considerably smaller than the full boson space B.

In our calculations, for instance, we have assumed $2\Omega = 10$ and this implies that the space B can have up to ten-boson states, while $B^{(1)}$ contains only up to two-boson states. However, if $|\Psi_0^{(1)})$ denotes the lowest eigenstate resulting from this diagonalization, one can only expect that $|\Psi_0^{(1)})$ will provide an approximation of the ground state better than (or, at worst, equal to) $|\Psi_0^{(0)})$. This is due to the fact that we are allowing the new state to have more components than $|\Psi_0^{(0)})$ and that the coefficients of $|\Psi_0^{(1)})$ are fixed to guarantee the lowest energy of the state. We define $|\Psi_0^{(1)})$ as the first-order approximation of the ground state.

As a next step, let us consider the space

$$B^{(2)} \equiv \left\{|\Psi_0^{(1)}), b_i^\dagger|\Psi_0^{(1)}), b_i|\Psi_0^{(1)})\right\}_{i=1,2} \tag{9}$$

and diagonalize H_B in this space. If $|\Psi_0^{(2)})$ is the lowest eigenstate resulting from this diagonalization, the above arguments lead us to expect that also $|\Psi_0^{(2)})$ will be better than $|\Psi_0^{(1)})$. We define $|\Psi_0^{(2)})$ as the second-order approximation of the ground state. The procedure can go on as many times as one wishes. By performing a sequence of diagonalizations in spaces whose dimensionality remains unchanged (and much smaller than that of the full boson space), one can construct approximations of the ground state which improve step-by-step.

It turns out to be interesting to reformulate the procedure just described as follows. Let us define the operator

$$(Q_0^\dagger)^{(\nu)} = \sum_i X_i^{(\nu)} b_i^\dagger + \sum_i Y_i^{(\nu)} b_i + Z^{(\nu)}. \tag{10}$$

It is, then,

$$|\Psi_0^{(0)}) = (Q_0^\dagger)^{(0)}|0) \tag{11}$$

with $X_i^{(0)} = Z^{(0)} = 1/\sqrt{3}$ (the coefficients $Y_i^{(0)}$ remain undetermined in this case). Similarly, one can define an operator $(Q_0^\dagger)^{(1)}$ such that

$$|\Psi_0^{(1)}) = (Q_0^\dagger)^{(1)}|\Psi_0^{(0)}) \tag{12}$$

and so on for all other approximations. In general, if $|\Psi_0^{(k)})$ denotes the kth approximation of the ground state, one can write

$$\begin{aligned}|\Psi_0^{(k)}) &= (Q_0^\dagger)^{(k)}|\Psi_0^{(k-1)}) \\ &= (Q_0^\dagger)^{(k)}(Q_0^\dagger)^{(k-1)}\cdots(Q_0^\dagger)^{(0)}|0).\end{aligned} \tag{13}$$

Therefore $|\Psi_0^{(k)})$ is a product of $k+1$ operators $Q^\dagger$ of the type (10), k corresponding to the k diagonalizations in the $B^{(k)}$ subspaces plus the operator $(Q_0^\dagger)^{(0)}$ corresponding to the starting ansatz $|\Psi_0^{(0)})$. Concerning this state, some comments are necessary to justify its use. In principle, one could have started with a diagonalization similar to all the other ones, namely, in a space of the type (8) where $|\Psi_0^{(0)}) \equiv |0)$. However, the coefficients β_i of the boson Hamiltonian (7) are nothing but the matrix elements of H_F between the HF state $|0\rangle$ and the $1p$–$1h$ states $K_{i0}|0\rangle$. These coefficients turn out to be zero in our model, and the same would happen in a realistic case. In consequence of that, no mixing is possible between the states $|0)$ and $b_j^\dagger|0)$, and so a diagonalization in the space $\{|0), b_j^\dagger|0)\}$ could generate (what indeed happens in our model) the boson vacuum $|0)$ as the lowest eigenstate. This would lead to a crash of the iterative mechanism.

Once a sufficient number of iterations have been performed, the procedure is expected to reach convergence. If this is the case, any diagonalization beyond a given one, let us say the kth one, will have to leave the results unmodified. This necessarily implies that the operator $(Q_0^\dagger)^{(k+1)}$ which will emerge from the $(k+1)$th diagonalization will have coefficients

$$X_i^{(k+1)} = Y_i^{(k+1)} = 0, \qquad Z^{(k+1)} = \pm 1. \tag{14}$$

Convergence of the procedure therefore means convergence towards these values of the coefficients X, Y, and Z.

As a result of the same $(k+1)$th diagonalization, besides the operator $(Q_0^\dagger)^{(k+1)}$, one will also obtain the operators $(Q_i^\dagger)^{(k+1)}$ associated with the remaining eigenstates. The number of these eigenstates is (up to) $2N$, where N is the number of the $1p$–$1h$ excitations ($N = 2$ in our model). If we call $|\mathrm{gs})$ our best approximation for the ground state, i.e., $|\mathrm{gs}) \equiv |\Psi_0^{(k)})$, these further eigenstates can be written as

$$|\Psi_i^{(k+1)}) \equiv (Q_i^\dagger)^{(k+1)}|\mathrm{gs}) \qquad (i = 1, ..., 2N). \tag{15}$$

This procedure therefore leads us to define a set of operators $(Q_i^\dagger)^{(k+1)}$ whose action on the ground state gives rise to a set of excited states which, considering the nature of the operators (10), all carry excitations of the type $1p$–$1h$.

Of course, the same procedure discussed so far can be extended in a natural way to include $2p$–$2h$ excitations as well. The basic difference consists in performing each diagonalization of the iterative sequence in spaces of the type

$$B^{(k)} = \left\{|\Psi_0^{(k-1)}), b_i^\dagger|\Psi_0^{(k-1)}), b_i^\dagger b_j^\dagger|\Psi_0^{(k-1)}), b_i|\Psi_0^{(k-1)}), b_i b_j|\Psi_0^{(k-1)})\right\}_{i\leq j=1,2}. \tag{16}$$

Moreover, differently from the $1p$–$1h$ case, there is no more need for an initial ansatz for the ground state. The iterative procedure simply begins by performing a diagonalization in a space $B^{(1)}$ of the form (16) where $|\Psi_0^{(0)}) \equiv |0)$.

3. RESULTS

The calculations we are going to describe refer to the following choice of the parameters: $2\Omega = 10$, $\epsilon(1) = \epsilon$, $\epsilon(2) = 1.5\epsilon$, $V_x(i,j) = -2\chi$, $V_v(i,j) = \frac{1}{2}\chi$, and $V_y(i,j,k) = -\frac{3}{4}\chi$ $(i,j,k,= 1,2)$. Both ϵ and χ are parameters expressed in units of energy. Due to space reasons, we are forced to reduce considerably the analysis of the results. A complete description of the numerical tests can be found in [20].

In Fig. 1, we show the energies calculated according to the procedure described in (8)–(15) and so with $Q^\dagger$ operators carrying only $1p$–$1h$ excitations. In the lower part, we plot the ground state energies corresponding to different orders of approximation as indicated by the numbers which label the dash-dotted curves. For comparison, we plot (solid curve) the energies which result from the diagonalization of H_B in B since this represents the best one can hope to reproduce in this approach. These energies are found to be very close to the exact ones [20]. A clear improvement of the quality of the approximation is observed in correspondence with the increasing of its order.

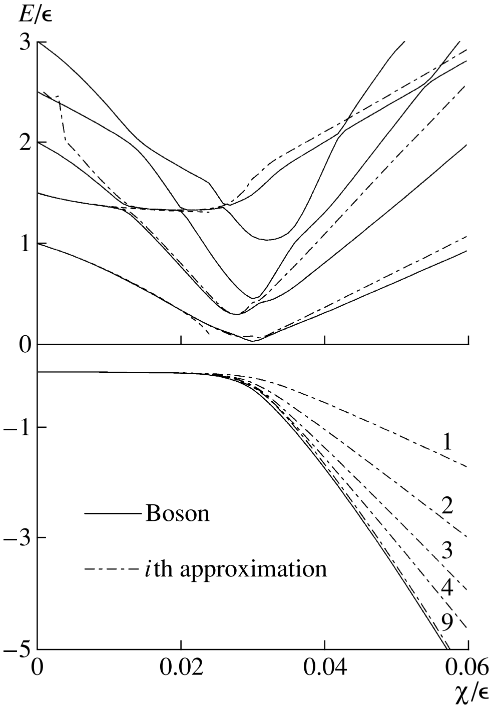

Fig. 1. Ground state energy (lower panel) and excitation energies of the lowest five states (upper panel) as functions of the strength χ/ϵ. The solid curves are obtained by diagonalizing H_B (7) in B (5), while the dash-dotted curves are obtained with the procedure described in Section 2 (only $1p$–$1h$ excitations are included). The numbers label different orders of approximation. The dashed curves (upper pannel) show the RPA one-phonon energies.

Still in Fig. 1, upper part, the dash-dotted curves show the spectrum obtained within this approach (the spectrum is found in correspondence with the best approximation of the ground state shown in the lower part of the figure). Also shown are the energies of the two RPA states (dashed curves). RPA undergoes a collapse as soon as the ground state energy starts deviating significantly from zero ($\chi/\epsilon \approx 0.024$). The same states, but within the whole range of χ/ϵ, are well reproduced within the present approach.

Results shown in Fig. 2 refer to calculations which include up to $2p$–$2h$ excitations [see (16)]. As compared to results of Fig. 1, one observes a faster convergence of the procedure and a quite good agreement for all low-lying excited states.

4. BOSONS AS COLLECTIVE PARTILCLE–HOLE EXCITATIONS

When performing the boson mapping, we have established a one-to-one correspondence between the states $|n_1 n_2\rangle$ and $|n_1 n_2)$ defined in (4) and (5), respectively. In such a correspondence, bosons $b_j^\dagger$ are images of the $1p$–$1h$ operators K_{j0}. However, as already anticipated, this is not the only possibility of correspondence. To show an alternative choice, let us proceed as in Takada *et al.* [19] and first define the Tamm–Dancoff (TD) phonon operator

$$V_\lambda^\dagger = \frac{1}{\sqrt{2\Omega}} \sum_i v_i^{(\lambda)} K_{i0}. \tag{17}$$

In terms of these TD operators we construct the space

$$\left\{\overline{|n_1 n_2\rangle} = \frac{1}{\sqrt{\mathcal{N}'_{n_1 n_2}}} (V_1^\dagger)^{n_1} (V_2^\dagger)^{n_2} |0\rangle\right\}_{0\leq n_1+n_2\leq 2\Omega}. \tag{18}$$

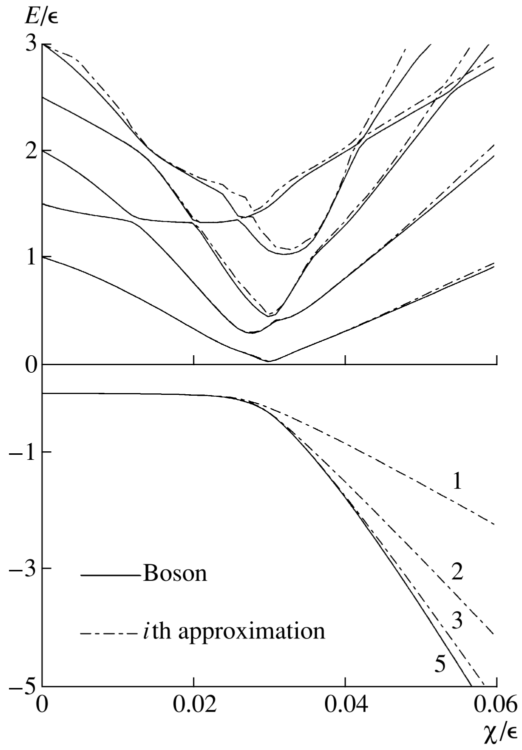

Fig. 2. The same as in Fig. 1, but the dash-dotted curves refer now to calculations involving up $2p$–$2h$ excitations.

This space is the same as (4) but just a different representation. Therefore, if we establish a one-to-one correspondence between states (18) and (5) and we reconstruct the boson image of H_F, the new boson Hamiltonian will have different coefficients but its spectrum will remain unchanged. In this new representation, bosons correspond to *collective* particle–hole excitations and so play a role very similar to that of the standard $s, d, \ldots$ bosons in the Interacting Boson Model picture [21] (where they are meant to represent collective particle–particle excitations). As in this case, then, it is natural to expect that the structure of the low-lying part of the spectrum may be described in terms of only a selected group of collective bosons.

Space reasons force us again to omit a detailed discussion of this important point, for which we address to [20]. Here, we simply say that in this model, by introducing only one boson in correspondence with the lowest TD excitation and repeating the calculations illustrated in Section 2, we have obtained a surprisingly good description of the low-lying levels of the spectrum.

5. SUMMARY AND CONCLUSIONS

We have presented a multistep variational approach for the study of many-body correlations. The approach has been developed in a boson formalism (bosons representing particle–hole excitations) and based on an iterative sequence of diagonalizations in subspaces of the full boson space. The purpose of these diagonalizations has been that of searching for the best approximation of the ground state of the system. The procedure has also led us to define a set of excited states and, at the same time, of operators generating these states as a result of their action on the ground state. We have considered two cases: (i) the case in which these operators carried only $1p$–$1h$ excitations and (ii) the case in which also $2p$–$2h$ excitations were included. The approach has been tested within an exactly solvable three-level model and has provided encouraging results.

We have also reformulated the fermion–boson correspondence and identified bosons with TD phonons. The possibility of selecting a restricted set of collective particle–hole excitations and therefore of constructing the boson space only in terms of the corresponding bosons appears to be quite appealing. It may represent, in fact, an effective way to reduce the dimensionalities of the system and so to lead to a much simplified application of the procedure to realistic cases.

REFERENCES

1. P. Ring and P. Schuck, *The Nuclear Many-Body Problem* (Springer-Verlag, New York, 1980).
2. Ken-ji Hara, Prog. Theor. Phys. **32**, 88 (1964).
3. D. J. Rowe, Phys. Rev. **175**, 1283 (1968).
4. J. da Providencia, Phys. Rev. C **2**, 1682 (1970).
5. J. Dukelsky and P. Schuck, Nucl. Phys. A **512**, 466 (1990).
6. D. Janssen and P. Schuck, Z. Phys. A **339**, 43 (1991).
7. A. Klein *et al.,* Nucl. Phys. A **535**, 1 (1991).
8. F. Catara *et al.,* Nucl. Phys. A **579**, 1 (1994).
9. J. Dukelsky and P. Schuck, Phys. Lett. B **387**, 233 (1996).
10. E. R. Marshalek, Phys. Rev. C **36**, 2538 (1987).
11. D. Beaumel and Ph. Chomaz, Ann. Phys. (N.Y.) **213**, 405 (1992).
12. M. Sambataro and J. Suhonen, Phys. Rev. C **56**, 782 (1997).
13. F. Catara *et al.,* Phys. Rev. B **54**, 17536 (1996).
14. F. Catara *et al.,* Phys. Rev. B **58**, 16070 (1998).
15. M. Sambataro and N. Dinh Dang, Phys. Rev. C **59**, 1422 (1999).
16. M. Sambataro, Phys. Rev. C **59**, 2056 (1999).
17. S. Y. Li *et al.,* J. Math. Phys. **11**, 975 (1970).
18. M. Matsuo and K. Matsuyanagi, Prog. Theor. Phys. **74**, 288 (1985).
19. K. Takada *et al.,* Nucl. Phys. A **485**, 189 (1988).
20. M. Sambataro, Phys. Rev. C **60**, 064320 (1999).
21. F. Iachello and A. Arima, *The Interacting Boson Model* (Cambridge Univ. Press, Cambridge, 1991).

Physics of Atomic Nuclei, Vol. 64, No. 6, 2001, pp. 1069–1075. From Yadernaya Fizika, Vol. 64, No. 6, 2001, pp. 1144–1150.
Original English Text Copyright © 2001 by Vdovin, Storozhenko.

TFD Extension of a Self-Consistent RPA to Finite Temperatures*

A. I. Vdovin** and **A. N. Storozhenko*****

Joint Institute for Nuclear Research, Dubna, Moscow oblast, 141980 Russia

Received October 11, 2000

Abstract—The self-consistent RPA (SCRPA) developed by Schuck and coauthors is extended to finite temperatures. The corresponding equations are derived by using the formalism of thermofield dynamics. The intrinsic energy of a system is calculated as the expectation value of the Hamiltonian with respect to a T-dependent thermal vacuum state for a thermal-phonon operator. A nonvanishing number of thermal quasiparticles in the vacuum state are assumed. By virtue of the assumption, the thermal Hartree–Fock (HF) equations appear to be coupled to the equations of motion for phonon variables. The thermal occupation numbers are also calculated in a consistent way with the energies of the HF quasiparticles. The approximation is applied to the two-level Lipkin model. Advantages of the thermal SCRPA (TSCRPA) are most obvious at temperatures near the phase-transition point. In the TSCRPA, the phase transition occurs at lower T than in other approximations. Moreover, within the TSCRPA, a statistical behavior of the Lipkin model is described with an appropriate accuracy at any T even if the HF transformation parameter is kept fixed at a value corresponding to the "spherical" phase of the HF field. *© 2001 MAIK "Nauka/Interperiodica".*

1. INTRODUCTION

The random-phase approximation (RPA) is a standard theoretical tool for studying collective vibrations in nuclei. This approximation has known many generalizations from the so-called extended RPA developed by Ken-ji Hara and Rowe [1]. One of the recent and seemingly the most consistent improvements of the RPA is the self-consistent RPA (SCRPA) proposed by Schuck and coauthors [2, 3]. There is no place here to discuss all ingredients of numerous versions of the RPA, and we point out only the most important one, a redefinition of the RPA vacuum state, thus incorporating new kinds of particle–hole or particle–particle (hole–hole) correlations in it.

While the aforementioned new approximations were carefully examined for cold nuclei, much less is known about the influence of new correlations on the statistical (thermal) properties of nuclei. This problem was studied in [4–7]. A thermal version of the extended RPA (referred to as a thermal renormalized RPA or TRRPA) was proposed and studied in detail elsewhere [4, 5]. Moreover, a more sophisticated version of the TRRPA was presented in [6, 7], where the coupling of Hartree–Fock (HF) variables to collective ones was taken into account. In this respect, this approximation is quite close to the aforementioned SCRPA.

In this article, we present a fully consistent version of a thermal self-consistent RPA (TSCRPA), thus extending the ideas developed in [2, 6]. As before [4–7], we use the formalism of thermofield dynamics (TFD) [8]. For the first time, it was applied to a nuclear-structure problem in [9]. This is a real-time formalism—i.e., in contrast to the method of thermal (Matsubara) Green's functions, temperature and time are independent variables within TFD. The formalism is convenient for our present purposes because temperature effects arise explicitly as T-dependent vertices, thus providing a good starting point for various approximations. Moreover, the TFD approach is the most powerful when combined with variational methods, which are our main tools in the present consideration.

2. GENERAL SCHEME OF TSCRPA

We consider a system of N fermions that is governed by a two-body interaction and write the Hamiltonian as

$$H = \sum_{12} t_{12} a_1^+ a_2 + \frac{1}{4} \sum_{1234} V_{1234} a_1^+ a_2^+ a_4 a_3, \quad (2.1)$$

where a^+ and a are the fermion creation and annihilation operators, respectively. The one-body part of the Hamiltonian, $t_{12} = T_{12} - \lambda\delta_{12}$, contains the kinetic energy matrix T_{12} and the chemical potential λ.

In order to describe, at thermal equilibrium ($T \neq 0$), a system whose behavior is governed by the

---

[*] This article was submitted by the authors in English.

[**] e-mail: `vdovin@thsun1.jinr.ru`

[***] e-mail: `astorozh@thsun1.jinr.ru`

1063-7788/01/6406-1069$21.00 © 2001 MAIK "Nauka/Interperiodica"

Hamiltonian in (2.1), it is necessary to find a minimum of the model grand canonical thermodynamic potential

$$\Omega_{\rm mod}(H) = \Omega_0 + \langle\langle H - H_0\rangle\rangle_0, \qquad (2.2)$$

where

$$\Omega_0 = \langle\langle H_0\rangle\rangle_0 - TS_0$$

is the probing grand canonical thermodynamic potential of a model N-fermion system characterized by the Hamiltonian H_0 and the entropy S_0 [10]. The statistical average $\langle\langle\ \ \rangle\rangle_0$ is taken with respect to the grand partition function of this model system. In the thermal HF approximation (THFA), H_0 is chosen as the Hamiltonian of a system of noninteracting quasiparticles moving in a common mean field, the corresponding creation and annihilation operators being denoted by α_i^+ and α_i, respectively. Then, the entropy is

$$S_0 = -\sum_1 \left[n_1 \ln(n_1) + (1 - n_1)\ln(1 - n_1)\right], \qquad (2.3)$$

where $n_1 = \langle\langle \alpha_1^+ \alpha_1\rangle\rangle_0$ is the quasiparticle density matrix.

In terms of TFD, the statistical average $\langle\langle\ \ \rangle\rangle_0$ is evaluated as a matrix element with respect to the thermal vacuum state $|0(T)\rangle$ of the model system. The vacuum state $|0(T)\rangle$ is an eigenstate of the thermal Hamiltonian $\mathcal{H}_0 = H_0(\alpha_i^+, \alpha_i) - \widetilde{H}_0(\widetilde{\alpha}_i^+, \widetilde{\alpha}_i)$ with zero eigenvalue. It controls the thermal behavior of the system. To find the "best" H_0, one makes a unitary transformation D from the operators a_1^+ and a_1 characterizing the initial ("bare") fermions to the quasiparticle operators α_1^+ and α_1,

$$a_1^+ = \sum_2 D_{21}^* \alpha_2^+, \qquad a_1 = \sum_2 D_{21}\alpha_2, \qquad (2.4)$$

and then finds a minimum of $\Omega_{\rm mod}$ with respect to small variations of the coefficients D_{ik}. With expression (2.3) for the entropy, one also gets the Fermi–Dirac formula for thermal occupation numbers of the HF quasiparticles,

$$n_1 = \left[1 + \exp\left(\frac{E_1}{T}\right)\right]^{-1}, \qquad (2.5)$$

where E_1 is the HF quasiparticle energy.

The state $|0(T)\rangle$ appears to be a vacuum for the operators of the so-called thermal quasiparticles defined as

$$\beta_1 = x_1\alpha_1 - y_1\widetilde{\alpha}_1^+, \qquad (2.6)$$
$$\widetilde{\beta}_1 = x_1\widetilde{\alpha}_1 + y_1\alpha_1^+,$$

where $x_1^2 + y_1^2 = 1$ and $y_1^2 = n_1$ from (2.5). The unitary transformation $\{x, y\}$ is referred to as the thermal Bogolyubov transformation.

Usually, the THFA basis $\{\beta_1, \beta_1^+, \widetilde{\beta}_1, \widetilde{\beta_1^+}\}$ is used to build the thermal RPA (TRPA) scheme that includes some long-range correlations of a motion of thermal quasiparticles. Within TRPA, a thermal vacuum state $|\Psi_0(T)\rangle$ and excited states $|\Psi_\nu(T)\rangle$ of a heated system are defined by the relations

$$|\Psi_\nu(T)\rangle = Q_\nu^+|\Psi_0(T)\rangle, \quad Q_\nu|\Psi_0(T)\rangle = 0, \quad (2.7)$$

where the thermal phonon creation operator Q_ν^+ is

$$Q_\nu^+ = \sum_{12} \psi_{12}^\nu \beta_1^+ \widetilde{\beta}_2^+ - \phi_{12}^\nu \widetilde{\beta}_2 \beta_1. \qquad (2.8)$$

To find the energy ω_ν and the amplitudes ψ_{12} and ϕ_{12}, use is usually made of the equation-of-motion method. A feature peculiar to the TRPA (like RPA) is the additional assumption that the operators Q_ν^+ and Q_ν obey bosonic commutation rules, which is equivalent to averaging with respect to the thermal HF vacuum state in the equations of motion. In this respect, the THFA and the TRPA are consistent with each other. Moreover, the vacuum states $|0(T)\rangle$ and $|\Psi_0(T)\rangle$ are related by a unitary transformation, and, within the TRPA, the thermal occupation numbers (2.5) are identical to those within the THFA. In addition, the THFA equations are decoupled from those of TRPA.

In order to retain the aforementioned consistency of the two stages of our treatment of collective vibrations in a heated N-fermion system, one should use a new vacuum state already in the THFA if new correlations are taken into account in the equations of motion. This leads us to a generalization of the THFA. Actually, this was proposed in [2] for the HF procedure at $T = 0$ and then in [6] for $T \neq 0$. Thus, one should calculate the expectation value of $H - H_0$ in $\Omega_{\rm mod}$ (2.2) over a correlated vacuum state $|\Psi_0(T)\rangle$ defined by (2.7) but not over $|0(T)\rangle$; that is, we propose to use a new $\Omega_{\rm mod}$,

$$\Omega_{\rm mod} = \langle\Psi_0(T)|H|\Psi_0(T)\rangle - TS. \qquad (2.9)$$

If $|\Psi_0(T)\rangle$ includes correlations beyond the TRPA, the quantity $\langle|H|\rangle$[1] appears to be dependent on thermal phonon variables [6] and the parameters of the HF transformation (2.4) can be determined only together with the amplitudes ψ_{12} and ϕ_{12}. To evaluate (2.9), we need to know the properties of the vacuum state $|\Psi_0(T)\rangle$ and an expression for the entropy S, which can also differ from expression (2.3).

To determine the properties of $|\Psi_0(T)\rangle$, we must diagonalize $\mathcal{H}$. To this aim, let us first write the

---

[1] Hereafter, the expectation values are implied to be taken over the thermal vacuum state defined in (2.7), unless otherwise stated.

thermal Hamiltonian $\mathcal{H}$ in terms of thermal quasiparticles. At this stage, we only assume that the transformations D (2.4) and $\{x\,, y\}$ (2.6) are unitary.

The Hamiltonian $\mathcal{H}$ is equal to the sum of the terms $\mathcal{H}_{ik}$, each consisting of i creation operators and k annihilation operators for thermal quasiparticles,

$$\begin{aligned}\mathcal{H} &= \mathcal{H}_{11} + \mathcal{H}_{22} + \mathcal{H}_{20} + \mathcal{H}_{02} \\ &+\mathcal{H}_{40} + \mathcal{H}_{04} + \mathcal{H}_{31} + \mathcal{H}_{13}. \end{aligned} \qquad (2.10)$$

Only the terms $\mathcal{H}_{11}, \mathcal{H}_{22}, \mathcal{H}_{40}$, and $\mathcal{H}_{04}$,

$$\begin{aligned}\mathcal{H}_{11} &= \sum_{12} \left(P_{12} + \sum_{3} y_3^2 U_{1323} \right) \qquad (2.11) \\ &\times (x_1 x_2 + y_1 y_2) \left(B_{12} - \widetilde{B}_{12} \right), \\ \mathcal{H}_{22} &= \sum_{1234} U_{1234} \left[(x_1 x_4 y_2 y_3 - x_2 x_3 y_1 y_4)\, A_{13}^{+} A_{42} \right. \\ &\left. +\frac{1}{4} (x_1 x_2 x_3 x_4 - y_1 y_2 y_3 y_4) \left(: B_{13} B_{24} - \widetilde{B}_{13} \widetilde{B}_{24} : \right) \right], \\ \mathcal{H}_{40} &= \sum_{1234} U_{1234} (x_1 x_2 y_3 y_4 - x_3 x_4 y_1 y_2)\, A_{13}^{+} A_{24}^{+}, \end{aligned}$$

$$\mathcal{H}_{40} = \mathcal{H}_{04}^{+},$$

are relevant to the present consideration. Here, we have used the newly defined bifermionic operators

$$\begin{aligned} A_{12}^{+} &= \widetilde{A}_{21}^{+} = \beta_1^{+} \widetilde{\beta}_2^{+}, \quad A_{12} = \widetilde{A}_{21} = \widetilde{\beta}_2 \beta_1, \\ B_{12} &= \beta_1^{+} \beta_2, \quad \widetilde{B}_{12} = \widetilde{\beta}_1^{+} \widetilde{\beta}_2. \end{aligned}$$

The coefficients P_{12} and U_{1234} are given by

$$P_{12} = \sum_{34} t_{34} D_{13}^{*} D_{24},$$

$$U_{1234} = \sum_{5678} V_{5678} D_{51}^{*} D_{62}^{*} D_{73} D_{84}.$$

At this stage, our main assumption is the relation [1, 4]

$$\begin{aligned} M_{1234} &= \langle| \left[A_{12}, A_{34}^{+} \right] |\rangle \qquad (2.12) \\ &= \langle| \delta_{13}\delta_{24} - \delta_{13} \widetilde{B}_{42} - \delta_{24} B_{31} |\rangle \\ &= \delta_{13}\delta_{24} (1 - q_1 - q_2) = \delta_{13}\delta_{24} (1 - q_{12}), \end{aligned}$$

where q_i is a c number to be determined. Formula (2.12) means that there is a nonvanishing number of thermal quasiparticles in the vacuum state $|\Psi_0(T)\rangle$,

$$\langle| B_{12} |\rangle = \langle| \widetilde{B}_{12} |\rangle = q_1 \delta_{12}\,.$$

The set of equations for the phonon amplitudes and energies then takes the form

$$\begin{aligned} &\sum_{34} \psi_{34}^{\nu} \langle| \left[A_{12}, \left[\mathcal{H}, A_{34}^{+} \right] \right] |\rangle \qquad (2.13) \\ &- \sum_{34} \phi_{34}^{\nu} \langle| \left[A_{12}, \left[\mathcal{H}, A_{34} \right] \right] |\rangle = \omega_\nu \sum_{34} \psi_{34}^{\nu} M_{1234}, \\ &\sum_{34} \psi_{34}^{\nu} \langle| \left[A_{12}^{+}, \left[\mathcal{H}, A_{34}^{+} \right] \right] |\rangle \\ &- \sum_{34} \phi_{34}^{\nu} \langle| \left[A_{12}^{+}, \left[\mathcal{H}, A_{34} \right] \right] |\rangle = -\omega_\nu \sum_{34} \phi_{34}^{\nu} M_{1234}. \end{aligned}$$

The normalization condition for the one-phonon state is

$$\begin{aligned} &\langle| Q_\nu Q_{\nu'}^{+} |\rangle \qquad (2.14) \\ &= \sum_{12} (1 - q_{12}) \left(\psi_{12}^{\nu} \psi_{12}^{\nu'} - \phi_{12}^{\nu} \phi_{12}^{\nu'} \right) = \delta_{\nu\nu'}. \end{aligned}$$

In deriving the coefficients of the phonon amplitudes ψ and ϕ in (2.13), one meets four types of two-body matrix elements, $\langle| A_{12}^{+} A_{34} |\rangle$, $\langle| A_{12} A_{34} |\rangle$, $\langle| A_{12}^{+} A_{34}^{+} |\rangle$, and $\langle| B_{12} B_{34} |\rangle$. To demonstrate what kinds of approximations we made in diagonalizing the thermal Hamiltonian, we display the expressions for these matrix elements

$$\begin{aligned} \langle| A_{12}^{+} A_{34} |\rangle &= \sum_{\nu} (1 - q_{12})(1 - q_{34})\, \phi_{12}^{\nu} \phi_{34}^{\nu}, \quad (2.15) \\ \langle| A_{12}^{+} A_{34}^{+} |\rangle &= \sum_{\nu} (1 - q_{12})(1 - q_{34})\, \phi_{12}^{\nu} \psi_{34}^{\nu}, \\ \langle| A_{12} A_{34} |\rangle &= \sum_{\nu} (1 - q_{12})(1 - q_{34})\, \psi_{12}^{\nu} \phi_{34}^{\nu}. \end{aligned}$$

To evaluate the fourth matrix element, an expansion in the complete phonon basis is used,

$$\begin{aligned} \langle| B_{12} B_{34} |\rangle &= \langle| B_{12} |\rangle \langle| B_{34} |\rangle \qquad (2.16) \\ &+ \sum_{\nu_1 \nu_2} \frac{\langle| B_{12} Q_{\nu_1}^{+} Q_{\nu_2}^{+} |\rangle \langle| Q_{\nu_2} Q_{\nu_1} B_{34} |\rangle}{\langle| Q_{\nu_2} Q_{\nu_1} Q_{\nu_1}^{+} Q_{\nu_2}^{+} |\rangle} \\ &+ \sum_{\nu_1 \nu_2 \nu_3 \nu_4} \ldots + \ldots, \end{aligned}$$

and only the two lowest order terms of (2.16) are taken (see [2]).

An equation for q_1 is derived by applying the number-operator method. Denoting the operator of the number of HF quasiparticles, $\widehat{N} = \sum_1 \alpha_1^{+} \alpha_1$, we obtain

$$\begin{aligned} q_1 &= \langle| B_{11} |\rangle = \langle| \beta_1^{+} \widetilde{\widehat{N}} \beta_1 |\rangle - \langle| \beta_1^{+} \widehat{N} \beta_1 |\rangle \qquad (2.17) \\ &= \sum_{2} (\langle| A_{12}^{+} A_{12} |\rangle - \langle| : B_{12} B_{21} : |\rangle). \end{aligned}$$

Equation (2.17) closes the set of equations for the thermal phonon characteristics. Moreover, expressions (2.15) and (2.16) must be used in evaluating $\langle| H |\rangle$ in Ω_{mod}. Because of coupling to collective variables, thermal quasiparticles cannot be treated as a system of independent ingredients and expression

(2.3) is not valid any more. Instead, we have to use a general formula for the entropy,

$$S = \int_0^T \frac{1}{T'} \frac{\partial \langle |H| \rangle}{\partial T'} dT'.$$

By using the same expression for $\langle |H| \rangle$ as in $\Omega_{\text{mod}}(H)$, we arrive at

$$S = -\sum_1 (1 - 2q_1) \left[x_1^2 \ln x_1^2 + y_1^2 \ln y_1^2 \right]. \quad (2.18)$$

The coupling of phonon and HF variables affects the HF basis and, hence, the thermal occupation numbers of HF quasiparticles. Therefore, we must include a determination of x and y in the general scheme requiring stability for $\Omega_{\text{mod}}(H)$ against small variations in x_1 and y_1. Unfortunately, we are forced to assume additionally that y_1^2 is the Fermi–Dirac function (2.5) of the HF energies and temperature.

Thus, the complete set of equations of the TSCRPA includes the variational equations for $D_{ik}, x_i,$ and y_i with Ω_{mod} (2.9), the equations of motion (2.13), and equations (2.17) for q_i.

3. APPLICATION OF THE TSCRPA TO THE LIPKIN MODEL

As an example of a system of N fermions that is governed by a two-body interaction, we consider the two-level Lipkin model [11, 12] in the version where only a pair of particles with parallel spins interact. The model system consists of N fermions distributed over two levels with a degeneracy multiplicity Ω ($\Omega = N$). The energies of the lower and the upper level are $-\varepsilon/2$ and $+\varepsilon/2$, respectively. Thus, the Hamiltonian has the form

$$H_{\text{L}} = \varepsilon J_z - \frac{1}{2} V \left(J_+ J_+ + J_- J_- \right), \quad (3.1)$$

where the operators of the quasispin, J, and of its components J_+, J_-, and J_z are defined as

$$J^2 = \frac{1}{2} \left(J_+ J_- + J_- J_+ \right) + J_z^2,$$

$$J_z = \frac{1}{2} \sum_{p=1}^{\Omega} \left(a_{2p}^+ a_{2p} - a_{1p}^+ a_{1p} \right),$$

$$J_+ = \sum_{p=1}^{\Omega} a_{2p}^+ a_{1p}, \quad J_- = (J_+)^+,$$

where the indices "1" and "2" label the lower and the upper level, respectively, and the index p numbers sublevels.

First, we make a unitary transformation to the HF quasiparticle operators. In the present particular case of a 2×2 transformation matrix, it is convenient to parameterize the coefficients D_{ik} as in [12],

$$D_{11} = D_{22} = \cos\theta, \qquad D_{12} = -D_{21} = \sin\theta.$$

The second step is the thermal Bogolyubov transformation (2.6), and the thermal Hamiltonian of the Lipkin model takes the form

$$\begin{aligned} \mathcal{H}_{\text{L}} &\equiv H_{\text{L}} - \widetilde{H}_{\text{L}} \quad (3.2) \\ &= \frac{1}{2} \left(B_2 - B_1 - \widetilde{B}_2 + \widetilde{B}_1 \right) \left[\varepsilon \cos 2\theta + 2V_1 N \right] \\ &\quad - \frac{V_2}{2} \left[A^+ A^+ + AA - \widetilde{A}^+ \widetilde{A}^+ - \widetilde{A}\widetilde{A} \right] \\ &\quad - \frac{V_1}{2} \left[A^+ A + AA^+ - \widetilde{A}^+ \widetilde{A} - \widetilde{A}\widetilde{A}^+ \right] \\ &\quad - \frac{V_1}{2} \left[(B_2 - B_1)^2 - \left(\widetilde{B}_2 - \widetilde{B}_1 \right)^2 \right], \end{aligned}$$

where we have introduced the notation

$$B_k = \sum_{p=1}^{\Omega} \beta_{kp}^+ \beta_{kp} \ (k = 1, 2), \ A^+ = \sum_{p=1}^{\Omega} \beta_{2p}^+ \widetilde{\beta}_{1p}^+,$$

$$\widetilde{A}^+ = \sum_{p=1}^{\Omega} \beta_{1p}^+ \widetilde{\beta}_{2p}^+, \quad V_1 = \frac{1}{2} V \left(y_1^2 - y_2^2 \right) \sin^2 2\theta,$$

$$V_2 = \frac{1}{2} V \left(y_1^2 - y_2^2 \right) \left(1 + \cos^2 2\theta \right).$$

The thermal Hamiltonian (3.2) can be diagonalized in the space of two one-phonon states

$$|\Psi_1(T)\rangle = Q_1^+ |\Psi_0(T)\rangle = \left(\psi^1 A_+ - \phi_1 A \right) |\Psi_0(T)\rangle,$$

$$|\Psi_2(T)\rangle = Q_2^+ |\Psi_0(T)\rangle = (\psi_2 \widetilde{A}^+ - \phi_2 \widetilde{A}) |\Psi_0(T)\rangle.$$

Their norms are

$$N (1 - 2q) \left(\psi_k^2 - \phi_k^2 \right) = 1, \quad k = 1, 2,$$

where q is defined as

$$q \equiv q_k = \frac{\langle |B_k| \rangle}{N} = \frac{\langle |\widetilde{B}_k| \rangle}{N}.$$

The equations of motion for the vectors $|\Psi_1(T)\rangle$ and $|\Psi_2(T)\rangle$ are decoupled, and their normalized solutions are

$$\omega = \omega_1 = -\omega_2 = \sqrt{M_1^2 - M_2^2}, \quad (3.3)$$

$$\psi_1^2 = \psi_2^2 = \frac{M_1 + \omega}{2\omega N (1 - 2q)} \equiv \psi^2, \quad (3.4)$$

$$\phi_1^2 = \phi_2^2 = \frac{M_1 - \omega}{2\omega N (1 - 2q)} \equiv \phi^2,$$

where

$$M_1 = \varepsilon \cos 2\theta$$
$$+ 3V_1 \left[N (1 - 2q) - 1 \right] - 6V_1 t_1 + 2V_2 t_2,$$
$$M_2 = -V_2 \left[N (1 - 2q) - 1 \right] - 6V_1 t_2 + 2V_2 t_1$$

with

$$t_1 = N\left(1-2q\right)\phi^2\left[1-\frac{8\psi^2}{R}\right],$$
$$t_2 = N\left(1-2q\right)\psi\phi.$$

Equation (2.17) for q takes the form

$$q = \phi^2\left(1-2q\right)^2\left[1+\frac{4\psi^2}{R}\right]+q^2-\frac{q}{N}, \qquad (3.5)$$

where the norm of a two-phonon state, R, can be found from the equation

$$R = 2\left(1-\psi^2-\phi^2+\frac{4\psi^2\phi^2}{R}\right).$$

Equations (3.3), (3.4), and (3.5) are the TSCRPA equations of motion for the Lipkin model. In the limit $T\to 0$, they take a form of equations of the SCRPA [2].

The final expression for the model grand canonical potential Ω_L defined in accordance with (2.9) is

$$\Omega_L = -\frac{N\left(1-2q\right)}{2}\Bigg\{\varepsilon\left(y_1^2-y_2^2\right)\cos 2\theta+V_1\left(y_1^2-y_2^2\right)\left[N\left(1-2q\right)-1\right] \qquad (3.6)$$
$$+\frac{1+\left(y_1^2-y_2^2\right)^2}{y_1^2-y_2^2}\left(V_2t_2-V_1t_1\right)\Bigg\}+NT\left(1-2q\right)\sum_{k=1,2}\left(x_k^2\ln x_k^2+y_k^2\ln y_k^2\right).$$

Of course, we bear in mind the number-conservation condition. After variation of (3.6) with respect to θ, we find that the HF parameter satisfies the equation

$$\sin 2\theta\left\{-\varepsilon\left(y_1^2-y_2^2\right)\right.$$
$$+V\left(y_1^2-y_2^2\right)^2\left[N\left(1-2q\right)-1\right]\cos 2\theta$$
$$\left.-V\left[1+\left(y_1^2-y_2^2\right)^2\right]\left(t_1+t_2\right)\cos 2\theta\right\}=0,$$

which has two solutions. The first one, $\theta=0$, determines the so-called "spherical" phase. The second

$$\theta=\frac{1}{2}\arccos\left\{\frac{\varepsilon\left(y_1^2-y_2^2\right)}{\left[V\left(y_1^2-y_2^2\right)^2\left[N\left(1-2q\right)-1\right]-V\left(1+\left(y_1^2-y_2^2\right)^2\right)\left(t_1+t_2\right)\right]}\right\} \qquad (3.7)$$

determines the "deformed" phase.

A variation of Ω_L with respect to x_i and y_i produces equations for the single-quasiparticle energies

$$E_{1,2}=\mp\frac{1}{2}\left\{\varepsilon\cos 2\theta\right. \qquad (3.8)$$
$$+V\left(y_1^2-y_2^2\right)\left[N\left(1-2q\right)-1-t_1\right]\sin^2 2\theta$$
$$\left.+V\left(y_1^2-y_2^2\right)t_2\left(1+\cos^2 2\theta\right)\right\}.$$

One can see from (3.7) and (3.8) that the parameters of the HF transformation, as well as the parameters of the thermal Bogolyubov transformation, depend on the collective variables ψ and ϕ. But if one sets $q=0$, $\psi=N^{-1}$, and $\phi=0$, this dependence disappears, with the result that one gets equations of the conventional thermal HF approximation for the Lipkin model. Equations (3.3), (3.4), and (3.5), together with (3.7) and (3.8), form the complete set of the TSCRPA equations for the Lipkin model.

By way of example, we calculate the temperature dependence of the intrinsic energy of the system, $\langle|H_{\mathrm{L}}|\rangle$. The results of the TSCRPA are compared with those of other approximations as well as the exact ones.[2)]

The expression for the intrinsic energy is

$$\langle|H_{\mathrm{L}}|\rangle=-\frac{N\left(1-2q\right)}{2}\Bigg\{\varepsilon\left(y_1^2-y_2^2\right)\cos 2\theta$$
$$+V_1\left(y_1^2-y_2^2\right)\left[N\left(1-2q\right)-1\right]$$
$$+\frac{1+\left(y_1^2-y_2^2\right)^2}{y_1^2-y_2^2}\left(V_2t_2-V_1t_1\right)\Bigg\}.$$

The calculations were performed for the system of $N=20$ particles with $\varepsilon=1$ (i.e., we adopt ε as an energy unit). Here, we discuss the results for the strong-coupling case ($V=0.1$).

At $T=0$, the system is in a deformed phase. Since the interaction between particles effectively weakens

---

[2)] The description of the exact grand-canonical calculations with the Lipkin model can be found in [5, 13].

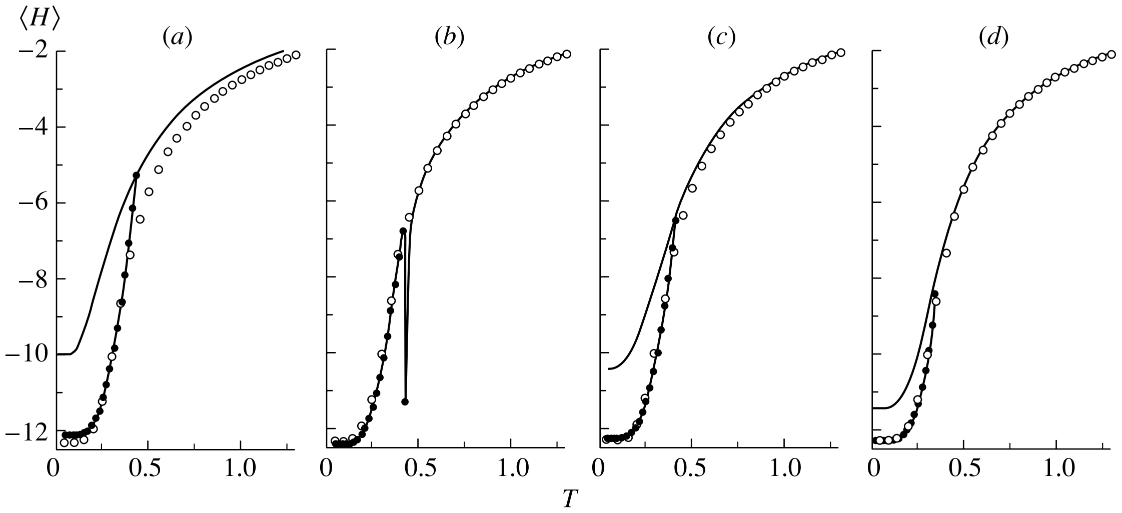

Fig. 1. Temperature dependence of the intrinsic energy $\langle |H| \rangle$ at $V = 0.1$ according to calculations within various approximations [(a) THFA, (b) TRPA, (c) TRRPA, and (d) TSCRPA]: (open circles) exact result (the grand-canonical-ensemble calculations), (closed circles) results of the calculations with a deformed HF field, and (solid line) result of the calculations with a spherical HF field.

with increasing T, a rearrangement of the HF field (i.e., a phase transition) occurs at a certain temperature T_{cr}, whereupon the system appears to be in a normal phase. Within the THFA and the TRPA, the phase transition occurs at $T_{\text{cr}} = 0.5$ (Figs. 1*a*, 1*b*).

In the TRRPA and the TSCRPA, the phase transition occurs at lower temperature (Fig. 1*c*). The reason is the following. Within the TRPA, the RPA solution collapses at $T = T_{\text{cr}}$ (i.e., $\omega \to 0$); at $T < T_{\text{cr}}$, the RPA root is pure imaginary if one formally stays in the spherical phase. A pleasant feature of the TSCRPA (and the TRRPA) is that ω is finite at all values of the coupling strength V. It follows that, within the TSCRPA, one can formally calculate the intrinsic energy $\langle |H| \rangle$ at $T < T_{\text{cr}}$ with the HF field of the spherical phase. It appears that, in a small but noticeable temperature range at $T < T_{\text{cr}}$, the value of $\langle |H| \rangle$ calculated with the spherical HF field is lower than the value calculated with the deformed HF field. As can be seen from Fig. 1*d*, the critical temperature is shifted down to $T_{\text{cr}} \approx 0.35$ and the temperature range where the spherical phase gives a minimum of Ω_{L}, broadens. The same tendency can be seen in the TRRPA as well (Fig. 1*c*), but T_{cr} is higher ($\approx$0.42) in this approximation.

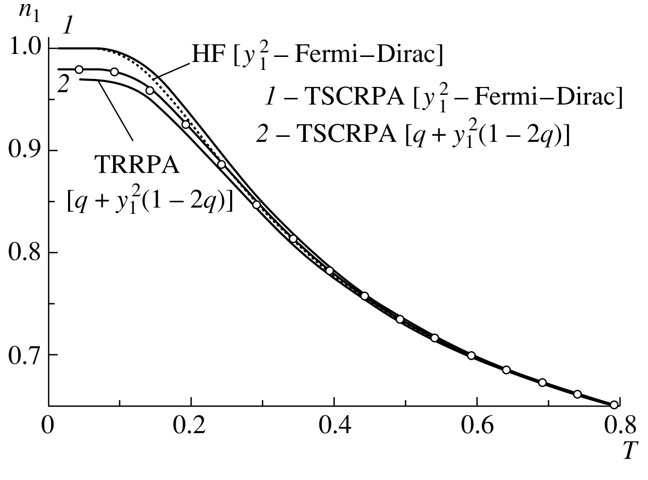

Fig. 2. Occupation number n_1 for the lower level as a function of temperature.

It is worthwhile to note that, if one calculates $\langle |H| \rangle$ within the TSCRPA with the spherical HF field in the whole temperature range from $T = 0$ to $T \gg T_{\text{cr}}$, the difference between the exact and the approximate value of $\langle H \rangle$ does not exceed 10%. This means that the TSCRPA describes the statistical properties of the Lipkin system quite well even without a rearrangement of the HF field. Thus, correlations in quasiparticle motion that are taken into account within the TSCRPA compensate, to a great extent, the effect of fluctuations that are produced by the grand-canonical-ensemble approach.

It is also interesting to examine what various approximations tell us about the occupation numbers $n_{1,2}$ of single-quasiparticle levels. The expression for n_1 normalized to unity is

$$n_1 = \frac{1}{2} + \frac{\langle |J_z| \rangle}{N}.$$

The results are shown in Fig. 2. The THFA (and the TRPA) overestimates n_1, although the difference between the exact and approximate values is only 2 to 3%. The difference is the largest at small temperatures ($T < 0.2$). When quantum effects (i.e., a nonvanishing number of thermal quasiparticles in the thermal ground state) are taken into account within the TRRPA, the agreement between the approximate and the exact results becomes better. However, the approximate values of n_1 in the TRRPA are slightly lower than the exact ones. Thus, the TRRPA overestimates the effect of a residual interaction. In the TSCRPA, the values of n_1 appear to be almost equal to the exact ones. In addition to the total values of n_1, we also display, in Fig. 2, the pure thermal part of them (y_1^2). It can be compared with the HF values. The difference associated with the tuning of the HF field and collective oscillations is not large, but it is noticeable.

4. CONCLUSION

On the basis of the above results, we conclude that, on the whole, the TSCRPA describes the statistical properties of a finite Fermi system better than other approximate schemes. Its advantages are most evident in the vicinity of the phase-transition point. Moreover, within the TSCRPA, one can describe, with an appropriate accuracy, the temperature dependence of the intrinsic energy, keeping the HF field in the "spherical" phase, i.e., avoiding a phase transition. The main effect that is responsible for these improvements is a more correct treatment of the Pauli exclusion principle in the thermal vacuum state (or, in other words, a nonvanishing number of thermal quasiparticles in the thermal vacuum state).

REFERENCES

1. Ken-ji Hara, Prog. Theor. Phys. **32**, 88 (1964); D. J. Rowe, Phys. Rev. **175**, 1283 (1968).
2. J. Dukelsky and P. Schuck, Nucl. Phys. A **512**, 466 (1990).
3. P. Schuck and S. Ethofer, Nucl. Phys. A **212**, 269 (1973); J. Dukelsky and P. Schuck, Phys. Lett. B **387**, 233 (1996); **464**, 164 (1999).
4. A. V. Avdeenkov, D. S. Kosov, and A. I. Vdovin, Mod. Phys. Lett. A **11**, 853 (1996).
5. A. N. Storozhenko, D. S. Kosov, and A. I. Vdovin, Yad. Fiz. **62**, 63 (1999) [Phys. At. Nucl. **62**, 58 (1999)]; A. N. Storozhenko and A. I. Vdovin, Eur. Phys. J. A **5**, 263 (1999).
6. A. I. Vdovin, D. S. Kosov, and W. Nawrocka, Teor. Mat. Fiz. **111**, 279 (1997) [Theor. Math. Phys. **111**, 613 (1997)].
7. D. S. Kosov, A. I. Vdovin, and J. Wambach, in *Proceedings of the International Conference "Nuclear Structure and Related Topics," Dubna, Russia, 1997,* E4-97-327, p. 254.
8. Y. Takahashi and H. Umezawa, Collect. Phenom. **2**, 55 (1975); H. Umezawa, H. Matsumoto, and M. Tachiki, *Thermo Field Dynamics and Condensed States* (North-Holland, Amsterdam, 1982; Mir, Moscow, 1985).
9. K. Tanabe, Phys. Rev. C **37**, 2802 (1988); T. Hatsuda, Nucl. Phys. A **492**, 187 (1989).
10. S. V. Tyablikov, *Methods in the Quantum Theory of Magnetism* (Nauka, Moscow, 1975, 2nd ed.; Plenum, New York, 1967).
11. H. J. Lipkin, N. Meshkov, and A. J. Glick, Nucl. Phys. **62**, 188 (1965).
12. P. Ring and P. Schuck, *The Nuclear Many-Body Problem* (Springer-Verlag, New York, 1980).
13. A. Kuriyama *et al.,* Prog. Theor. Phys. **95**, 339 (1996).

Physics of Atomic Nuclei, Vol. 64, No. 6, 2001, pp. 1076–1080. From Yadernaya Fizika, Vol. 64, No. 6, 2001, pp. 1151–1155.
Original English Text Copyright © 2001 by Almehed, Dönau, Nazmitdinov.

Quantum Correlations in Rotating Nuclei[*]

D. Almehed[**], **F. Dönau**, and **R. G. Nazmitdinov**[1)]

Institut für Kern- und Hadronenphysik, Dresden, Germany

Received September 11, 2000

Abstract—Using the Hamiltonian that consists of the separable quadrupole + pairing forces and the cranking term, we analyze the correlations associated with shape, orientation, and particle-number fluctuations in rotating nuclei. Quantum fluctuations around mean field solutions are treated in the random phase approximation (RPA), with special emphasis on the restoration of rotational symmetry and particle number conservation. The mean field calculations have been made within the self-consistent cranking model. The effect of the RPA correlation energy for the moment of inertia is studied with the integral representation method proposed. © *2001 MAIK "Nauka/Interperiodica".*

1. INTRODUCTION

The mean field approximation is quite successful in describing various nuclear phenomena [1, 2]. However, a mean field solution often breaks one or more fundamental symmetries, e.g., translation, rotation, reflection, and gauge rotation, of a many-body Hamiltonian. For instance, a spontaneous breaking of the spherical symmetry for a nucleus with a partially filled shell gives rise to a deformed shape and to a fixed orientation in space characterized by the principal axis of the mass distribution. As a result, the deformed mean field functions span a subspace of the many-body Hilbert space containing the ground state and low-lying excited states which exhibit a rotational spectrum [3]. One way to restore broken symmetries of the mean field functions is to use different projection techniques onto eigenspaces of the corresponding symmetry operator.

A more advanced quantum mechanical description should take into account quantum fluctuations around the mean field minimum. The quantal fluctuations lead not only to a series of collective excitations like rotation and vibration but also give rise to correlations in the mean field ground state which may change its properties. The random phase approximation permits one to consider quantum fluctuations in a harmonic order [3, 4]. The RPA correlations improve the mean field solution and give a better approximation to the exact solution [3, 5]. In addition, the RPA is another systematic approach of the approximate restoration of broken symmetries of mean field solutions.

Our aim is to demonstrate an effective method for calculating the RPA correlations in rotating nuclei. The model Hamiltonian will be presented in Section 2. The method for calculating the RPA correlation energy is described in Section 3 followed by the results for two cases in Section 4 and conclusions.

2. THE HAMILTONIAN

We start our discussion with a Nilsson-like oscillator Hamiltonian with quadrupole–quadrupole plus pairing forces

$$\hat{H}' = \hat{h}_0 + \hat{h}_\ell - \mathbf{J}\cdot\boldsymbol{\omega} - \frac{\kappa}{2}\hat{Q}\cdot\hat{Q} - \sum_{\tau=n,p} G_\tau \hat{P}_\tau^\dagger \hat{P}_\tau. \quad (1)$$

Here, $\hat{h}_0$ is a spherical Hamiltonian containing the kinetic energy term and the spherical oscillator potential, $\hat{h}_\ell$ contains the spin-orbit and ℓ^2 terms

$$\hat{h}_\ell = -\hbar\omega_0\kappa_\ell \left[2\ell\cdot\mathbf{s} + \mu_\ell\left(\ell^2 - \left\langle \ell^2\right\rangle_N\right)\right], \quad (2)$$

and $\mathbf{J}\cdot\boldsymbol{\omega}$ is a cranking term [6]. The index τ corresponds to the proton and neutron part, and it will be left out in the following discussion where it is not necessary. Notice that the model Hamiltonian can be generalized easily. The quadrupole $\hat{Q}_m$ and pairing $\hat{P}_\tau$ operators are given by

$$\hat{Q}_m = \sum_{kl} q_{m,kl}\ \hat{c}_k^\dagger \hat{c}_l, \qquad \hat{P} = \sum_{i>0} \hat{c}_{\bar{i}}\hat{c}_i. \quad (3)$$

The index $\bar{i}$ refers to time-reversed spherical single-particle orbit labeled so that $\bar{i} < 0$, and $\hat{c}$ ($\hat{c}^\dagger$) is the particle annihilation (creation) operator. The standard quadrupole matrix element

$$q_{m,kl} \sim \frac{1}{\sqrt{2}}\left(\langle k|\, r^2 Y_{2m}\,|l\rangle + \frac{m}{|m|}\langle k|\, r^2 Y_{2-m}\,|l\rangle\right)$$

---

[*] This article was submitted by the authors in English.

[1)] Joint Institute for Nuclear Research, Dubna, Russia.

[**] e-mail: `D.Almehed@fz-rossendorf.de`

1063-7788/01/6406-1076$21.00 © 2001 MAIK "Nauka/Interperiodica"

and $q_{0,kl} \sim \langle k|\, r^2 Y_{20}\, |l\rangle$ is expressed in the spherical basis $|nljm\rangle$ [2]. The mean field approximation of the total Hamiltonian (1) determines the mean field Hamiltonian which consists of a modified harmonic oscillator and a pairing potential

$$\hat{h}' = \hat{h}_0 + \hat{h}_\ell - \mathbf{J}\cdot\boldsymbol{\omega} \tag{4}$$
$$-\sqrt{\frac{5}{4\pi}}\hbar\omega_0\beta(\cos\gamma\hat{Q}_0 - \sin\gamma\hat{Q}_2) - \Delta(\hat{P}^\dagger + \hat{P}),$$

where β and γ are the deformation parameters [2, 3]. Taking into account the mean field Hamiltonian (4), we have

$$\hat{H}' = \hat{h}' + \sqrt{\frac{5}{4\pi}}\hbar\omega_0\beta\left(\cos\gamma\hat{Q}_0 - \sin\gamma\hat{Q}_2\right) \tag{5}$$
$$-\frac{\kappa}{2}\hat{Q}\cdot\hat{Q} + \Delta\left(\hat{P}^\dagger + \hat{P}\right) - G\hat{P}^\dagger\hat{P}.$$

The energy minimum of the Hamiltonian (5) requires the fulfillment of the self-consistent conditions

$$\kappa\langle Q_0\rangle = \sqrt{\frac{5}{4\pi}}\beta\cos\gamma,\ \kappa\langle Q_2\rangle = \sqrt{\frac{5}{4\pi}}\beta\sin\gamma, \tag{6}$$
$$\langle Q_{\pm 1,-2}\rangle = 0,\ \text{and}\ G\langle\hat{P}\rangle = \Delta.$$

Consequently, the Hamiltonian (5) has the following form:

$$\hat{H}' = \hat{h}' + \frac{\kappa}{2}\sum_m \langle\hat{Q}_m\rangle^2 + G\langle\hat{P}\rangle^2 - \hat{H}_{\text{int}}, \tag{7}$$

$$\hat{H}_{\text{int}} = \frac{\kappa}{2}\sum_m\left(\hat{Q}_m - \langle\hat{Q}_m\rangle\right)^2 \tag{8}$$
$$+ G\left(\hat{P}^\dagger - \langle\hat{P}\rangle\right)\left(\hat{P} - \langle\hat{P}\rangle\right),$$

if (6) are fulfilled. The remaining interaction, $\hat{H}_{\text{int}}$, will be treated in the RPA order in Section 3.

The quadrupole operator $\hat{Q}$ mixes states with different main oscillator quantum numbers N. Using the stretched transformation [2]

$$\bar{x}_i = x_i\sqrt{\frac{M\omega_i}{\hbar}}, \quad i = 1, 2, 3, \tag{9}$$

we diagonalize our Hamiltonian for each N shell separately. Here, ω_i are the oscillator frequencies. As a result, the mean field Hamiltonian (4) expressed in the stretched basis has the form

$$\hat{h}' = \bar{h}_0 + \hat{h}_\ell - \mathbf{J}\cdot\boldsymbol{\omega} \tag{10}$$
$$-\sqrt{\frac{5}{4\pi}}\hbar\bar{\omega}_0\bar{\beta}\left(\cos\bar{\gamma}\bar{Q}_0 - \sin\bar{\gamma}\bar{Q}_2\right) - \Delta\left(\hat{P}^\dagger + \hat{P}\right).$$

The $\hat{h}_\ell$ part is not affected, and it does not become N-diagonal from the stretched transformation. The same is true for the cranking term.

To diagonalize (10), we use the standard Hartree–Fock–Bogoliubov transformation to quasiparticle operators [4]

$$\hat{\alpha}_i^\dagger = \sum_k\left(u_{ki}\hat{c}_k^\dagger - v_{ki}\hat{c}_k\right), \tag{11}$$
$$\hat{\alpha}_i = \sum_k\left(u_{ki}\hat{c}_k - v_{ki}\hat{c}_k^\dagger\right), \quad \sum_k\left(v_{ki}^2 + u_{ki}^2\right) = 1.$$

The ground state wave function is the vacuum state for quasiparticles $\hat{\alpha}_i\,|\text{HFB}\rangle = 0$, and the total energy can be calculated as $E_0 = \sum e_i$, where e_i are the eigenvalues of $\hat{h}'$ in (10).

3. THE RPA CORRELATIONS

Using the quasiboson approximation [3, 4]

$$\hat{b}_\mu^\dagger = \hat{\alpha}_i^\dagger\hat{\alpha}_j^\dagger, \quad \hat{b}_\mu = \hat{\alpha}_j\hat{\alpha}_i, \quad \text{and} \quad i > j \leftrightarrow \mu, \tag{12}$$

in which the operators in (12) obey the boson commutation rules

$$\left[\hat{b}_\mu, \hat{b}_\nu\right] = \left[\hat{b}_\mu^\dagger, \hat{b}_\nu^\dagger\right] = 0 \tag{13}$$

and

$$\left[\hat{b}_\mu, \hat{b}_\nu^\dagger\right] = \delta_{\mu\nu},$$

we express the Hamiltonian (7) and (8) in terms of the operators (12). In the RPA, one includes all terms of the boson Hamiltonian that is of the second order in $\hat{b}$. $\hat{H}_{\text{RPA}}$ can be diagonalized in the form [3, 7]

$$\hat{H}_{\text{RPA}} = \sum_{\lambda>0}\omega_\lambda\hat{O}_\lambda^\dagger\hat{O}_\lambda + \frac{\hat{\mathcal{P}}^2}{2\mu} + E_{\text{RPA}}, \tag{14}$$

where $\hat{O}_\lambda^\dagger(\hat{O}_\lambda)$ is the phonon creation (annihilation) operator of the eigenmode λ and $\hat{\mathcal{P}}$ is the operator connected with the spurious mode. The spurious mode is a zero energy motion without a restoring force, e.g., rotation around a symmetry axis. The zero energy phonon in (14) restores the symmetry broken in the mean field treatment [8]. The ground state energy correlation, E_{RPA}, of the RPA Hamiltonian is then given by

$$E_{\text{RPA}} = \frac{1}{2}\left(\sum_{\lambda>0}\Omega_\lambda - \sum_\mu E_\mu\right) + E_{\text{exch}}, \tag{15}$$

where E_μ is the sum of two quasiparticle energies $E_\mu = e_i + e_j$ and E_{exch} is the standard exchange energy (see, e.g., [9]). In this formulation of the RPA energy, we do not have to treat the energy contribution of the spurious mode explicitly and a $\Omega_\nu = 0$ solution does not cause any complication in the evaluation of (15). The total RPA energy can in principle be calculated by diagonalizing the Hamiltonian (7). Since the RPA matrix is so large in realistic calculations, of the order 10^4, and none of the eigenfrequencies can be neglected, the evaluation of (15) is very difficult even for the separable interaction [10].

Possible spurious solutions of the $Q \cdot Q +$ pairing RPA Hamiltonian

$$\hat{H}_{\mathrm{RPA}} = \sum_{\mu\tau} E_{\mu\tau}\hat{b}_\mu^\dagger \hat{b}_\mu - \frac{\kappa}{2}\sum_m \left(\hat{Q}_m - \langle \hat{Q}_m\rangle\right)^2 - \sum_\tau G_\tau \left(\hat{P}_\tau^\dagger - \langle \hat{P}_\tau\rangle\right)\left(\hat{P}_\tau - \langle \hat{P}_\tau\rangle\right) \quad (16)$$

will be connected with the particle number operator $\hat{N}$ for the pairing force and different components of the angular momentum, if the self-consistency conditions in (6) are fulfilled. Writing our operators in a Hermitian form and expressing them in terms of the boson operators, $\hat{b}$, we get the following expressions:

$$\tilde{S}_\tau^+ = \frac{1}{\sqrt{2}}\left(\hat{P}_\tau^\dagger + \hat{P}_\tau - 2\langle \hat{P}_\tau\rangle\right) = \sum_\mu s_{\mu\tau}^+ \left(b_{\mu\tau}^\dagger + b_{\mu\tau}\right), \quad (17)$$

$$\tilde{S}_\tau^- = \frac{i}{\sqrt{2}}\left(\hat{P}_\tau^\dagger - \hat{P}_\tau\right) = i\sum_\mu s_{\mu\tau}^- \left(b_{\mu\tau}^\dagger + b_{\mu\tau}\right), \quad (18)$$

$$\tilde{Q}_{m\tau} = \hat{Q}_{m\tau} - \langle \hat{Q}_{m\tau}\rangle = \sqrt{\varphi_m}\sum_\mu \tilde{q}_{m\mu\tau}\left(b_{\mu\tau}^\dagger + \varphi_m b_{\mu\tau}\right), \quad (19)$$

$$\varphi_m = \begin{cases} 1, & m = 0, -1, 2, \\ -1, & m = 1, -2. \end{cases} \quad (20)$$

The boson matrix elements are defined as

$$s_\mu^\pm = \sum_{k>0}\left[\left(u_{ki}u_{\bar{k}j} \pm v_{kj}v_{\bar{k}i}\right) - \left(u_{kj}u_{\bar{k}i} \pm v_{ki}v_{\bar{k}j}\right)\right], \quad (21)$$

$$\tilde{q}_{0,\mu} = \sum_{k,l>0} q_{0,kl}\left(u_{ki}v_{lj} - u_{lj}v_{ki} + u_{\bar{k}i}v_{\bar{l}j} - u_{\bar{l}j}v_{\bar{k}i}\right), \quad (22)$$

$$\tilde{q}_{\pm1,\mu} = \sum_{k,l>0} q_{\pm1,kl}\left(u_{ki}v_{\bar{l}j} \pm u_{\bar{k}i}v_{lj} - u_{kj}v_{\bar{l}i} \mp u_{\bar{k}j}v_{li}\right), \quad (23)$$

$$\tilde{q}_{\pm2,\mu} = \sum_{k,l>0} q_{\pm2,kl}\left(u_{ki}v_{lj} + u_{lj}v_{ki} \pm u_{\bar{k}i}v_{\bar{l}j} \pm u_{\bar{l}j}v_{\bar{k}i}\right), \quad (24)$$

where $q_{m,kl}$ are the single-particle matrix elements of $\hat{Q}_m$ in (3). The Hamiltonian can be expressed as

$$\hat{H}_{\mathrm{RPA}} = \sum_{\mu\tau} E_{\mu\tau}\hat{b}_{\mu\tau}^\dagger \hat{b}_{\mu\tau} - \frac{1}{2}\sum_m \kappa_0\left(\tilde{Q}_{m,p} + \tilde{Q}_{m,n}\right)^2 + \kappa_1\left(\tilde{Q}_{m,p} - \tilde{Q}_{m,n}\right)^2 - \frac{1}{2}\sum_\tau G_\tau\left(\tilde{S}^{+^2} + \tilde{S}^{-^2}\right), \quad (25)$$

where $\kappa_{0,1}$ are the isoscalar and isovector quadrupole coupling constants. Using the equation-of-motion approach to solve the RPA equations (see [11]), we obtain the determinant of the secular equations

$$F(\Omega) = \begin{vmatrix} R^+ - \frac{\hat{1}}{2\kappa_0} & R^- & T_{m=1}^{-,n} & T_{m=-1}^{+,n} & T_{m=1}^{-,p} & T_{m=-1}^{+,p} \\ R^- & R^+ - \frac{\hat{1}}{2\kappa_1} & T_{m=1}^{-,n} & T_{m=-1}^{+,n} & -T_{m=1}^{-,p} & -T_{m=-1}^{+,p} \\ T_{k=1}^{-,n} & T_{k=1}^{-,n} & S_{--}^n - \frac{1}{2G_n} & S_{+-}^n & 0 & 0 \\ T_{k=-1}^{+,n} & T_{k=-1}^{+,n} & S_{+-}^n & S_{++}^n - \frac{1}{2G_n} & 0 & 0 \\ T_{k=1}^{-,p} & -T_{k=1}^{-,p} & 0 & 0 & S_{--}^p - \frac{1}{2G_p} & S_{+-}^p \\ T_{k=-1}^{-,p} & -T_{k=-1}^{-,p} & 0 & 0 & S_{+-}^p & S_{++}^p - \frac{1}{2G_p} \end{vmatrix}, \quad (26)$$

where the matrix elements have the following forms:

$$S_\tau^{\pm\pm}(\Omega) = \sum_\mu \frac{s_{\mu\tau}^{\pm^2}E_{\mu\tau}}{E_{\mu\tau}^2 - \Omega^2}, \quad (27)$$

$$S_\tau^{+-}(\Omega) = \sum_\mu \frac{s_{\mu\tau}^+ s_{\mu\tau}^- \Omega}{E_{\mu\tau}^2 - \Omega^2}, \quad (28)$$

$$R_{km}^\pm(\Omega) = \sum_\mu \left(\frac{\tilde{q}_{k,\mu n}\tilde{q}_{m,\mu n}C_{\mu n}^{km}}{E_{\mu n}^2 - \Omega^2} \pm \frac{\tilde{q}_{k,\mu p}\tilde{q}_{m,\mu p}C_{\mu p}^{km}}{E_{\mu p}^2 - \Omega^2}\right), \quad (29)$$

$$T_{km}^{\pm,\tau}(\Omega) = \sum_\mu \frac{\tilde{q}_{m,\mu\tau}s_{\mu\tau}^\pm C_{\mu\tau}^{km}}{E_{\mu\tau}^2 - \Omega^2}. \quad (30)$$

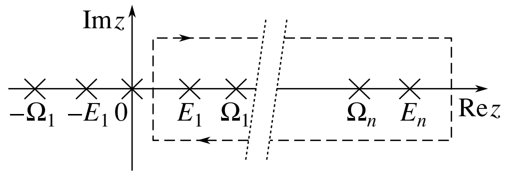

Fig. 1. A schematic picture of the integration contour (dashed line) in the complex plane. The roots Ω_ν and poles E_μ of $F(z)$ are marked with crosses.

Here,

$$C^{km}_{\mu\tau} = \begin{cases} E_{\mu\tau}, & k = 0, -1, 2;\ m = 0, -1, 2, \\ \text{and} & k = 1, -2;\ m = 1, -2; \\ \Omega, & k = 0, -1, 2;\ m = 1, -2, \\ \text{and} & k = 1, -2;\ m = 0, -1, 2. \end{cases} \quad (31)$$

The zeros of the function F determine the RPA eigenfrequencies, i.e., Ω_ν,

$$F(\Omega_\nu) = 0. \quad (32)$$

Continuing the variable $\Omega \to z$ into the complex plane, one can form the spectral function $F'(z)/F(z)$ which obviously has first order poles at Ω_ν and E_μ, and it is analytic for all other complex values of z. We can now use the Cauchy theorem and formulate the integral

$$\frac{1}{2\pi i}\oint\limits_C dz g(z)\frac{F'(z)}{F(z)} \quad (33)$$

$$= \sum_\nu g(\Omega_\nu) - \sum_\mu g(E_\mu),$$

where $g(z)$ is an arbitrary complex function which is analytic within the region enclosed by the integration path C [12]. Ω_ν and E_μ are the roots and poles of $F(z)$ in the same region. By choosing $g(z) = z$, we obtain for the RPA correlation energy (15),

$$E_{\text{RPA}} = \frac{1}{4\pi i}\oint\limits_C dz z\frac{F'(z)}{F(z)} + E_{\text{exch}}, \quad (34)$$

where the integration path C goes around the right half of the complex plane. The integral in (33) is independent of the path C as long as all poles in the positive plane are enclosed (see Fig. 1). Therefore, the path C can always be chosen in such a way that the spectral function becomes smooth and the integration is numerically stable even for a small number of grid points used in the integration procedure.

We would like to mention that the correlation energy (34) is in general a negative (gain) term, the value of which depends on the rotational frequency as well as on the configuration under study. When one calculates the correlation energy for excited quasiparticle configurations, possible negative RPA solutions have to be treated with special care.

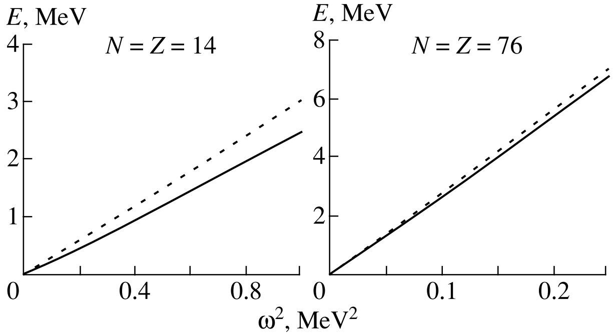

Fig. 2. The energy of a rotating deformed harmonic oscillator with (solid line) and without (dashed line) $Q \cdot Q$ isoscalar RPA correlations as a function of ω^2. The self-consistent deformed oscillator is filled with 14 (76) protons and 14 (76) neutrons in the left (right) picture.

4. DISCUSSION OF THE RESULTS

To investigate the effect of the ground state RPA correlations in rotating nuclei, we start with a harmonic oscillator with the $Q \cdot Q$ forces and without the $\ell \cdot \mathbf{s}$ and ℓ^2 terms but including a cranking term. The self-consistent mean field solution gives a three-dimensional cranking deformed oscillator. The energy spectrum of this system is the one of a rigid rotor (see Fig. 2), which means that the energy is proportional to the square of the rotational frequency, ω^2. The RPA treatment of the isoscalar $Q \cdot Q$ interaction allows one to include shape and orientation fluctuations in all three dimensions. Taking into account the RPA correlations, we obtain a large decrease in the total energy and also a dependence of E_{RPA} on ω. It turns out that $E_{\text{RPA}} \propto \omega^2$. The nucleus still has a rigid rotation, but the RPA correlation reduces the moment of inertia, as seen in Fig. 2. In the $N = Z = 14$ system shown in Fig. 2, we see a 16% reduction of the moment of inertia, which is proportional to the slope of the curves. In the heavier $N = Z = 76$ system in Fig. 2, the moment of inertia is reduced by 4%. We see that RPA correlations cause a relatively smaller effect on the moment of inertia in the heavier system than in the lighter one. This is because (i) the absolute ω dependence of the E_{RPA} becomes a little bit smaller and (ii) the mean field moment of inertia becomes much larger in the heavier system.

An explicit calculation of the commutation rules

$$\left[\hat{H}_{\text{RPA}}, \tilde{Q}\right] = \left[\hat{H}_{\text{RPA}}, \hat{J}_i\right] = 0, \quad i = 1, 2, 3, \quad (35)$$

gives a stringent check of the RPA restoration of the rotational symmetry. In the numerical calculation of the $N = Z = 14$ case above, we found that (35) was fulfilled with an accuracy of 10^{-3}.

5. SUMMARY

The self-consistent scheme to calculate the total energy for a three-dimensional cranking Hamiltonian which includes the pairing + quadrupole separable interactions has been developed. The basic element of our approach is the novel method based on the integral representation which permits efficient calculations of the RPA correlation energy. Applying the approach to a Hamiltonian that consists of a harmonic oscillator plus a plain isoscalar quadrupole–quadrupole interaction, we obtain a reduction of the moment of inertia in the ground band. The effect is found to be large in small systems and decreasing with increasing mass. To carry out more qualitative calculations, one has to include the spin–orbit and ℓ^2 terms in the Hamiltonian. The analysis of pairing vibrations in high-K rotational bands was presented in [13]. The particle number restoring calculations gave an improvement of the relative energy with respect to the experiment and showed the importance of pairing vibrations to describe the relative energy between different K bands. In the cases where we have a static pair field, the T terms in (26) mix $Q \cdot Q$ and pairing vibrational modes. How they will affect each other and the total correlation energy is yet to be examined.

ACKNOWLEDGMENTS

This work was supported in part by the Heisenberg–Landau program of the BLTP, JINR, and by the RFBR under grant no. 00-02-17194.

REFERENCES

1. A. Bohr and B. R. Mottelson, *Nuclear Structure* (Benjamin, New York, 1975; Mir, Moscow, 1977), Vol. 2.
2. S. G. Nilsson and I. Ragnarsson, *Shapes and Shells in Nuclear Structure* (Cambridge Univ. Press, Cambridge, 1995).
3. P. Ring and P. Schuck, *The Nuclear Many-Body Problem* (Springer-Verlag, New York, 1980).
4. V. G. Soloviev, *Theory of Atomic Nuclei: Quasiparticles and Phonons* (Institute of Physics, Bristol, 1992).
5. K. Hagino and G. F. Bertsch, Phys. Rev. C **61**, 024307 (2000); nucl-th/0003016.
6. S. Frauendorf, Nucl. Phys. A **557**, 259c (1993); Rev. Mod. Phys. **73** (2), 463 (2001).
7. J. P. Blaizot and G. Ripka, in *Quantum Theory of Finite Systems* (MIT Press, Cambridge, 1986), p. 66.
8. E. R. Marshalek and J. Weneser, Ann. Phys. (N.Y.) **53**, 568 (1969).
9. Y. R. Shimizu, J. D. Garrett, R. A. Broglia, *et al.*, Rev. Mod. Phys. **61**, 131 (1989).
10. J. L. Egido, H. J. Mang, and P. Ring, Nucl. Phys. A **341**, 224 (1980).
11. J. Kvasil and R. G. Nazmitdinov, Fiz. Élem. Chastits At. Yadra **17**, 613 (1986) [Sov. J. Part. Nucl. **17**, 265 (1986)].
12. F. Dönau, D. Almehed, and R. G. Nazmitdinov, Phys. Rev. Lett. **83**, 280 (1999).
13. D. Almehed, S. Frauendorf, and F. Dönau, Phys. Rev. C **63**, 044311 (2001); D. Almehed, F. Dönau, S. Frauendorf, and R. G. Nazmitdinov, Phys. Scr. T **T88**, 62 (2000).

Physics of Atomic Nuclei, Vol. 64, No. 6, 2001, pp. 1081–1086. From Yadernaya Fizika, Vol. 64, No. 6, 2001, pp. 1156–1161.

Long $K^\pi = 0^+$ and 4^- Bands in Deformed Nuclei[*]

E. P. Grigoriev[**]

Institute of Physics (Petrodvorets Branch), St. Petersburg State
University, Ul'yanovskaya ul. 1, Petrodvorets, 198904 Russia

Received November 9, 2000

Abstract—Experimental data on some long bands in $N = 88$–98 deformed nuclei are analyzed on the basis of a method systematizing the energies of levels and inertial parameters and a method employing the analogy between neighboring. Beta bands built on low-lying 0_2^+ levels are identified in $N = 90$ isotones, including the ^{158}Er, ^{160}Yb, and ^{162}Hf nuclei. Some of intermediate members of these bands have not been found yet. The systematic properties of 4^- bands are presented, and the dynamics of the inertial parameters of these bands in $N = 88$–98 isotones is revealed. The bands are identified in ^{158}Yb, ^{156}Dy, ^{156}Er, ^{162}Yb, and ^{166}Hf. © *2001 MAIK "Nauka/Interperiodica"*.

1. INTRODUCTION

Extensive development of experimental techniques of nuclear spectroscopy has resulted in finding many new high-spin levels. A considerable number of these levels belong to rotational bands characterized by small values of the K projection of the spin J onto the symmetry axis of a nucleus. High-spin levels are excited mostly in heavy-ion reactions, but low-lying levels of the bands having low spins (including bandheads) are not so often revealed. Because of this it is difficult to determine the K values of the bands.

This study is devoted to finding the rules of ordering of levels in rotational bands in the nuclei being considered and to comparing the positions of the head levels in analogous bands.

Our method of analysis is based on a comparison of the energies of levels and inertial parameters as calculated by using the energies of neighboring levels (A), or neighboring levels with even spins (A^+), or neighboring levels with odd spins (A^-). The simplest formula for a rotator energy,

$$E = \frac{\hbar^2}{2J} J(J+1), \tag{1}$$

is used to evaluate the formulas

$$\Delta E = E(J) - E(J-1) = A \times 2J,$$
$$A(J) = \Delta E / 2J,$$
$$\Delta E^+, \Delta E^- = E(J) - E(J-2),$$
$$A^\pm(J) = \frac{\Delta E^\pm}{2(2J-1)},$$

where J is even for E^+ and odd for E^-.

2. GROUND-STATE BANDS AND BETA-VIBRATIONAL BANDS IN $N = 90$ ISOTONES

The $N = 90$ isotones have very special properties. First of all, nine $N = 90$ nuclides are known (from ^{146}Ba to ^{162}Hf), and long rotational bands are observed in each of them (Fig. 1). Second, the first $K^\pi = 0^+$ excited states in these isotones (Fig. 1) have the properties of beta-vibrational states and relatively low excitation energies. The Rasmussen parameter $X = B(E0)/B(E2)$ takes a value that is quite close to that predicted by the vibrational model ($X = 0.4$). Third, it was shown in [1] that, in these isotones, the back-bending in the ground-state band is due to the crossing with the beta band. Difficulties arise when one tries to identify the origin of the levels near the crossing point. We give here unambiguous interpretation of the data (see Table 1 and Fig. 1). Levels with $J = 6$, 8, and 10 in the beta band of ^{158}Er, as well as those with $J = 4$–10 in ^{160}Yb and with $J = 0$–10 in ^{162}Hf, have not yet been observed. But a smooth dependence of the energies of the levels in the ground-state band and in the beta band on Z is revealed in the $N = 90$ isotones. Therefore, the positions of unknown levels can be found by extrapolating their energies along the isotone chain (i.e., along the Z axis; see circles in Fig. 1). In Fig. 1, the scale $\sqrt{E(J)}$ is used for the ordinate, whereby almost equal intervals between the points for each isotone are obtained.

Figure 2 shows the inertial parameter A^+ as a function of the spin J. The values of A^+ for the ground-state and beta bands are indicated by closed circles and crosses, respectively. One can see a similar behavior of A^+ values in the isotones from ^{154}Gd

---

[*] This article was submitted by the author in English.

[**] e-mail: `epgri@snoopy.phys.spbu.ru`

Table 1. Energies of levels (in keV) of the 0^+ bands built on the ground and beta-vibrational states in the $N = 90$ isotones

Nucleus		$J = 0$	2	4	6	8	10	12	14	16	18	20
^{146}Ba	g	0	181	513	958	1182	2051	2632	3192	3737	-	-
	β	1052										
^{148}Ce	g	0	158	454	840	1192	1792	2329	2889	-	-	-
^{150}Nd	g	0	130	381	720	1129	1599	2119	-	-	-	-
	β	675	851	1138	1541	-	-	-	-	-	-	-
^{152}Sm	g	0	122	366	707	1125	1609	2149	2736	3362	-	-
	β	685	810	1023	1310	1666	2079	2525	2977	-	-	-
^{154}Gd	g	0	123	371	718	1144	1673	2185	2777	3404	4087	4782
	β	681	815	1048	1366	1756	2192	2622	3027	3491	4016	4646
^{156}Dy	g	0	138	404	770	1216	1725	2286	2888	3523	4178	4859
	β	676	828	1088	1437	1859	2316	2706	3065	3499	4026	4635
^{158}Er	g	0	192	527	970	1493	2073	2681	3374	4026	4674	5373
	β	806	989	1257	-	-	-	2881	3191	3663	4230	4888
^{160}Yb	g	0	243	638	1147	1736	2373	3137	3746	4376	5091	-
	β	1086	1293	-	-	-	-	2959	3363	3847	4425	5089
^{162}Hf	g	0	285	730	1293	1940	2635	3386	3997	4555	5168	5807
	β	-	-	-	-	-	-	3185	3667	4068	4652	5310

Table 2. Energies of levels of the $K^\pi = 4^-$ bands (in keV)

N	Nucleus	$J = 4$	6	8	10	12	20	5	7	9	11	13	21
88	^{156}Er	1814	2206	2603	2905	3387	6062	-	-	-	3083	3675	6441
	^{158}Yb	-	2230	2650	2923	3407	6007	-	-	-	-	-	-
90	^{156}Dy	-	-	2346	2588	2942	5201	-	-	2408	2710	3104	5428
	^{158}Er	-	-	2333	2570	2955	5538	-	1853	2432	2731	3155	5739
	^{160}Yb	1568	2051	2363	2579	2979	5693	-	-	2481	2703	3195	5948
	^{162}Hf	1735	2118	2439	2623	3031	5776	1649	2039	-	2819	3248	6065
92	^{160}Er	1638	1908	2294	2533	2876	5020	-	-	2104	2520	2980	5326
	^{162}Yb	-	-	2280	2573	2938	5170	-	1768	2153	2605	3077	5482
94	^{164}Yb	1551	1799	2124	2484	2865	5069	1443	1674	2000	2401	2864	5206
	^{166}Hf	-	-	2197	2540	2911	5090	-	1726	2078	2497	2962	5253
	^{168}W	1578	1916	2318	2620	2967	5097	1537	1835	2213	2629	3074	5288
98	^{174}Os	1550	1790	2102	2476	2906	5112	1596	1860	2206	2613	3073	5266
	^{176}Pt	1736	2004	2320	2689	3091	-	1699	2010	2373	2787	3252	-
100	^{170}Yb	1258	1450	1716	2057	2474	4886	1345	1573	1872	2242	2681	-
	^{172}Hf	1419	1598	1852	2156	2598	4942	1503	1727	1969	2337	2778	5184
	^{174}W	1365	1628	1963	2330	2752	-	1401	1676	1999	2396	2862	5449

to ^{162}Hf. At the same time, the functions $A^+(J)$ for the ground-state and beta bands strongly differ from each other. (In Fig. 2, asterisks indicate the crossings of the ground-state and beta bands.)

In Fig. 3, we give a more detailed picture of the two band levels in the ^{154}Gd–^{162}Hf isotones in the vicinity of possible crossings. In this figure, one can clearly see that the spin value and the excitation energy

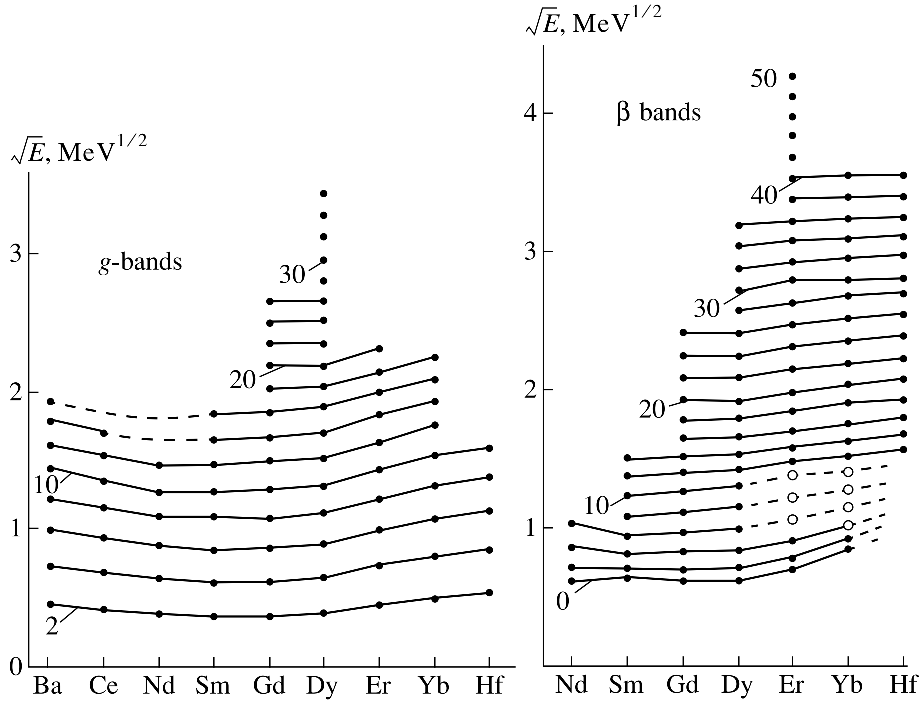

Fig. 1. Energies of rotational levels of ground-state and beta-vibrational bands in the $N = 90$ isotones.

where the band crossing occurs smoothly decrease with increasing Z. The arrows indicate the places of crossings of the ground-state and beta bands. The spin values at which the crossing occurs are written in the circles. It seems worthwhile to note that, in Figs. 2 and 3, some individual special features of each nucleus can be seen, but they are not so meaningful to mask the regularities discussed above.

3. $K^\pi = 4^-$ STATES

3.1. N = 88 Isotones: ^{156}Er *and* ^{158}Yb

In addition to a long $K^\pi = 0^-$ band, two level sequences are known in the ^{156}Er nuclide: $J^\pi = 6^-$ (2206.1 keV)–38^- (13066.3 keV) and $J^\pi = 11^-$ (3082.8 keV)–33^- (10934.8 keV) [2]. We attribute them to one $K^\pi = 4^-$ band, adding the known $J^\pi = 4^-$ level at 1814.48 keV to this band. Figure 4 shows the inertial parameters (closed circles) A^+ and (open circles) A^- versus J. The above interpretation can be confirmed by a similar behavior of the function $A^+(J)$ for the known even-spin band in ^{158}Yb up to $J^\pi = 30^-$ (9740.5 keV) [2] (Table 2). From Fig. 4, it can be seen that the values of the parameters A^+ in the ^{156}Er and ^{158}Yb nuclei are quite close. Since the differences of the absolute energies of the $J = 6$–30 states in these two nuclei are less than 50 keV, we conclude that these bands have similar structures. Thus, our interpretation of the origin of the band in ^{156}Er seems valid. At the same time, very small values of A^+ at $J = 10$ have yet to be explained.

3.2. N = 90 Isotones: ^{156}Dy, ^{158}Er, ^{160}Yb, *and* ^{162}Hf

The rotational bands in ^{156}Dy, ^{158}Er, and ^{160}Yb have similar properties. In ^{160}Yb, the even-spin level sequence starts from the 4^- level ($E_x = 1567.5$ keV, Table 2). It seems very probable that its structure is $4^-, p505\uparrow, -p651\uparrow$. According to the quasiparticle–vibrational model, the bandhead is expected to be at E_x= 2.0 MeV [3]. The bands in ^{156}Dy, ^{158}Er, and ^{162}Hf have the same structure. In ^{156}Dy, the level sequences were observed up to the $J^\pi = 42^-$ level at 15234.8 keV and up to the $J^\pi = 53^-$ level at 21665.2 keV. In ^{158}Er, they were observed up to the $J^\pi = 48^-$ level at 18131 keV (with the exception of the $J^\pi = 24^-$ and 26^- levels) and up to the $J^\pi = 47^-$ level at 18345 keV. In ^{160}Yb, the bands were traced up to the $J^\pi = 42^-$ level at 15403 keV and up to the $J^\pi = 39^-$ level at 13740 keV. In ^{162}Hf, the levels of these bands were observed up to, respectively, the $J^\pi = 24^-$ level at 7421.8 keV and the $J^\pi = 29^-$ level at 9184.8 keV (with the exception of the $J^\pi = 9^-$ level). The energies of lower levels of these bands are given in Table 2.

From the analysis of the available data, we can therefore conclude the following:

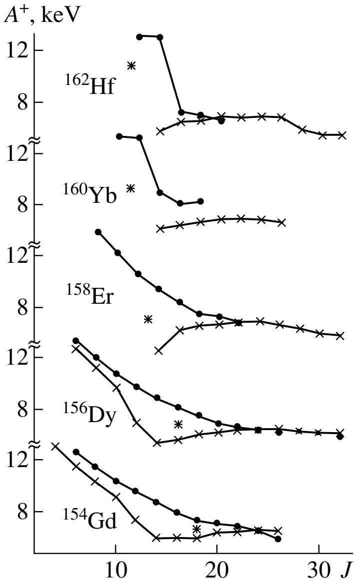

Fig. 2. Inertial parameter A^+ as a function of the spin J in the $N = 90$ isotones: (asterisks) band crossings, (closed circles) ground-state bands, and (crosses) beta bands.

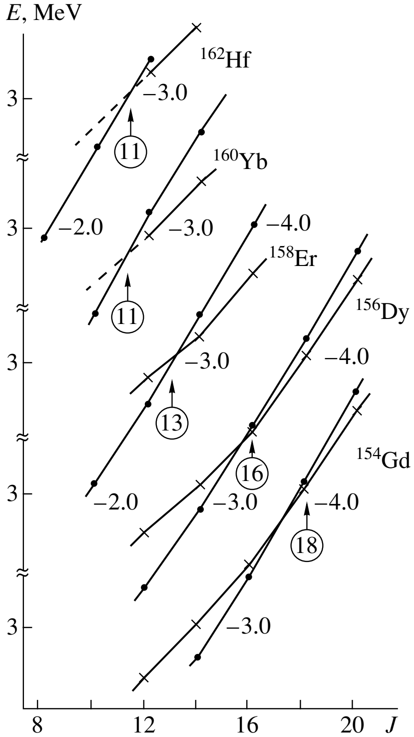

Fig. 3. Levels of the ground-state and beta bands in the vicinity of their crossings in the $N = 90$ isotones: (closed circles) levels of the ground-state bands and (crosses) levels of the beta-vibrational bands.

(1) The energies of the bandheads in the four isotones considered here are very close. The energy differences of the rotational levels are also small.

(2) The functions $A^+(J)$ and $A^-(J)$ are very similar in all four isotones (Fig. 4). These functions have a deep minimum at $J = 10$ and a bump at $J \approx 16$. The points corresponding to the levels with positive and negative signatures—i.e., with even and odd spins—refer to the same sequence. The same dependence was observed in ^{156}Er and in ^{158}Yb (Fig. 4).

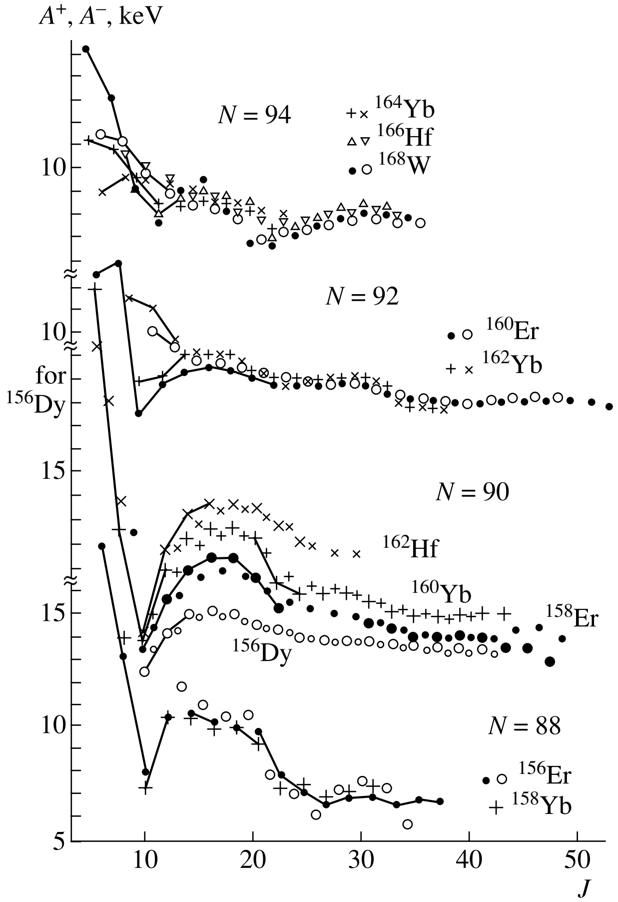

Fig. 4. Inertial parameters A^+ and A^- as functions of the level spin J for the $K^\pi = 4^-$ bands in the $N = 88$–94 isotones.

(3) The signature splitting is similar at the spin values of $J = 12$–30 (Fig. 5). The splitting increases for spin values of $J > 40$. The splitting inversion occurs at $J = 30$ in ^{160}Yb and at $J = 42$ in ^{158}Er.

3.3. $N = 92$ Isotones: ^{160}Er and ^{162}Yb

The dynamics of long $K^\pi = 4^-$ bands is determined by the properties of ^{160}Er and ^{162}Yb. It can be seen from Table 2 that the energies of the levels in these bands are quite close to each other in both nuclei. At the same time, they do not deviate far from the energies of the levels in the $N = 90$ isotones. In ^{160}Er, levels up to $J = 52$, 21515 keV and up to $J = 49$, 19938 keV were observed. Here, the quantum numbers $K^\pi = 4^-$ were assigned to the

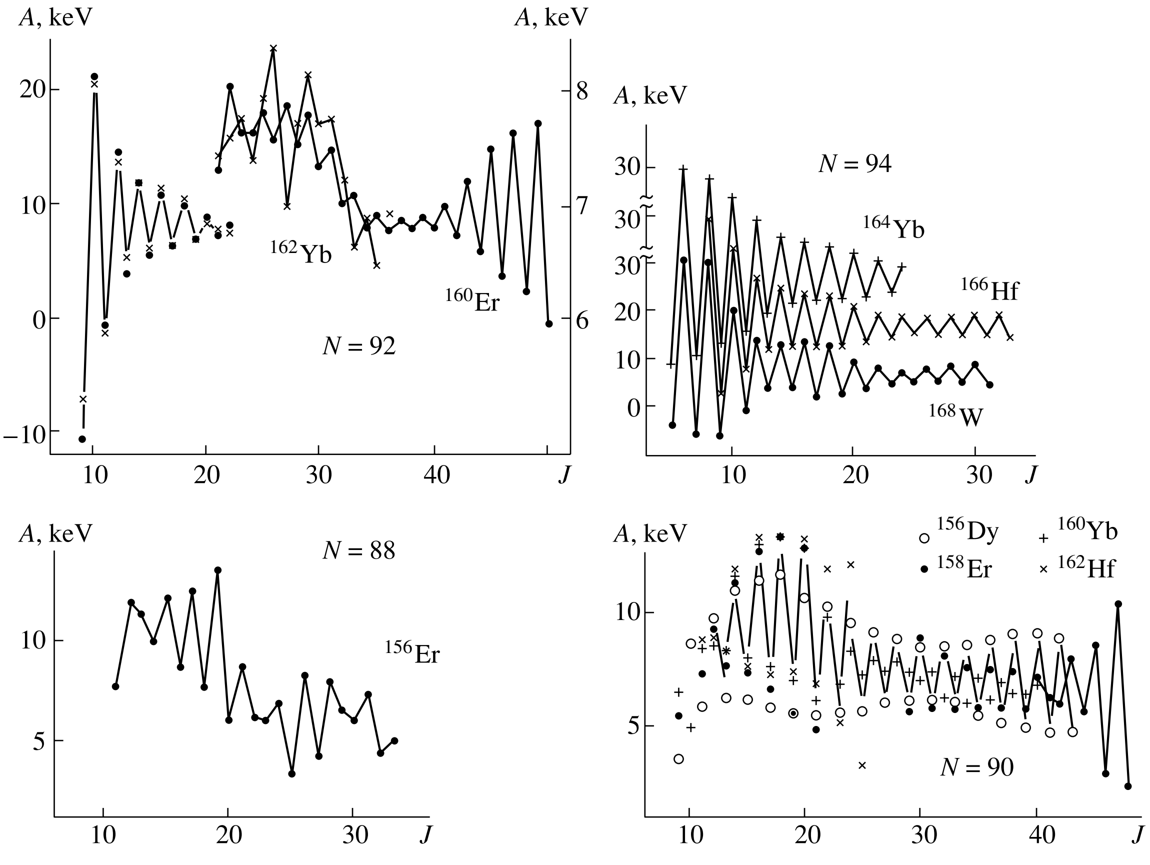

Fig. 5. Inertial parameter A as a function of the level spin J for the $K^\pi = 4^-$ bands in the $N = 88$–94 isotones.

bands in accordance with the characteristics of the lowest $J^\pi = 4^-$ head level at 1638 keV. In ^{162}Yb, two bands are known that extend up to the $J^\pi = 37^-$ level at 12392 keV and up to the $J^\pi = 36^-$ level at 11917.8 keV. The identification is made on the basis of the same arguments as for the $N = 88$ and $N = 90$ isotones.

Figure 4 shows the functions $A^+(J)$ and $A^-(J)$ in the ^{160}Er and ^{162}Yb nuclei. A deep minimum at $J = 10$ and a bump at $J = 16$ are observed in just the same was as in the $N = 88$ and $N = 90$ isotones (see Subsections 3.1 and 3.2). Moreover, there exists a more pronounced bump at $J = 29$.

Figure 5 displays the function $A(J)$. It demonstrates explicit signature splitting. The same can be seen in ^{156}Er and in the $N = 90$ isotones.

3.4. N = 94 Isotones

In ^{164}Yb, two $K^\pi = 4^-$ level sequences up to the $J^\pi = 24^-$ level at 6374.0 keV and up to the $J^\pi = 23^-$ level at 5308.1 keV are observed. In ^{166}Hf, these sequences can be traced up to the $J^\pi = 32^-$ level at 9991.2 keV and up to the $J^\pi = 33^-$ level at 10330.0 keV; in ^{168}W, these extend up to the $J^\pi = 34^-$ level at 10813 keV and up to the $J^\pi = 35^-$ level at 11128 keV. From Table 2, one can see that there are no $J = 4$, 6, and 5 levels in ^{166}Hf. The behavior of moments of inertia and the energies of the levels (Figs. 4 and 5) makes it possible to assign the quantum numbers $K^\pi = 4^-$ to this band. According to [3], it has the structure 4^-, $n521\uparrow + n642\uparrow$.

It should be noted that the dependences of A^+ and A^- on J in $N = 94$ isotones differ from those in $N \leq 92$ isotones.

4. CONCLUSIONS

The present study has been carried out in order to determine the structure of long ground-state and beta bands in $N = 90$ isotones and to examine the effects of their crossings. Moreover, we aimed at determining the structure of long $K^\pi = 4^-$ bands in deformed nuclei. Special attention has been given to "incomplete" bands where low-spin members have not yet been observed. From the analysis of the energies of the levels and of the inertial parameters by the method of analogies, we deduced the following results:

(1) The moments of inertia of different bands approach the rigid-body value (A≈ 7) with increasing spin.

(2) The point of crossing of the ground-state band and the beta band in the $N = 90$ nuclei moves to low spins with increasing Z. The beta bands in ^{158}Er, ^{160}Yb, and ^{162}Hf have been identified.

(3) Special features of the $K^\pi = 4^-$ bands have been investigated. The $K^\pi = 4^-$ bands in ^{158}Yb, ^{156}Dy, ^{158}Er, ^{162}Yb, and ^{166}Hf have been identified. A deep minimum of A^+ and A^- at $J = 10$ has been found in $N = 88$–92 nuclei. There is no such effect in bands having other values of K^π. A similar minimum was not observed in $N = 94$ isotones. Bumps at $J \approx 16$ and $J \approx 30$ and a minimum at $J \approx 22$ have been found in all the bands studied here. Similar features of signature splitting have been revealed in different bands. These facts call for a theoretical explanation.

ACKNOWLEDGMENTS

I am grateful to V.O. Sergeev for a discussion and enlightening comments.

REFERENCES

1. V. M. Belenkiĭ and E. P. Grigoriev, *Structure of Even–Even Nuclei* (Énergoatomizdat, Moscow, 1987).
2. Nucl. Data Sheets, various volumes.
3. E. P. Grigoriev and V. G. Soloviev, *Structure of Even–Even Nuclei* (Nauka, Moscow, 1974).

Physics of Atomic Nuclei, Vol. 64, No. 6, 2001, pp. 1087–1092. From Yadernaya Fizika, Vol. 64, No. 6, 2001, pp. 1162–1167.
Original English Text Copyright © 2001 by Leoni.

Mass and Deformation Dependence of Rotational Damping*

S. Leoni**

Dipartimento di Fisica, Università di Milano, and INFN Sezione di Milano, Italy

Received September 11, 2000

Abstract—The rotational motion in thermally excited nuclei and its damping at high excitation energy is discussed here with reference to the role of effects beyond mean-field approximation. The experimental results for different mass regions and deformations are presented and compared with a cranked-shell-model calculation including a two-body residual interaction of surface delta type. Altogether, it is found that the dependence of the mixing process on the nuclear mass and deformation is well reproduced by the data. *© 2001 MAIK "Nauka/Interperiodica".*

1. INTRODUCTION

The understanding of the rotational motion in thermally excited nuclei and of its damping at high excitation energy is one of the central issues in nuclear structure, and more in general in the study of the effects beyond mean field. In fact, the study of the collective rotation with increasing excitation energy is expected to shed light on the mechanisms which bring the zero temperature regular ordered motion, characterized by complete sets of quantum numbers for every state, into the chaotic compound nucleus regime, described by random combinations of the available configurations [1].

In rare-earth nuclei, on the order of 20 excited rotational bands, carrying strong $E2$ transitions, can be resolved at rather low heat energy. They can be well described by a rotating mean field, although interactions at crossings between them point beyond the mean field description [2, 3]. Such splitting of the rotational strength can be considered as a precursor of the fragmentation of the rotational decay, known as damping of the rotational motion at higher heat energies [4, 5].

With present-day techniques, our knowledge of damped rotation stems from the analysis of unresolved coincidence spectra. In particular, in double coincidence energy spectra, transitions along regular bands can be separated from damped transitions, forming a landscape of ridges and valleys [6]. While the ridges are formed by transitions from states at low excitation energy obeying rotational energy correlations, the valley is formed by γ rays from the region of higher level density above yrast. By a statistical analysis of the counts fluctuations of $\gamma\gamma$ spectra, one can extract the number $N_{\text{path}}^{(2)}$ of paths available to the nucleus in the γ decay through different regions of level density, namely, the number of excited bands, as well as the effective number of damped transitions [7, 8]. The very existence of a finite number of decay paths leads, in fact, to enhanced fluctuations μ_2/μ_1, whose magnitude is fixed by the number of paths through the simple relation $\mu_2/\mu_1 = N_{\text{even}}/N_{\text{path}} + 1$. Here, μ_1, μ_2, and N_{even} are the statistical moments and the number of counts in a $4/\Im \times 4/\Im$ sector, in which each rotational cascade contributes on the average one count, $\Im$ being the dynamical moment of inertia of the nucleus.

Systematic results have been obtained from a number of rare-earth nuclei analyzed ($A = 160$) [8]. Large fluctuations are observed in the ridge structures, showing that only a rather low number ($\approx$40) of discrete rotational bands exist up to excitation energy $\approx$800 keV above yrast. In contrast, very weak fluctuations are found along the central valley, revealing a number of coincidence combinations ($\approx 10^4$–10^5) larger than expected assuming that the rotational decay leads to a unique final state. These experimental findings have unambiguously shown that the rotational transition strength gets progressively fragmented with increasing excitation energy above yrast, a manifestation of the damping of the rotational motion [4].

The results of the fluctuation analysis are found to be well in accordance with a model of the thermally excited states as obtained from cranked mean bands interacting via a two-body surface-delta (SDI) residual interaction that includes high-multiple terms [5] and that in some cases is found to be configuration-dependent [9]. In particular, simulations of decay cascades on the basis of this model produce spectra

---

[*] This article was submitted by the author in English.

[**] e-mail: `silvia.leoni@mi.infn.it`

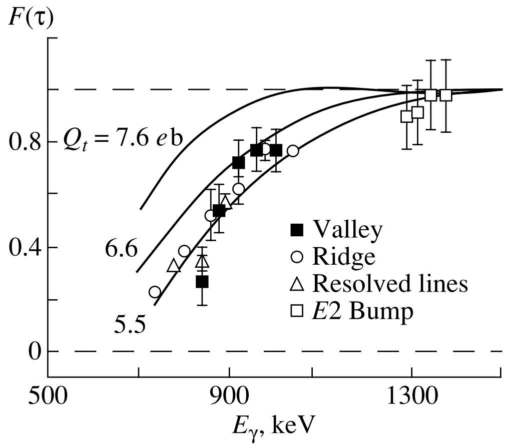

Fig. 1. The measured fractional Doppler shifts for some discrete transitions and for different parts of the quasi-continuum $\gamma\gamma$ spectra of ^{164}Yb. The curves represent the expected theoretical values for $Q_t = 5.5$, 6.6, and 7.6 e b [corresponding to 200, 300, and 400 W.u. (Weisskopf unit), respectively] [11].

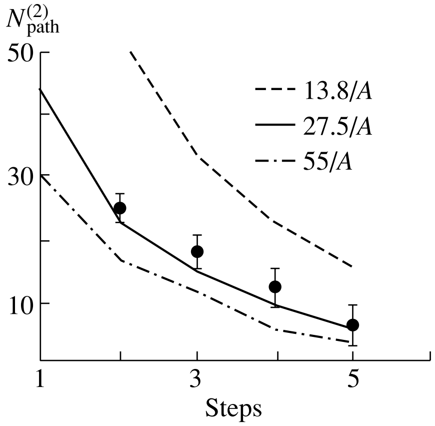

Fig. 2. The average number of bands obtained from the experimental analysis of the measured ridge structures of ^{168}Yb as a function of the number of decay steps (points), in comparison with the predictions from cranked shell model calculations plus a two-body residual interaction with interaction strength $V_0 = 13.8/A$, $27.5/A$, and $55/A$ MeV (lines) [13].

of approximately the same shape, carrying quantitatively the same count fluctuations in the different regions of the spectra as seen experimentally [10].

The basic assumption behind the damping model, namely, that the warm nucleus is strongly collective with a quadrupole moment Q_t of the same order as that of the cold regular rotational bands, has been experimentally verified in the case of the typical rare-earth nucleus ^{164}Yb by a lifetime measurements of the damped transitions [11]. Using an experimental technique based on the fluctuation pattern (covariance method) [12], the fractional Doppler shifts of unresolved transitions along the valley of $\gamma\gamma$ spectra have been extracted. As shown in Fig. 1, the experimental results show that the rotational collectivity persists with full strength also when the rotational bands are strongly mixed, giving further support to the rotational damping model.

In order to test the sensitivity to the strength of the SDI residual interaction used in the model, which is known to strongly affect the properties of the nuclear many-body system at finite temperature, a more detailed comparison between experimental data and theoretical predictions has been made. This has been obtained by the analysis of rotational energy correlations extending over several decay steps. Such correlations can be especially emphasized in the so-called tilted rotational planes of triple γ-ray coincidence matrices [13], which pick out and much enhance the ridge structures compared to the background of uncorrelated coincidences. Each plane, defined by the equation $E_{\gamma_1} - E_{\gamma_3} = N \times (E_{\gamma_3} - E_{\gamma_2}) \pm \delta/2$, δ being the thickness of the plane and $N = 1, 2, 3, \ldots$ [6], selects different types of coincidences along rotational bands: the $N = 1$ plane will select three consecutive γ-ray transitions, the $N = 2$ plane will contain three γ-ray transitions out of four consecutive transitions, and so on.

Figure 2 shows the average number of bands obtained from the fluctuation analysis of the measured ridge structures of the tilted rotational plane of ^{168}Yb as a function of the cascade length, in comparison with the prediction from cranked shell model calculations plus a two-body SDI residual interaction with interaction strength $V_0 = 13.8/A$, $27.5/A$, and $55/A$ MeV. As one can see, good agreement is found between data and calculations using the interaction strength $V_0 = 27.5/A$ MeV, which agrees with the analysis of low-lying collective vibrations and the pairing in rare-earth deformed nuclei [14].

Until recently, a convincing picture of collective damped rotation has mainly been obtained for the mass region $A \approx 160$. However, in the original formulation of the rotational damping model [4], large variations with mass number and deformation were predicted. In particular, the onset energy U_0, at which damping sets in, is expected to depend on the level density and on the strength of the residual interaction and is predicted to vary with mass number as $U_0 \approx A^{-2/3}$. In addition, the rotational damping width $\Gamma_{\rm rot}$, expressing the width of the quadrupole transition strength distribution, is expected to follow the relation $\Gamma_{\rm rot} \approx IA^{-5/2}\epsilon^{-1}$, where I, A, and ϵ are the spin, mass number, and deformation, respectively.

To determine the validity of the relations given above, one needs to compare data from nuclei in

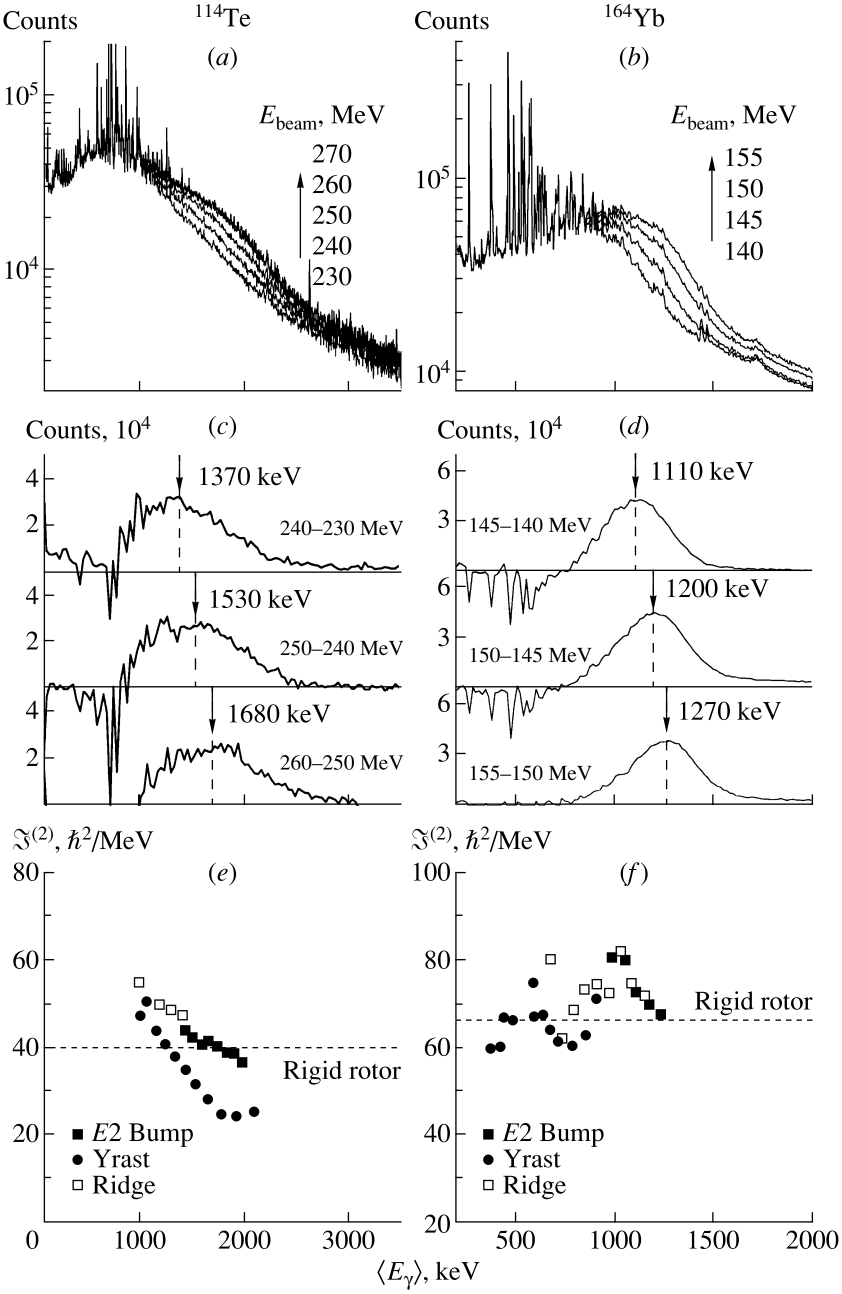

Fig. 3. (*a*, *b*) γ spectra measured at different bombarding energies for ^{114}Te and ^{164}Yb, respectively. The arrows indicate that the spectra with the lowest number of counts in the continuous distribution correspond to the lowest bombarding energy. (*c*, *d*) Difference spectra between two consecutive bombarding energies. The arrows indicate the positions of the centroids of the distributions. (*e*, *f*) The dynamical moment of inertia $\Im^{(2)}$ for ^{114}Te and ^{164}Yb, respectively [16].

different regions of mass and deformation. For this purpose, dedicated experiments were recently made with the EUROBALL array [15], as described in the next sections.

2. MASS DEPENDENCE OF ROTATIONAL DAMPING

The mass dependence of rotational damping has been tested by a comparative analysis of the unresolved γ transitions of the ^{114}Te and ^{164}Yb nuclei, having very similar deformation $\epsilon \approx 0.25$ [16]. The two nuclei can be considered as representative examples of the mass region $A = 110$ [17] and $A = 160$ [8], for which a factor of 2 difference in the damping width is expected.

The nucleus ^{114}Te has been produced by the fusion reaction ^{64}Ni + ^{54}Cr → ^{118}Te at bombarding

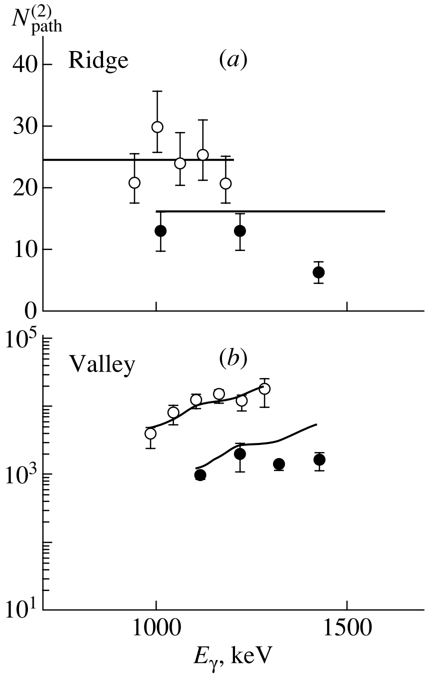

Fig. 4. (*a*) The quantity $N^{(2)}_{\text{path}}$ obtained with the fluctuation analysis of the measured first ridges of ^{114}Te and ^{164}Yb (closed and open circles, respectively), in comparison with the theoretical results (solid lines). (*b*) The quantity $N^{(2)}_{\text{path}}$ extracted from the valley analysis for ^{114}Te and ^{164}Yb (closed and open circles, respectively), in comparison with the corresponding theoretical results (solid lines) [16].

energies $E_{\text{beam}} = 230, 240, 250, 260,$ and 270 MeV. The largest fraction of the data was taken at $E_{\text{beam}} =$ 250 MeV, which populated the residual nucleus ^{114}Te at ≈20% level. The data for the nucleus ^{164}Yb were instead obtained in a previous measurement made with the EUROGAM II array using the reaction ^{30}Si + ^{138}Ba at the bombarding energies of 140, 145, 150, and 155 MeV [11].

Figures 3*a* and 3*b* show the spectra obtained at the different bombarding energies for the ^{114}Te and ^{164}Yb nuclei. In both cases, one can observe the presence of a pronounced continuous bump of increasing intensity with bombarding energy, with characteristic transition energy at ≈1.8–2 MeV in ^{114}Te and ≈1.2–1.3 MeV in ^{164}Yb. This is consistent with the fact that at a given spin the rotational transition energy is higher for a nucleus with smaller value of the moment of inertia, being $E_\gamma \propto \Im^{-1} \propto A^{-5/3}$. In particular, the average energy of the rotational bump is observed to move to higher transition energy with increasing bombarding energy and maximum angular momentum, which is a typical feature of rotational nuclei. This can be clearly seen in the difference between spectra corresponding to two consecutive bombarding energies, as shown in Figs. 3*c* and 3*d*. In addition, values of the fractional Doppler shifts for the edge of the rotational bump measured in forward and backward angles have been obtained using the same type of analysis carried out in [18]. The values show that the transitions at the edge of the bump are fully shifted, thus supporting the strong collective character of the continuous bumps observed in both ^{114}Te and ^{164}Yb nuclei. The widths of the distributions of the difference spectra shown in Figs. 3*c* and 3*d* are expected to give an upper limit for the rotational damping width Γ_{rot} [17]. In the present case, the widths are found to be larger by a factor of ≈2 in the case of ^{114}Te (with values 800–1000 keV), as compared to those of ^{164}Yb (with values 300–400 keV), supporting the scaling of Γ_{rot} with mass number.

Figures 3*e* and 3*f* show the dynamical moment of inertia $\Im^{(2)}$ for ^{114}Te and ^{164}Yb nuclei, as extracted from the analysis of the yrast transitions (circles), of the excited regular bands forming the ridges (open squares), and of the damped rotational transitions populating the continuous bump (closed squares). As one can see, in both nuclei the moment of inertia of the excited rotational transitions shows rather high values, close to that of a rigid rotor, indicating that the thermally excited nucleus rotates collectively.

More quantitative information on the rotational motion at thermal energy in the two different mass regions $A = 110$ and $A = 160$ has been obtained by the study of $\gamma\gamma$-coincidence spectra of ^{114}Te and ^{164}Yb nuclei. Figure 4 shows the experimental results obtained from the fluctuation analysis of the ridge and valley structures of both nuclei, in comparison with theoretical predictions from a cranked shell model calculation including the two-body SDI residual interaction [5]. As one can see, the calculations are found to reproduce both the ridge and the valley results quite well, strongly supporting the scaling with the mass number of the residual interaction and the level density. According to the present calculation, damping should set in around heat energy $U_0 \approx 0.9$–1.0 MeV in ^{114}Te, compared to $U_0 \approx 0.7$–0.8 MeV in ^{164}Yb. In addition, the values of the damping widths predicted by the band mixing calculations are approximately a factor of two larger for ^{114}Te than for ^{168}Yb, in good agreement with the scaling of Γ_{rot} with mass number, as given in the original formulation of the damping model [4].

3. DEFORMATION DEPENDENCE OF ROTATIONAL DAMPING

The dependence of rotational damping on the nuclear deformation has been tested in a EUROBALL

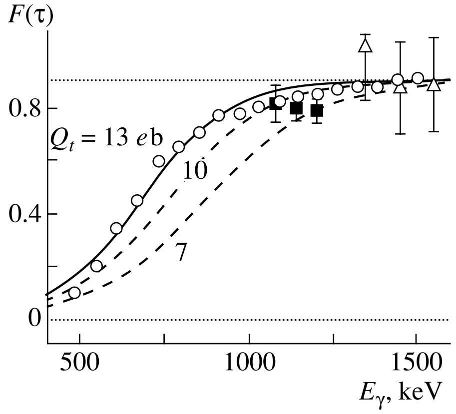

Fig. 5. The measured fractional Doppler shifts for the superdeformed yrast (circles), the superdeformed ridges (squares), and the $E2$ bump (triangles) of ^{143}Eu. The curves represent the expected theoretical values for $Q_t = 13$, 10, and 7 *e* b.

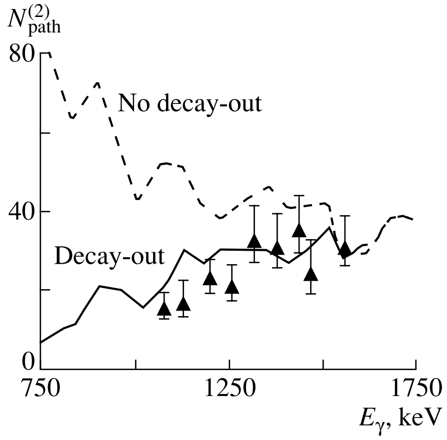

Fig. 6. The number of excited rotational bands obtained with the fluctuation analysis of the superdeformed ridge structures of ^{143}Eu, compared with cranked shell model calculations plus a two-body residual interaction including (solid line) or not (dashed line) the decay-out process into the normal deformed well.

experiment aiming at the study of the superdeformed (SD) nucleus ^{143}Eu. The nucleus was populated by the fusion reaction $^{37}\mathrm{Cl} + {}^{110}\mathrm{Pd} \rightarrow {}^{147}\mathrm{Eu}$, at beam energies of 165 and 170 MeV. As shown in previous works, the nucleus ^{143}Eu is characterized by a very complex and irregular level scheme at low spin, due to the existence of both spherical and triaxially deformed shapes [19], while a strong superdeformed minimum is expected to dominate at high angular momenta [20]. In addition, the population of the SD excited states is found to be particularly strong [21], as a consequence of the low crossing between the normal and superdeformed yrast lines, which occurs already around angular momentum $\approx 40\hbar$, compared to $\approx 54\hbar$ in the more typical case of ^{152}Dy. In fact, $\gamma\gamma$-coincidence spectra of ^{143}Eu show, in the high transition energy region, a pronounced ridge-valley structure corresponding to the moment of inertia of a superdeformed nucleus with deformation $\epsilon \approx 0.55$, while a strong $E2$ bump of superdeformed nature can be seen in one-dimensional spectra.

Figure 5 shows the fractional Doppler shift values experimentally obtained from the analysis of the discrete yrast transitions of the SD band (circles), of the superdeformed ridges (squares), and of the continuous bump (triangles), in comparison with the prediction corresponding to different values of the quadrupole moment Q_t. As one can see, the experimental results are in agreement with a quadrupole deformation of the order of 10–13 *e* b, which proves the superdeformed nature of the excited rotational bands. This gives further support to the basic assumption of the rotational damping model, namely, that the nucleus maintains its collectivity up to rather high excitation energy, both in normal and superdeformed nuclei.

The number of superdeformed excited rotational bands forming the ridge structures of ^{143}Eu has been obtained from the fluctuation analysis method and is shown in Fig. 6. As one can see, the number of bands is found to depend very strongly on the transition energy, reaching a value of ≈ 35 at the maximum of the population. The experimental results have been compared with a microscopic-cranked-shell model calculation plus a two-body SDI residual interaction for the specific nucleus ^{143}Eu. As shown in Fig. 6, the calculation (dashed line) is close to the data at the maximum of the distribution, while it deviates strongly at lower transition energies. This is generally expected for the lower part of the ridge structure, since barrier penetration into the first well removes intensity from the excited bands, eventually leaving only the yrast band together with a few low-lying bands to survive further down in angular momentum. The reduction observed in the number of bands at low transition energy (low spin) can also be explained by the theoretical model once the decay-out mechanism of the excited states is taken into account (solid line) [22]. In the model, the decay-out of the excited superdeformed states is treated as a quantum tunneling between the compound states in the superdeformed and normal well, extending a statistical model which has been previously applied to the decay-out of the superdeformed yrast band [23].

4. CONCLUSIONS

The rotational motion in thermally excited nuclei and its damping at high excitation energy have been discussed here in connection with experimental data from different regions of mass and deformation. Several results have been obtained mainly by using the experimental technique of the statistical fluctuations and compared with cranked-shell-model calculations plus a two-body residual interaction. This model predicts a dependence on both deformation and mass number for the damping mechanism. The good agreement found for the three different nuclei here discussed (^{164}Yb, ^{114}Te, and ^{143}Eu) has therefore allowed a very stringent test to the damping model, which describes the nucleus on its way to the chaotic compound nucleus regime.

ACKNOWLEDGMENTS

This work is based an several experiments with the EUROGAM II and EUROBALL arrays.

In particular, I thank the participation of Angela Bracco, Franco Camera, Sergio Frattini, Benedicte Million, and Enrico Vigezzi from University of Milano; Mats Bergstrom, Bent Herskind, Gudrun Hagemann, and Thomas Døssing from the Niels Bohr Institute; and Masayuki Matsuo from Niigata University.

REFERENCES

1. B. R. Mottelson, Nucl. Phys. A **557**, 717c (1993).
2. G. B. Hagemann *et al.,* Nucl. Phys. A **618**, 199 (1997).
3. J. M. Espino *et al.,* Nucl. Phys. A **640**, 163 (1998).
4. B. Lauritzen, T. Døssing, and R. A. Broglia, Nucl. Phys. A **457**, 61 (1986).
5. M. Matsuo, T. Døssing, E. Vigezzi, *et al.,* Nucl. Phys. A **617**, 1 (1997).
6. S. Leoni, B. Herskind, T. Døssing, *et al.,* Nucl. Phys. A **587**, 513 (1995).
7. B. Herskind, A. Bracco, R. A. Broglia, *et al.,* Phys. Rev. Lett. **68**, 3008 (1992).
8. T. Døssing, B. Herskind, S. Leoni, *et al.,* Phys. Rep. **268**, 1 (1996).
9. P. Bosetti, S. Leoni, A. Bracco, *et al.,* Phys. Rev. Lett. **76**, 1204 (1996).
10. A. Bracco, P. Bosetti, S. Frattini, *et al.,* Phys. Rev. Lett. **76**, 4484 (1996).
11. S. Frattini, A. Bracco, S. Leoni, *et al.,* Phys. Rev. Lett. **81**, 2659 (1998).
12. S. Leoni, T. Døssing, A. Bracco, *et al.,* Nucl. Phys. A **671**, 71 (2000).
13. S. Leoni, A. Bracco, T. Døssing, *et al.,* Eur. Phys. J. A **4**, 229 (1999).
14. A. Faessler, Fortschr. Phys. **16**, 18 (1968).
15. J. Simpson, Heavy Ion Phys. **6**, 253 (1997).
16. S. Frattini, A. Bracco, S. Leoni, *et al.,* Phys. Rev. Lett. **83**, 5234 (1999).
17. A. Bracco, S. Frattini, S. Leoni, *et al.,* Nucl. Phys. A **673**, 64 (2000).
18. B. Million, S. Leoni, A. Bracco, *et al.,* Phys. Lett. B **415**, 321 (1997).
19. M. Piiparinen, A. Atac, J. Blomqvist, *et al.,* Nucl. Phys. A **605**, 191 (1996).
20. A. Atac, M. Piiparinen, B. Herskind, *et al.,* Phys. Rev. Lett. **70**, 1069 (1993).
21. S. Leoni, B. Herskind, T. Døssing, *et al.,* Phys. Rev. Lett. **76**, 3281 (1996).
22. K. Yoshida, M. Matsuo, and Y. R. Shimizu, in *Proceedings of the Workshop of the Yukawa Institute "Dissipation and Damping in Nuclear Dynamics," Soryushirou Kenkyu, Kyoto, 1999,* Vol. C7, p. 99.
23. Y. R. Shimizu, E. Vigezzi, T. Døssing, and R. A. Broglia, Nucl. Phys. A **557**, 99c (1993).

Physics of Atomic Nuclei, Vol. 64, No. 6, 2001, pp. 1093–1097. From Yadernaya Fizika, Vol. 64, No. 6, 2001, pp. 1168–1172.
Original English Text Copyright © 2001 by Pavlichenkov.

Superfluid-to-Normal Phase Transition in Superdeformed Bands[*]

I. M. Pavlichenkov[**]

Russian Research Centre Kurchatov Institute, pl. Kurchatova 1, Moscow, 123128 Russia

Received September 11, 2000

Abstract—A semiclassically exact solution for the second inertial parameter $\mathcal{B}$ is found for the superfluid and normal phases. An interpolation between these limiting values shows that $\mathcal{B}$ changes sign in the transition region at the spin I_c that is critical for the rotational spectrum. A superfluid-to-normal transition reveals itself in a specific variation of $\mathcal{B}$ versus the spin I. Experimental data show the existence of a transition for superdeformed bands in the $A \sim 80, 130$, and 150 mass regions and for some bands characterized by a normal deformation. A transition to the normal phase explains the extreme regularity of superdeformed bands. © *2001 MAIK "Nauka/Interperiodica".*

One of the amazing features of superdeformed (SD) rotational bands is the extreme regularity of their rotational spectra: an SD nucleus is the best quantum rotor known in nature. Although numerous theoretical calculations [1–4] successfully reproduce the measured intraband γ-ray energies, the underlying microscopic mechanism of this phenomenon has yet to be well understood. To explain the regularity of SD rotational spectra, we parameterize the relevant energy as the three-term expression

$$E(I) = E_0 + \mathcal{A}I(I+1) + \mathcal{B}I^2(I+1)^2, \tag{1}$$

which is valid for an axisymmetric deformed nucleus with $K = 0$. The inertial parameters $\mathcal{A} = \hbar^2/2\Im^{(1)}$ ($\Im^{(1)}$ is the kinematic moment of inertia) and $\mathcal{B}$ are the objects of our investigation. They are determined by the transition energies $E_\gamma(I) = E(I+2) - E(I)$ as follows:

$$\mathcal{A}(I) = \frac{1}{4(2I+5)} \tag{2}$$

$$\times \left[\frac{I^2+7I+13}{2I+3}E_\gamma(I) - \frac{I^2+3I+3}{2I+7}E_\gamma(I+2)\right],$$

$$\mathcal{B}(I) = \frac{1}{8(2I+5)}\left[\frac{E_\gamma(I+2)}{2I+7} - \frac{E_\gamma(I)}{2I+3}\right].$$

The coefficient $\mathcal{B}(I)$ characterizes the nonadiabatic properties of a band and realizes the relationship of kinematic and dynamic ($\Im^{(2)}$) moments of inertia,

$$\mathcal{B} = \frac{\hbar^2}{2(2I+3)(2I+7)}\left[\frac{1}{\Im^{(2)}} - \frac{2I}{(2I+5)\Im^{(1)}}\right]. \tag{3}$$

The ratio $\mathcal{B}/\mathcal{A}$ determines the convergence radius [5] of the expansion in (1), which is large for SD bands. A faster convergence is obtained with the Harris formula

$$E(\omega) = E_0 + \frac{1}{2}\alpha\omega^2 + \frac{3}{4}\beta\omega^4, \tag{4}$$

which is based on the fourth-order cranking expansion

$$\alpha = \frac{1}{\omega}\mathrm{tr}(\ell_x\rho^{(1)}), \quad \beta = \frac{1}{\omega^3}\mathrm{tr}(\ell_x\rho^{(3)}), \tag{5}$$

where $\rho^{(n)}$ is the nth correction to the nucleus density matrix; ℓ_x is the projection of the single-particle angular momentum onto the rotational axis x, which is perpendicular to the symmetry axis z; and ω is the rotational frequency. It follows from (1) and (4) that

$$\alpha = \frac{\hbar^2}{2\mathcal{A}}, \quad \beta = -\frac{\hbar^4\mathcal{B}}{4\mathcal{A}^4}. \tag{6}$$

For the sake of simplicity, we will deal with the parameter β.

The problem of microscopically calculating the parameter $\mathcal{B}$ for normal deformed (ND) nuclei has attracted considerable attention. It has been shown that this quantity receives contributions from four types of nonadiabatic effects: (i) perturbation of quasiparticle motion by rotation (quasiparticle alignment), (ii) attenuation of pairing correlation by the Coriolis force, (iii) a change in the nuclear equilibrium deformation (centrifugal stretching), and (iv) vibration–rotation interaction. The first two effects are dominant for well-deformed nuclei, as was shown in the first attempts at obtaining $\mathcal{B}$ [6–8] and confirmed by subsequent calculations (see the review article [9] and references therein). Of the remaining two effects, the quasiparticle alignment depends strongly on pairing correlations because the pairing force tries to bind

---

[*] This article was submitted by the author in English.

[**] e-mail: `pavi@pretty.mbslab.kiae.ru`

1063-7788/01/6406-1093$21.00 © 2001 MAIK "Nauka/Interperiodica"

pairs of particles in time-reversal states, reducing the ability of nucleons to carry an angular momentum. Therefore, the parameter $\mathcal{B}$ sensitively depends on the variation of the pairing correlations along a band.

There are two features of pairing correlations in SD bands compared to ND ones. First, owing to a large shell gap stabilizing the SD minimum, the static pairing field Δ is small and can be commensurate with its fluctuation $\delta\Delta$ (dynamical pairing correlations). A qualitative conclusion concerning the role of static and dynamical pairing in SD bands is presented in [10]. Second, since intruder single-particle states, which are unavailable at normal deformations, appear in the case of superdeformations, it is necessary to go beyond the commonly used monopole pairing force [11]. A gauge-invariant pairing interaction expands the correlation space and stabilizes the pairing field. The coordinate-dependent (nonuniform) pairing is crucial for nucleon-current conservation in a rotating nucleus as well [12]. These features do not allow one to use the results of previous theoretical calculations of the parameter $\mathcal{B}$ for superdeformations. For the first time, we present an exact solution for the second inertial parameter in the superfluid ($\Delta \gg \delta\Delta$) and normal ($\Delta = 0$) phases. Since present-day theoretical methods do not allow one to describe correctly the transition region ($\Delta \sim \delta\Delta$), we use interpolation that reveals the critical spin I_c of a rotational spectrum, $\mathcal{B}(I_c) = 0$.

The semiclassical method developed in [6] is used to represent the parameter β in the superfluid phase as

$$\beta_s = -\frac{\hbar^4}{4\Delta^2}\sum \ell^x_{12}\ell^x_{23}\ell^x_{34}\ell^x_{41} \times F(x_{12}, x_{23}, x_{34}, x_{41})\delta(\varepsilon_1 - \varepsilon_{\mathrm{F}}), \tag{7}$$

where the summation indices $i = 1, 2, 3, 4$ refer to the single-particle states i of the nonrotating mean field with the energy ε_i. The delta function implies that summation over the states 1 is replaced by an integral in the semiclassical approximation [12]. The dimensionless quantities $x_{ii'} = (\varepsilon_i - \varepsilon_{i'})/2\Delta$, where Δ is the state-independent pairing gap at $\omega = 0$, correspond to the energy differences between states permitted by the selection rules for the matrix element of ℓ_x. The function F depending on these quantities can be represented in the form

$$F = \sum_{k=0}^{3} \hat{P}_k G_{12} + \sum_{k=0}^{1} \hat{P}_k H_{13} - 8D_2^2 x_{12}x_{23}x_{34}x_{41}h(x_{13}), \tag{8}$$

where the permutation operators $\hat{P}_k x_{i,i'} = x_{i+k,i'+k}$ in the space of four indices i ($i \mod 4 = i$) are used to simplify the formulas. The expressions for G_{12} and H_{13} involve the well-known functions [12]

$$h(x) = (1 + x^2)g(x), \qquad g(x) = \frac{\operatorname{arg\,sinh} x}{x\sqrt{1+x^2}} \tag{9}$$

and have the form

$$\begin{aligned} G_{12} = \frac{g(x_{12})}{x_{23}x_{41}x_{13}x_{24}}\{&(1 - D_1 x_{12}^2) \\ &\times \left[-1 - x_{12}^2 - x_{23}x_{41} \right. \\ &+ D_1\left[x_{23}^2(1 - x_{12}x_{24}) + x_{41}^2(1 + x_{12}x_{13})\right] \\ &\left. + D_1^2 x_{23}x_{34}x_{41}(x_{23} + x_{41}) + D_1^3 x_{12}x_{23}^2x_{34}x_{41}^2\right] \\ &+ D_1(x_{34} - D_1 x_{12}x_{23}x_{41}) \\ &\times (x_{34} + x_{12}x_{13}x_{24} - D_1 x_{12}x_{23}x_{41})\}, \end{aligned} \tag{10}$$

$$\begin{aligned} H_{13} = \frac{h(x_{13})}{x_{12}x_{23}x_{34}x_{41}} &\times \left[1 - D_1(x_{12}^2 + x_{23}^2 + x_{34}^2 + x_{41}^2)^2 \right. \\ &\left. + D_1^2(x_{12}x_{41} + x_{23}x_{34})\right]. \end{aligned}$$

The quantity β_s in (7) multiplied by ω^3 is the third-order cranking correction to the total angular momentum of the neutron or proton system. We want to emphasize that (7) represents the first theoretically correct expression for a high-order effect of the Coriolis pairing interaction at a fixed deformation. The result is obtained by taking into account the effect of rotation on Cooper pairs in the gauge-invariant form. This effect is described by the first and second corrections to the pairing energy,

$$\Delta^{(1)}(\mathbf{r}) = -\frac{i\hbar^2\omega}{2\Delta}D_1\dot{\ell}_x, \tag{11}$$

$$\Delta^{(2)}(\mathbf{r}) = \frac{\hbar^4\omega^2}{4\Delta^3}D_2\dot{\ell}_x^2,$$

where D_1 and D_2 are the amplitudes of the nonuniform pairing fields that are found in a self-consistent way. The theory incorporating nonuniform pairing also allows one to consider various limiting cases for the inertial parameters, which make it possible to study the interplay between rotation, pairing correlations, and the mean-field deformation in a SD band.

In order to consider this problem quantitatively, we will use an axially deformed oscillator potential with frequencies ω_x and ω_z along the corresponding axes. In this model, the matrix element ℓ^x_{12} is nonzero for two types of transitions: (i) transitions inside a single oscillator shell (close transitions) with $x_{12} = \pm\nu_1$ and (ii) transitions over a shell (distant transitions) with $x_{12} = \pm\nu_2$. The quantities ν_1 and ν_2 are well-known parameters involved in the moment of inertia [12],

$$\nu_{1,2} = \frac{\hbar(\omega_x \mp \omega_z)}{2\Delta} = \frac{k \mp 1}{2\xi k^{2/3}}, \qquad \xi = \frac{\Delta}{\hbar\omega_0}, \tag{12}$$

where $\hbar\omega_0 = 41A^{-1/3}$ MeV. Hereafter, we use the axis or the frequency ratio $k = c/a = \omega_x/\omega_z$ and the volume-conservation condition $\omega_x^2\omega_z = \omega_0^3$. The quantities ν_1 and ν_2 are both large for superdeformation. For the fixed state 1, there are 36 combinations of these basis transitions in the sum in (7). Performing summation over the states 1 in the Thomas–Fermi approximation, we find in the oscillator potential that

$$\beta_s = \frac{(k+1)^4}{1875\hbar^2 k^{4/3}} AM^3R^6\Phi(\xi, k), \qquad (13)$$

where $R = 1.2A^{1/3}$ fm is the radius of the sphere whose volume is equal to that of the spheroid with half-axis $a < c$, M is the nucleon mass, and A is the number of nucleons. The function Φ, along with its limiting cases, is shown in Fig. 1. It can be seen that nonuniform pairing reduces substantially β_s and consequently the parameter $\mathcal{B}$. On the other hand, the contribution of distant transitions is minor for small ξ. Nevertheless, the latter is necessary to obtain the hydrodynamic limit. Since $\Phi \sim 1$ for a reasonable pairing gap, $\Delta \sim 0.5$ MeV, β_s is of order $\hbar^4(A/\varepsilon_{\mathrm{F}})^3$. This, together with the estimate $\mathcal{A} \sim \varepsilon_{\mathrm{F}}A^{-5/3}$, yields $\mathcal{B}/\mathcal{A} \sim A^{-2}$, which overestimates the minimal value of this ratio in all SD mass regions. Thus, a small Δ and nonuniform pairing do not solve the problem of the regularity of SD bands.

Let us now consider the normal phase. The right-hand side of Eq. (7) vanishes in the limiting case $\Delta = 0$. This result is an artifact of the semiclassical approximation used in (7). For the parameter β in the normal phase, the correct expression obtained with the limiting values of the Bogolyubov amplitudes ($u_i = 0$ and $v_i = 1$ for $n_i = 1$ and $u_i = 1$ and $v_i = 0$ for $n_i = 0$, where n_i is the nucleon occupation numbers) has the form

$$\beta_n = -\hbar^4 \sum \ell_{12}^x \ell_{23}^x \ell_{34}^x \ell_{41}^x \sum_{k=0}^{3} \hat{P}_k \left\{ \frac{n_1}{\varepsilon_{12}\varepsilon_{13}\varepsilon_{14}} \right\}. \qquad (14)$$

The odd function of the differences $\varepsilon_{ii'} = \varepsilon_i - \varepsilon_{i'}$ leads to the cancellation of the leading terms in the sum in (14), whereby β_n is substantially reduced, $\beta_n \sim \hbar^4 A^{7/3}/\varepsilon_{\mathrm{F}}^3$. In the normal phase, the centrifugal-stretching effect is therefore of the same order as the particle-alignment effect, $\beta_{\mathrm{str}} \sim \beta_n$. For the oscillator potential, we have

$$\beta_n + \beta_{\mathrm{str}} = \frac{k^4 - 10k^2 + 1}{6\omega_0^2 k^{4/3}} AMR^2. \qquad (15)$$

It can be seen that $\beta_n + \beta_{\mathrm{str}} < 0$ for prolate nuclei with $c/a < 3.15$, whereas β_s is always positive. Thus, the ratio $\mathcal{B}/\mathcal{A}$ has to change sign with increasing spin I and approach its limiting value of $\mathcal{B}_n/\mathcal{A}_n \sim A^{-8/3}$, $\sim 10^{-6}$ for the SD bands in the 130 and 150 mass regions. The limiting ratio for a nucleus consisting of Z protons and N neutrons is

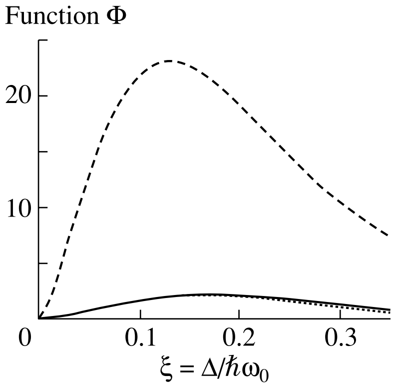

Fig. 1. Plot of the function Φ from (13) against the dimensionless quantity ξ for the axis ratio $c/a = 2$. The solid, dotted, and dashed curves correspond, respectively, to the exact value, the limit of close transitions, and uniform pairing. The abscissa scale must be multiplied by a factor of about 7.7 for nuclei in the $A \sim 150$ mass region in order to obtain the gap energy in MeV.

$$\frac{\mathcal{B}_n}{\mathcal{A}_n} = -2.56\frac{(k^4 - 10k^2 + 1)k^{2/3}}{(k^2+1)^3 A^{8/3}} \times \left[\left(\frac{2Z}{A}\right)^{1/3} + \left(\frac{2N}{A}\right)^{1/3}\right]. \qquad (16)$$

An interpolation between the quantities in (13) and (15) allows one to conclude that there are two distinct regions in the variation of $\mathcal{B}/\mathcal{A}$ versus I. The lower part of an SD band is characterized by a gradual decrease in the pairing gap Δ. According to (13), the ratio $\mathcal{B}/\mathcal{A}$ must exhibit a sharp increase. It then changes sign at the spin value of I_c and approaches the plateau value of (16) at the top of a band. Such behavior of the ratio $\mathcal{B}/\mathcal{A}$ is the signature of quenching static pairing correlations. Pairing fluctuations in the normal phase reduce the value in (16) (by analogy with the dealignment effect of [13]), but they do not change our conclusion. This statement is confirmed by the ω dependence of the difference $\Im^{(1)} - \Im^{(2)}$ [which is proportional to $\mathcal{B}/\mathcal{A}$ in the high-I limit according to (3)] calculated with and without pairing vibrations in [14].

We have analyzed all the SD bands of [15] with known or suggested spins of levels. Figure 2 shows $\mathcal{B}/\mathcal{A}$ as a function of I for SD bands representing different mass regions. Apart from the bands ^{192}Hg(1) and ^{194}Hg(3), where frequencies are so low that $\mathcal{B}/\mathcal{A}$ rises continuously in the superfluid phase, and ^{84}Zr(1), for which pairing is quenched completely and $\mathcal{B}/\mathcal{A}$ is close to the limiting value in (16), all these bands display the behavior described above.

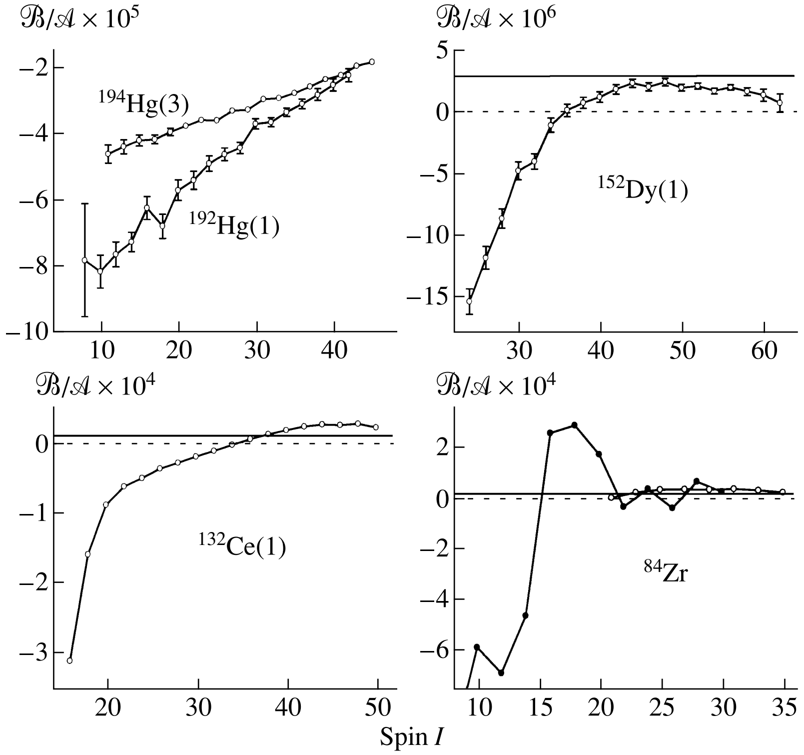

Fig. 2. Ratio $\mathcal{B}/\mathcal{A}$ versus spin for SD and ND bands with predominantly collective behavior. Expressions (2) are used to obtain this ratio from experimental data for (closed circles) ND and (open circles) SD bands. The solid straight line is the limiting value of $\mathcal{B}_n/\mathcal{A}_n$ for the normal phase with the deformation c/a found from the quadrupole moment. The error bars (if they are greater than symbol sizes) include only the uncertainties in the γ-ray energies. The uncertainties in the spin assignment are immaterial for all SD bands [with the exception of ^{152}Dy(1)], since the spin variation of $2\hbar$ would merely shift the curves along the abscissa.

The pronounced plateau is a consequence of the weak dependence of the nuclear deformation c/a on I. A slow decrease in the ratio $\mathcal{B}/\mathcal{A}$ in the upper parts of all the SD bands considered here seems to result from the stretching of nuclei at highest spins. It is important to note that the behavior characteristic of static pairing quenching is observed in the upper part of the yeast ND bands of ^{84}Zr [where $\mathcal{B}/\mathcal{A}$ reaches the same limiting value (16) as in the SD band ^{84}Zr(1)], ^{168}Yb, and ^{168}Hf. Thus, the plots of Fig. 2 demonstrate the universality of the superfluid-to-normal transition for SD and ND bands.

The problem of the pairing phase transition in the ND and SD bands has been the subject of intensive discussions in high-spin physics for a long time [10, 13]. The main difficulty lies in the finiteness of the system. The presence of fluctuations and the configuration dependence make this transition very diffuse and ambiguous. The phenomenon is analogous to the transition from deformed to spherical nuclei. The physical reality of the two critical phenomena lies in the possibility of observing the change in the collective excitations of the system. In the case of deformation, the rotational–vibrational spectrum transforms into a pure vibrational one. The transition being considered is more delicate. It manifests itself in a modification to the rotational spectrum: the spectrum compressed relative to the rigid-rotor one below the critical point I_c transforms into the extended one above I_c. Following [16], we can represent the effective rotational Hamiltonian describing the levels of a band in the transition region as

$$H_{\text{eff}} = a\mathbf{I}^2 + (I/I_c - 1)b\mathbf{I}^4 + c\mathbf{I}^6, \qquad (17)$$

where the parameters a, b, and c and the critical spin I_c are the subjects of a microscopic theory that has to take into account static, dynamical, and uniform pairing. Upon incorporating the critical spin, which can be found from the plots in Fig. 2, this concept of the superfluid-to-normal transition is free from ambiguities characteristic of the approach based on a change in the single-particle spectra [17, 18]. This also allows one to explain the extreme regularity of SD bands. Figure 2 shows that, for the most part, the SD bands from the 80, 130, and 150 mass regions belong to the normal and transition phases, where the nonadiabatic parameter $\mathcal{B}$ is small or close to zero.

As an example of the configuration-dependent effect, which destroys the characteristic features of the

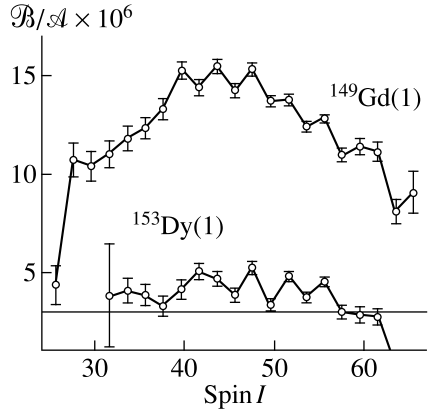

Fig. 3. As in Fig. 2, but for the bands with high-N configurations, which have a nonzero alignment i. The straight line represents the value of $\mathcal{B}_n/\mathcal{A}_n$ for ^{153}Dy(1).

transition, Fig. 3 shows the ratio $\mathcal{B}/\mathcal{A}$ for two SD bands of odd nuclei. The staggering behavior of the ratio is a point of particular interest. This new phenomenon is associated with an odd neutron and cannot be explained by pairing correlations. It should be noted that staggering is reproduced very well, the error bars being smaller than the staggering amplitude.

In summary, an exact solution for the inertial parameter $\mathcal{B}$ demonstrates the importance of nonuniform pairing, which allows one to find correctly the different limits of this quantity. The limit of zero static pairing is of special interest because it shows that the parameter $\mathcal{B}$ changes sign as the spin I increases in a band. The critical point I_c, $\mathcal{B}(I_c) = 0$, is a signature of the superfluid-to-normal transition, which leads to a modification of the rotational spectrum of a band. This modification reveals itself in the characteristic dependence of the ratio $\mathcal{B}/\mathcal{A}$ on the spin I. The application of this criterion to experimental data indicates the existence of the transition in the SD bands of the three mass regions and in some ND bands. As a rule, the closer the critical point to the beginning of a band, the more regular its rotational spectrum.

ACKNOWLEDGMENTS

This work was supported in part by the Russian Foundation for Basic Research (project no. 00-15-96590).

REFERENCES

1. W. Satuła and R. Wyss, Phys. Rev. C **50**, 2888 (1994).
2. J. Dobaczewski and J. Dudek, Phys. Rev. C **52**, 1827 (1995).
3. P.-H. Heenen *et al.,* Nucl. Phys. A **598**, 169 (1996).
4. Yang-Sun *et al.,* Phys. Rev. Lett. **78**, 2321 (1997).
5. A. Bohr and B. R. Mottelson, *Nuclear Structure*, vol. 2: *Nuclear Deformations* (Benjamin, New York, 1974; Mir, Moscow, 1977).
6. Yu. T. Grin' and I. M. Pavlichenkov, Zh. Éksp. Teor. Fiz. **43**, 465 (1962) [Sov. Phys. JETP **16**, 333 (1963)].
7. I. M. Pavlichenkov, Nucl. Phys. **55**, 225 (1964).
8. E. R. Marshalek, Phys. Rev. **158**, 993 (1967).
9. I. N. Mihailov *et al.,* Fiz. Élem. Chastits At. Yadra **8**, 1338 (1977) [Sov. J. Part. Nucl. **8**, 550 (1977)].
10. Y. R. Shimizu, Nucl. Phys. A **520**, 477c (1990).
11. I. Hamamoto and W. Nazarewicz, Phys. Rev. C **49**, 2489 (1994).
12. A. B. Migdal, Nucl. Phys. **13**, 655 (1959).
13. Y. R. Shimizu *et al.,* Rev. Mod. Phys. **61**, 131 (1989).
14. Y. R. Shimizu *et al.,* Nucl. Phys. A **509**, 80 (1990).
15. B. Singh *et al.,* Nucl. Data Sheets **78**, 1 (1996).
16. I. M. Pavlichenkov, Phys. Rep. **226**, 175 (1993).
17. J. D. Garrett, G. B. Hagemann, and B. Herskind, Annu. Rev. Nucl. Part. Sci. **36**, 419 (1986).
18. J. R. B. Oliveira *et al.,* Phys. Rev. C **47**, R926 (1993).

Physics of Atomic Nuclei, Vol. 64, No. 6, 2001, pp. 1098–1104. From Yadernaya Fizika, Vol. 64, No. 6, 2001, pp. 1173–1179.
Original English Text Copyright © 2001 by Minkov, Drenska, Raychev, Roussev, Bonatsos.

Rotations of Nuclei with Reflection Asymmetry Correlations*

N. Minkov**, **S. B. Drenska**, **P. P. Raychev**, **R. P. Roussev**, **and D. Bonatsos**[1)]

Institute for Nuclear Research and Nuclear Energy, Sofia, Bulgaria

Received September 11, 2000

Abstract—We propose a collective Hamiltonian that incorporates interactions capable of generating rotations in nuclei with simultaneous presence of octupole and quadrupole deformations. It is demonstrated that the model formalism could be applied to reproduce the staggering effects observed in nuclear octupole bands. On this basis, we propose that the interactions involved would provide a relevant handle in the study of collective phenomena in nuclei and other quantum mechanical systems with reflection asymmetry correlations. © *2001 MAIK "Nauka/Interperiodica".*

The properties of nuclear systems with octupole deformations [1] are of current interest due to the increasing amount of evidence for the presence of octupole instability in different regions of the nuclear table [2]. Various parametrizations of the octupole degrees of freedom have opened a useful tool for understanding the role of the reflection asymmetry correlations and for analysis of the collective properties of such kind of systems [3–5]. As an important step in this direction, it is necessary to elucidate the question: Which are the collective nuclear interactions that correspond to the different octupole shapes and how do they determine the structure of the respective energy spectra? A physically meaningful answer could be obtained by taking into account the simultaneous presence of other collective degrees of freedom, such as the quadrupole ones.

In the present work, we address the above problem by examining the interactions that generate collective rotations in a system with octupole deformations. Based on the octahedron point symmetry parametrization of the octupole shape [4], we propose a general collective Hamiltonian which incorporates the interactions responsible for the rotations associated with the different octupole deformations. It will be shown that after taking into account the quadrupole degrees of freedom and the appropriate higher order quadrupole–octupole interaction the model formalism would be able to reproduce schematically some interesting effects of the fine rotational structure of nuclear octupole bands. The study is strongly motivated by the need of theoretical explanation of the recently observed staggering patterns in octupole bands of light actinides [6] as well as by the possibility of gaining an insight into the fine structure of negative parity rotational bands based on octupole vibrations.

Our model formalism is based on the understanding that the collective properties of a physical system in which octupole correlations take place should be influenced by the following most general octupole field $V_3 = \sum_{\mu=-3}^{3} \alpha_{3\mu}^{\text{fix}} Y_{3\mu}^*$ (in the intrinsic, body-fixed frame), which can be written in the form [4]

$$V_3 = \epsilon_0 A_2 + \sum_{i=1}^{3} \epsilon_1(i) F_1(i) + \sum_{i=1}^{3} \epsilon_2(i) F_2(i), \quad (1)$$

where the quantities

$$A_2 = -\frac{i}{\sqrt{2}}(Y_{3\,2} - Y_{3\,-2}) = \frac{1}{r^3}\sqrt{\frac{105}{4\pi}}xyz, \quad (2)$$

$$F_1(1) = Y_{3\,0} = \frac{1}{r^3}\sqrt{\frac{7}{4\pi}}z\left(z^2 - \frac{3}{2}x^2 - \frac{3}{2}y^2\right), \quad (3)$$

$$\begin{aligned} F_1(2) &= -\frac{1}{4}\sqrt{5}(Y_{3\,3} - Y_{3\,-3}) \\ &+ \frac{1}{4}\sqrt{3}(Y_{3\,1} - Y_{3\,-1}) \\ &= \frac{1}{r^3}\sqrt{\frac{7}{4\pi}}x\left(x^2 - \frac{3}{2}y^2 - \frac{3}{2}z^2\right), \end{aligned} \quad (4)$$

$$\begin{aligned} F_1(3) &= -i\frac{1}{4}\sqrt{5}(Y_{3\,3} + Y_{3\,-3}) \\ &- i\frac{1}{4}\sqrt{3}(Y_{3\,1} + Y_{3\,-1}) \\ &= \frac{1}{r^3}\sqrt{\frac{7}{4\pi}}y\left(y^2 - \frac{3}{2}z^2 - \frac{3}{2}x^2\right), \end{aligned} \quad (5)$$

---

*This article was submitted by the authors in English.

[1)] Institute of Nuclear Physics, N.C.S.R. "Demokritos," Attiki, Greece.

**e-mail: `nminkov@inrne.bas.bg`

1063-7788/01/6406-1098$21.00 © 2001 MAIK "Nauka/Interperiodica"

$$F_2(1) = \frac{1}{\sqrt{2}}(Y_{3\,2} + Y_{3\,-2}) \tag{6}$$
$$= \frac{1}{r^3}\sqrt{\frac{105}{16\pi}}z(x^2 - y^2),$$

$$F_2(2) = \frac{1}{4}\sqrt{3}(Y_{3\,3} - Y_{3\,-3}) \tag{7}$$
$$+ \frac{1}{4}\sqrt{5}(Y_{3\,1} - Y_{3\,-1})$$
$$= \frac{1}{r^3}\sqrt{\frac{105}{16\pi}}x(y^2 - z^2),$$

$$F_2(3) = -i\frac{1}{4}\sqrt{3}(Y_{3\,3} + Y_{3\,-3}) \tag{8}$$
$$+ i\frac{1}{4}\sqrt{5}(Y_{3\,1} + Y_{3\,-1})$$
$$= \frac{1}{r^3}\sqrt{\frac{105}{16\pi}}y(z^2 - x^2)$$

(with $r^2 = x^2 + y^2 + z^2$) belong to the irreducible representations (irreps) of the octahedron group (O). A_2 is one-dimensional, while F_1 and F_2 are three-dimensional irreps. The seven real parameters ϵ_0 and $\epsilon_r(i)$ ($r = 1, 2$; $i = 1, 2, 3$) determine the amplitudes of the octupole deformation. Their relation to the $\alpha_{3\,\mu}^{\text{fix}}$ is given in [4].

Our proposition is that the general collective Hamiltonian which incorporates the shape characteristics of the octupole field (1) can be constructed on the basis of the above octahedron irreps. For this purpose, we introduce operator forms of the quantities A_2, $F_1(i)$, and $F_2(i)$ ($i = 1, 2, 3$) in which the cubic terms of the Cartesian variables x, y, and z in (2)–(8) are replaced by appropriately symmetrized combinations of cubic terms of the respective angular momentum operators $\hat{I}_x$, $\hat{I}_y$, $\hat{I}_z$ (with $\hat{I}^2 = \hat{I}_x^2 + \hat{I}_y^2 + \hat{I}_z^2$). The following Hamiltonian is then obtained:

$$\hat{H}_{\text{oct}} = \hat{H}_{A_2} + \sum_{r=1}^{2}\sum_{i=1}^{3}\hat{H}_{F_r(i)} \tag{9}$$

with

$$\hat{H}_{A_2} = a_2\frac{1}{4}[(\hat{I}_x\hat{I}_y + \hat{I}_y\hat{I}_x)\hat{I}_z + \hat{I}_z(\hat{I}_x\hat{I}_y + \hat{I}_y\hat{I}_x)], \tag{10}$$

$$\hat{H}_{F_1(1)} = \frac{1}{2}f_{11}\hat{I}_z(5\hat{I}_z^2 - 3\hat{I}^2), \tag{11}$$

$$\hat{H}_{F_1(2)} = \frac{1}{2}f_{12}(5\hat{I}_x^3 - 3\hat{I}_x\hat{I}^2), \tag{12}$$

$$\hat{H}_{F_1(3)} = \frac{1}{2}f_{13}(5\hat{I}_y^3 - 3\hat{I}_y\hat{I}^2), \tag{13}$$

$$\hat{H}_{F_2(1)} = f_{21}\frac{1}{2}[\hat{I}_z(\hat{I}_x^2 - \hat{I}_y^2) + (\hat{I}_x^2 - \hat{I}_y^2)\hat{I}_z], \tag{14}$$

$$\hat{H}_{F_2(2)} = f_{22}(\hat{I}_x\hat{I}^2 - \hat{I}_x^3 - \hat{I}_x\hat{I}_z^2 - \hat{I}_z^2\hat{I}_x), \tag{15}$$

$$\hat{H}_{F_2(3)} = f_{23}(\hat{I}_y\hat{I}_z^2 + \hat{I}_z^2\hat{I}_y + \hat{I}_y^3 - \hat{I}_y\hat{I}^2). \tag{16}$$

The Hamiltonian parameters a_2 and $f_{r\,i}$ ($r = 1, 2$; $i = 1, 2, 3$) are formally related to the parameters in (1) as follows: $a_2 = \epsilon_0\sqrt{105/(4\pi)}$, $f_{1\,i} = \epsilon_1(i)\sqrt{7/(4\pi)}$, $f_{2\,i} = \epsilon_2(i)\sqrt{105/(16\pi)}$, $i = 1, 2, 3$.

During the procedure described above, the r^3 factors appearing in the denominators of (2)–(8) are replaced by $\hat{I}^3$ factors. In the final result, (10)–(16), we normalize with respect to $\hat{I}^3$, i.e., we multiply the results by $\hat{I}^3$, an operation which is equivalent to the transition to a unit sphere, a natural thing to do since we are interested in surface shapes.

We remark that the terms of the Hamiltonian obtained (as a function of the angular momentum operators $\hat{I}_x$, $\hat{I}_y$, $\hat{I}_z$) correspond to the same octupole shapes which appear in (2)–(8) and belong to the same irreps of the octahedron group. In other words, through the above procedure we determine the octahedron point symmetry properties of the system in angular momentum space.

Our analysis shows that the operator $\hat{H}_{F_1(1)}$ (11), which corresponds to $Y_{3\,0}$ (with axial deformation) is the only one octupole operator possessing diagonal matrix elements in the states with collective angular momentum I. Below, it will be shown that it is of major importance for determining the fine structure of collective bands with octupole correlations. Actually, it is well known that the $Y_{3\,0}$ (axial) deformation is the leading mode in the systems with reflection asymmetric shape (see for review [2]).

Further, it is known that the use of the pure octupole field (1) is not sufficient to incorporate the collective shape properties of the system. More specifically, a unique parametrization of the pure octupole field in an intrinsic frame has not been obtained yet in a consistent way [2]. In this respect, the consideration of octupole degrees of freedom together with the quadrupole deformations is important. A general treatment of a combined quadrupole–octupole field is proposed in the framework of a general collective model for coupled multipole surface modes [7, 8].

Based on the above consideration, we suggest that the most general collective Hamiltonian of a system with octupole correlations should also contain the quadrupole rotation part

$$\hat{H}_{\text{rot}} = A\hat{I}^2 + A'\hat{I}_z^2, \tag{17}$$

where A and A' are the inertial parameters. In addition, the following higher order diagonal quadrupole–octupole interaction term (corresponding to the product $Y_{2\,0} \cdot Y_{3\,0}$) could be introduced:

$$\hat{H}_{\text{qoc}} = f_{\text{qoc}}\frac{1}{\hat{I}^2}(15\hat{I}_z^5 - 14\hat{I}_z^3\hat{I}^2 + 3\hat{I}_z\hat{I}^4). \tag{18}$$

The "yrast" energy levels, $E(I)$ (in keV), and the respective K values obtained by (23) for the parameter set $E_0 = 500$ keV, $f_k = -7.5$ keV, $A = 12$ keV, $A' = 6.6$ keV, $f_{11} = 0.56$ keV, and $f_{\text{qoc}} = 0.085$ keV

I	$E(I)$	K	I	$E(I)$	K	I	$E(I)$	K
1	522.772	1	13	2335.81	5	25	5453.12	11
2	568.327	1	14	2576.57	6	26	5694.49	12
3	637.095	1	15	2827.57	6	27	5935.5	12
4	728.71	1	16	3082.36	7	28	6157.5	13
5	840.857	2	17	3344.94	7	29	6378.29	13
6	971.155	2	18	3608.18	8	30	6575.37	14
7	1123.22	2	19	3877.05	8	31	6770.62	14
8	1288.09	3	20	4143.16	9	32	6937.23	15
9	1472.71	3	21	4413.03	9	33	7101.62	15
10	1668.56	4	22	4676.45	10	34	7232.21	16
11	1880.56	4	23	4942.01	10	35	7360.44	16
12	2101.68	5	24	5197.18	11	36	7449.45	17

This operator is normalized with respect to the multiplication factor I^3. (More precisely, we use the product $I^3 Y_{20} \cdot Y_{30}$ so as to keep all nonquadrupole Hamiltonian terms of the same order.)

Then, the Hamiltonian of the system can be written as

$$\hat{H} = \hat{H}_{\text{bh}} + \hat{H}_{\text{rot}} + \hat{H}_{\text{oct}} + \hat{H}_{\text{qoc}}. \tag{19}$$

Here,

$$\hat{H}_{\text{bh}} = \hat{H}_0 + f_k \hat{I}_z \tag{20}$$

is a pure phenomenological part introduced to reproduce the bandhead energy in the form

$$E_{\text{bh}} = E_0 + f_k K, \tag{21}$$

where E_0 and f_k are free parameters. The K dependence of E_{bh}, which can reasonably be referred to the intrinsic motion, provides the correct value of the bandhead angular momentum projection K in the variation procedure described below.

We remark that the Hamiltonian (19) is not a rotational invariant in general. It does not commute with the total angular momentum operators, and any state with given angular momentum is energy split with respect to the quantum number K. Therefore, the physical relevance of this Hamiltonian depends on the possibility of determining in a unique way the angular momentum projection. The basic assumption of our consideration is that K is not frozen within the states of the collective rotational band. We suggest that for any given angular momentum it should be determined so as to minimize the respective collective energy. The resulting energy spectrum represents the yrast sequence of energy levels for our model Hamiltonian. We remark that similar procedure is used in [9, 10] in reference to the $\Delta I = 2$ staggering effect in superdeformed nuclei.

As a first step in testing our Hamiltonian, we consider its diagonal part

$$\hat{H}^d = \hat{H}_{\text{bh}} + \hat{H}_{\text{rot}} + \hat{H}^d_{\text{oct}} + \hat{H}_{\text{qoc}}, \tag{22}$$

where the operator $\hat{H}^d_{\text{oct}} \equiv \hat{H}_{F_1(1)}$ represents the diagonal part of the pure octupole Hamiltonian $\hat{H}_{\text{oct}}$, (9).

The following diagonal matrix element is then obtained:

$$\begin{aligned} E_K(I) = E_0 + f_k K + AI(I+1) + A'K^2 \\ + f_{11}\left(\frac{5}{2}K^3 - \frac{3}{2}KI(I+1)\right) \\ + f_{\text{qoc}}\frac{1}{I^2}\left(15K^5 - 14K^3 I(I+1) + 3KI^2(I+1)^2\right). \end{aligned} \tag{23}$$

Following the above assumption for the third angular momentum projection, we determine the yrast sequence $E(I)$ after minimizing (23) as a function of integer K in the range $-I \le K \le I$. The obtained energy spectrum depends on six model parameters: E_0 essentially responsible for the bandhead energy; f_k which provides minimal energy for $K = K_{\text{bh}} = I_{\text{bh}}$; A and A' are the quadrupole inertial parameters which should generally correspond to the known quadrupole shapes (axes ratios) of nuclei; f_{11} and f_{qoc} are the parameters of the diagonal octupole (11) and quadrupole–octupole (18) interactions, respectively. We consider the latter two parameters as free parameters.

We applied several exemplary sets of the above parameters and obtained the corresponding schematic energy spectra. One of them is given in the table. It is seen that the "yrast" values of the quantum number K gradually increase with the increase in the angular momentum I. We remark that they correspond to the local minima of (23) as a function of K. This is illustrated on Fig. 1. We see that these minima are well determined and their depth increases with the increase in the angular momentum. Such a behavior of the spectrum corresponds to a wobbling motion and could also be interpreted as a multiband-crossing phenomenon. The obtained yrast sequence can be considered as the envelope of the curves with different values of the quantum number K, as is illustrated in Fig. 2.

In addition, we see that the K values of the odd and the even sequence of levels are grouped by couples

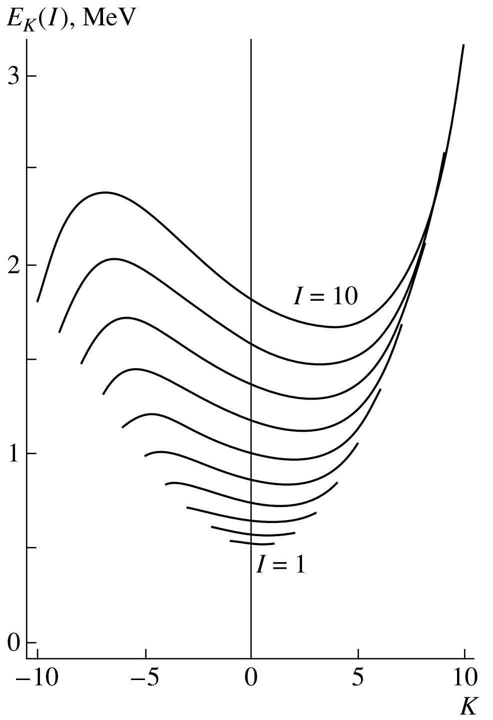

Fig. 1. The diagonal energy matrix element $E_K(I)$ (23) is plotted as a function of K for $I = 1, 2, ..., 10$ for the parameter set $E_0 = 500$ keV, $f_k = -7.5$ keV, $A = 12$ keV, $A' = 6.6$ keV, $f_{11} = 0.56$ keV, and $f_{\rm qoc} = 0.085$ keV.

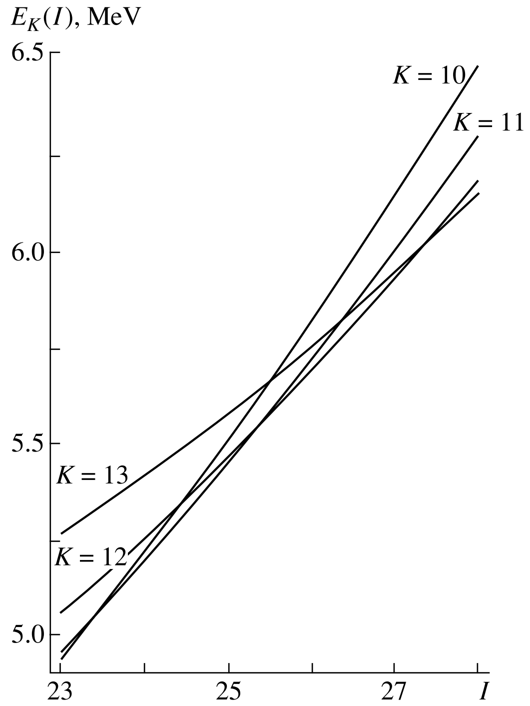

Fig. 2. The diagonal energy matrix element $E_K(I)$ (23) is plotted as a function of I for $K = 10, 11, 12, 13$ for the parameter set of Fig. 1.

which imply the presence of an odd–even staggering effect. Indeed, the presence of such an effect is demonstrated in Figs. 3*a*–3*e*, where the quantity

$$\mathrm{Stg}(I) = 6\Delta E(I) \tag{24}$$
$$- 4\Delta E(I-1) - 4\Delta E(I+1)$$
$$+ \Delta E(I+2) + \Delta E(I-2)$$

with $\Delta E(I) = E(I+1) - E(I)$ is plotted as a function of angular momentum I for several different sets of model parameters. (The quantity $\mathrm{Stg}(I)$ is the discrete approximation of the fourth derivative of the function $\Delta E(I)$, i.e., the fifth derivative of the energy $E(I)$. Its physical relevance has been discussed extensively in [6, 11].)

Figure 3*a* illustrates a long $\Delta I = 1$ staggering pattern with several irregularities, which looks similar to the "beats" observed in the octupole bands of some light actinides such as ^{220}Ra, ^{224}Ra, and ^{226}Ra [6]. Also, it is rather similar to the staggering patterns observed in rotational spectra of diatomic molecules [12]. In Fig. 3*b*, the increased values of f_{11} and $f_{\rm qoc}$ provide a wide angular momentum region (up to $I \sim 40$) with a regular staggering pattern. The further increase of $f_{\rm qoc}$ results in a staggering pattern with different amplitudes, shown in Fig. 3*c*. These two figures resemble the staggering behavior of some rotational (negative parity) bands based on octupole vibrations [13]. The further increase of f_{11} and $f_{\rm qoc}$ leads to a staggering pattern with many "beats," as shown in Fig. 3*d*. Notice that in Fig. 3*d* the first three "beats" are completed by $I \approx 40$, while in Fig. 3*a* the first three "beats" are completed by $I \approx 70$. An example with almost constant staggering amplitude is shown in Fig. 3*e*. It resembles the form of the odd–even staggering predicted in the $SU(3)$ limit of various algebraic models (see [6] for details and relevant references). It also resembles the odd–even staggering seen in some octupole bands of light actinides, such as ^{220}Th [6].

Now, we can discuss the general Hamiltonian structure (19), including the various nondiagonal terms (10), (12)–(16). Here, the major problem is the circumstance that K is generally not a good quantum number. However, we are able to provide our analysis for small values of the respective parameters which conserve K "asymptotically" well. This requirement assumes a weak K-bandmixing interaction which guarantees that for any explicit energy minimum appearing in the diagonal case the corresponding perturbed Hamiltonian eigenvalue will be uniquely determined. Thus we are able to obtain the respective K-mixed yrast energy sequence. Our numerical analysis of the Hamiltonian eigenvector systems shows that the parameters of the nondiagonal terms

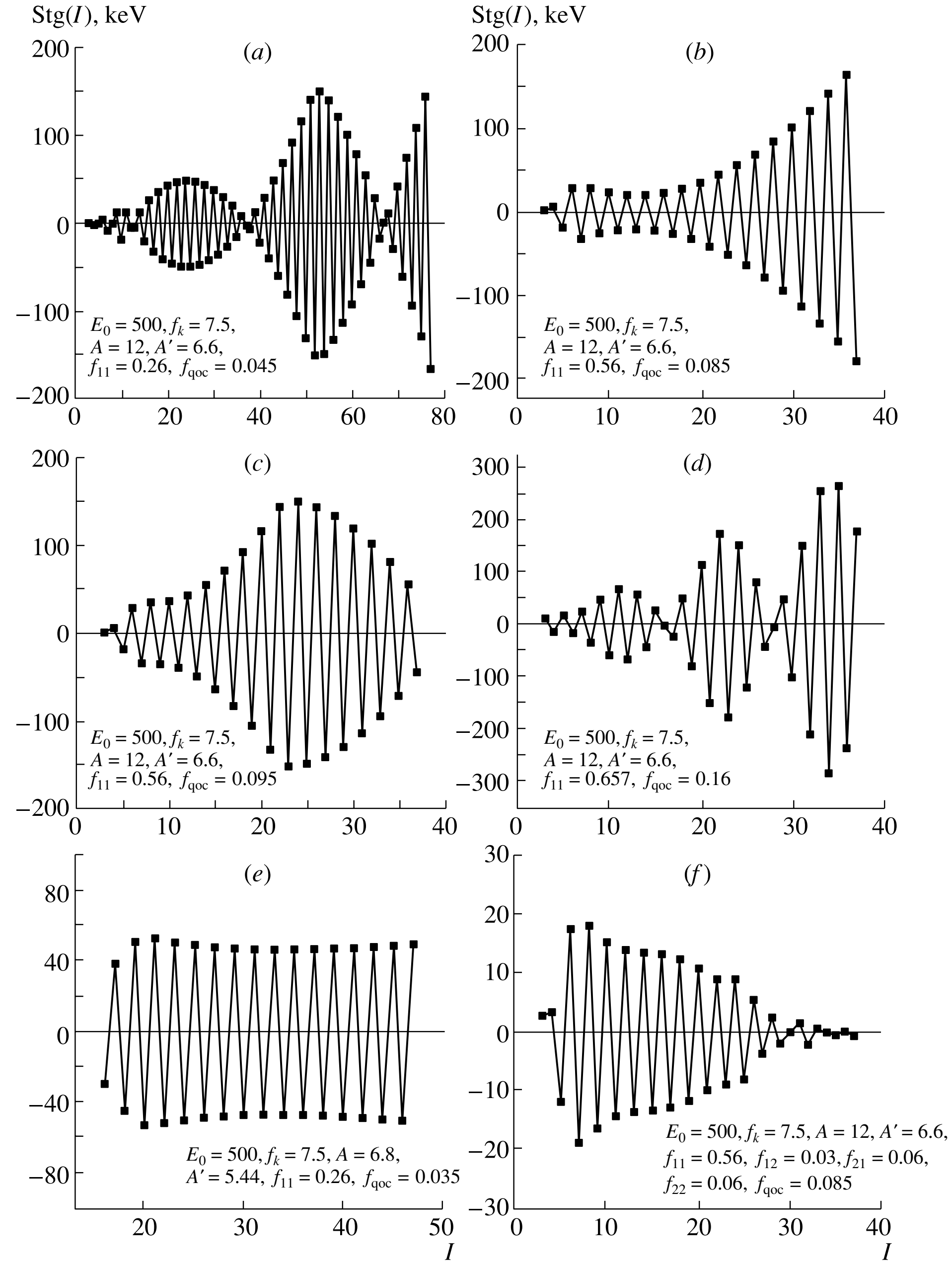

Fig. 3. $\Delta I = 1$ staggering patterns (24) (in keV) obtained (*a*–*e*) by the diagonal Hamiltonian (22) for several different sets of model parameters; (*f*) by adding three nondiagonal terms $\hat{H}_{F_1(2)}$ (12), $\hat{H}_{F_2(1)}$ (14), and $\hat{H}_{F_2(2)}$ (15) to the diagonal Hamiltonian (22).

should be an order smaller in value than the parameter f_{11}. In addition, we established that the following couples of nondiagonal terms make the same contribution to the energy spectrum: $\hat{H}_{A_2}$ and $\hat{H}_{F_2(1)}$; $\hat{H}_{F_1(2)}$ and $\hat{H}_{F_1(3)}$; $\hat{H}_{F_2(2)}$ and $\hat{H}_{F_2(3)}$.

In Fig. 3*f*, a staggering pattern with a presence of K-bandmixing is illustrated. In fact, we added the following three nondiagonal terms $\hat{H}_{F_1(2)}$, $\hat{H}_{F_2(1)}$, and $\hat{H}_{F_2(2)}$ to the already considered diagonal Hamiltonian (22), with the parameters of the latter being kept the same as in Fig. 3*b* (and in the table). We see that the mixing leads to a decrease in the staggering amplitude with the increase in angular momentum, so that the staggering pattern is reduced completely in the higher spin region. This pattern resembles the experimental situation in ^{218}Rn and ^{228}Th [6] (odd–even staggering with amplitude decreasing as a function of I).

So, the staggering patterns illustrated so far (Fig. 3) cover almost all known $\Delta I = 1$ staggering patterns in nuclei and molecules. The amplitudes obtained for the examined sets of parameters vary up to 300 keV. Some reasonable theoretical patterns with $\mathrm{Stg}(I) \sim 500$ keV can be easily obtained. On this basis, we suppose that the model parameters can be adjusted appropriately so as to reproduce the staggering effects in nuclear octupole bands as well as in some rotational negative parity bands built on octupole vibrations. Also, an application of the present formalism to the spectra of diatomic molecules could be reasonable.

Here, the following comments on the structure of the collective interactions used and the related symmetries would be relevant:

1. The equal contribution of the three couples of nondiagonal terms (mentioned above) indicates that only four octupole Hamiltonian terms are enough to determine the energy spectrum. This result reflects the circumstance that in the intrinsic frame three octupole degrees of freedom, from the seven ones, are related to the orientation angles. For example, we could suggest that the following terms (applied in Fig. 3*f*) give an independent contribution to the total Hamiltonian: $\hat{H}_{F_1(1)}$, $\hat{H}_{F_1(2)}$, $\hat{H}_{F_2(1)}$, and $\hat{H}_{F_2(2)}$. We remark that our analysis (related to the collective rotations of the system) gives a natural way to determine the four collective octupole interaction terms.

2. From a symmetry point of view, we remark that the diagonal term $\hat{H}_{F_1(1)}$, which corresponds to Y_{30}, possesses an axial symmetry, while the nondiagonal terms $\hat{H}_{F_1(2)}$, $\hat{H}_{F_2(1)}$, and $\hat{H}_{F_2(2)}$ (of previous item 1) are constructed by using the combinations $(Y_{31} - Y_{3\,-1})$ with C_{2v} symmetry, $(Y_{32} + Y_{3\,-2})$ with T_d symmetry, and $(Y_{33} - Y_{3\,-3})$ with D_{3h} symmetry. This, our analysis shows that the axial symmetric term should play the major role in the structure of the collective rotational Hamiltonian, while the nonaxial parts could be considered as small K-band-mixing interactions. From a microscopic point of view, a detailed analysis of the above spherical harmonic combinations and the respective symmetries has been provided on the basis of the one-particle spectra of the octupole-coupled two-level model [14].

3. The observed influence of the nondiagonal Hamiltonian terms on the fine structure of our "schematic" spectra suggests an important physical conclusion: the nondiagonal K-mixing interactions suppress the staggering pattern. In such a way, we find that the axial symmetric term $\hat{H}_{F_1(1)}$ is the only one pure octupole degree of freedom which provides "beat" staggering behavior of the quantity (24) (see Fig. 3*e*). (The quadrupole–octupole term $\hat{H}_{\mathrm{qoc}}$ gives an additional contribution and provides wider angular momentum regions with regular staggering.) So, our analysis suggests that the $\Delta I = 1$ staggering effect observed in systems with octupole deformations could be referred to the dominant role of the axial symmetric "pearlike" octupole shape.

In addition, it is important to remark that the fine (staggering) behavior of our schematic energy spectra reflects the structure of the interactions considered through the K sequences generated in the above minimization procedure. Thus, our analysis suggests that in the high-angular-momentum region, some high-K-band structures should be involved. From a microscopic point of view, the values $K = 0$, 1, 2, 3 have been included in the calculations, showing that in the beginning of the rare-earth region the values $K = 0$, 1 are important for the lowest 3^- state, while in the middle of the region the values $K = 1$, 2 are important and in the far end of the region the values $K = 2$, 3 are important [15]. The same authors deal with nuclei with $A \geq 222$ in [15]. One of the authors of [15, 16] in [17] finds that the restriction to $K \leq 3$ is not justifiable for large energies. This is in agreement with our findings in the table.

In conclusion, we remark that the collective interactions considered in this work suggest the presence of various fine rotational band structures in quantum mechanical systems with collective octupole correlations. In particular, they provide various forms of staggering patterns which appear as the results of a delicate interplay between the terms of a pure octupole field and the terms of a high-order quadrupole–octupole interaction. The analysis carried out outlines the dominant role of the axial symmetric "pearlike" octupole shape for the presence of a $\Delta I = 1$ staggering effect. The obtained multi-K-band crossing structures could be referred to a wobbling collective motion of the system. We propose that the interactions involved would provide a relevant handle in the study of collective phenomena in nuclei and other quantum mechanical systems with complex shape correlations.

ACKNOWLEDGMENTS

We are grateful to Prof. P. Quentin for the illuminating discussions.

This work was supported by the Bulgarian National Fund for Scientific Research under contract no. MU-F-02/98.

REFERENCES

1. A. Bohr and B. R. Mottelson, *Nuclear Structure* (Benjamin, New York, 1975; Mir, Moscow, 1977), Vol. II.
2. P. A. Butler and W. Nazarewicz, Rev. Mod. Phys. **68**, 349 (1996).
3. S. G. Rohozinski, J. Phys. G **16**, L173 (1990).
4. I. Hamamoto, X. Zhang, and H. Xie, Phys. Lett. B **257**, 1 (1991).
5. C. Wexler and G. G. Dussel, Phys. Rev. C **60**, 014305 (1999).
6. D. Bonatsos, C. Daskaloyannis, S. B. Drenska, *et al.,* Phys. Rev. C **62**, 024301 (2000).
7. S. G. Rohozinski, M. Gajda, and W. Greiner, J. Phys. G **8**, 787 (1982).
8. S. G. Rohozinski, Rep. Prog. Phys. **51**, 541 (1988).
9. I. Hamamoto and B. Mottelson, Phys. Lett. B **333**, 295 (1994).
10. I. N. Mikhailov and Ph. Quentin, Phys. Rev. Lett. **74**, 3336 (1995).
11. N. Minkov, S. Drenska, P. Raychev, *et al.,* Phys. Rev. C **61**, 064301 (2000).
12. P. Raychev, S. Drenska, and J. Maruani, Phys. Rev. A **56**, 2759 (1997).
13. N. Minkov and S. Drenska (work in progress).
14. I. Hamamoto, B. Mottelson, H. Xie, and X. Z. Zhang, Z. Phys. D **21**, 163 (1991).
15. K. Neergård and P. Vogel, Nucl. Phys. A **145**, 33 (1970).
16. K. Neergård and P. Vogel, Nucl. Phys. A **149**, 217 (1970).
17. P. Vogel, Phys. Lett. B **60**, 431 (1976).

Physics of Atomic Nuclei, Vol. 64, No. 6, 2001, pp. 1105–1109. From Yadernaya Fizika, Vol. 64, No. 6, 2001, pp. 1180–1184.
Original English Text Copyright © 2001 by Sobiczewski, Muntian, Patyk.

Calculated Properties of Superheavy Nuclei*

A. Sobiczewski[**], **I. Muntian**(1), **and Z. Patyk**

Soltan Institute for Nuclear Studies, Warsaw, Poland

Received September 11, 2000

Abstract—Ground-state properties of the heaviest nuclei are analyzed within a macroscopic–microscopic approach. The main attention is paid to such properties as deformation, deformation energy, energy of the first rotational state 2^+ of a nucleus, and the branching ratio of α decay to this 2^+ state with respect to the decay to the ground state 0^+. The analysis concerns the problem of experimental confirmation of theoretically predicted deformed shapes of superheavy nuclei situated in the region around the nucleus ^{270}Hs. A large region of even-even nuclei with proton, $Z = 82$–128, and neutron, $N = 126$–190, numbers is considered. *© 2001 MAIK "Nauka/Interperiodica".*

1. INTRODUCTION

The objective of this paper is to present results of our recent studies on the properties of superheavy nuclei. The studies are a continuation of our previous works (e.g., [1–3]) in this field. They are closely connected with extensive experimental studies of superheavy nuclei (e.g., [4–6]). A wider review of recent theoretical studies of these nuclei may be found, e.g., in [7–9]. In this paper, we mainly concentrate on the problem of the deformation of superheavy nuclei. Calculations of this deformation (e.g., [1, 10–13]) indicate that most of these nuclei, especially those around the nucleus ^{270}Hs, are expected to be deformed. These predictions are not yet, however, confirmed by experiment. The heaviest nuclei, for which ground-state rotational bands have been observed, are $^{254,\,256}$Fm. Very recently, such bands have also been seen for ^{254}No [14, 15] and ^{252}No [16]. The observations were done by γ spectroscopy. There is, however, only a small chance to do this for heavier nuclei by γ spectroscopy, because its efficiency is too low for nuclei whose production cross sections are very small. There is a better chance to measure directly the energy of the first rotational state, E_{2^+}, in the respective α transition or conversion electrons. For example, the two close lines already seen in the α-decay spectrum of ^{260}Sg [17] may be interpreted [18] as the observation of the lowest rotational state of ^{256}Rf.

To help such experiments, calculations of the energy E_{2^+} [19] and of the branching ratio b_{2^+}/b_{0^+} have been done for many even–even superheavy nuclei. The latter is the ratio of the probability of α decay of a nucleus to the first 2^+ state of its daughter, to that to the ground-state 0^+ of the daughter. It is important to estimate its value before doing an experiment, to get some idea of the chance to measure it for nuclei with very small cross sections for their synthesis. Some results of these calculations are presented in this paper.

2. METHOD OF THE CALCULATIONS

The potential energy E of a nucleus is calculated by a macroscopic–microscopic method, with the Yukawa-plus-exponential model [20] taken for the macroscopic part and the Strutinski shell correction used for the microscopic part of the energy. The Woods–Saxon single-particle potential, with the "universal" version of its parameters [21], is taken for the calculation of the shell correction.

The equilibrium deformation parameters β_λ^0 of a nucleus are found by minimization of the potential energy E in a large deformation space. The 7-dimensional space $\{\beta_\lambda\}$, $\lambda = 2, 3, \ldots, 8$, is taken.

The moment of inertia of a nucleus is calculated in the cranking approximation.

3. RESULTS

We find, similar to [2, 22], that only a few nuclei in the concidered region are reflection asymmetric, i.e., have the odd-multipolarity components β_λ^0, $\lambda = 3, 5, 7$, different from zero. Due to this, we only show the results for even-multipolarity components β_λ^0, $\lambda = 2, 4, 6, 8$. They are given in Fig. 1.

---

[*] This article was submitted by the authors in English.

(1) Institute for Nuclear Research, Kiev, Ukraine.

[**] e-mail: `sobicz@fuw.edu.pl`

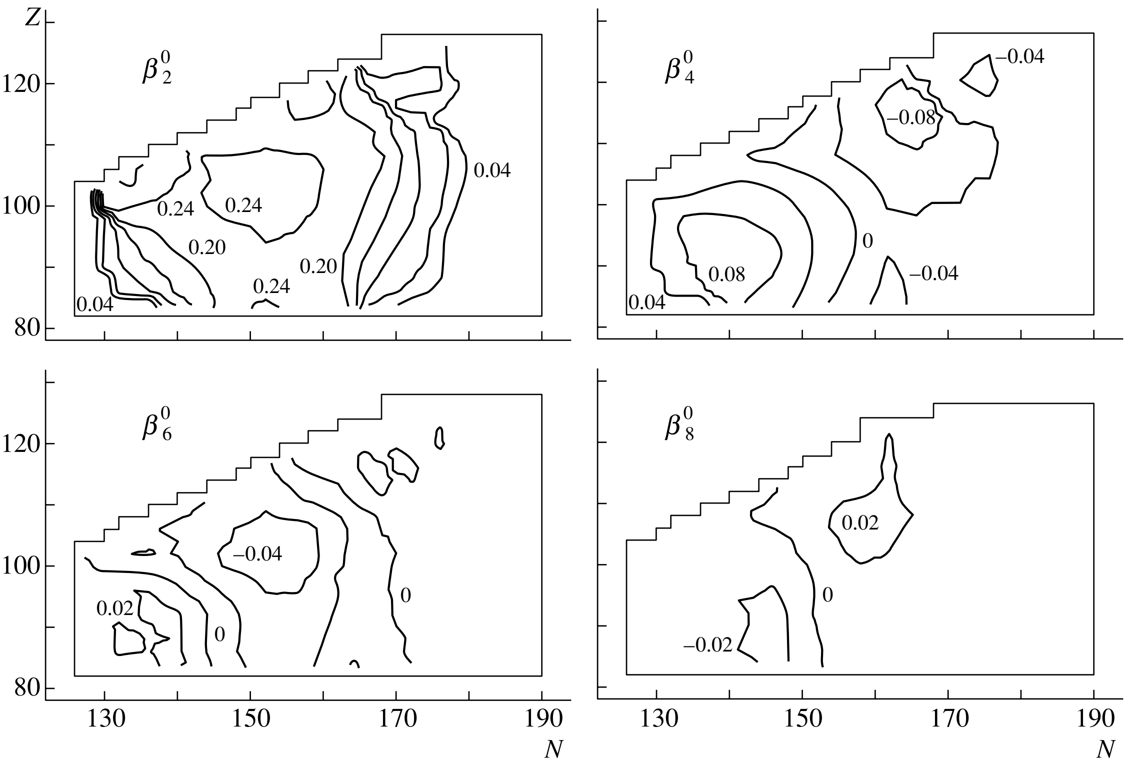

Fig. 1. Contour maps of the equlibrium deformations β_λ^0, $\lambda = 2, 4, 6, 8$, plotted as functions of proton Z and neutron N numbers. Numbers at the contour lines give the values of the deformations.

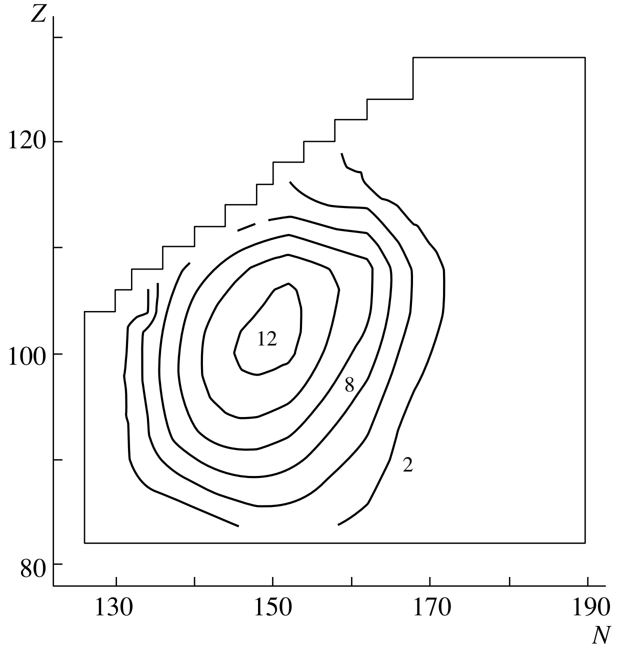

Fig. 2. Contour map of the deformation energy $E_{\rm def}$ (MeV).

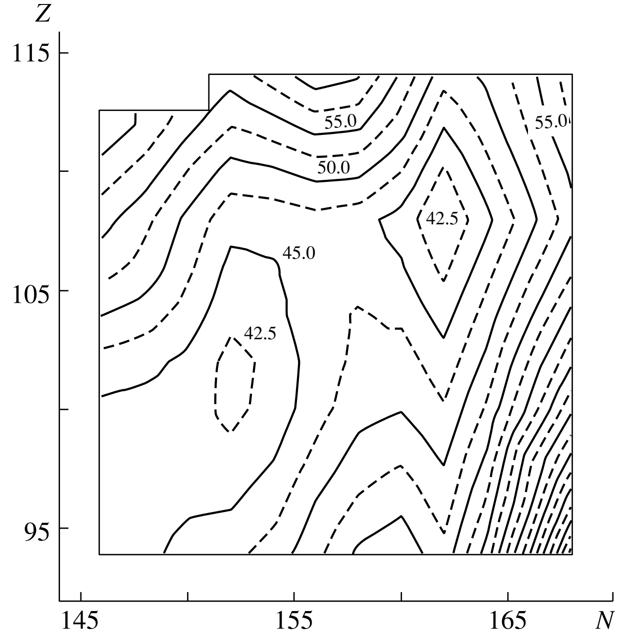

Fig. 3. Contour map of calculated energy E_{2^+} (keV) of the first rotational state 2^+.

One can see that most of the investigated nuclei are deformed. Only two relatively small regions of spherical nuclei appear: one (smaller) region of nuclei near those with a closed neutron shell at $N = 126$, and the other (larger) near to nuclei with a closed neutron shell at $N = 184$. Relatively small effects of weaker proton spherical closed shells at $Z = 82$ and $Z = 114$ are also visible.

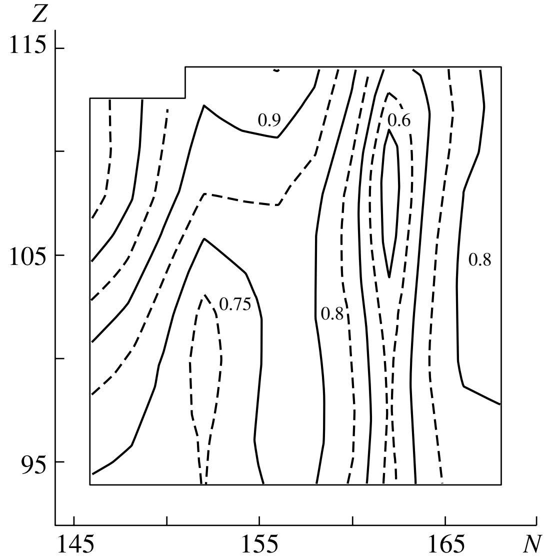

Fig. 4. Same as in Fig. 3, but for the neutron pairing-energy gap Δ_n (MeV).

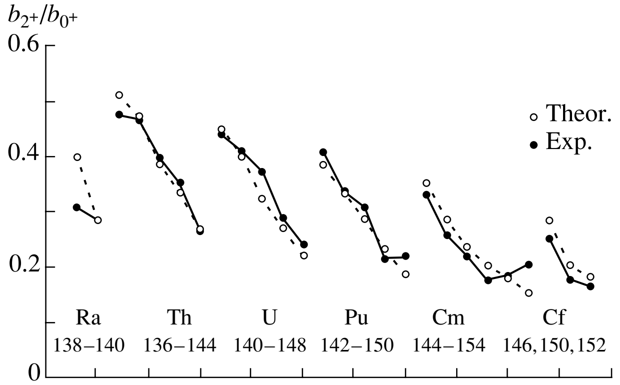

Fig. 5. The ratio b_{2^+}/b_{0^+} plotted as a function of neutron number N specified below the symbol of each element.

One can also see that the main, quadrupole, component of the deformation, β_2^0, is the largest. It is large ($\beta_2^0 \approx 0.24$) and approximately constant in a large part of the studied region and rapidly decreases as one moves to the boundaries of this region. The higher multipolarity components are smaller, and they change sign as one moves across the region.

Figure 2 shows the deformation energy of the nuclei, E_{def}. This quantity is defined as the difference between the energy of a nucleus at its spherical and equilibrium shapes,

$$E_{\mathrm{def}} \equiv E(0) - E(\beta_\lambda^0), \tag{1}$$

i.e., as the gain in energy of a nucleus due to its deformation. The analysis of this quantity in various nuclei [23] indicates that nuclei with $E \gtrsim 2$ MeV are well deformed, while those with $E < 2$ MeV are spherical or transitional. One can see in Fig. 2 that most of the considered nuclei are well deformed. The largest values of E_{def} (above 12 MeV) are obtained for nuclei around the nucleus ^{254}No, i.e., for nuclei with the largest quadrupole deformation β_2^0.

It is worth noting here that, although there is a general similarity between the maps of E_{def} and β_2^0, there also exist some differences. For example, for nuclei with $N = 152$ (i.e., with about a half-filled neutron shell between $N = 126$ and $N = 184$), E_{def} decreases rather fast when the proton number Z decreases from $Z = 102$ to $Z = 82$, or when it increases above $Z = 102$, while β_2^0 remains almost unchanged with these changes of Z. Thus, for ^{234}Pb (i.e., for the nucleus with the magic proton number $Z = 82$), the calculated value of β_2^0 is large ($\beta_2^0 = 0.244$), while E_{def} is rather small ($E_{\mathrm{def}} = 1.9$ MeV). This means that this nucleus is predicted to be rather transitional than well deformed. In other words, the large deformation of this nucleus is expected to be of a dynamical rather than static nature.

Figure 3 shows a map of the energies E_{2^+} of the first rotational state 2^+, calculated for even–even nuclei from about the central part of the considered region [19]. According to Fig. 2, they are expected to be well deformed. The energies are obtained from the calculated values of the moment of inertia J by the formula

$$E_{I^+} = (\hbar^2/2J)I(I+1), \tag{2}$$

valid for an ideal even–even rotor, where I is its spin. Two minima of E_{2^+} appear. One (41.7 keV) is obtained for the nucleus ^{254}No, and the other (40.0 keV) for ^{270}Hs. One may note that the value 44 keV, deduced for E_{2^+} from the recently observed rotational band of ^{254}No [14] is quite close to the value predicted theoretically.

The appearance of two minima of E_{2^+} at ^{254}No and ^{270}Hs is due to significant proton energy gaps at $Z = 102$ and 108 and especially large neutron energy gaps at $N = 152$ and 162 [1]. A large energy gap weakens pairing correlations and, this way, increases the moment of inertia of a nucleus, which is a very sensitive function of these correlations. The coincidence of minima of E_{2^+} (maxima of the moment of inertia J) with minima of the pairing correlations is directly illustrated by the map of the neutron pairing-energy gap Δ_n shown in Fig. 4, to be compared with the map of E_{2^+} given in Fig. 3. This way, a measurement of E_{2^+} for nuclei in the studied region may give us a knowledge on their shell structure, besides the knowledge on their deformation. Up to now, the basic information about the shell structure of these nuclei comes from the analysis of their half-lives (e.g., [2, 3]). This knowledge is especially important

Values of E_{2^+}, $Q_\alpha^{\rm par}$, and b_{2^+}/b_{0^+} calculated for isotopes of the elements Rf ($Z = 104$), Sg ($Z = 106$), and Hs ($Z = 108$)

N	A	E_{2^+}, keV	$Q_\alpha^{\rm par}$, MeV	b_{2^+}/b_{0^+}, %
$Z = 104$				
148	252	49.1	10.19	18.9
150	254	46.9	9.90	16.7
152	256	43.4	9.96	15.1
154	258	44.5	9.60	13.1
156	260	46.4	9.06	11.0
158	262	47.3	8.54	9.3
160	264	47.2	8.05	8.0
162	266	44.3	8.66	7.6
164	268	49.0	8.46	6.4
166	270	54.9	8.11	5.2
$Z = 106$				
150	256	48.4	10.97	15.4
152	258	44.7	11.02	14.0
154	260	45.0	10.69	12.2
156	262	45.9	10.20	10.4
158	264	45.6	9.65	9.0
160	266	45.0	9.13	7.7
162	268	41.9	9.79	7.3
164	270	46.5	9.58	6.2
166	272	51.8	9.22	5.1
168	274	57.0	8.77	4.2
$Z = 108$				
154	262	46.2	12.17	11.4
156	264	46.6	11.76	9.9
158	266	45.8	11.24	8.6
160	268	43.9	10.80	7.5
162	270	40.2	11.39	7.0
164	272	44.5	11.03	5.9
166	274	49.1	10.52	5.0
168	276	53.8	9.84	4.1
170	278	61.6	8.86	3.2

for the superheavy nuclei as they exist due to their shell structure [24].

The table gives values of the ratio b_{2^+}/b_{0^+} calculated for even–even isotopes of the elements 104, 106, and 108, i.e., for nuclei which show a great increase in their half-lives due to their shell structure [1–3] and which, simultaneously, are predicted to be well deformed. One can see that for a given atomic number Z, b_{2^+}/b_{0^+} decreases with increasing neutron number N. Thus, among all isotopes, for which one would like to obtain the rotational state 2^+ and measure its energy E_{2^+}, one should choose the lightest one. For this isotope, the probability of the $2^+ \to 0^+$ transition from the 0^+ ground state of the parent nucleus, with respect to the probability of the $0^+ \to 0^+$ transition in α decay, is expected to be the largest. The calculated values of the rotational energy E_{2^+} and of the α-decay energy of the corresponding parent nucleus $Q_\alpha^{\rm par}$ are also given in the table.

To check the quality of our calculation of the ratio b_{2^+}/b_{0^+}, we have compared the calculated values with the experimental ones for nuclei for which this ratio has been measured. The result is shown in Fig. 5. One can see that the description is rather good. In particular, the isotopic dependence of this ratio is correctly reproduced by the calculation.

ACKNOWLEDGEMENTS

The authors would like to thank S. Hofmann, T.L. Khoo, M. Leino, and G. Münzenberg for helpful discussions.

Support by the Polish State Committee for Scientific Research (KBN), grant no. 2 P03B 117 15, and by the Bogoliubov–Infeld Programme is gratefully acknowledged.

REFERENCES

1. Z. Patyk and A. Sobiczewski, Nucl. Phys. A **533**, 132 (1991).
2. R. Smolańczuk and A. Sobiczewski, in *Proceedings of the XV EPS Conference on Nuclear Physics: "Low Energy Nuclear Dynamics," St. Petersburg, 1995,* Ed. by Yu. Ts. Oganessian, W. von Oertzen and R. Kalpakchieva (World Scientific, Singapore, 1995), p. 313.
3. R. Smolańczuk, J. Skalski, and A. Sobiczewski, Phys. Rev. C **52**, 1871 (1995).
4. S. Hofmann, Rep. Prog. Phys. **61**, 639 (1998); Acta Phys. Pol. B **30**, 621 (1999).
5. Yu. Ts. Oganessian, A. V. Eremin, A. G. Popeko, *et al.,* Nature **400**, 242 (1999).
6. V. Ninov, K. E. Gregorich, W. Loveland, *et al.,* Phys. Rev. Lett. **83**, 1104 (1999).
7. A. Sobiczewski, Fiz. Élem. Chastits At. Yadra **25**, 295 (1994) [Phys. Part. Nucl. **25**, 119 (1994)].
8. P. Möller and J. R. Nix, J. Phys. **20**, 1681 (1994).
9. A. Sobiczewski, Usp. Fiz. Nauk **166**, 943 (1996) [Phys. Usp. **39**, 885 (1996)].
10. P. Möller, J. R. Nix, W. D. Myers, and W. J. Świątecki, At. Data Nucl. Data Tables **59**, 185 (1995).

11. J. F. Berger, L. Bitaud, J. Decharge, *et al.,* in *Proceedings of the International Workshop "Extremes of Nuclear Structure," Hirschegg, Austria, 1996,* Ed. by H. Feldmeier, J. Knoll, and W. Nörenberg (GSI, Darmstadt, 1996), p. 43.
12. S. Ćwiok, J. Dobaczewski, P.-H. Heenen, *et al.,* Nucl. Phys. A **611**, 211 (1996).
13. R. R. Chasman and I. Ahmad, Phys. Lett. B **392**, 255 (1997).
14. P. Reiter, T. L. Khoo, C. J. Lister, *et al.,* Phys. Rev. Lett. **82**, 509 (1999).
15. M. Leino, H. Kankaanpää, R.-D. Herzberg, *et al.,* Eur. Phys. J. A **6**, 63 (1999).
16. R.-D. Herzberg and M. Leino, private communication (1999).
17. G. Münzenberg, S. Hofmann, H. Folger, *et al.,* Z. Phys. A **322**, 227 (1985).
18. G. Münzenberg and P. Armbruster, in *Exotic Nuclear Spectroscopy,* Ed. by W. C. McHarris (Plenum, New York, 1990), p. 181.
19. I. Muntian, Z. Patyk, and A. Sobiczewski, Acta Phys. Pol. B **30**, 689 (1999); Phys. Rev. C **60**, 041302 (1999).
20. H. J. Krappe, J. R. Nix, and A. J. Sierk, Phys. Rev. C **20**, 992 (1979).
21. S. Ćwiok, J. Dudek, W. Nazarewicz, *et al.,* Comput. Phys. Commun. **46**, 379 (1987).
22. A. Sobiczewski, Z. Patyk, S. Ćwiok, and P. Rozmej, Nucl. Phys. A **485**, 16 (1988).
23. I. Ragnarsson, A. Sobiczewski, R. K. Sheline, *et al.,* Nucl. Phys. A **233**, 329 (1974).
24. Z. Patyk, A. Sobiczewski, P. Armbruster, and K.-H. Schmidt, Nucl. Phys. A **491**, 267 (1989).

Physics of Atomic Nuclei, Vol. 64, No. 6, 2001, pp. 1110–1115. From Yadernaya Fizika, Vol. 64, No. 6, 2001, pp. 1185–1190.
Original English Text Copyright © 2001 by Mikhailov, Quentin, Briançon.

Angular Momentum of Fission Fragments*

I. N. Mikhailov**, **P. Quentin**[1)], and **Ch. Briançon**[2)]

Joint Institute for Nuclear Research, Dubna, Russia
and Centre de Spectrométrie Nucléaire et de Spectrométrie de Masse
(IN2P3–CNRS), Orsay, France

Received September 11, 2000

Abstract—We continue the discussion on the respective roles of individual and collective motion in the angular momentum distribution in fission fragments. As in our prior publications on the subject, the role of individual nucleon motion in fragments in the postscission configuration is underlined, and the central part in the discussion concerns phenomena observed in the spontaneous fission of even–even nuclei. A formalism is prepared to study the spin distribution of fragments in induced fission from high-spin states. *© 2001 MAIK "Nauka/Interperiodica".*

1. INTRODUCTION

A rather high-spin population in fission fragments is a general property of all types of fission processes (see references in the review paper [1]): it was discovered already long ago in thermal-neutron-induced fission [2] and in spontaneous fission from ground states of heavy nuclei [3, 4], as well as in photofission, fast-neutron-induced fission, and alpha-particle-induced fission [5] and, finally, in the fission process following heavy ion collisions (see, e.g., [1]). Recent detailed measurements provide important information on the spin distribution in chosen pairs of fragments from the same compound nucleus [6] and on the angular distribution of γ rays deexciting the fragments in binary (and in some cases ternary [7]) fission.

Most of the theoretical accounts of the spin content in fission fragments consider dynamical sources of generation of rotational currents inside the fission fragments issuing from quantum or thermal activation of collective degrees of freedom before the scission. As a typical example of the collective mechanism, we mention the excitation of the bending mode considered in [8–11] and, in particular, in [12]. Naturally, the mean field rotation, present in the case of fission following heavy ion fusion, must also be considered as a possible mechanism of fragments' angular momentum generation.

These explanations leave unresolved a number of questions raised by experimental studies [13]. It is found that in most cases the zero-point motion must be complemented with temperature effects. The temperature needed to explain the bulk of the data even roughly turns out to be unreasonably high (2–3 MeV in [6], yielding an excitation energy $\geq$50 MeV). The prescission excitation of a fissioning nucleus cannot explain the drop down to low values (2–$3\hbar$) of the mean square angular momentum found in some particular pairs of fragments. Another problem, remaining unresolved by the theory based exclusively on the account of collective currents excitation, is discussed in [7], where the angular distributions of photons in binary fission and in fission accompanied by a light charged particle (ternary) are compared and found to be virtually the same, contrary to theoretical estimations.

In [14, 15] a "postscission" mechanism of the spin generation is suggested: the pumping of spin by orientation of the fragments in the reference system attached to the fission direction. The deformed fragments before separating at distances larger than the length of internucleon interaction keep their neck-to-neck orientation due to the polarizing effects of nuclear and Coulomb forces. The single-particle states in a field without central symmetry are not states with a definite value of angular momentum. Consequently, the individual particle motions contribute to the angular momentum in each fragment. In [14, 15], it was shown that the bulk of angular-momentum content of the fragments of spontaneously fissioning nuclei from the ground and weakly excited states has precisely this origin: it is generated by the single-particle motion in the deformed field of primary fragments.

The discussion presented in this paper concerns mostly the spontaneous fission from the ground state. However, we add here to the formalism developed in

---

[*] This article was submitted by the authors in English.

[1)] CENBG–IN2P3/CNRS and Université Bordeaux I, France.

[2)] CSNSM–IN2P3/CNRS, Orsay, France.

[**] e-mail: `imikh@thsun1.jinr.ru`

[14, 15] some material which will allow us to study in the future the spin distribution in fragments from nuclei having large rotational angular momentum.

2. THE STATE OF PRIMARY FRAGMENTS

As the "building blocks" from which the wave function of a fissioning nucleus is constructed, we consider products of two Slater determinants or BCS functions $\Phi^{(i)}_{J_i}$ ($i = 1$ or 2). As a rule, the single-particle states in the Slater determinants stem from rotating deformed potential wells. This introduces in the game "collective" angular momenta

$$\mathbf{J}_i = \langle \Phi^{(i)}_{J_i} \mid \hat{\mathbf{J}}^{(i)} \mid \Phi^{(i)}_{J_i} \rangle. \tag{1}$$

To fix the geometry, we assume that the reference frame has the origin at the center of mass of the fissioning nucleus with the z axis coincident with the line connecting the centers of mass of fragments, e.g., with the instantaneous direction of their flight. We assume also that the collective angular momenta of fragments are directed along the x axis ($\mathbf{J}_i = (J_i, 0, 0)$). Thus, the y–z plane is understood as the reaction plane in the induced fission case. In the case of the spontaneous fission of an even–even nucleus from the ground state, all directions in the plane perpendicular to the direction of fission are equivalent and the measurable quantities represent some appropriately averaged calculation results.

Some comments on the properties of Slater determinants are appropriate. One expects that at the moment of scission the fragments are deformed. Then, the corresponding Slater determinants are superpositions of eigenstates of the angular momentum operators:

$$\Phi^{(i)}_{J_i} = \sum_{I_i, K_i} a^{(i)}_{I_i, K_i} \Psi^{(i)}(I_i, K_i). \tag{2}$$

Consequently, they are not eigenstates of Hamiltonians of primary fragments separated by distances greater than the length of the fragment–fragment interaction. Let us recall that eigenstates of individual nuclei are associated with the wave functions in which all possible orientations of the inertia tensor are represented with appropriately chosen weights (equal weights for all orientations in the case of the ground state of an even–even nucleus). In the late 1950s and early 1960s, this character of "deformed Slater determinants" originated theoretical studies on the accuracy of the cranking model in the determination of nuclear inertia properties. The description of the relevant properties of Slater determinant eigenfunctions of a Schrödinger equation corresponding to a single particle deformed potential is given in [16]. The use of Slater determinants projected onto the space of functions with fixed angular momentum showed that the cranking approach gives numerically close results for the moment of inertia as compared with the results obtained with projected functions [16]. Probably, the first formal proof of the accuracy of the cranking approach was reported in [17], where it was shown that the accuracy in determining the moment of inertia is in inverse proportion to the dispersion of the squared angular momentum in the unprojected BCS or Slater determinant function:

$$\langle \Phi^{(i)}_{J_i} \mid \hat{\mathbf{J}}^2 \mid \Phi^{(i)}_{J_i} \rangle_{\text{int}} = \hbar^2 \sum_{I_i, K_i} \mid a^{(i)}_{I_i, K_i} \mid^2 \; I_i(I_i+1).$$

The typical values of the dispersion for some of rare earth nuclei in their ground states have been estimated and found to be of the order of $\sqrt{\langle \hat{\mathbf{J}}^2 \rangle_{\text{int}}} = 10\hbar$, e.g., the same order of magnitude as found in fission fragments. Later on, numerous authors [18, 19] contributed to the analysis of the quantities $a_{I,K}$. A development of the mathematical structure of the theory which happens to be important for our purpose was suggested by Bhaduri and Das Gupta in [20]. Here, a nice simple form of these expansion coefficients was proposed for even–even nuclei when the deformation is large and stable enough so that the fragments may be considered as good axial rotors. Through an analogy with the statistical mechanics description of a rotational band, these authors deduced in this limit that the factors $a^{(i)}_I \equiv a^{(i)}_{I,0}$ should be of the form of a Boltzmann factor as

$$\mid a^{(i)}_I \mid^2 = \frac{2(2I+1)}{\langle J_i^2 \rangle_{\text{int}}} \exp\left(-\frac{I(I+1)}{\langle J_i^2 \rangle_{\text{int}}}\right). \tag{3}$$

These results were confirmed for "cranked" Slater determinants, and the correspondence between the cranking and projection methods was further clarified in an elegant paper by Kamlah (see the presentation of these ideas in Section 11.4 of [21]).

The above discussion shows that the spin of fragments in the states described by the product of two Slater determinants $\Phi^{(1)}_{J_1}\Phi^{(2)}_{J_2}$ is spread over a rather large region with weights similar to that in the case of the thermal distribution. Then, it follows that such product functions cannot be associated with the state of a fissioning nucleus having a definite angular-momentum value. This leads us to the following suggestion concerning the structure of the wave function of primary fragments from the mother nucleus fissioning from the quantum state α with the angular momentum quantum numbers I_m, M_m:

$$\Psi(\alpha, I_m, M_m \mid \{c_{\alpha, I_m}(J_1, J_2, L, I)\}) \tag{4}$$

$$= \int dJ_1 \int dJ_2 \sum_{I, L; M_I, M_L} c_{\alpha, I_m}(J_1, J_2, L, I)$$

$$\times\, C^{I_m,M_m}_{I,M_I;L,M_L}\,\Phi_{L,M_L}(\mathbf{R})\Psi^{(1,2)}_{J_1,J_2;I,M_I}$$

[where $c_{\alpha,I_m}(J_1,J_2,L,I)$ is a weight factor which will be discussed below and $C^{J,M}_{I_1,M_1;I_2,M_2}$ is a Clebsch–Gordan coefficient]. In the above, $\Phi_{L,M_L}(\mathbf{R})$ and $\Psi^{(1,\,2)}_{J_1,J_2;I,M_I}$ are the terms describing the orbital and intrinsic motions, respectively. This definition of the wave function also allows for a functional dependence on the distribution of fragments in collective angular momenta J_1 and J_2 or in the frequencies of their rotation. In the spirit of the cranking approach, collective angular momenta may be considered to have a continuous spectrum.

The orbital motion of fragments is described by

$$\Phi_{L,M_L}(\mathbf{R}) = \frac{F_L(R)}{R}Y_{L,\,-M_L}(\theta,\phi). \qquad (5)$$

We specify the radial wave functions $F_L(R)$ by setting a normalization condition

$$\lim_{R\to\infty} F_L(R) = 1.$$

The intrinsic state of fragments having fixed angular-momentum quantum numbers I, M_I is given by

$$\Psi^{(1,\,2)}_{J_1,J_2;\,I,M} = \frac{1}{N_{J_1,J_2,I}}\hat{P}_{I,M}\left(\Phi^{(1)}_{J_1}\Phi^{(2)}_{J_2}\right), \qquad (6)$$

where the restoration of rotational properties of $\Phi^{(1)}_{J_1}\Phi^{(2)}_{J_2}$ is achieved by introducing the projection operator

$$\hat{P}_{I,\,M_I} = \sum_{K=-I}^{I}\hat{P}^{I}_{M_I,\,K},$$

$$\hat{P}^{I}_{M,\,K} = \frac{2I+1}{8\pi^2}\int\limits_0^{2\pi} d\alpha \int\limits_0^{\pi}\sin\beta\, d\beta \qquad (7)$$

$$\times\int\limits_0^{2\pi} d\gamma\, D^{I}_{M,K}(\alpha,\beta,\gamma)^{*}\,\hat{D}(\alpha,\beta,\gamma),$$

$D^{I}_{M,K}(\alpha,\beta,\gamma)$ and $\hat{D}(\alpha,\beta,\gamma)$ being the Wigner rotation D function and the operator of rotation, respectively [22]. The operator $\hat{P}_{I,M_I}$ picks up all the components with angular-momentum quantum numbers I, K $(-I \le K \ge I)$, transforming each of them into the eigenfunction of the angular momentum with the quantum numbers I, M_I. The quantity

$$N^2_{J_1,J_2,I} = \langle\Phi^{(1)}_{J_1}\Phi^{(2)}_{J_2} \mid \sum_{K=-I}^{I}\hat{P}^{I}_{K,K} \mid \Phi^{(1)}_{J_1}\Phi^{(2)}_{J_2}\rangle \qquad (8)$$

is the squared norm of the projected wave function.

The wave function in (4) manifestly possesses the proper symmetry with respect to the group of rotation. What is not clear, in fact, is its connections with the mean-field approaches to the fission dynamics. One may establish such a relation introducing the averaged density matrix

$$\hat{\rho}\,\{c(J_1,J_2,L,I)\} \qquad (9)$$

$$= \frac{1}{\Gamma}\sum_{\alpha,I_m,M_m}\int d\Omega\;\Psi^{\dagger}(\alpha,I_m,M_m \mid \{J_1,J_2\})$$

$$\times\,\Psi(\alpha,I_m,M_m \mid \{J_1,J_2\}).$$

Here, the integration goes over the angular variables $\Omega = \theta,\phi$ determining the variable $\mathbf{R}$ ($\mathbf{R}\to R,\theta,\phi$). The sum runs over the states of the fissioning nucleus, contributing significantly to the primary fragments having a distribution of matter and currents similar to that in the states described by Slater functions $\Phi^{(i)}$. The factor Γ stands for the number of different states of fissioning nucleus entering into the sum.

We suggest now that the weight function $c_{\alpha,I_m}(J_1,J_2,L,I)$ can be approximated as

$$F_L(R)c_{\alpha,I_m}(J_1,J_2,L,I) \qquad (10)$$

$$= \tilde{c}_{\alpha,I_m}(J_1,J_2)\sqrt{\frac{2I+1}{2I_m+1}}\,N_{J_1,J_2,I}.$$

The R dependence introduced in the preceding makes the new c coefficients depend on R. In (10), R is defined by its value at scission. Using the upper expression, one readily finds $\hat{\rho} = \sum_{I,M}\hat{P}_{I,M}\,\hat{\rho}_{\mathrm{m.f}}\,\hat{P}^{\dagger}_{I,M}$ with

$$\hat{\rho}_{\mathrm{m.f}} = \int dJ_1 dJ_2 dJ'_1 dJ'_2 \mid \Phi^{(1)}_{J'_1}\Phi^{(2)}_{J'_2}\rangle \qquad (11)$$

$$\times\langle J'_1,J'_2 \mid \rho \mid J_1,J_2\rangle_{\mathrm{m.f}}\langle\Phi^{(1)}_{J_1}\Phi^{(2)}_{J_2}\mid,$$

$$\langle J'_1,J'_2 \mid \rho \mid J_1,J_2\rangle_{\mathrm{m.f}}$$

$$= \frac{1}{\Gamma}\sum_{\alpha,I_m}\tilde{c}_{\alpha,I_m}(J_1,J_2)\,\tilde{c}_{\alpha,I_m}(J'_1,J'_2).$$

The mean values of arbitrary operators commuting with the angular-momentum operators of fragments calculated with $\hat{\rho}_{\mathrm{m.f}}$ and with the density matrix $\hat{\rho}$ in (9) coincide. Thus, the density matrix $\hat{\rho}_{\mathrm{m.f}}$ may be considered as containing the basic information on the states of primary fragments averaged over the initial state (and the angular momentum) of the fissioning nucleus. On the other hand, the density matrix $\hat{\rho}_{\mathrm{m.f}}$ given in terms of the unprojected Slater determinants may be obtained, in principle, in approaches based on the mean-field dynamics. If the structure of primary fragments can be approximated by projected Slater determinants and the mean-field theory is capable of producing averaged information on the fission process, the factorization of coefficients $c_{\alpha,I_m}(J_1,J_2,L,I)$ in (10) seems plausible. Note, however, that such an interpretation implies the existence of a relation between the yields of fragments with different values of orbital angular momentum L and the quantity $(2I+1)N^2_{J_1,J_2,I}$.

3. SPINS OF FRAGMENTS IN SPONTANEOUS FISSION

Hereafter, we discuss the spin distribution in fragments of the spontaneous fission of an even–even nucleus from its ground (0^+) state. We summarize the essential results of [14, 15] corresponding to a simple special case of the wave function in (4) when the weighting function $c(J_1, J_2, L, I)$ in (4) is proportional to $\delta(J_1 + J_2 + L)$. More precisely, we assume that

$$\Psi(I_m, M_m, J_1, J_2) \tag{12}$$
$$= \sum_{M_I,M_L} C^{I_m,M_m}_{I,M_I;L,M_L}\Phi_{L,M_L}(\mathbf{R})\Psi^{(1,2)}_{J_1,J_2;\,I,M_I}.$$

This total wave function manifestly possesses the proper symmetry with respect to the group of rotation and describes the quantum state with a vanishing value of the total angular momentum operator $\hat{\mathbf{J}}_{\rm tot} = \hat{\mathbf{L}} + \hat{\mathbf{J}}_1 + \hat{\mathbf{J}}_2$. It is also an eigenfunction of the orbital angular momentum $\hat{\mathbf{L}}^2$ with the eigenvalue $L(L+1)$. Since $\hat{\mathbf{J}}_{\rm tot}|\Psi\rangle = 0$, these properties lead to the following relations :

$$\langle\hat{\mathbf{L}}\cdot(\hat{\mathbf{J}}_1 + \hat{\mathbf{J}}_2)\rangle = -\langle\hat{\mathbf{L}}^2\rangle, \tag{13}$$
$$\langle\mathbf{J}_1^2\rangle + \langle\mathbf{J}_2^2\rangle + 2\langle\mathbf{J}_1\cdot\mathbf{J}_2\rangle = \langle\hat{\mathbf{L}}^2\rangle.$$

Valuable informations on the spin distribution in the fission fragments may be obtained using (2), where $\Psi^{(i)}(I_i, K_i)$ are normalized wave functions of each of fragments having good angular momentum quantum numbers I_i, K_i. The operator $\hat{P}_{L,M}$ from (7) applied to the product of two wave functions $\Phi^{(1)}_{J_1}$ and $\Phi^{(2)}_{J_2}$ yields

$$\hat{P}_{L,M}\left(\Phi^{(1)}_{J_1}\Phi^{(2)}_{J_2}\right) \tag{14}$$
$$= \sum_{I_1,I_2}\sum_{K_1,K_2} C^{L,K}_{I_1,K_1;\,I_2,K_2}a^{(1)}_{I_1,K_1}a^{(2)}_{I_2,K_2}$$
$$\times\sum_{M_1,M_2} C^{L,M}_{I_1,M_1;\,I_2,M_2}\Psi^{(1)}(I_1,M_1)\Psi^{(2)}(I_2,M_2).$$

The mean values $\langle\hat{\mathbf{J}}_i^2\rangle$ expressed in terms of the expansion coefficients $a^{(i)}_{I_i,K_i}$ are

$$\langle\hat{\mathbf{J}}_i^2\rangle = \frac{1}{N^2_{J_1,J_2,L}}\sum_{I_1,K_1}\sum_{I_2,K_2} I_i(I_i+1) \tag{15}$$
$$\times\left(C^{L,K}_{I_1,K_1;I_2,K_2}a^{(1)}_{I_1,K_1}a^{(2)}_{I_2,K_2}\right)^2,$$

where the norm of the projected function is given by

$$N^2_{J_1,J_2,L} \tag{16}$$
$$= \sum_{I_1,K_1}\sum_{I_2,K_2}\left(C^{L,K}_{I_1,K_1;I_2,K_2}a^{(1)}_{I_1,K_1}a^{(2)}_{I_2,K_2}\right)^2.$$

In the special case when $L = 0$, one obtains from the above formulas

$$\langle\hat{\mathbf{J}}_i^2\rangle = -\langle\hat{\mathbf{J}}_1\hat{\mathbf{J}}_2\rangle \tag{17}$$
$$= \frac{\sum_{I,K}\left(a^{(1)}_{I,K}a^{(2)}_{I,K}\right)^2(I(I+1)/(2I+1))}{\sum_{I,K}\left(a^{(1)}_{I,K}a^{(2)}_{I,K}\right)^2(1/(2I+1))}.$$

This result generalizes an expression obtained in [14] to the case in which the fragments have no axial symmetry.

4. STRUCTURE OF $\Phi^{(i)}_{J_i}$ FUNCTIONS

In this section, we repeat for the sake of completeness a discussion already presented by the authors in [15]. The functions $\Phi^{(i)}_{J_i}$ should in principle be found from the dynamical equations describing the scission. However, the angular momentum distributions do not change much prior to γ emission. Indeed, only the Coulomb interaction is liable to change the orbital and intrinsic angular momenta of fragments during this time. Leaving aside the study of the Coulomb interaction effects (which were found to be small in [11]), one may describe the intrinsic structure of the separated fragments in the framework of the cranking approach [21]. Some further approximations to the latter will be added in the course of the discussion so that more transparent conclusions can be drawn.

An approximate solution of the variational cranking equation

$$\delta\langle\Phi_i(\Omega_i)|\hat{H}_i - \Omega_i\hat{J}^{(i)}_x - E_i(\Omega_i)\mid\Phi_i(\Omega_i)\rangle = 0 \tag{18}$$

with Lagrange multipliers Ω_i determined from the condition

$$\langle\Phi_i(\Omega_i)\mid\hat{J}^{(i)}_x\mid\Phi_i(\Omega_i)\rangle = J_i \tag{19}$$

is given at lowest order in Ω by

$$\Phi^{(i)}(\Omega_i) = \Phi^{(i)}_0 - \Omega_i\sum_n\mid n\rangle \tag{20}$$
$$\times\frac{\langle n\mid\hat{J}^{(i)}_x\mid\Phi^{(i)}_0\rangle}{E^{(i)}_n - E^{(i)}_0} + \cdots,$$

containing the sum over all intrinsic excited states $|n\rangle = \alpha^\dagger_p\alpha^\dagger_q\Phi_i(0)$. The rotational frequencies Ω_i are related to the collective spins of the fragments by $\mathcal{J}_i\Omega_i = |J_i|$, where

$$\mathcal{J}_i = \sum_n\frac{|\langle n\mid\hat{J}^{(i)}_x\mid\Phi^{(i)}_0\rangle|^2}{E^{(i)}_n - E^{(i)}_0} \tag{21}$$

are the corresponding moments of inertia. In the case of axially symmetrical fragments with strong deformation, the matrix element

$$\langle\Phi^{(i)}(\Omega)|\hat{D}(R)(\hat{\mathbf{J}}^{(i)})^2 \mid \Phi^{(i)}(\Omega)\rangle$$

(where R represents the relative rotation between the two fragments) appearing in the expression of the expectation value of the angular momentum of fragment i may be approximated as

$$\langle\Phi^{(i)}(\Omega) \mid \hat{D}(R)(\hat{\mathbf{J}}^{(i)})^2 \mid \Phi^{(i)}(\Omega)\rangle$$
$$\sim \sum_{\mu}(-1)^{-\mu}\langle\Phi^{(i)}(\Omega) \mid \hat{J}^{(i)}_{-\mu}\hat{D}(R)\hat{J}^{(i)}_{\mu} \mid \Phi^{(i)}(\Omega)\rangle.$$

The action of the angular momentum operator $\hat{J}^{(i)}_k$ $(k = x, y, z)$ on $\Phi^{(i)}(\Omega)$ is given by

$$\hat{J}^{(i)}_k\Phi^{(i)}(\Omega_i) = \hat{J}^{(i)}_k\Phi^{(i)}(0) \tag{22}$$
$$-\,\Omega_i\sum_{n,m} \mid m\rangle\langle m \mid J^{(i)}_k \mid n\rangle\frac{\langle n \mid \hat{J}^{(i)}_x \mid \Phi^{(i)}_0\rangle}{E^{(i)}_n - E^{(i)}_0}$$
$$\sim \left(\hat{J}^{(i)}_k - \delta_{k,x}J_i\right)\Phi^{(i)}(0).$$

Using the projection procedure described before, one then obtains

$$\langle\mathbf{J}^2_i\rangle = (J^{(i)})^2 \tag{23}$$
$$+\,\frac{\sum_{I_1,I_2} I^{(i)}(I^{(i)}+1)\left(C^{L,0}_{I_1,0;I_2,0}a^{(1)}_{I_1,0}a^{(2)}_{I_2,0}\right)^2}{\sum_{I_1,I_2}\left(C^{L,0}_{I_1,0;I_2,0}a^{(1)}_{I_1,0}a^{(2)}_{I_2,0}\right)^2}.$$

Thus, the mean angular momentum due to the fragment rotation and the one generated via the orientation pumping add up quadratically.

5. NUMERICAL ESTIMATES

To evaluate approximately the second term in the sum of (23), we may use, as in [14], the simple ansatz of [20], where it is suggested that $a^{(i)}_I$ could be approximated as a Boltzmann factor [see (3)]. Using this ansatz, we find that the mean square of the angular momentum of the fragment i is given by

$$\langle\mathbf{J}^2\rangle_i = (J^{(i)})^2 + \left(\frac{1}{\langle J^2_1\rangle_{\text{int}}} + \frac{1}{\langle J^2_2\rangle_{\text{int}}}\right)^{-1} \tag{24}$$

in the case of a small value of the orbital angular momentum.

In [20], a good correspondence was found between the Boltzman distribution of the angular momentum of deformed Slater determinants and the results of microscopic calculations made for s–d nuclei. The calculations of $|a_I|^2$ coefficients and of $\langle J^2\rangle_{\text{int}}$ for even–even rare-earth nuclei were also reported in [18, 19, 21]. It is found that typically $\langle J^2\rangle_{\text{int}} = 100\hbar^2$. From these estimations, it is possible to conclude that for strongly deformed fission fragments spins up to approximately $7\hbar$ or more could be generated by the orientation pumping mechanism, which coincides with the mean angular momentum of fragments found experimentally in most cases.

When one of the fragments is nearly spherical, the second term in (24) is small. Then, the role of the collective rotation becomes dominant. Nevertheless, even in such cases the orientation pumping mechanism of the population of high-spin states in a well deformed nucleus may not be ignored if the orbital angular momentum is large.

6. MEAN ORBITAL ANGULAR MOMENTUM AND RELATED CORRELATIONS

Preliminary conclusions about the distribution on L and on the correlations of angular momenta of fragments may be obtained assuming a thermal distribution

$$p(\mathbf{J}^{(1)}_{\text{coll}}, \mathbf{J}^{(2)}_{\text{coll}}, \mathbf{L})$$
$$\sim \exp\left[-(a(\mathbf{J}^{(1)}_{\text{coll}})^2 + b(\mathbf{J}^{(2)}_{\text{coll}})^2 + c\mathbf{L}^2)/\Theta\right].$$

Qualitative estimations may be done applying the techniques appropriate for large angular momenta. Then, one finds $\overline{\mathbf{J}^{(1)}_{\text{coll}}} = \overline{\mathbf{J}^{(2)}_{\text{coll}}} = \overline{\mathbf{L}} = 0$,

$$\overline{\left(\mathbf{J}^{(1)}_{\text{coll}}\right)^2} = \frac{\Theta}{2}\left[\frac{\cos^2\phi}{\Lambda^2_1} + \frac{\sin^2\phi}{\Lambda^2_2}\right],$$
$$\overline{\left(\mathbf{J}^{(2)}_{\text{coll}}\right)^2} = \frac{\Theta}{2}\left[\frac{\sin^2\phi}{\Lambda^2_1} + \frac{\cos^2\phi}{\Lambda^2_2}\right],$$
$$\overline{\mathbf{L}^2} = \frac{\Theta}{2}\left[\frac{(\cos\phi - \sin\phi)^2}{\Lambda^2_1} + \frac{(\cos\phi + \sin\phi)^2}{\Lambda^2_2}\right]$$
$$\Big(\tan(2\phi) = -2c/(a-b),$$
$$\Lambda_1 = \left[a\cos\phi^2 + b\sin\phi^2 + c(\cos\phi - \sin\phi)^2\right]^{1/2},$$
$$\Lambda_2 = \left[a\sin\phi^2 + b\cos\phi^2 + c(\cos\phi - \sin\phi)^2\right]^{1/2}\Big).$$

Consider the mean angular momenta for two particular cases:

$$\mathbf{a} = \mathbf{b} \Longrightarrow \overline{\left(\mathbf{J}^{(1)}_{\text{coll}}\right)^2} = \overline{\left(\mathbf{J}^{(2)}_{\text{coll}}\right)^2} = \frac{1}{2}\overline{\mathbf{L}^2} = \frac{\Theta}{2a},$$
$$\mathbf{a} \gg \mathbf{b},\ \mathbf{a} \gg \mathbf{c}$$
$$\Longrightarrow \overline{\left(\mathbf{J}^{(1)}_{\text{coll}}\right)^2} \sim \frac{\Theta}{2a},\ \overline{\left(\mathbf{J}^{(2)}_{\text{coll}}\right)^2} \sim \frac{\Theta}{2(b+c)},$$
$$\overline{\mathbf{L}^2} = \overline{\left(\mathbf{J}^{(1)}_{\text{coll}}\right)^2} + \overline{\left(\mathbf{J}^{(2)}_{\text{coll}}\right)^2}.$$

In both cases, $\overline{\mathbf{J}^{(1)}_{\text{coll}} \cdot \mathbf{J}^{(2)}_{\text{coll}}} = 0$. Angular momenta generated by the pumping mechanism are highly correlated. In particular, when $L = 0$, $\overline{\mathbf{J}_1 \cdot \mathbf{J}_2} = -2\overline{(\mathbf{J}_1)^2} = -2\overline{(\mathbf{J}_2)^2}$. Thus, it is the pumping mechanism which is responsible for the correlation of angular momenta of fragments.

7. CONCLUSIONS

From the present analysis, we can draw some conclusions in the realm of both experimental and theoretical aspects of this fascinating process where vortical modes emerge out of what could be reasonably described at its start like a purely potential mode. Any data pertaining to the determination of the orbital angular momentum L can be deemed from our analysis as carrying very valuable informations on the scission phenomenon. As we have seen, this could be achieved by measuring the quantity $\langle \mathbf{J}_1 \cdot \mathbf{J}_2 \rangle$.

From a theoretical point of view, we would like to stress that the inclusion of the pumping mechanism in estimating the spin of fission fragments is not optional. If it does not work, the mean field approach to the fission dynamics is dubious.

Taking into account the pumping mechanism, one settles the problem of the high value of the "effective temperature" needed to explain the "large" values of the mean square angular momenta in fission fragments. Moreover, it makes plausible the "effective temperature" variations in different pairs of fragments. Finally, it works when the collective generation of angular momentum takes place.

The material presented here constitutes a basis for a quantitative analysis of the spin distribution in fission fragments. Such a task, however, still remains ahead of us for many reasons. In particular, the scarcity of experimental information on the subject should be stressed, that being said, notwithstanding the long and profound experimental study of such a difficult subject which is carried out, nowadays, with state-of-the-art multidetector arrays.

ACKNOWLEDGMENTS

The authors express their sincere gratitude to the experimentalists and theoreticians involved in the studies of nuclear fission and associated problems for numerous discussions and, in particular, to G. Ter-Akopian, G. Popeko, W.I. Furman, Yu. Kopach, R. Kulessa, E. Lubkiewicz, S. Misicu, F. Hannachi, F. Goennenwein, A.G. Smith, G. Barreau, and T.P. Doan. The support of the collaboration agreement no. 97-30 between JINR (Dubna) and CSNSM and CENBG laboratories of IN2P3/CNRS (France) is gratefully acknowledged.

REFERENCES

1. W. R. Phillips, Acta Phys. Pol. B **28**, 59 (1997).
2. P. Armbruster *et al.,* Z. Naturforsch. A **26**, 59 (1971).
3. F. Pleasonton, R. L. Ferguson, and H. W. Schmitt, Phys. Rev. C **6**, 1023 (1972).
4. J. W. Wilhelmi *et al.,* Phys. Rev. C **5**, 2041 (1972).
5. D. Frenne, in *The Nuclear Fission Process,* Ed. by C. Wagemans (CRC Press, Boca Raton, 1991), p. 287.
6. G. S. Popeko *et al.,* in *Proceedings of the International Conference on Fission and Properties of Neutron–Rich Nuclei* (World Scientific, Singapore, 1998), p. 645.
7. Yu. N. Kopach *et al.,* Phys. Rev. Lett. **82**, 303 (1999).
8. M. M. Hoffman, Phys. Rev. B **133**, 714 (1964).
9. J. O. Rasmussen, W. Nörenberg, and H. J. Mang, Nucl. Phys. A **136**, 465 (1969).
10. J. R. Nix and W. J. Swiatecki, Nucl. Phys. **71**, 1 (1965).
11. S. Misicu, A. Sandulescu, G. M. Ter-Akopian, and W. Greiner, Phys. Rev. C **60**, 034613 (1999).
12. M. Zielinska-Pfabe and K. Dietrich, Phys. Lett. B **49**, 123 (1974).
13. J. O. Rasmussen and R. Donangelo, in *Proceedings of the International Conference on Fission and Properties of Neutron–Rich Nuclei* (World Scientific, Singapore, 1998), p. 1.
14. I. N. Mikhailov and P. Quentin, Phys. Lett. B **462**, 7 (1999).
15. I. N. Mikhailov, P. Quentin, and Ch. Briançon, in *Proceedings of the International Symposium "Quasiparticle and Phonon Excitations in Nuclei," RIKEN, Wako, Saitama, Japan, 1999* (World Scientific, Singapore, 2000), p. 184.
16. R. E. Peierls and J. Yoccoz, Proc. Phys. Soc. London, Sect. A **70**, 381 (1957).
17. I. N. Mikhailov, Dok. Akad. Nauk SSSR **154**, 68 (1964) [Sov. Phys. Dokl. **9**, 42 (1964)].
18. S. Islam, H. J. Mang, and P. Ring, Nucl. Phys. A **326**, 161 (1979).
19. D. W. L. Sprung, S. G. Lie, M. Vallicres, and P. Quentin, Nucl. Phys. A **326**, 37 (1979).
20. R. K. Bhaduri and S. Das Gupta, Nucl. Phys. A **212**, 18 (1973).
21. P. Ring and P. Schuck, *Nuclear Many-Body Theory* (Springer-Verlag, New York, 1980).
22. D. A. Varshalovich, A. N. Moskalev, and V. K. Khersonskii, *Quantum Theory of Angular Momentum* (World Scientific, Singapore, 1988).

Physics of Atomic Nuclei, Vol. 64, No. 6, 2001, pp. 1116–1120. From Yadernaya Fizika, Vol. 64, No. 6, 2001, pp. 1191–1196.
Original English Text Copyright © 2001 by Volkov, Adamian, Antonenko, Cherepanov, Scheid.

Synthesis of Superheavy Elements and the Process of Complete Fusion of Massive Nuclei*

V. V. Volkov**, **G. G. Adamian**[1),2)], **N. V. Antonenko**, **E. A. Cherepanov**, and **W. Scheid**[1)]

Joint Institute for Nuclear Research, Dubna, Moscow oblast, 141980 Russia

Received September 11, 2000

Abstract—The development of various approaches to describing the complete fusion of nuclei and their connections with experimental studies is discussed. A brief account of the dinuclear-system concept (DNSC), the approach proposed at Dubna, is given. The DNSC revealed two important features of the complete fusion of massive nuclei: the existence of the inner fusion barrier B^*_{fus} and the competition between complete fusion and quasifission channels in a dinuclear system formed at the capture stage. The DNSC was applied to the analysis of reactions used to synthesize superheavy elements (SHE). The DNSC provided a basis for the models of competition between complete-fusion and quasifission channels. Using these models, one can describe the cross section for SHE production in cold- and warm-fusion reactions.

1. INTRODUCTION

There are two main aspects in the problem of synthesis of superheavy elements (SHE).

The first one is associated with the properties of superheavy nuclei—i.e., with the magic values of Z and N, modes of radioactive decay, and the half-life with respect to radioactive decay. The second aspect concerns nuclear reactions that can be used to synthesize SHE: the type of reaction, the expected production cross section, and the optimal value of the excitation energy of a compound nucleus. The synthesis of SHE may be realized only in the complete fusion of two massive nuclei. This means that we must understand the mechanism of this nuclear process and create a realistic model for its description.

The main problem of the complete-fusion process is the mechanism of compound-nucleus formation. There are two difficulties inherent in this problem.

The first stems from the closed character of the complete-fusion process. Fusing nuclei do not send any signals that would allow one to reveal the mechanism of compound-nucleus formation. Experimentalists detect the products of compound-nucleus decay. But it is well known that a compound nucleus forgets the history of its formation.

The second is a high complexity of the theoretical analysis of the transformation of two multinucleon nuclear systems into a new one. Theorists developed various approaches to describing the complete-fusion process. These approaches reflect the progress in the experimental study of this fundamental nuclear process.

2. THREE APPROACHES TO DESCRIBING THE COMPLETE-FUSION PROCESS

2.1. First Approach

Consideration of the compound-nucleus-formation mechanism is omitted.

In the first approach, the compound-nucleus-formation mechanism is not considered at all. Early experiments employed rather light heavy ions (^{12}C, ^{14}N, ^{16}O, and ^{20}Ne). In reactions induced by these ions, the capture of a projectile by a target nucleus inevitably leads to the formation of a compound nucleus. The compound-nucleus-production cross section σ_{cn} was equal to the capture cross section σ_c:

$$\sigma_{\text{cn}} = \sigma_c. \tag{1}$$

The efforts of theorists were aimed at creating models for calculating the capture cross section σ_c. These were the optical model [1], the model of the critical distance [2], the surface friction model [3], and the model with a "pocket" in the nucleus–nucleus potential $V(R)$ [4]. In all these models, a critical orbital angular momentum l_{cr} was the most important characteristic of the complete-fusion process. The compound-nucleus-production cross section σ_{cn} is defined by the well-known relation

$$\sigma_{\text{cn}} = \pi\lambda\!\!\!^{-}{}^2 \sum_{l=0}^{l=l_{\text{cr}}} (2l+1)T_l, \tag{2}$$

---

*This article was submitted by the authors in English.

[1)] Justus-Liebig Universität, Giessen, Germany.

[2)] Institute of Nuclear Physics, Tashkent, Uzbekistan.

**e-mail: `cher@jinr.ru`

where T_l is the penetration factor.

2.2. Second Approach

The complete-fusion process is described on the basis of the liquid-drop model.

The use of heavier ions, such as ^{40}Ar and ^{84}Kr, in the relevant experiments revealed new nuclear processes: fast fission and quasifission. These processes were also realized in collisions with orbital angular momenta $l_i < l_{\rm cr}$ but without compound-nucleus formation. The main postulate of the first approach, $\sigma_{\rm cn} = \sigma_c$, was violated. The capture may be realized, but a compound nucleus is not formed.

The new approach to the complete fusion of the massive nuclei was proposed by W. Swiatecki. It was the macroscopic dynamical model (MDM) [5]. This model describes the whole history of the fusion process from the contact between nuclear surfaces to compound-nucleus formation. The fusion process was substantially simplified in the MDM. Actual nuclei consisting of protons and neutrons and having a shell structure were replaced by drops of a viscous nuclear liquid. The MDM introduced new characteristics of the fusion of massive nuclei: an extra push E_x and an extra–extra push E_{xx}. For the production of a compound nucleus, the bombarding energy E_i must be higher than $B_c + E_{xx}$. The MDM was very popular among experimentalists. However, serious difficulties arose in attempts at using the MDM to describe reactions employed to synthesize SHE. From our point of view, these shortcomings of the MDM stem from the replacement of actual nuclei by drops of a hypothetical nuclear liquid.

2.3. Third Approach

Complete fusion is the process of formation and evolution of a dinuclear system.

The third approach was proposed at Dubna [6]. The basic idea of the third approach is the assumption that complete fusion and deep-inelastic-transfer reactions (DITR) are similar nuclear processes. What does this assumption give us? In contrast to fusion and fission, DITRs are open reactions. They provide unique information about the interaction of two nuclei that appear to be in close contact after the full dissipation of the collision kinetic energy. It is this unique information that was used to reveal the mechanism of compound-nucleus formation. This approach, which was due to G.G. Adamian, N.V. Antonenko, E.A. Cherepanov, A.K. Nasirov, W. Scheid, and V.V. Volkov, was dubbed the dinuclear-system concept (DNSC) [7].

According to the DNSC, the main features of the fusion process are the following:

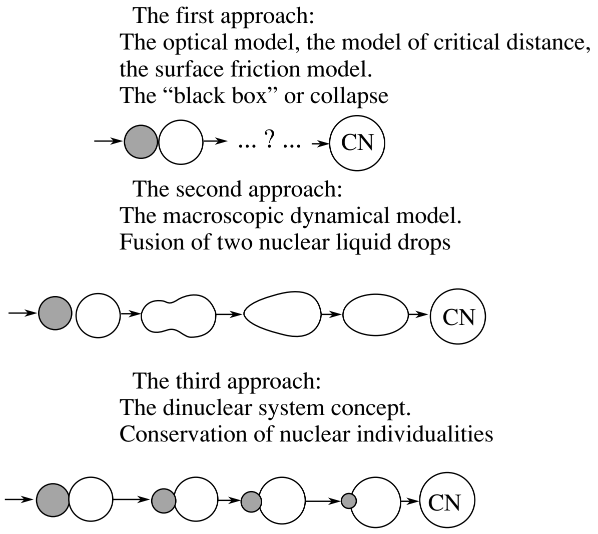

Fig. 1. Schematic illustration of the compound-nucleus-formation mechanism within various approaches to describing the complete-fusion process.

(i) A dinuclear system (DNS) is formed at the capture stage, after the full dissipation of the collision kinetic energy.

(ii) Complete fusion is an evolutionary process in which the nucleons of one nucleus gradually, shell by shell, are transferred to the other nucleus.

(iii) The nuclei of the DNS retain their individuality until the end of the fusion process (this important feature of DNS evolution is a consequence of the shell structure of nuclei).

Figure 1 highlights the fundamental difference between the pictures of the compound-nucleus-formation process that are offered by the first, the second, and the third approach. In the first approach, the restructuring stage of the process is regarded as a “black box” or collapse. In the second approach, fusing nuclear drops rapidly lose their individuality as the result of neck formation. Complete fusion is a dynamical process that develops in the space of deformation, as is the case in the fission process. In the DNSC, the fusing nuclei retain their individuality until the end of the fusion process. Complete fusion is mainly a statistical process that develops along the mass-asymmetry coordinate of the system.

3. SPECIAL FEATURES OF THE COMPLETE FUSION OF MASSIVE NUCLEI WITHIN THE DNSC

The DNSC reveals two important features of the complete fusion of massive nuclei: the appearance of a specific inner fusion barrier $B^*_{\rm fus}$ and the competition between the complete fusion and quasifission channels in the DNS formed at the capture stage.

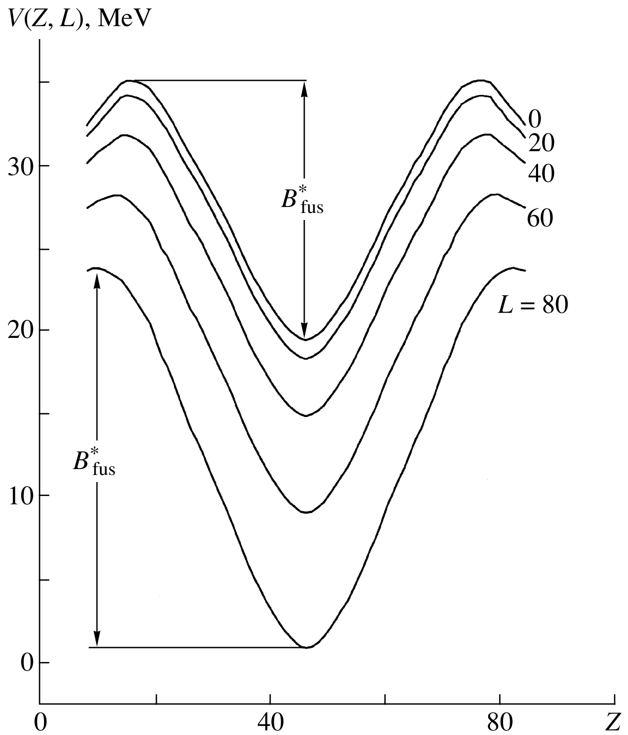

Fig. 2. Potential energy of the dinuclear system formed in ^{110}Pd + ^{110}Pd interaction. Z is the atomic number of one of the DNS nuclei.

As is known from DITR, DNS evolution is determined by the potential energy of the system, which is a function of the charge (mass) asymmetry and the collision angular momentum. Figure 2 shows the potential energy $V(Z, L)$ of the DNS formed in the reaction ^{110}Pd + ^{110}Pd. The potential energy is normalized to the compound-nucleus potential energy, which is taken as zero. The initial DNS is situated at the minimum of the potential energy. It looks like a gigantic nuclear molecule. To realize complete fusion and to form a compound nucleus, the initial DNS must overcome a potential barrier. It was called the inner fusion barrier $B^*_{\rm fus}$". The asterisk symbolizes that the energy to overcome the barrier is taken from the DNS excitation energy E^*.

The initial asymmetric DNS has two ways of evolution. It may increase its charge asymmetry and, after overcoming the barrier $B^*_{\rm fus}$, transform into a compound nucleus, or it may evolve into a symmetric shape. In a symmetric shape, the Coulomb repulsion between the DNS nuclei reaches its maximal value and the DNS decays into two nearly equal fragments. This means that quasifission occurs. In the quasifission process, the DNS must overcome the quasifission barrier $B_{\rm qf}$. The competition between complete fusion and quasifission arises naturally as the consequence of the statistical nature of DNS evolution.

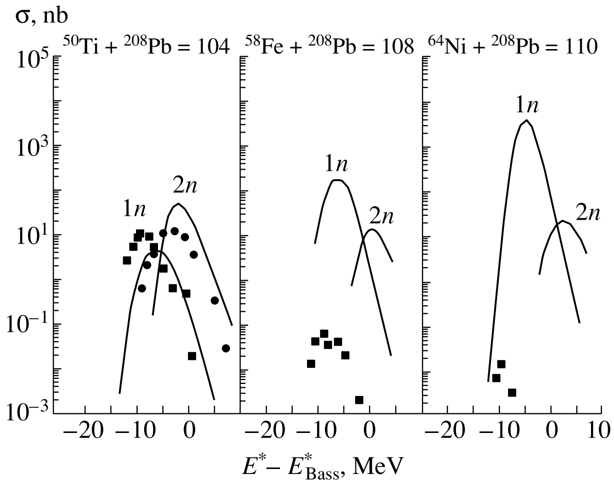

Fig. 3. Experimental and calculated evaporation-residue cross sections in the cold synthesis of the elements 104, 108, and 110: (closed squares and circles) experimental data from [9] and (curves) results of the calculations from [8].

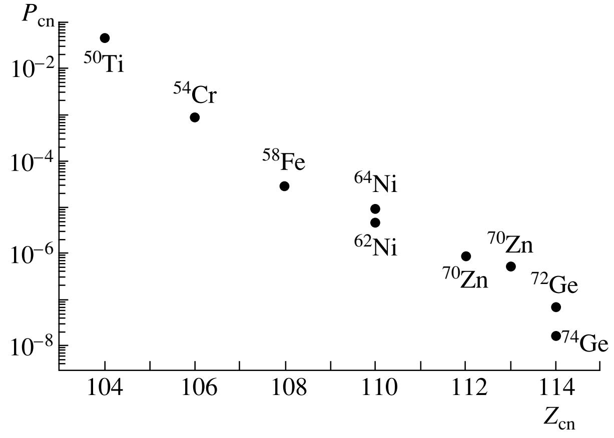

Fig. 4. Value of $P_{\rm cn}$ in the cold synthesis of the elements with Z from 104 to 114. The calculations were performed within the model of the competition between complete-fusion and quasifission channels [12].

4. ANALYSIS OF NUCLEAR REACTIONS USED TO SYNTHESIZE SUPERHEAVY ELEMENTS WITHIN THE DNSC

4.1. Role of Quasifission in the Synthesis of Superheavy Elements

Figure 3 shows the experimental and calculated cross sections for the production of the elements 104, 108, and 110 synthesized in cold-fusion reactions. The calculations were made by Pustylnik [8] within the first approach. The optical model was used to calculate the capture cross section σ_c; the statistical model was invoked to calculate the survival probability for the excited compound nucleus, $W_{\rm sur}$. The experimental data were obtained at GSI [9]. One can see more or less good agreement between the

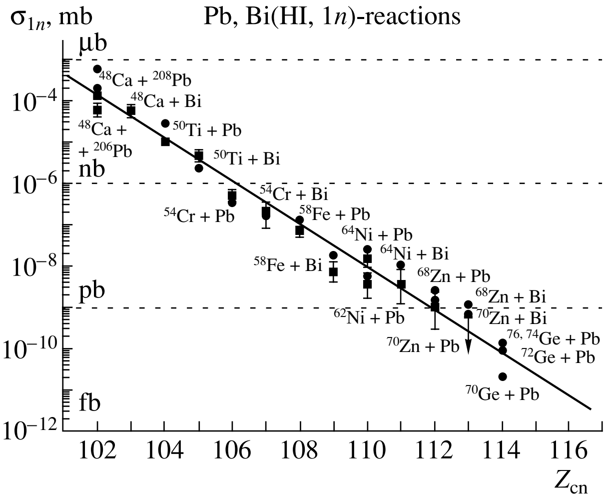

Fig. 5. Cross section for the production of elements with Z from 102 to 114 synthesized in cold-fusion reactions: (closed squares) experimental data from [9] and (circles) results of the calculations based on the DNSC [13, 14].

calculated and experimental data for the element 104. But there is dramatic disagreement in the case of the elements 108 and 110. This disagreement is due to quasifission. However, the competition with quasifission was not taken into account in the first approach. The calculations were made according to the relation

$$\sigma_{\rm ER} = \sigma_c W_{\rm sur}. \qquad (3)$$

There is no term that reflects the influence of quasifission.

According to the DNSC, the cross section for the formation of the evaporation residue of a heavy element is given by

$$\sigma_{\rm ER} = \sigma_c P_{\rm cn} W_{\rm sur}, \qquad (4)$$

where $P_{\rm cn}$ is the probability of compound-nucleus formation in the competition with quasifission. It should be emphasized that only the DNSC provides a basis for developing a realistic model of the competition between complete fusion and quasifission channels.

Our first model of the competition between complete fusion and quasifission was created for symmetric nuclear reactions [7]. We also proposed two models for asymmetric nuclear reactions. In the first model, the Monte Carlo method was used to calculate DNS evolution [10]. In the second model, the evolution of the DNS was considered as a diffusion process proceeding along two collective coordinates. Diffusion along the mass-asymmetry coordinate $\eta = (A_1 - A_2)/(A_1 + A_2)$ leads to complete fusion. Diffusion along the R coordinate leads to quasifission (R is the distance between the two centers of the DNS nuclei) [11]. A quasistationary solution to the two-dimensional Fokker–Planck equation is used to describe DNS evolution. The parameter of the model is the DNS viscosity. The second model was employed to calculate $P_{\rm cn}$ in the synthesis of transfermium and SHE [12]. Figure 4 presents the dependence of $P_{\rm cn}$ on the atomic number of the compound nucleus for cold-fusion reactions. For the element 104, $P_{\rm cn}$ is 5×10^{-2}. However, for the elements 112 and 114, $P_{\rm cn}$ drops to 10^{-6} and 10^{-7}, respectively. One can say that quasifission is the main factor responsible for decreasing the production cross section in the cold-fusion reactions with increasing atomic number of the element.

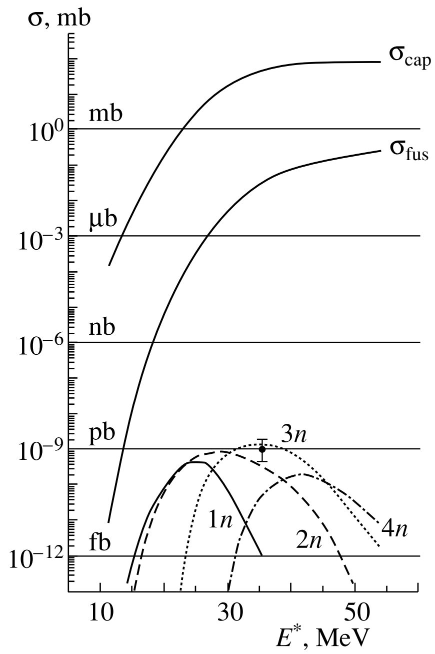

Fig. 6. Calculated cross section for the production of the element 114 synthesized in ^{48}Ca + ^{244}Pu interaction: ($\sigma_{\rm cap}$) capture cross section, ($\sigma_{\rm fus}$) cross section for compound-nucleus formation, and ($1n$–$4n$ curves) results reflecting the competition between fission and the emission of various numbers of neutrons from the excited compound nucleus [14]. The closed circle represents the experimental result from [15].

4.2. Cross Section of SHE Production in Cold- and Warm-Fusion Reactions

On the basis of the calculated values of $P_{\rm cn}$, it is possible to reproduce experimental data on the cross sections for the production of transfermium and SHE synthesized in cold- and warm-fusion reactions. Figure 5 shows the experimental production cross sections for the elements with Z from 102 to 112 obtained in cold-fusion reactions. Experimental data are represented by closed squares. The circles correspond to the production cross sections calculated by using the DNSC [13, 14]. One can see that the agreement is satisfactory. Figure 6 shows

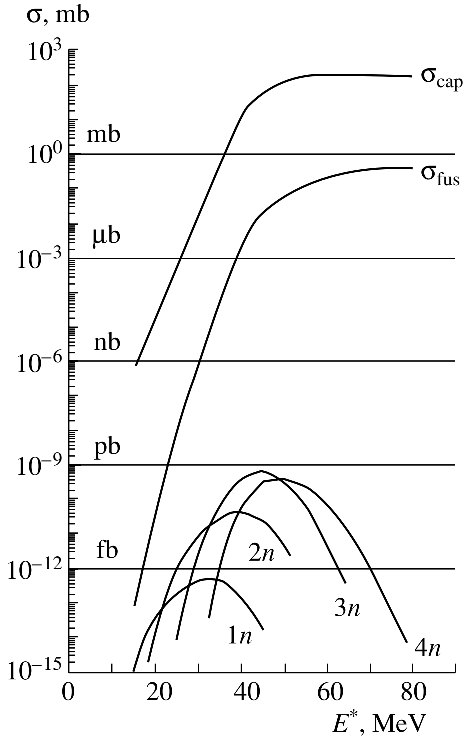

Fig. 7. Calculated cross section for the production of the element 116 synthesized in ^{48}Ca + ^{248}Cm interaction. The notation for the curves is identical to that in the Fig. 6 [16].

the calculated production cross section of the element 114 synthesized in the warm-fusion reaction $^{48}\mathrm{Ca} + {}^{244}\mathrm{Pu} \to {}^{289}114 + 3n$ [14]. The calculated production cross section at the maximum of the (HI, 3*n*) channel is 1.6 pb, whereas the experimental value is 1.0 pb [15]. These calculations were made while the experiment was still in progress.

At the Flerov Laboratory of Nuclear Reactions (JINR, Dubna), the experiment aimed at synthesizing the element 116 has recently been started. The warm-fusion reaction $^{48}\mathrm{Ca} + {}^{248}\mathrm{Cm} \to {}^{296}116$ is used for this purpose. The cross section for the synthesis of the element 116 has been calculated by using the DNSC [16]. The results of these calculations are presented in Fig. 7. One can see that the expected production cross section for the (HI, 3*n*) channel is 0.6 pb. The production cross section for the element 114 was 1.0 pb. This means that the element 116 may be synthesized in a warm-fusion reaction using ^{48}Ca ions.

5. CONCLUSION

Analyzing experimental data on the synthesis of transfermium and superheavy elements within the DNSC, one may arrive at the conclusion that, nowadays, the DNSC provides the most realistic description of the complete-fusion process and the mechanism of compound-nucleus formation.

REFERENCES

1. J. A. Kuehner and E. Almgvist, in *Proceedings of the 3rd Conference on Reaction between Complex Nuclei, Asilomar, USA, 1963* (Univ. of California Press, Berkeley, 1963), p. 11.
2. J. Galin, D. Guerreau, M. Lefort, and X. Tarrago, Phys. Rev. C **9**, 1081 (1974).
3. D. H. E. Gross and H. Kalinowski, Phys. Lett. B **48**, 302 (1974); Phys. Rep. **45**, 175 (1978).
4. H. Ngo and C. Ngo, Nucl. Phys. A **348**, 140 (1980).
5. W. J. Swiatecki, Phys. Scr. **24**, 113 (1981); S. Bjornholm and W. J. Swiatecki, Nucl. Phys. A **391**, 471 (1982); J. P. Blocki, H. Feldmeier, and W. J. Swiatecki, Nucl. Phys. A **459**, 145 (1986).
6. V. V. Volkov, Izv. Akad. Nauk SSSR, Ser. Fiz. **50**, 1879 (1986); V. V. Volkov, in *Proceedings of International School-Seminar on Heavy Ion Physics, Dubna, Russia, 1989* (Joint Inst. for Nuclear Research, Dubna, 1990), D7-90-142, p. 462.
7. N. V. Antonenko, E. A. Cherepanov, A. K. Nasirov, *et al.,* Phys. Lett. B **319**, 425 (1993); Phys. Rev. C **51**, 2635 (1995).
8. B. I. Pustylnik, in *Proceedings of the 3rd International Conference on Dynamical Aspects of Nuclear Fission, Casta-Papiernicka, Slovak Republic, 1996* (Joint Inst. for Nuclear Research, Dubna, 1997), p. 121.
9. S. Hofmann, Rep. Prog. Phys. **61**, 639 (1998).
10. E. A. Cherepanov, V. V. Volkov, N. V. Antonenko, and A. K. Nasirov, in *Proceedings of International Conference on Heavy Ion Physics and Its Application, Lanzhou, China, 1995* (World Sci., Singapore, 1996), p. 272.
11. G. G. Adamian, N. V. Antonenko, W. Scheid, and V. V. Volkov, Nucl. Phys. A **627**, 361 (1997).
12. G. G. Adamian, N. V. Antonenko, V. V. Volkov, *et al.,* JINR Rapid Commun., No. 6 [86]-97, 39 (1997).
13. E. A. Cherepanov and V. V. Volkov, in *Extended Abstracts of the 1st International Conference on the Chemistry and Physics of Transactinide Elements, Seeheim, Germany, 1999.*
14. E. A. Cherepanov, Pramana (J. Phys.) **53**, 619 (1999).
15. Yu. Ts. Oganessian, V. K. Utyonkov, Yu. V. Lobanov, *et al.,* Phys. Rev. Lett. **83**, 3154 (1999).
16. E. A. Cherepanov, in *Proceedings of International Workshop on Fusion Dynamics at the Extremes, Dubna, Russia, 2000* (in press).

Physics of Atomic Nuclei, Vol. 64, No. 6, 2001, pp. 1121–1126. From Yadernaya Fizika, Vol. 64, No. 6, 2001, pp. 1197–1202.
Original English Text Copyright © 2001 by Penionzhkevich.

Research on Neutron-Rich Nuclei in the Region of the Nuclear Shells $N = 20$ and $N = 28$*

Yu. E. Penionzhkevich**

Joint Institute for Nuclear Research, Dubna, Moscow oblast, 141980 Russia

Received October 25, 2000

Abstract—The results of the joint experiments carried out by the Dubna–GANIL (France) and the Dubna–RIKEN (Japan) collaborations aimed at synthesizing new isotopes close to the neutron shells $N = 20$ and $N = 28$ and at studying their properties are presented. Gamma-spectroscopic methods were used to study low-lying states in ^{30,32}Mg, $^{26-28}$Ne, ^{22}O, and ^{18}C. The ratios $E(4^+)/E(2^+)$ were determined. A direct method was used to measure the masses of 20 nuclides located between the shells $N = 20$ and $N = 28$. The decay properties were determined for ^{30}Ne and ^{26,27,29}F. Information obtained in this way suggests the existence of a deformation close to the neutron shell $N = 20$. The results of experiments devoted to searches for the doubly magic nucleus ^{28}O are also presented. Only the upper limit on the cross section for its production was deduced, which can be taken as evidence of its instability. *© 2001 MAIK "Nauka/Interperiodica".*

1. INTRODUCTION

Interest in neutron-rich nuclei featuring more than 20 neutrons is associated with the experimental discovery of their unusual properties. The $N = 20$ shell was shown to have no influence on the properties of nuclei in that region, which are basically accounted for by deformation effects. This may be evidenced by the anomalies observed in the neutron binding energy of Na and Mg, by the great quadrupole momentum of ^{32}Mg, etc. Deformation effects can markedly manifest themselves in half-lives, neutron-emission probability, and nuclear masses and sizes and correspondingly be responsible for nuclear stability.

More recently, a determination of the lifetime and of the deformation of ^{44}S has indicated the existence of a similar effect at $N = 28$. This is the first shell closure that arises from spin–orbit splitting and is responsible for the gap in the $1f_{7/2}$–$2p_{3/2}$ shell.

It is particularly interesting to study the shell closure $N = 20$ and 28, since the vanishing of the latter one could be the first piece of evidence for the weakening of the spin–orbit force in neutron-rich nuclei. A determination of the neutron and the proton drip line is also very important, since they limit the region of particle stability.

This article reports on the results of the latest experiments aimed at synthesizing new isotopes in the region of the $N = 20$ and $N = 28$ shells and at measuring their characteristics.

The new isotopes ^{31}F, ^{31}Ne, ^{36}Mg, and ^{40,41}Al were produced in the experiments carried out within the framework of the JINR–RIKEN (Japan) collaboration. Situated beyond the predicted drip line, these nuclei show increased stability. Their half-lives and neutron decay probabilities were measured and compared with the theoretical predictions.

In the collaborative JINR–GANIL (France) experiments, an attempt was made to produce ^{26}O and ^{28}O nuclei; that attempt resulted in obtaining only an upper limit on the cross section for their production. The results of these experiments suggest that these nuclei are unstable. Direct measurement of the nuclear masses in the region of $N = 20$ and $N = 28$ was carried out to high accuracy (10^{-4}–10^{-6}). For the first time, data on the masses of 12 nuclei close to the drip lines were obtained and compared with the results of the calculations based on semiempirical mass formulas. The data obtained indicate that strong deformations must be introduced to explain the properties of nuclei in that region.

2. DECAY PROPERTIES OF NEUTRON-RICH NUCLEI NEAR THE $N = 20$ CLOSED SHELL

The decay properties in the region of $N = 20$ nuclei can be explained by the transition from spherical to deformed shapes in the so-called "island of inversion."

The lack of experimental information on very neutron-rich isotopes in the C–Al region is due

---

*This article was submitted by the author in English.

**e-mail: `pyuer@nrsun.jinr.dubna.su`

Experimental values of the β-decay half-lives of neutron-rich nuclei and experimental neutron-emission probabilities for them close to $N = 20$

Isotope	Experimental results			
	This work		Table of Isotopes, 1996	
	$T_{1/2}$, ms	P_n, %	$T_{1/2}$, ms	P_n, %
^{22}N	31(5)	37(14)	24(7)	35(5)
^{24}O	67(10)	12(8)	61(26)	58(12)
^{25}F	70(10)	14(5)	59(4)	15(10)
^{27}F	9.6(0.8)	11(4)		
^{29}F	2.4(0.8)	100(80)		
^{27}Ne	22(6)	0(3)	32(2)	2(0.5)
^{28}Ne	20(3)	11(3)	17(4)	22(3)
^{29}Ne	15(3)	27(9)	200(10)	
^{30}Ne	7(2)	9(17)		
^{30}Na	50(4)			
^{31}Na	18(2)		48(2)	30(4)

predominantly to very small production cross sections. Therefore a very exotic primary beam of ^{36}S (78 MeV/u) ions, which makes it possible to study β-delayed neutron emission from neutron-rich nuclei with the magic neutron number of $N = 20$, such as ^{29}F, ^{30}Ne, and ^{31}Na, was used in the experiment. The experiment was carried out at GANIL [1].

For the first time the β-decay half-lives and the neutron-emission probability were measured for ^{30}Ne and ^{26,27,29}F. Additionally, the cases of ^{22}N, ^{24}O, $^{24-29}$Ne, ^{25}F, and ^{30,32}Na were reexamined (see table).

The measured half-lives of ^{28}Ne and ^{30,31}Na agree, within the errors, with the results of previous experiments. The only important discrepancy is observed for ^{29}Ne. The experimental half-lives obtained here are in good agreement (within a factor of two) with the *sd*-shell-model calculations of Wildenthal *et al.* [2], including the values for ^{27,29}F and ^{29,30}Ne. The last suggest that the deformation phenomenon, predicted and observed in the Mg–Na region, disappears below $Z = 11$. Thus, the standard shell-model space seems to be sufficient to predict the half-lives of fluorine and neon isotopes in the vicinity of $N = 20$.

3. EVIDENCE FOR THE PARTICLE STABILITY OF ^{31}F AND THE PARTICLE INSTABILITY OF ^{25}N AND ^{28}O

The recent discovery of the particle stability of ^{31}Ne [3], in contrast to the majority mass predictions, has motivated us to reexamine the location of the fluorine drip line. The ^{31}Ne nucleus is located in the deformation region centered at $Z \sim 11$ and $N \sim 20$, the so-called island-of-inversion region. A particular feature of this region is the tendency toward a prolate deformation despite the effect of spherical stability due to the magicity of the neutron number 20 [4]. Toward lower Z along $N = 20$, much attention has recently been given to the question of the possible stability of the magic nucleus ^{31}F and the doubly nucleus ^{28}O, even though the particle instability of ^{30}F and ^{25,26}O beyond ^{29}F and ^{24}O was clearly shown by two experiments [5, 6]. The expectation for ^{28}O to be stable stems from an enhanced stability anticipated from the double magicity or the deformation. The stability of ^{28}O was discussed in several theoretical studies, which however yielded conflicting results. In the framework of the Dubna–RIKEN collaboration, new isotopes around $N = 20$ (^{28}O, ^{31}F, ^{25}N) were sought by using the RIKEN accelerator facility and an ^{40}Ar beam of energy 94.1 MeV per projectile nucleon [7]. In this experiment, the new isotope ^{31}F (eight events) was observed for the first time (Fig. 1). The absence of events corresponding to the $^{25-28}$O isotopes, as well as ^{24,25}N and ^{30}F, was clearly confirmed.

The nonobservation of an isotope does not necessarily prove its unbound character. To achieve more definitive evidence, we have plotted the observed yields versus Z for the $N = 2Z + 4$ nuclei, as shown in Fig. 2. The calculated yields are in good agreement with the observed yields over the whole range, which connects smoothly the results on ^{22}C and ^{31}F. The yields of ^{25}N and ^{28}O, which lie between ^{22}C and ^{31}F, can therefore be estimated with fair reliability by the interpolation method.

The fact that the experimental results showing no events distinctly deviate from the estimated yields provides strong evidence for the particle instability of ^{24,25}N, ^{27,28}O, and ^{30}F. A sudden change in stability from oxygen to fluorine indicates an extra push of stability for the very neutron-rich fluorine isotopes.

Experiments to study the properties of nuclei in the vicinity of the $N = 20$ and $N = 28$ shells and the deformation of nuclei in this region must be continued. This can be achieved by means of γ spectroscopy and the direct method of level-mixing resonances (LMR), as well as by mass and structure measurements of unbound nuclei by using the missing-mass method. For instance, one could use the reaction $^{26}\mathrm{F}(d,{}^{3}\mathrm{He})^{25}\mathrm{O}$ in the case of ^{25}O and the reaction $^{24}\mathrm{O}(t,p)^{26}\mathrm{O}$ in the case of ^{26}O.

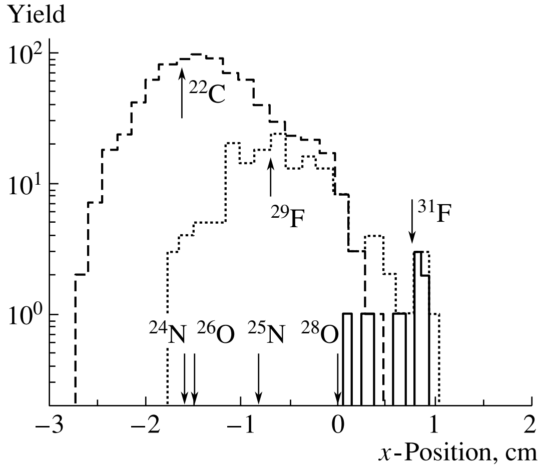

Fig. 1. Experimental distributions of the horizontal positions for isotopes transmitted to the first focal plane (F2) of the RIPS spectrometer. The centroids experimentally detected for the (dashed histogram) ^{22}C and (dotted histogram) ^{29}F isotopes are in agreement with the values (upward arrows) obtained by an energy-loss calculation. The position distribution of the ^{31}F isotope (solid-line histogram) is also in accord with the calculation. The expected events for ^{24,25}N and ^{26,28}O could be centered at the middle of F2, and their expected center positions are shown by the downward arrows.

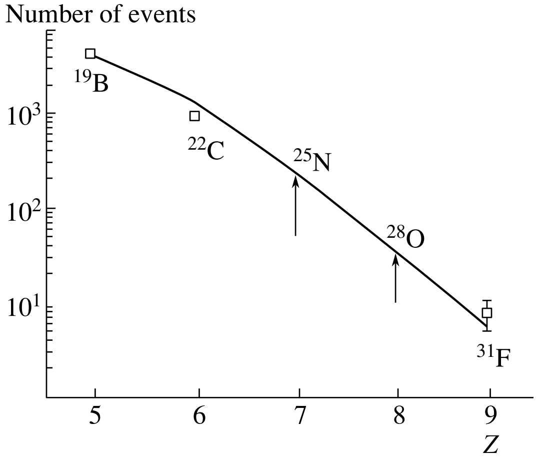

Fig. 2. Isotope production for nuclei with the neutron numbers of $N = 2Z + 4$. The solid curve represents the expected yields according to the INTENSITY code using the modified EPAX parametrization. The expected yields for ^{28}O and ^{25}N are indicated by arrows.

4. IN-BEAM γ SPECTROSCOPY OF VERY NEUTRON-RICH NUCLEI

One of the most challenging goals of nuclear-structure physics is to determine how the structure of nuclei changes far away from the stability line. Recent results on the structure of light neutron-rich nuclei suggest that some major shell gaps are weakened when large isospin values are encountered. The typical cases of ^{32}Mg ($N = 20$) and ^{44}S ($N = 28$), which show a high degree of collectivity [8, 9], provide some evidence for such shell-gap weakening at a large neutron excess.

However, information about the excitation energies of the first 2^+ states and about the $B(E2)$ values for the $2^+ \longrightarrow 0^+$ transitions is not sufficient to understand fully the structure of these nuclei. For instance, measurement of the $E(4^+)/E(2^+)$ ratio is expected to shed some light on the origin of the large quadrupole collectivity observed.

A novel experimental method has been used to obtain more spectroscopic information on ^{32}Mg and neighboring nuclei. This method is based on the production of very neutron-rich nuclei in relatively higher excited states, through the projectile-fragmentation process, and on the detection of their in-beam gamma decay. Such an experiment has recently been performed at GANIL [10] in order to measure the ratio $E(4^+)/E(2^+)$ in ^{30,32}Mg, $^{26-28}$Ne, and ^{22}O. A ^{36}S beam of energy 77 MeV per projectile nucleon was used with a 2.77-mg/cm^2 Be target.

It is worth pointing out that the majority of the product nuclei are terra incognita for nuclear spectroscopy; thus, the γ spectroscopy of these nuclei (such as ^{22,23}O, ^{27,28}Ne, ^{32,33}Mg) is completely unknown. For all product exotic nuclei, γ spectroscopy is obtained by performing coincidences between the analyzed fragments at the SPEG focal plane and γ rays emitted in flight during their decay to the ground state. For this purpose, a highly efficient (25% at 1.33 MeV) gamma array of 74 BaF2 crystals was used around the target covering symmetrically the upper and lower hemispheres (roughly 80% of the solid angle around the target is covered). This array is supposed to provide fragment–γ–γ coincidences.

The γ spectra obtained by gating on the ^{18}C fragment revealed for the first time γ-spectroscopy information about this neutron-rich nucleus. A γ line is clearly visible at 1.6 MeV in the BaF2 spectrum, probably the $2^+ \longrightarrow 0^+$ transition. Furthermore, the same spectrum shows a shoulder at a gamma energy around 2.0 MeV, indicating the decay of an unknown higher excited state.

The γ line observed for the first time for ^{22}O at 3.1 MeV corresponds to the $2^+ \longrightarrow 0^+$ transition; this extends the systematics of the 2^+ transition energies of oxygen isotopes up to $N = 14$. It was shown that oxygen isotopes exhibit the lowest 2^+ energy at half-occupancy of the $d_{5/2}$ state ($N = 12$), just as the Ne and Mg isotopes do. Whether it will continue to follow the same trend up to $N = 16$ (or not) is a

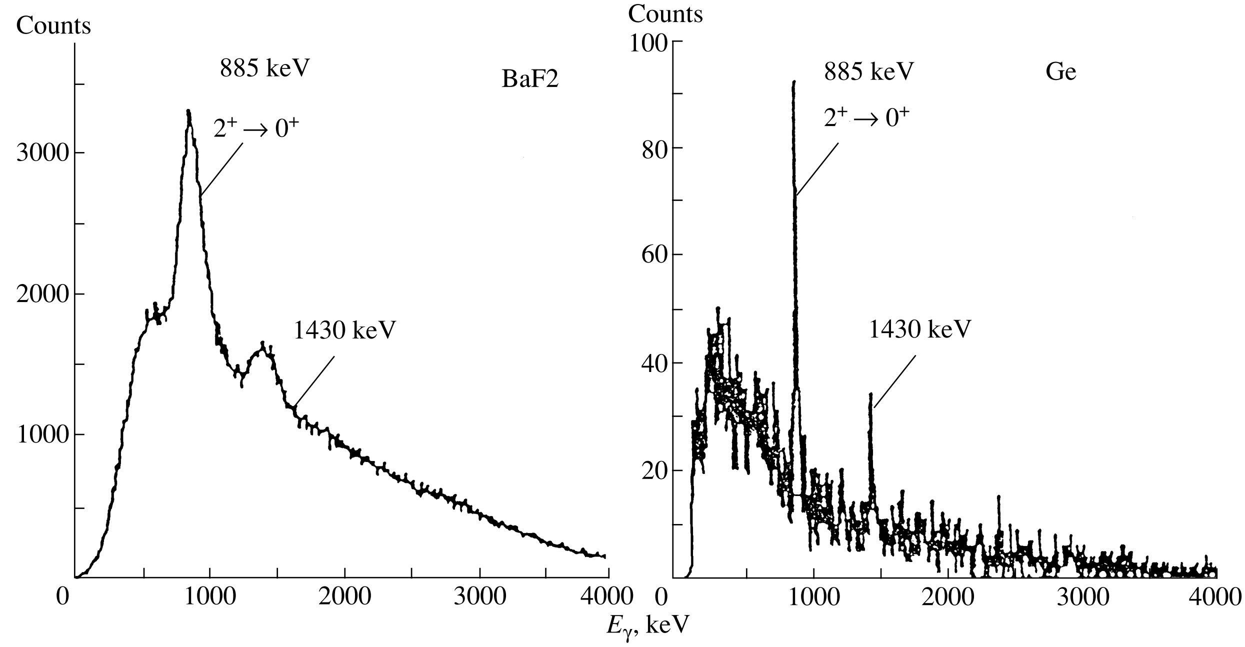

Fig. 3. Gamma-energy spectra of ^{32}Mg in the (left panel) BaF2 and in the (right panel) Ge.

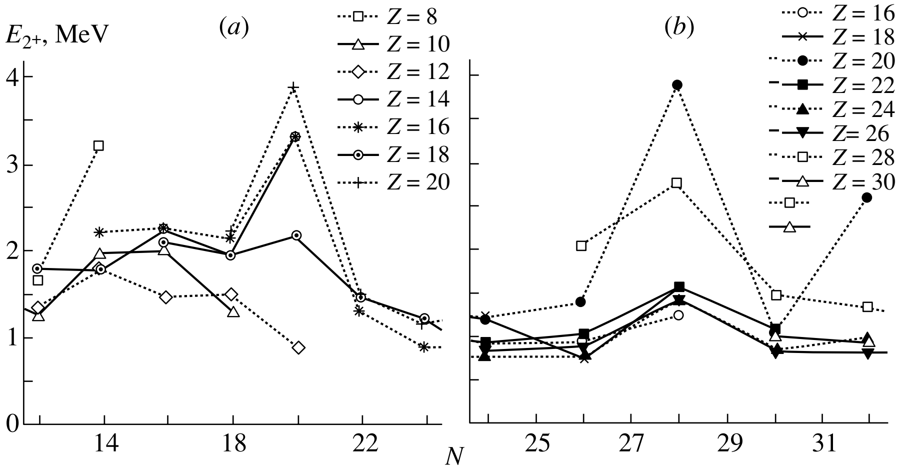

Fig. 4. Gamma-ray energy of the first 2^+ level for even–even nuclei.

key point to understand why the last oxygen isotope seems to be ^{24}O.

A γ line at 1.3 MeV was observed for ^{28}Ne. This γ line is very likely to represent the $2^+ \longrightarrow 0^+$ transition in ^{28}Ne, which shows, for the first time, that the 2^+ energies in the Ne isotopes decrease dramatically as we approach $N = 20$. The 2^+ energy drops from around 2 MeV in ^{24}Ne and ^{26}Ne to 1.3 MeV in ^{28}Ne (it is worth pointing out that the 2^+ excitation energy of ^{26}Ne was measured in a β-decay experiment at GANIL [1]). This behavior is presumably indicative of a change in the shell structure of neutron-rich Ne isotopes similar to that observed long ago in the Mg isotopes [8].

Figure 3 shows the BaF2 spectra and the Ge spectra of ^{32}Mg. As for many other fragments, the gamma spectra (Ge and BaF2) of ^{32}Mg exhibit more than one line. For all these fragments, γ angular distributions and γ–γ coincidences between BaF2 detectors must be analyzed in order to deduce a level scheme. This type of analysis is quite in progress for ^{32}Mg and reveals that two lines, that at 885 keV (the well-known $2^+ \longrightarrow 0^+$ transition in ^{32}Mg [1]) and the line at 1.4 MeV newly observed, are in coincidence. The nature (multipolarity) of the 1.4-MeV γ ray has not yet been extracted from the data. However, it is likely to be either a 4^+ to a 2^+ transition or a transition from a second to the first state. In both cases, this

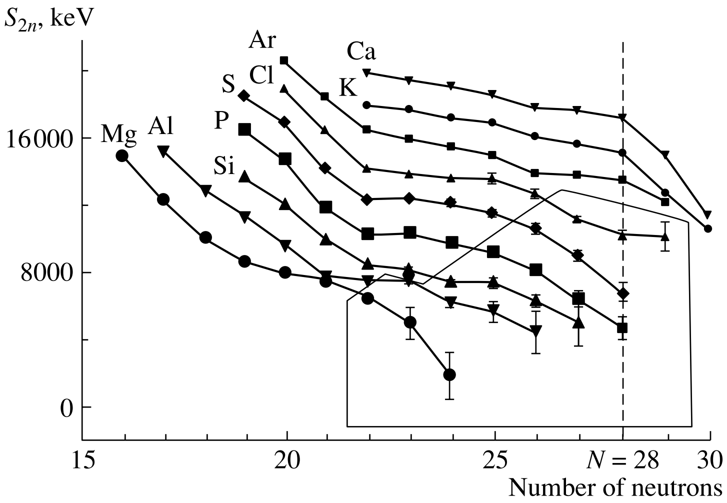

Fig. 5. Experimental S_{2n} values between the $N = 20$ and $N = 28$ shell closures. The S_{2n} values in the frame are the new points added by the present experiment.

will shed more light on the physics underlying the so-called shell-effect quenching on the neutron-rich side of the valley of stability.

Figure 4 displays the γ-ray energy of the first 2^+ level for even–even nuclei for the N range 12–32. In Fig. 4b, we can clearly see a peak corresponding to doubly magic nuclei $Z, N = 20$, 28 and 28, 28; a similar situation appears in Fig. 4a at $N = 20$ for $Z = 14$, 16, and 20. Only a small enhancement is visible at $N = 16$ for $Z = 10$, 14, 16, and 18, while an apparent decrease reveals itself for ^{28}Mg.

5. MASS MEASUREMENT FOR HEAVY ISOTOPES FROM Ne UP TO Ar

Only a few masses of neutron-rich nuclei are known between the $N = 20$ and $N = 28$ shell closures [11]. However, the measurements of these masses are directly related to the binding energies and therefore constitute the most fundamental information one can get for these nuclei. In particular, the evolution of the isotope binding energy is illustrated by one of its derivatives, the separation energy of the two last neutrons S_{2n},

$$S_{2n}(A, Z) = [M(A-2, Z) - M(A, Z) + 2M_n]c^2.$$

At GANIL, we have performed a mass-measurement experiment by using a direct time-of-flight technique to investigate the $N = 20$ and $N = 28$ shell closures for nuclei from carbon ($Z = 6$) to calcium ($Z = 20$) [12]. The production of these neutron-rich nuclei was implemented through the fragmentation of a ^{48}Ca beam of energy 60 MeV per projectile nucleon on a Ta target located in the SISSI device [7]. A precision of 10^{-6}–10^{-5}, depending on statistics, was obtained, which corresponded to a mass uncertainty from 100 keV (thousands of events) to 1 MeV (a few tens of events). During this experiment, 20 masses were measured in the region of interest with at least a precision better than the one in the table of masses [13].

The new S_{2n} values deduced from this experiment are shown in Fig. 5. Here, we just comment on S_{2n} for P and S isotopes. If one considers the behavior of S_{2n} for Ca isotopes as a reference of the standard shell structure ($f_{7/2}$ closed shell), the P and S isotopes clearly do not follow this trend. From $N = 20$ to $N = 26$, the S_{2n} values include an extra energy given by deformation, which allows the nuclei to minimize their binding energies with one more degree of freedom. At $N = 26$, a strong decrease is observed. This may be the result of the possible vanishing of the $N = 28$ shell closure at least for these two elements.

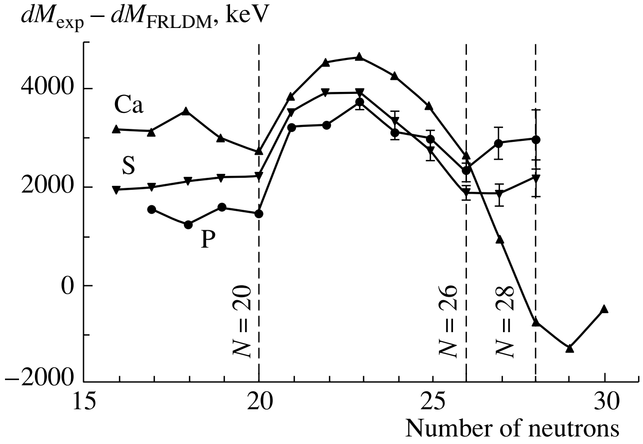

Fig. 6. Shell corrections to the mass excess of the macroscopic part of the FRLDM for P, S, and Ca isotopes.

The values of S_{2n} appear to be at least 2 MeV lower than that expected on the basis of mass extrapolations for $N = 28$ [13].

In the case of the standard shell structure, the microscopic energy should be minimized at the shell closures. An example is given in Fig. 6 by the Ca isotopic chain, where the $N = 20$ and $N = 28$ shell closures are clearly identified. One can see a sudden change at $N = 26$ already pointed out in the preceding figure for P and S isotopes. Up to $N = 26$, no anomaly is observed in relation to the Ca. The magic number of $N = 28$ does not coincide anymore with the minimum of the microscopic energy, which can be related to the vanishing of the shell closure. This trend is well reproduced by the shell calculation [14]. The RMF calculation gives very good agreement with the data if one eliminates the odd–even effect associated with the adjustment of the pairing force.

A more qualitative interpretation is obtained by the observation of a new isomeric state in ^{43}S during the same experiment [12]. The existence of such an isomer can be explained in the shell model by the inversion of a spherical with a deformed configuration. In this model, the standard spherical configuration is no longer the ground state, its spin being $3/2^-$ instead of $7/2^-$. The coexistence and inversion of spherical and deformed configurations would thus be the origin of the observed behavior.

6. CONCLUSION

The synthesis and investigation of these extremely neutron-rich isotopes are crucial for a better understanding of the nature of nuclear interaction. The study of the shell closures $N = 20$ and 28 is particularly interesting since the vanishing of the latter one could be the first piece of evidence for the weakening of the spin–orbit force in neutron-rich nuclei.

In particular, the $N = 28$ ^{43}P, ^{44}S, and ^{45}Cl nuclei appeared to be less bound than what was predicted, which constitutes a new piece of evidence for the weakening of the $N = 28$ shell closure. On the other hand, there appears a discontinuity in the slope at $N = 26$. A comparison with the shell model and relativistic mean field calculations demonstrate that the observed effects arise from deformed prolate ground-state configurations associated with shape coexistence. Consequently, a pseudoshell closure can be considered to appear at $N = 26$.

A similar situation occurs for $N = 16$, where the shell closure at $N = 20$, which persists from $Z = 20$ down to $Z = 14$, may change into the pseudoshell closure at $N = 16$ for $6 \leq Z \leq 10$ and takes place between $2_{s1/2}$ and $1d_{3/2}$ orbitals. This fact is strongly supported by the instability of $N > 16$ carbon, nitrogen, and oxygen isotopes.

ACKNOWLEDGMENTS

I am grateful to the members of the Dubna–GANIL and Dubna–RIKEN collaborations for enlightening discussions on the results obtained in the joint experiments. Thanks are also due to Yu.Ts. Oganessian, S.M. Lukyanov, R. Kalpakchieva, H. Savajols, O.B. Tarasov, Z. Dlouhy, M. Lewitowicz, and H. Sakurai for their remarks and assistance in preparing the present article.

REFERENCES

1. A. T. Reed, O. B. Tarasov, *et al.,* Phys. Rev. C **60**, 024311 (1999).
2. B. H. Wildenthal *et al.,* Phys. Rev. C **28**, 1343 (1983).
3. H. Sakurai *et al.,* Phys. Rev. C **54**, R2802 (1996).
4. A. Poves and I. Retamosa, Nucl. Phys. A **571**, 221 (1994).
5. D. Guillemaud-Mueller, Yu. E. Penionzhkevich, *et al.,* Phys. Rev. C **41**, 937 (1990).
6. M. Fauerbach *et al.,* Phys. Rev. C **53**, 647 (1996).
7. H. Sakurai, S. M. Lukyanov, *et al.,* Phys. Lett. B **448**, 180 (1999).
8. T. Motobayashi *et al.,* Phys. Lett. B **346**, 9 (1995).
9. T. Glasmacker *et al.,* Phys. Lett. B **395**, 163 (1997).
10. M. J. Lopez-Jimenez *et al.,* Preprint GANIL P99-08 (1999).
11. N. Orr *et al.,* Phys. Lett. B **258**, 29 (1991).
12. F. Sarasin *et al.,* Preprint GANIL P99-36 (1999).
13. G. Audi *et al.,* Nucl. Phys. A **624**, 1 (1997).
14. I. Retamosa *et al.,* Phys. Rev. C **55**, 1266 (1997).

Physics of Atomic Nuclei, Vol. 64, No. 6, 2001, pp. 1127–1133. From Yadernaya Fizika, Vol. 64, No. 6, 2001, pp. 1203–1209.
Original English Text Copyright © 2001 by Jolos.

Supersymmetry in Some Nuclear-Structure Models*

R. V. Jolos**

Joint Institute for Nuclear Research, Dubna, Moscow oblast, 141980 Russia

Received October 25, 2000

Abstract—Application of the supersymmetry concept in nuclear-structure physics is considered. A Hamiltonian that is based on the $U(6/12)$ graded algebra and which does not possess, in general, a dynamic symmetry is constructed. However, part of the eigenstates of this Hamiltonian belonging to even–even and odd neighboring nuclei form supersymmetric multiplets. It is also shown that the particle–rotor model description of rotational bands in an odd nucleus that are built on the $K = 1/2$ pseudoorbital singlet Nilsson state belonging to the shell with an even principal pseudooscillator quantum number can be reformulated as a realization of supersymmetry. © *2001 MAIK "Nauka/Interperiodica"*.

The idea of supersymmetry was invented in particle physics. However, actual examples of supersymmetry were found in the spectra of nuclei. Investigation of supersymmetry in nuclear-structure physics was initiated by Iachello [1] and then continued in numerous publications [2–11].

The simplest textbook example of supersymmetry [12] is given by the Hamiltonian

$$H = \epsilon(a^+a + s^+s)\,, \tag{1}$$

which involves a monopole s boson. Its eigenstates having the same excitation energies ϵ are

$$(s^+)^n|0\rangle, \quad a^+(s^+)^{n-1}|0\rangle. \tag{2}$$

The second eigenstate in (2) featuring one fermion can be produced by applying the superoperator $P = a^+s$ to the first pure boson eigenstate. The superoperator P is the eigenmode operator,

$$[H, P] = 0.$$

A more realistic example is given by the Hamiltonian describing a system of monopole s bosons, quadrupole d bosons, and a fermion occupying $j = 1/2$ single-particle state,

$$H = \epsilon(\hat{N}_F + \hat{N}_s) + H_d,$$

where

$$\hat{N}_F = \sum_m a^+_{1/2m}a_{1/2m}, \qquad \hat{N}_s = s^+s,$$

$$H_d = \epsilon_d \sum_\mu d^+_\mu d_\mu + \sum_{L=0,\,2,\,4} C_L((d^+d^+)_L(\tilde{d}\tilde{d})_L)_{00}.$$

The superpartner eigenstates having the same eigenenergies are

$$(s^+)^n|0\rangle \longleftrightarrow a^+_{1/2m}(s^+)^{n-1}|0\rangle,$$
$$d^+(s^+)^{n-1}|0\rangle \longleftrightarrow (a^+_{1/2}d^+)_{JM}(s^+)^{n-2}|0\rangle,$$
$$(d^+d^+)_I(s^+)^{n-2}|0\rangle$$
$$\longleftrightarrow (a^+_{1/2}(d^+d^+)_I)_{JM}(s^+)^{n-3}|0\rangle.$$

In nuclear-structure physics, supersymmetry is considered mainly as dynamical supersymmetry. This means that corresponding Hamiltonians are constructed as linear combinations of the Casimir operators of the groups belonging to the reduction chains of the basic graded group $U(6/n_F = \sum_i(2j_i + 1))$ [13]. These reduction chains can include combined boson–fermion groups. The states of the boson subsystem are characterized by the quantum numbers of one of the reduction chains of the $U^B(6)$ group. The states of the fermion subsystem can be classified in terms of the quantum numbers of the reduction chain of the $U(n_F)$ group. If some of the groups in two reduction chains coincide or are isomorphic, they can be combined in the unified boson–fermion group

$$U(6/n_F) \supset U^B(6) \otimes U^F(n_F)$$
$$\supset G'^B \otimes G'^F \supset G'^{BF} \supset \ldots\,.$$

In this case, the Hamiltonian describing even–even, odd, and odd–odd nuclei takes the form

$$H = E_0 + \alpha \cdot C(U^B) + \beta \cdot C(U^F)$$
$$+\alpha' C(G'^B) + \beta' \cdot C(G'^F) + \gamma \cdot C(G'^{BF}) + \ldots\,.$$

The parameters of this Hamiltonian, determined by using the subset of known energy levels, are then used to describe all nuclei belonging to the same supersymmetric multiplet. In general, γ-transition

---

[*] This article was submitted by the author in English.

[**] e-mail: `jolos@thsun1.jinr.ru`

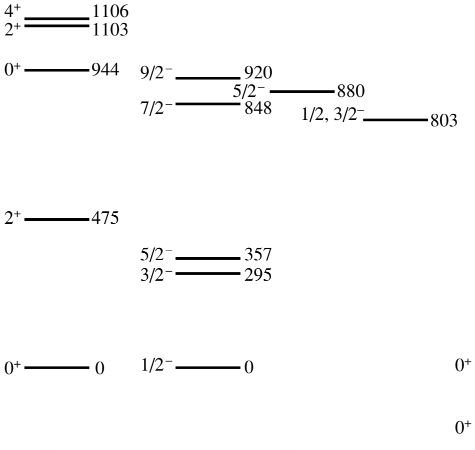

Fig. 1. An example of $U(6/2)$ supersymmetry in nuclei: part of the experimental spectra of the ^{102}Ru–^{103}Rh–^{104}Pd isotopes forming a supermultiplet [13]. The energies are given in keV. The two-quasiparticle states in ^{104}Pd are not identified. A possible candidate for the lowest state in ^{104}Pd belonging to the supermultiplet is the 0^+ (1793 keV) state seen in the β^- decay of ^{104}Rh with $\log ft = 5.5$.

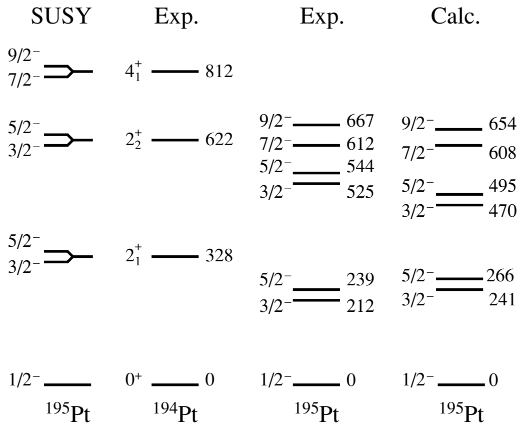

Fig. 2. Experimental low-lying states of ^{194}Pt and states of ^{195}Pt that form a supermultiplet with the states of ^{194}Pt. The predictions of the exact supersymmetry model for ^{195}Pt are shown on the left extreme. The calculated spectrum of ^{195}Pt is obtained under the assumption that the eigenvalues of the Hamiltonian in (4) for the even–even ^{194}Pt nucleus coincide with the corresponding experimental energies. The results of the calculations including the compression of the spectrum in odd ^{195}Pt and the pseudospin–orbit splitting of the doublets are shown on the right extreme. The energies are given in keV.

energies in even–even and odd nuclei do not necessarily coincide. However, there are several experimental examples where some γ-transition energies in even–even and odd nuclei are quite close. These examples are not the cases of weak coupling of the fermion to the even–even core. Perfect supersymmetry assumes the coincidence of the boson and fermion masses. Thus, the cases of approximate coincidence of γ-transition energies are examples of approximate supersymmetry. In this report, we consider only these cases. The report is based on the studies [14–16], written in collaboration with P. von Brentano.

A consideration based on the dynamical-symmetry approach has two limitations. First, only those even–even nuclei that belong to one of the dynamical-symmetry limits $O(6)$, $U(5)$, or $SU(3)$ can be considered as members of the boson–fermion multiplets. Second, a set of single-particle states that can be occupied by an odd particle is restricted by symmetry requirements.

In order to see whether these restrictions are in accord with the data (or they are created by the limitations of the theoretical technique used), we now consider existing experimental data on the eigenstates of even–even and odd nuclei that are characterized by approximately the same γ-transition energies.

A first example is provided by the spectra of ^{102}Ru and ^{103}Rh (Fig. 1). The spectrum of ^{103}Rh seems to result from the coupling of the odd proton in the $p_{1/2}$ state to the even–even ^{102}Ru core. Other possible negative-parity single-particle states are $p_{3/2}$ and $f_{5/2}$, which are separated, however, from $p_{1/2}$ by 1 MeV. It is seen that the negative-parity excited states of ^{103}Rh form doublets: $3/2^-$ and $5/2^-$ at excitation energies of 295 and 357 keV and $7/2^-$ and $9/2^-$ at energies of 848 and 920 keV. The center of gravity of the first doublet is close to the energy of the 2_1^+ state in ^{102}Ru (475 keV). The center of gravity of the second doublet is close to the excitation energy of the 4_1^+ state in ^{102}Ru (1106 keV). The coefficient of compression of the spectrum of ^{103}Rh relative to the spectrum of ^{102}Ru is 0.7–0.8. It approaches unity with increasing excitation energy. The $1/2^-$ state at the excitation energy of 803 keV corresponds to $p_{1/2} \otimes 0_2^+$ (944 keV).

The next example of an odd nucleus whose spectrum appears to be a result of the coupling of an odd particle in the $1/2^-$ state to low-lying states of an even–even core is ^{195}Pt. Figure 2 shows only those states of ^{195}Pt that form doublets based on the collective states of ^{194}Pt. The splitting of the doublets in ^{195}Pt is smaller than in ^{103}Rh. However, the compression of the spectrum relative to one of the neighboring even–even nuclei is identical to that in ^{103}Rh. In nuclei of the Pt region, negative-parity single-particle states $p_{1/2}, p_{3/2}$, and $f_{5/2}$ are quite

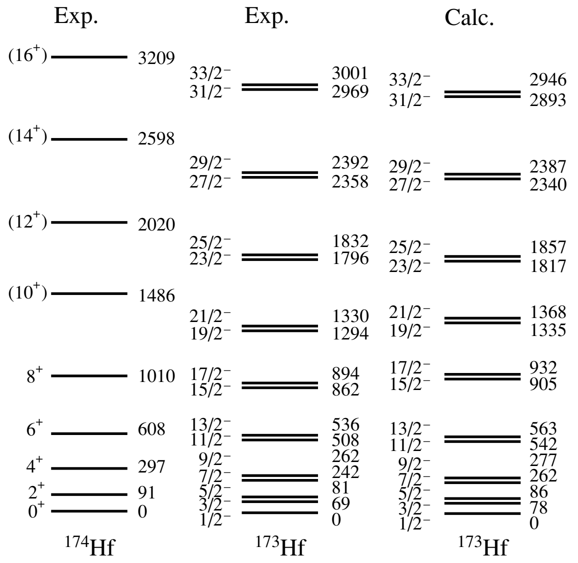

Fig. 3. Observed levels of the ground-state band of ^{174}Hf and experimental and calculated states of ^{173}Hf that form supermultiplets. The energies are given in keV. Experimental data were taken from [17–19].

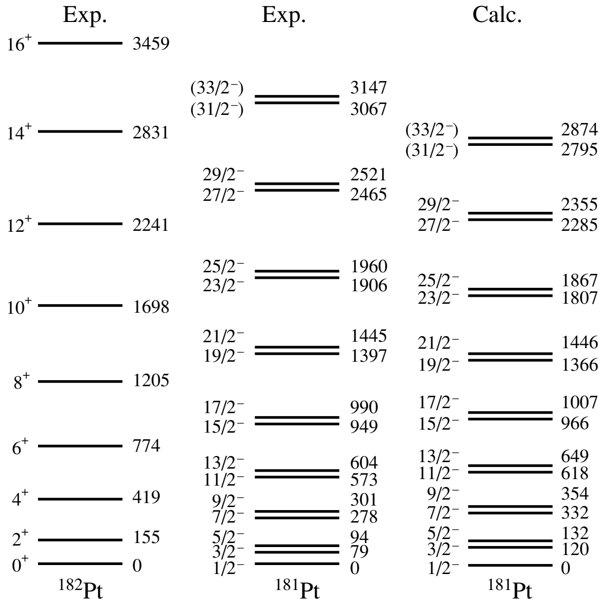

Fig. 4. As in Fig. 3, but for ^{181,182}Pt. Experimental data were taken from [17, 20, 21].

close in energy. This is also seen from the data on one-nucleon transfer from [11]. In addition to the doublets based on collective even–even core states, ^{195}Pt also features other negative-parity states at low excitation energies. This means that the scheme assuming the weak coupling of an odd particle to a collective core is not realized in this case. In these Pt isotopes, supersymmetry has deeper grounds.

Figures 3 and 4 display rotational bands belonging to odd deformed or nearly deformed nuclei. In both the cases, the bandheads are $1/2^-$ states. It is seen that these bands consist of weakly split doublets whose centers of gravity are close to the energies of the corresponding rotational states of the neighboring even–even nuclei. The coefficient of compression of the spectrum of ^{173}Hf relative to the spectrum of ^{174}Hf is 0.9.

Figures 5 and 6 show the levels of superdeformed rotational bands. It is seen that the energies of γ transitions in even–even and neighboring odd nuclei agree to within a few keV. Unfortunately, the angular momenta of the states are unknown or known only tentatively for superdeformed bands. The parities of the states are unknown too. It is not clear whether signature partners exist or not. Therefore, we cannot talk about doublets. However, these examples are included in the report because the first two papers devoted to interpreting the phenomenon of identical superdeformed bands presented theoretical arguments that, in both examples, we have $K=1/2$ negative-parity bands in odd nuclei [23, 24].

From these examples, we see that the members of supersymmetric multiplets can be even–even nuclei not necessarily belonging to the dynamical-symmetry limits. It is also seen that the restriction of the space of single-particle states to an artificially small subset can be at odds with a particle–core coupling strength, as it is in the case of deformed nuclei or nuclei close to deformed ones. Below, we will consider a theoretical possibility of removing these restrictions.

As can be seen from the figures shown above, the bandheads in odd nuclei are $1/2^-$ states in all cases where γ-transition energies in odd nuclei are close to the corresponding energies in the ground-state bands of even–even nuclei. Excited states in these rotational bands are weakly split doublets: $(3/2^-, 5/2^-)$, $(7/2^-, 9/2^-)$, and so on. This means that the angular momenta of the states of odd nuclei belonging to the supersymmetric multiplets can be treated as the result of the vector coupling of angular momenta $L = 0, 2, 4, \ldots$ of the even–even core and the fermion momentum $j^\pi = 1/2^-$. The fermion momentum is decoupled from the interaction. It is assumed below that it is a pseudospin. Because of approximate pseudospin symmetry that is realized in heavy nuclei [25, 26], a pseudospin–orbit interaction is weak. Therefore, the pseudospin–orbit doublets are only weakly split, and the quadrupole–quadrupole interaction of the odd fermion with the even–even core is approximately a pseudospin scalar.

Let us decompose the total angular momentum of the odd fermion into the pseudospin and pseudoor-

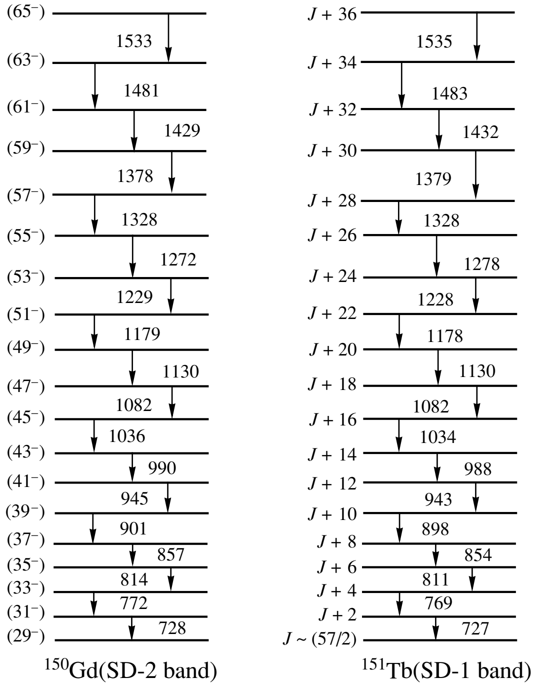

Fig. 5. Observed states of the identical superdeformed bands of ^{150}Gd and ^{151}Tb. The energies are given in keV. Experimental data were taken from [22].

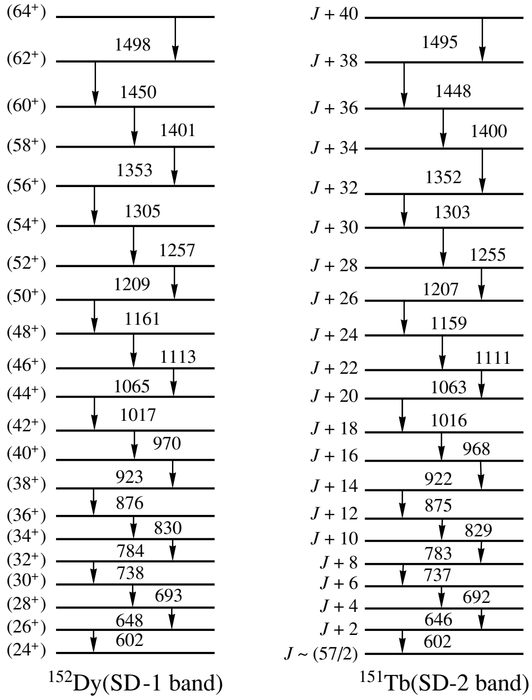

Fig. 6. Observed states of the identical superdeformed bands of ^{152}Dy and ^{151}Tb. The energies are given in keV. Experimental data were taken from [22].

bital angular momentum:

$$a^+_{jm} = \sum_{\mu,\sigma} C^{jm}_{\tilde{l}\mu 1/2\sigma} a^+_{\tilde{l}\mu,1/2\sigma}. \qquad (3)$$

Using the fermion operators $a^+_{\tilde{l}\mu,1/2\sigma}$ and $a_{\tilde{l}\mu,1/2\sigma}$, we can construct the operator of the fermion quadrupole moment,

$$Q^F_{2\mu}(\chi)$$
$$= \sum_\sigma \Bigg(a^+_{2\mu,1/2\sigma} a_{00,1/2\sigma} + a^+_{00,1/2\sigma}(-1)^\mu a_{2-\mu,1/2\sigma}$$
$$+ \chi \sum_{\eta,\eta'} C^{2\mu}_{2\eta 2\eta'} a^+_{2\eta,1/2\sigma} (-1)^{\eta'} a_{2-\eta',1/2\sigma} \Bigg),$$

which contains a free parameter χ, and the operators of the numbers of fermions with pseudoorbital angular momenta $\tilde{l} = 0$ and 2,

$$\hat{N}^F(\tilde{l} = 0) = \sum_\sigma a^+_{00,1/2\sigma} a_{00,1/2\sigma},$$
$$\hat{N}^F(\tilde{l} = 2) = \sum_{\mu,\sigma} a^+_{2\mu,1/2\sigma} a_{2\mu,1/2\sigma}.$$

Presented immediately below are the corresponding boson operators.

The operator of the boson quadrupole moment has the form

$$Q^B_{2\mu}(\chi) = d^+_\mu s + s^+(-1)^\mu d_{-\mu}$$
$$+ \chi \sum_{\eta,\eta'} C^{2\mu}_{2\eta 2\eta'} d^+_\eta (-1)^{\eta'} d_{-\eta'}.$$

The operators of the numbers of the s-bosons and d-bosons are $\hat{N}^B_s = s^+ s$ and $\hat{N}^B_d = \sum_\mu d^+_\mu d_\mu$, respectively.

The combined boson–fermion operators are

$$Q_{2\mu}(\chi) = Q^B_{2\mu}(\chi) + Q^F_{2\mu}(\chi),$$
$$\hat{N}(0) = \hat{N}^B_s + \hat{N}^F(\tilde{l} = 0),$$
$$\hat{N}(2) = \hat{N}^B_d + \hat{N}^F(\tilde{l} = 2).$$

The general form of the Hamiltonian used is

$$H(\chi) = \epsilon_0 \hat{N}(0) + \epsilon_2 \hat{N}(2) - \kappa Q_2(\chi) \cdot Q_2(\chi). \qquad (4)$$

This is the most general CQF IBM1 Hamiltonian for even–even nuclei, but it has a special form for odd nuclei. In general, the Hamiltonian cannot be represented as the sum of the Casimir operators of some subgroup chain. This can be done only if $\chi = 0$ and $\epsilon_0 = \epsilon_2$ [i.e., in the limit of $O(6)$ dynamical symmetry] or if $\chi = \pm\sqrt{7}/2$ and $\epsilon_0 = \epsilon_2$ [i.e., in the limit of $SU(3)$ dynamical symmetry].

The superoperator commuting with the Hamiltonian in (4) and with the combined boson–fermion quadrupole-moment operator for arbitrary χ, ϵ_0, and ϵ_2 is

$$P_{1/2m} = a^+_{00,1/2m} s + \sum_\mu a^+_{2\mu,1/2m} d_\mu.$$

Thus, we see that, although we get, for an even–even nucleus, a spectrum that does not belong to a dynamical-symmetry limit for arbitrary χ, we have a subset of eigenstates in an odd nucleus with the same relative energies as in the even–even nucleus. Together with the corresponding eigenstates of the even–even nucleus, these states form supersymmetric multiplets. The eigenvectors of these states are constructed by applying the superoperator $P_{1/2m}$ to the eigenvectors of the even–even nucleus with different values of the angular momentum I,

$$|JMN_F = 1, N_B = N-1, Ln\rangle$$
$$= \frac{1}{\sqrt{N}} \sum_{m,\mu} C^{JM}_{1/2mL\mu} P_{1/2m} |Ln\mu N_F = 0, N_B = N\rangle.$$

Since the operator $P_{1/2m}$ has the angular momentum of $j = 1/2$, we get doublets of states with the angular momenta of $J = I \pm 1/2$ in the odd nucleus.

Let us now consider the second limitation associated with the dimension of the single-particle configuration space. Let us show that the particle–rotor model description of the degenerate-signature partner bands built on the $K = 1/2$ pseudosinglet Nilsson orbit can be reformulated as a realization of supersymmetry. In this model, there is no restriction on the number of spherical single-particle orbits interacting with a quadrupole deformed core. Using the particle creation and annihilation operators introduced in (3) and assuming that the matrix elements of r^2 are independent of $\tilde{l}$, we obtain the particle quadrupole operator in the form

$$q_{2\mu} = \langle r^2 \rangle \sum_{\tilde{l},\tilde{l}',\nu,\nu',\sigma} \frac{\langle \tilde{l}' || Y_2 || \tilde{l} \rangle}{\sqrt{5}} C^{2\mu}_{\tilde{l}'\nu'\tilde{l}\nu} a^+_{\tilde{l}'\nu',\tilde{\frac{1}{2}}\sigma} \tilde{a}_{\tilde{l}\nu,\tilde{1/2}\sigma}.$$

We will also neglect a weak pseudospin–orbit interaction. In the pseudospin–orbit representation, the Hamiltonian of the particle–rotor model can be written, in the laboratory frame, as

$$H = \sum_{\tilde{l},\nu,\sigma} E_{\tilde{l}} a^+_{\tilde{l}\mu,\widetilde{1/2}\sigma} a_{\tilde{l}\mu,\widetilde{1/2}\sigma} + \frac{\hbar^2}{2\Im} L^2 \qquad (5)$$
$$-\hbar\omega_0 \sum_{\mu} (-1)^{\mu} q_{2\mu} Q^c_{2-\mu}.$$

In contrast to the standard particle–rotor model, it is assumed in (5) that the total orbital angular momentum $\mathbf{L}$ is the vector sum of the core rotational momentum $\mathbf{R}$ and the particle pseudoorbital angular momentum $\mathbf{l}$: $\mathbf{L} = \mathbf{R} + \tilde{\mathbf{l}}$. The operator $Q^c_{2\mu}$ is represented as $Q^c_{2\mu} = \beta D^2_{\mu 0}$. The operators

$$a^+_{\tilde{l}\mu,\widetilde{1/2}\sigma} a_{\tilde{l}'\mu',\widetilde{1/2}\sigma'}, \quad L_\nu, \quad D^L_{M0},$$

which are used to construct the Hamiltonian in (5), form, together with the operators

$$a^+_{\tilde{l}\mu,\tilde{1/2}\sigma} D^l_{m0}, \qquad a_{\tilde{l}\mu,\tilde{1/2}\sigma} D^l_{m0},$$

a graded Lie algebra. The superoperator that is an eigenmode operator for the Hamiltonian in (5) has the form

$$P_{1/2\sigma} \equiv \sum_{\tilde{l},\, m} \chi_{\tilde{l}} C^{00}_{\tilde{l}m\tilde{l}-m} a^+_{\tilde{l}m,\widetilde{1/2}\sigma} \sqrt{2\tilde{l}+1} D^{\tilde{l}}_{-m0}$$

and satisfies the relation

$$\left[H, P_{1/2\sigma}\right] = E_0 P_{1/2\sigma}. \qquad (6)$$

The coefficients $\chi_{\tilde{l}}$ obey the equation

$$\sum_{\tilde{l}'} h_{\tilde{l},\tilde{l}'} \chi_{\tilde{l}'} = E_0 \chi_{\tilde{l}},$$

where

$$h_{\tilde{l},\tilde{l}'} = E_{\tilde{l}} \delta_{\tilde{l}\tilde{l}'} - \hbar\omega_0 \beta \langle r^2 \rangle \langle \tilde{l}0 | Y_{20} | \tilde{l}'0 \rangle$$

are the matrix elements of the Nilsson single-particle Hamiltonian in the pseudooscillator basis calculated under the assumption that the matrix elements of r^2 are independent of $\tilde{l}$ and $\tilde{l}'$. More precisely, $h_{\tilde{l}\tilde{l}'}$ is the part of the Nilsson Hamiltonian matrix corresponding to the single-particle states characterized by zero projection of the pseudoorbital angular momentum ($\tilde{\Lambda} = 0$) onto the symmetry axis. It follows from (6) that the superoperator $P_{1/2\sigma}$ acting on the eigenstates of an even–even nucleus produces the eigenstates of the neighboring odd nucleus with $\tilde{\Lambda} = 0$. The γ-transition energies will be the same in even–even and odd nuclei for the states being considered.

As can be seen from the expression for $P_{1/2\sigma}$, its total orbital angular momentum is zero. For this reason, $P_{1/2\sigma}$ applied to even–even core rotational states creates only states of the odd nucleus with even L and $\tilde{\Lambda} = 0$. From the expression for the eigenvector of the Hamiltonian in (5) with $\tilde{\Lambda} = 0$, it follows that the total orbital angular momentum L of these states must satisfy the condition

$$(-1)^{L+\tilde{l}} = +1. \qquad (7)$$

Therefore, $P_{1/2\sigma}$ will create eigenstates of the odd nucleus only if $\tilde{l}$ is even. For instance, the normal-parity single-particle orbits $p_{1/2}$, $(p_{3/2}, f_{5/2})$, and $(f_{7/2}, h_{9/2})$ have even pseudoorbital angular momenta, and, in the case where a corresponding oscillator shell is a valence one, the energy intervals in the rotational band of the odd nucleus based on the Nilsson state with $\tilde{\Lambda} = 0$ can be identical to the corresponding energy intervals in the ground-state band of the even–even nucleus. In contrast, the normal-parity

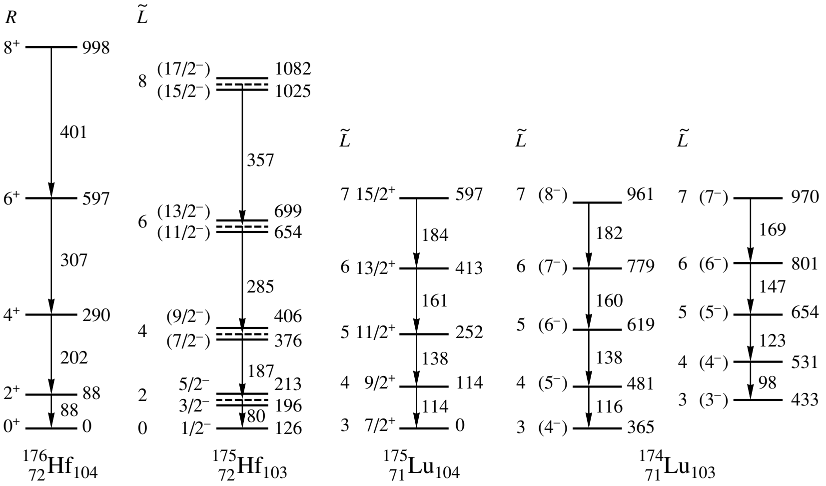

Fig. 7. States of the ground-state bands of ^{175,176}Hf and ^{175}Lu and excited bands of ^{174}Lu. The energies are given in keV. Experimental data were taken from [27–30]. The values of the pseudoorbital angular momentum $\tilde{L}$ are shown together with the values of the total angular momentum.

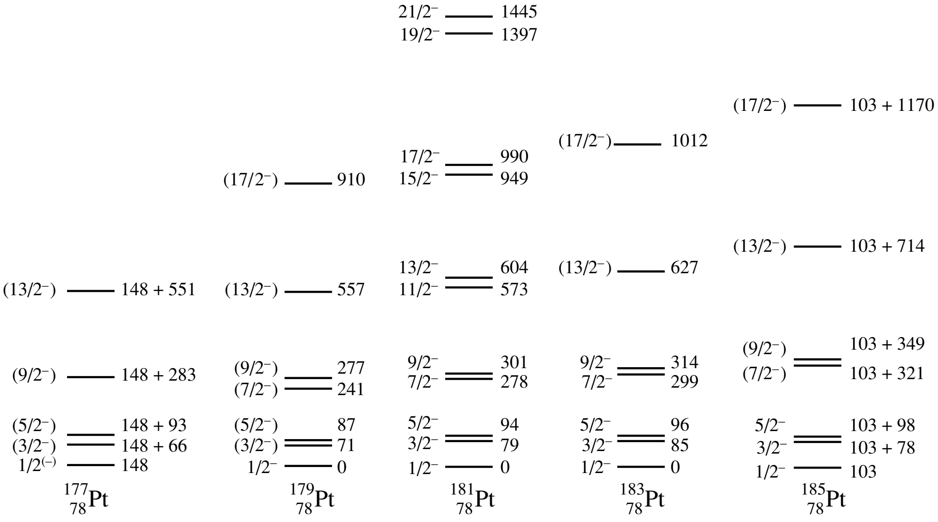

Fig. 8. States of the rotational bands of the odd Pt isotopes based on the [521]1/2$^-$ Nilsson state. Experimental data were taken from [22]. The energies are given in keV.

single-particle orbits $(s_{1/2}, d_{3/2})$ and $(d_{5/2}, g_{7/2})$ have odd pseudoorbital angular momenta. According to (7), L is therefore odd and the eigenstates of the odd nucleus based on these orbits cannot be created by applying $P_{1/2\sigma}$. It is possible to construct the corresponding operator. However, this operator must have a nonzero total orbital angular momentum, so that it will not commute with the Hamiltonian in (5); therefore, it will not create, in the odd nucleus, rotational bands identical to the bands of the even–even one. This situation is illustrated by the ground-state rotational bands of ^{171}Tm and ^{171}Yb. The ^{171}Tm nucleus has an odd proton hole produced in the even–even core ^{172}Yb. This proton hole occupies the [411]1/2$^+$ state in the case of the ground-state band, which is characterized by $\tilde{\Lambda} = 0$ and odd $\tilde{l}$. Since $\tilde{l}$ is odd, the total orbital momentum L of the odd nucleus takes the values of $L = 1, 3, 5\ldots$. Hence, the ground-state band of ^{171}Tm, which is constructed by the vector coupling of L to the pseudospin equal to 1/2, consists of the almost degenerate doublets $(1/2^+, 3/2^+), (5/2^+, 7/2^+)$, and so on. The ground-state band of ^{171}Yb is based on the [521]1/2$^-$ state with $\tilde{\Lambda} = 0$ and even $\tilde{l}$. In this case, L takes the values of $0, 2, 4, \ldots$. As a result, the ground-state band of ^{171}Yb consists of the singlet $1/2^-$ and almost degenerate doublets $(3/2^-, 5/2^-), (7/2^-, 9/2^-)$, and so on. The experimental energy intervals in the ground-state band of ^{171}Yb are quite close to those of ^{172}Yb, thus giving an example of approximate supersymmetry. In the ground-state band of ^{171}Tm, the energy intervals deviate to a greater extent from those in ^{172}Yb. However, they follow, with a good accuracy, the $L(L+1)$ rule (L is odd) with approximately the same value of the moment of inertia as in ^{172}Yb.

The operator $P_{1/2m}$, which creates a neutron hole, can also be applied to the states of rotational bands of the odd-proton nucleus, thus producing the rotational bands in the odd–odd nucleus with the same energy intervals as in the parent odd-proton nucleus. This case is illustrated by the spectra of ^{174,175}Lu shown in Fig. 7. Applying the operator $P_{1/2m}$ to the states of the ground-state band of ^{175}Lu based on the $7/2^+$ state, we create two rotational bands in ^{174}Lu based on the 4^- and 3^- states. The energies of the γ transitions in these bands are close to the γ-transition energies in ^{175}Lu. This is especially true for the band in ^{174}Lu that is based on the 4^- state, where the agreement is almost perfect.

The examples demonstrated above show that, in all cases, the rotational bands of an odd nucleus belonging to the supermultiplets are based on the $[521]1/2^-$ Nilsson state which is $[\widetilde{420}]$ pseudoorbital singlet. Thus, it is interesting to investigate the properties of the rotational bands based on this single-particle state in different nuclei at different excitation energies of the bandhead. The existing experimental data are rather scarce. Figure 8 shows the known levels belonging to the rotational bands based on the $[521]1/2^-$ state in the Pt isotopes. It can be seen that only in the nuclide ^{181}Pt is the band followed up to high spins and are the complete doublets observed. The same picture is characteristic of the Os and W isotopes. Thus, new experimental data are needed for obtaining deeper insights into supersymmetry phenomena in nuclear structure.

REFERENCES

1. F. Iachello, Phys. Rev. Lett. **44**, 772 (1980).
2. A. B. Balantekin, I. Bars, and F. Iachello, Nucl. Phys. A **370**, 284 (1981).
3. F. Iachello and S. Kuyucak, Ann. Phys. (N.Y.) **136**, 19 (1981).
4. R. Bijker and V. K. B. Kota, Ann. Phys. (N.Y.) **156**, 110 (1984).
5. R. Bijker and F. Iachello, Ann. Phys. (N.Y.) **161**, 360 (1985).
6. R. Bijker and V. K. B. Kota, Ann. Phys. (N.Y.) **187**, 148 (1988).
7. J. A. Cizewski, in *Nuclear Structure, Reactions and Symmetries* (World Sci., Singapore, 1986), Vol. 1, p. 181.
8. D. D. Warner, R. F. Casten, and A. Frank, Phys. Lett. B **180**, 207 (1986).
9. J. Vervier, P. van Isacker, J. Jolie, *et al.,* Phys. Rev. C **32**, 1406 (1985).
10. P. van Isacker, J. Jolie, K. Heyde, and A. Frank, Phys. Rev. Lett. **54**, 653 (1985).
11. A. Metz, J. Jolie, G. Graw, *et al.,* Phys. Rev. Lett. **83**, 1542 (1999).
12. M. Kaku, *Quantum Field Theory* (Oxford, 1993).
13. F. Iachello and P. van Isacker, *The Interacting Boson–Fermion Model* (Cambridge Univ. Press, Cambridge, 1991).
14. R. V. Jolos and P. von Brentano, Phys. Rev. C **60**, 064318 (1999).
15. R. V. Jolos and P. von Brentano, Phys. Rev. C **62**, 034310 (2000).
16. R. V. Jolos and P. von Brentano, Phys. Rev. C **63**, 024304 (2001).
17. *Tables of Isotopes,* Ed. by R. B. Firestone *et al.* (Wiley, New York, 1996, 8th ed.).
18. B. Fabricius *et al.,* Nucl. Phys. A **523**, 426 (1991).
19. J. H. Jett and D. A. Lind, Nucl. Phys. A **155**, 182 (1970).
20. M. J. A. Voigt *et al.,* Nucl. Phys. A **507**, 447 (1990).
21. D. G. Popesku *et al.,* Phys. Rev. C **55**, 1175 (1997).
22. B. Singh, R. B. Firestone, and S. Y. F. Chu, *Table of Superdeformed Nuclear Bands and Fission Isomers*, LBL-38004, UC–413 (1996).
23. W. Nazarewicz, P. J. Twin, P. Fallon, and J. D. Garrett, Phys. Rev. Lett. **64**, 1654 (1990).
24. A. Gelberg, P. von Brentano, and R. F. Casten, J. Phys. G **16**, L143 (1990).
25. K. T. Hecht and A. Adler, Nucl. Phys. A **137**, 129 (1969).
26. A. Arima, M. Harvey, and K. Shimizu, Phys. Lett. B **30**, 517 (1969).
27. A. J. Kreiner, Phys. Rev. C **38**, 2486 (1988).
28. A. Bruder *et al.,* Nucl. Phys. A **474**, 518 (1987).
29. P. Kemmitz *et al.,* Nucl. Phys. A **209**, 271 (1973).
30. P. Skensved *et al.,* Nucl. Phys. A **366**, 125 (1981).

Physics of Atomic Nuclei, Vol. 64, No. 6, 2001, pp. 1134–1140. From Yadernaya Fizika, Vol. 64, No. 6, 2001, pp. 1210–1216.
Original English Text Copyright © 2001 by Sauvage, Libert, Roussière, Verney, Cabaret, Crawford, Genevey, Huber, Ibrahim, Le Blanc, Lee, Oms, Pinard.

Deformation Properties of the Neutron-Deficient Odd-A Pt and Hg Nuclei*

J. Sauvage**, **J. Libert, B. Roussière, D. Verney, L. Cabaret**[1], **J. E. Crawford**[2],
J. Genevey[3], **G. Huber**[4], **F. Ibrahim, F. Le Blanc, J. K. P. Lee**[2], **J. Oms, and J. Pinard**[1],
and the ISOLDE Collaboration
Institut de Physique Nucléaire, IN2P3–CNRS, Orsay, France

Received October 25, 2000

Abstract—Nuclear and atomic spectroscopy measurements have provided a great number of data on the neutron-deficient Pt and Hg nuclei. The odd-A Pt and Hg with A <186 have a prolate shape, and the even–even isotopes have a triaxial shape, while the nuclear shape of the odd-A Pt and Hg with A >186 is still an open question. The energy of the low-lying levels and the nuclear moments have been calculated in the framework of a semimicroscopic "axial-rotor + 1 quasiparticle" coupling model. The predictions are compared with the experimental data and discussed. The results strongly suggest a prolate shape for the negative-parity low-lying states of the odd-A $^{187–191}$Pt and $^{187–193}$Hg isotopes. *© 2001 MAIK "Nauka/Interperiodica".*

1. INTRODUCTION

A great number of data on the neutron-deficient Hg, Au, Pt, and Ir nuclei have been obtained by both nuclear and atomic spectroscopy measurements performed during the last thirty years. The properties of these transitional nuclei have already been studied using different models [1–8]. But no single model is able to reproduce the whole set of data. The goal of the present work is to determine to what extent the semimicroscopic "axial-rotor + 1 quasiparticle" coupling model, developed and tested on well-deformed nuclei some years ago [9–11], can reproduce the properties of these soft nuclei and can help answer the remaining open questions. Firstly, known results of the even–even and odd-A Hg and Pt nuclei will be recalled. Then, the procedure used to calculate the energies of the low-lying levels and the nuclear moments in the framework of the "axial-rotor + 1 quasiparticle" coupling model will be very briefly described. Thereafter, the predictions will be compared with the experimental results in order to study the deformation and shape properties of the odd-A Pt and Hg nuclei. This will allow us to propose a prolate shape for the negative-parity low-lying states of the odd-A $^{187–191}$Pt and $^{187–193}$Hg isotopes.

2. RECALL OF KNOWN RESULTS

The energy evolution of the low-lying states in the even–even Pt and Hg isotopes [12] obtained by nuclear spectroscopy measurements is shown, against their mass number A, in Fig. 1. For Pt nuclei, the moment of inertia of the ground-state band progressively increases when A decreases from 198 to 186, remains almost constant between 186 and 178, and starts to decrease afterwards, which shows that the deformation of the even Pt nuclei changes with A. On the contrary, for the Hg nuclei, the energy of the first 2^+ state is almost constant, which indicates a very weak deformation change of these nuclei in their first levels. On the other hand, the sharp energy changes observed for the upper states of ^{180}Hg and ^{182}Hg reveal the coexistence of two different deformations for the lightest Hg isotopes. Furthermore, the existence of a 2^+ state located close to the 4^+ state of the ground-state band in $^{180-196}$Pt and $^{186–198}$Hg nuclei is a signature of triaxiality [13]. All the results support the contention that the even–even Pt nuclei progressively change from a triaxial-oblate to a triaxial-prolate shape when A decreases from 198 to 180, whereas the even–even Hg nuclei have a triaxial shape and keep a small deformation in their first two states.

The results obtained by atomic spectroscopy are illustrated in Fig. 2 by the curves of the mean square

---

*This article was submitted by the authors in English.

[1] Laboratoire Aimé Cotton, Orsay, France.

[2] Physics Department, McGill University, Montréal, Canada.

[3] Institut des Sciences Nucléaires, IN2P3–CNRS/UJF, Grenoble, France.

[4] Institut für Physik der Universität Mainz, Germany.

**e-mail: `sauvage@ipno.in2p3.fr`

1063-7788/01/6406-1134$21.00 © 2001 MAIK "Nauka/Interperiodica"

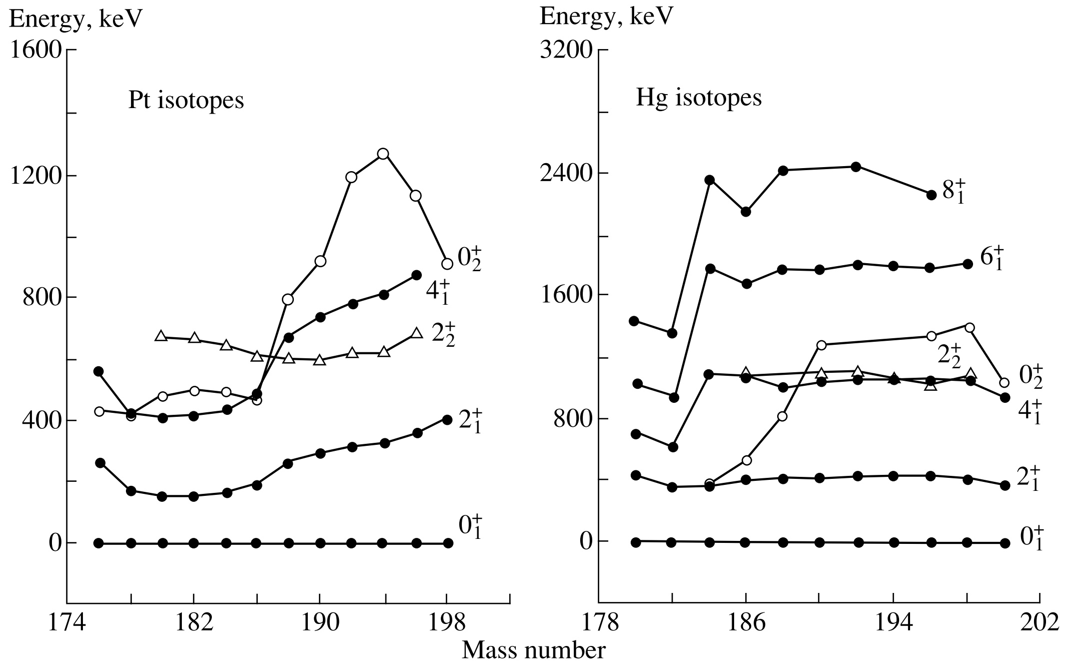

Fig. 1. Energy evolution of the low-lying levels of the even–even Pt and Hg nuclei.

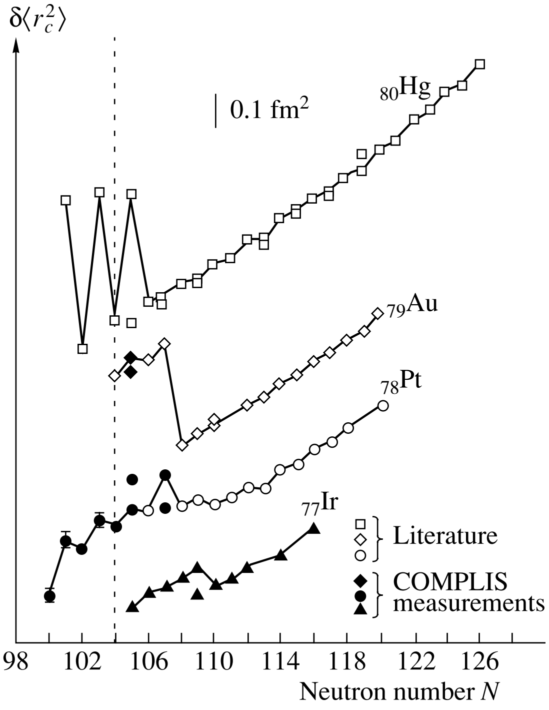

Fig. 2. Mean square charge radius change of the Hg, Au, Pt, and Ir isotopes. Open symbols for the results from [2, 4, 5, 14, 16–18], full symbols for the results from [15, 19, 20]. For convenience, values for the different elements are arbitrarily shifted along vertical axis and the scale ~0.1 fm^2.

charge radius change, $\delta\langle r_c^2\rangle$, of the Hg, Au, Pt, and Ir isotopes shown vs. their neutron number N. The $\delta\langle r_c^2\rangle$ values have been deduced from isotope shift (IS) measurements performed using optical methods as optical pumping or resonance ionization spectroscopy [2, 4, 5, 14–20]. These measurements

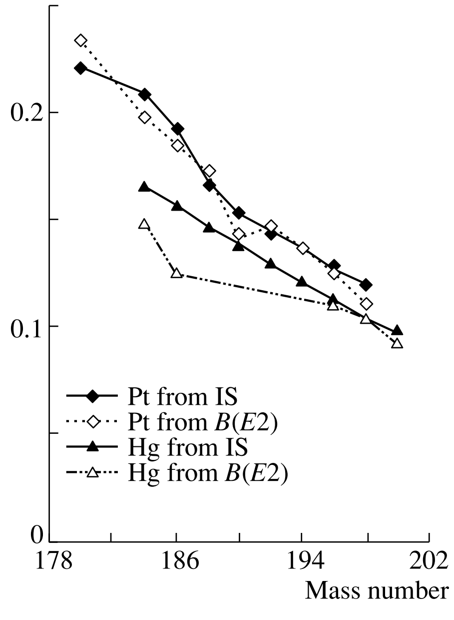

Fig. 3. β values extracted from $B(E2)$ and IS results for Pt (diamonds) and Hg (triangles) isotopes. ^{194}Pt and ^{198}Hg have been used as references.

provide, for odd-A and doubly-odd nuclei, the hyperfine structures from which the nuclear moments can be extracted. The charge radius decreases very regularly for the even Hg nuclei. There is no sudden deformation change, which is in agreement with the energy evolution of the first 2^+ state shown in Fig. 1. On the other hand, the famous huge odd–even staggering observed below $N = 106$ has been interpreted as alternating shape transitions: the odd-A Hg isotopes have a prolate shape, while the even ones have an oblate or triaxial shape [2]. From the results shown in Fig. 1, the even Hg nuclei (at least down to $A = 186$) have rather a triaxial shape. As for the Pt nuclei, below $N = 113$, the charge radius decreases with N more slowly than for the Hg nuclei, which corresponds to a quicker deformation increase. Moreover, the inverted odd–even staggering observed below $N = 109$ has been explained as due to alternating shape changes: the odd-A Pt have a prolate shape, while the even ones have a triaxial-prolate shape with an asymmetry parameter γ around 15° [15]. In addition to this, a large deformation change has been measured between the isomeric and ground states of ^{185}Hg, ^{183,185}Pt, and ^{186}Ir. The results reveal deformation instabilities especially around the neutron midshell.

From the $\delta\langle r_c^2\rangle$ values, it is possible to calculate the variation of the deformation parameters $\delta\langle\beta^2\rangle$. Thus, provided the β value is known for one isotope used as a reference, the β value of all the other isotopes can be determined. For the even nuclei, the β value can be extracted from the reduced transition probability $B(E2)$ of the $2^+ \to 0^+$ transition using the following relation:

$$B(E2;\ 2^+ \to 0^+) = \frac{1}{16\pi} Q_0^2,$$

where the intrinsic quadrupole moment Q_0 is given by

$$Q_0 = 0.757 Z r_0^2 A^{2/3} \beta (1 + 0.36\beta).$$

The β values of the even Pt and Hg nuclei reported in Fig. 3 have been deduced from both the $B(E2)$ values and IS results. The β values of the ^{194}Pt and ^{198}Hg isotopes, calculated from the $B(E2)$ values, have been used as references to extract the β values from the IS measurements. We can note that, for the Pt isotopes for which more data are available, the evolutions of the β values are in excellent agreement. Since two completely different methods lead to the same results, we can consider that the β values deduced from the IS results are quite reliable.

Finally, the behavior of the even–even Pt and Hg isotopes is rather well understood. It is in qualitative agreement with the predictions of the models. Furthermore, in the odd isotopes with $A < 186$, the single-particle levels have been identified as states corresponding to a prolate nuclear shape [12, 21–24]. This has been clearly confirmed by the properties of the rotational bands built on them [12, 25, 26]. On the other hand, the nuclear shape of the odd-A Pt and Hg isotopes with $A > 186$, is still an open question.

3. DESCRIPTION OF THE MODEL USED

In the attempt to determine the nuclear shape of the odd-A Pt and Hg isotopes with $A < 186$, we have calculated the energies of the low-lying levels and their nuclear moments in the framework of the semimicroscopic "rotor + 1 quasiparticle" coupling model [9–11]. For that, we proceed in three steps. First, constraint Hartree–Fock + BCS calculations are performed, assuming axial symmetry and using the Skyrme III force, to get the quasiparticle wave functions ϕ in the core. In these calculations, the core is constrained to take the deformation of the odd nucleus, extracted from the IS measurements. The constant matrix elements used for the pairing treatment are $G_{0p} = 13.5$ MeV, $G_{0n} = 15.2$ MeV for the Pt and $G_{0p} = 13.4$ MeV, $G_{0n} = 14.9$ MeV for the Hg isotopes. In the second step, the wave functions ϕ are used in the "axial-rotor + 1 quasiparticle" coupling model to get the wave functions Ψ that describe the coupled states of the odd nucleus. In this approach, the Coriolis force is treated exactly and all the quasiparticle states ϕ corresponding to an energy belonging to the interval $[E_{\text{Fermi level}} \pm 5\ \text{MeV}]$ from the Fermi level are taken into account. At last, the nuclear moments are calculated using the coupled-state wave functions Ψ obtained in the second step. The magnetic moments are calculated with $g_R = Z/A$ for $g_{s\,\text{free}}$ and $0.6\, g_{s\,\text{free}}$. An important property of this approach is that there are *no adjustable parameters*. But, the particle number is not conserved, which means that a given core provides the spectrum of the two adjacent odd-A nuclei.

4. COMPARISON OF THE EXPERIMENTAL AND THEORETICAL RESULTS

The energy evolution of the negative-parity states expected in the odd-A $^{185\text{–}193}$Pt nuclei from calculations performed assuming oblate and prolate shapes is shown in Fig. 4, on the left-hand side and right-hand side, respectively. For a given configuration, when the level predicted at the lowest energy is not the $I = K$ state, two levels are reported: the $I = K$ state and the state predicted at the lowest energy. This is the case for the 1/2[521] and 1/2[501] configurations in the oblate calculations and for the 1/2[510] and 3/2[512] configurations in the prolate calculations. All the negative-parity levels observed below 250 keV in the odd-A $^{187\text{–}193}$Pt are drawn in

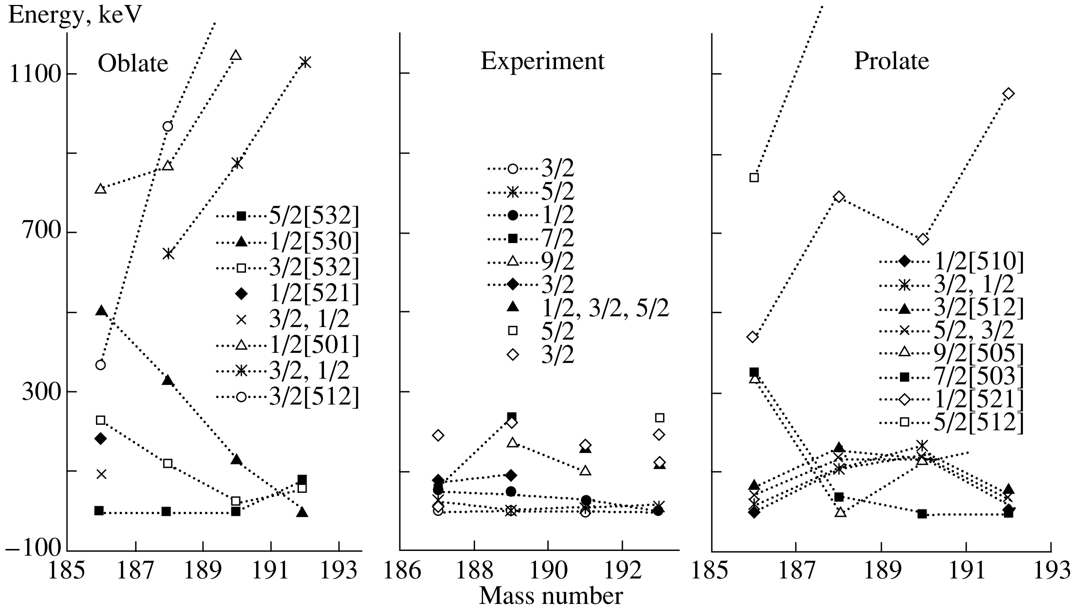

Fig. 4. Comparison of the energy evolutions of the negative-parity states predicted for the oblate and prolate shapes with that of the single-particle levels observed in the odd-A $^{187–193}$Pt.

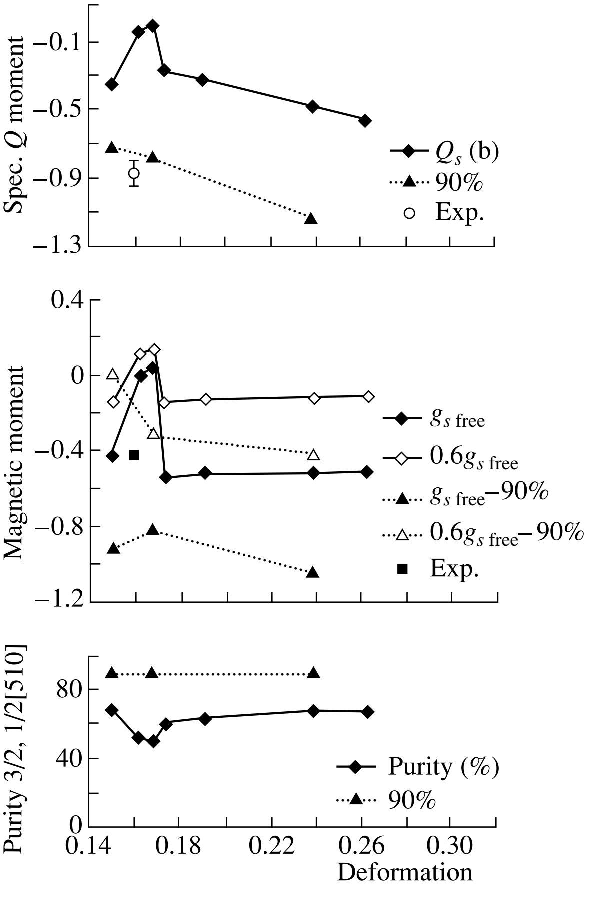

Fig. 5. Evolution of the purity of the 3/2, 1/2[510] state wave function and of the nuclear moments calculated for this state versus the ^{188}Pt core deformation.

the middle of Fig. 4. They are labeled with their spin value since they are not yet identified. The first observed levels have 3/2, 5/2, and 1/2 spin values; such states are predicted at low energy in both the oblate and prolate calculations. Besides this, 7/2 and 9/2 single-particle states have been observed at low energy. No 7/2 or 9/2 state is predicted below 1.2 MeV in the oblate calculations, whereas these two

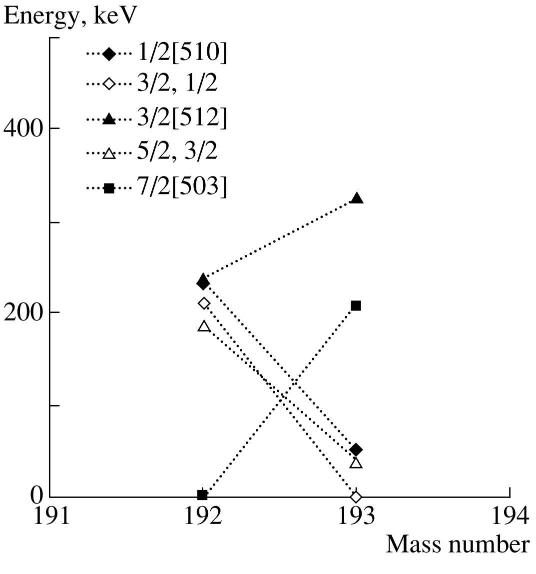

Fig. 6. Comparison of the single-particle spectrum observed in ^{193}Hg with that calculated using the ^{192}Hg prolate core.

Comparison of the measured and calculated nuclear moments (results for the oblate calculations are italicized)

Experiment					Theory					
nucleus	$\langle\beta^2\rangle^{1/2}$	$\mu_{\rm exp}, \mu_N$	$Q_{s\,\rm cor}$, b$^{1)}$	I^π	state	core	β	$\mu^{2)}, \mu_N$		Q_s, b
								$g_{s\,\rm free}$	$0.6g_{s\,\rm free}$	
^{193}Pt	0.133(10)	0.603(8)		$1/2^-$	*1/2[530]*	*^{192}Pt*	*−0.146*	*0.65*	*0.4*	
				$1/2^-$	1/2[510]		0.145	0.79	0.54	
^{187}Pt	0.184(3)	−0.399(8)	−0.98(5)	$3/2^-$	*1/2[521]*	*^{186}Pt*	*−0.191*	*−0.86*	*−0.53*	*0.93*
				$3/2^-$	*3/2[532]*			*0.33*	*0.28*	*−1.1*
				$3/2^-$	*3/2[512]*			*0.58*	*0.49*	*−0.9*
				$3/2^-$	*1/2[501]*			*0.88*	*0.9*	*0.81*
				$3/2^-$	1/2[510]		0.191	−0.21	−0.0014	−0.28
				$3/2^-$	3/2[512]			0.14	0.25	0.27
^{193}Hg	0.114(4)	−0.62757(18)	−0.72(38)	$3/2^-$	1/2[510]	^{192}Hg	0.127	−1.09	−0.53	−0.66
^{195}Pt	0.136(3)	+0.60949(6)		$1/2^-$	1/2[510]	^{194}Pt	0.141	0.8	0.55	
^{193}Pt	0.133(10)	+0.603(8)		$1/2^-$	1/2[510]	^{192}Pt	0.145	0.79	0.54	
^{191}Pt	0.141(10)	−0.501(5)	−0.78(10)	$3/2^-$	1/2[510]	^{190}Pt	0.14	−0.39	−0.11	−0.03
^{189}Pt	0.158(3)	−0.422(7)	−0.869(76)	$3/2^-$	1/2[510]	^{188}Pt	0.162	−0.0013	0.11	−0.048
^{187}Pt	0.184(3)	−0.399(8)	−0.98(5)	$3/2^-$	1/2[510]	^{186}Pt	0.191	−0.21	−0.0014	−0.28
^{185g}Pt	0.224(3)	−0.723(11)	+3.73(17)	$9/2^+$	9/2[624]	^{184}Pt	0.229	−1.46	−0.86	3.31
^{185m}Pt	0.200(3)	+0.503(5)		$1/2^-$	1/2[521]	^{186}Pt	0.206	0.63	0.37	
^{183g}Pt	0.220(3)	+0.502(5)		$1/2^-$	1/2[521]	^{184}Pt	0.229	0.63	0.38	
^{183m}Pt	0.239(3)	+0.782(14)	+3.37(27)	$7/2^-$	7/2[514]	^{184}Pt	0.245	1.46	0.99	3.25
^{181}Pt	0.232(4)	+0.484(21)		$1/2^-$	1/2[521]	^{182}Pt	0.236	0.63	0.38	
^{179}Pt	0.236(5)	+0.431(32)		$1/2^-$	1/2[521]	^{180}Pt	0.243	0.64	0.38	
^{189}Os		−0.320(46)		$3/2^-$	1/2[510]	^{190}Os	0.176	−0.040	0.085	−0.077

$^{1)}$ Spectroscopic quadrupole moment corrected for the Sternheimer shielding factor.

$^{2)}$ Calculated using $g_R = Z/A$.

states exist at low energy in the prolate calculations. The odd-A $^{187\text{–}191}$Pt have a 3/2 ground state. To determine which theoretical 3/2 state corresponds to the ground state we calculated the nuclear moments of all the 3/2 states predicted below 1.2 MeV, namely the 3/2, 1/2[521], 3/2[532], 3/2[512], and 3/2, 1/2[501] states in the oblate case and the 3/2, 1/2[510], and 3/2[512] states in the prolate case. In the same way, we calculated the μ value of the 1/2 ground state of the ^{193}Pt isotope. For ^{193,187}Pt, the μ and Q_s values obtained with both oblate and prolate calculations are compared with the experimental ones at the beginning of the table. The μ value of the 1/2 ground state of ^{193}Pt is perfectly reproduced in both calculations. Therefore, the nuclear shape cannot be clearly determined in this case. As for the ^{187}Pt nucleus, both the measured μ and Q_s have negative values. Only the prolate 3/2, 1/2[510] state has this property. However, the calculated values are too high relative to the experimental ones. We can note that the μ value varies quickly with the g_s value. To study the sensitivity of the nuclear moments to the nuclear deformation, we calculated the μ and Q_s values of the 3/2, 1/2[510] state using the ^{188}Pt core constrained to have different deformations (β from 0.15 to 0.27). In Fig. 5 are displayed the purity of the wave function and the evolutions of the μ and Q_s values. One can see that the evolutions of the μ and Q_s values have their maxima when the wave function purity is minimal. As shown with the dotted curves, a purity of 90% would be necessary to approach both the μ and Q_s experimental values. Therefore, the wave function admixtures are calculated too large for this configuration.

In spite of this, several clues suggest that the odd-A Pt and Hg nuclei with $A > 186$ have a prolate shape. The experimental levels of Pt and Hg nuclei have then been identified assuming a prolate shape. The comparison of the level energies of ^{193}Hg with the predictions obtained using the ^{192}Hg prolate core is shown in Fig. 6 as an example. The 7/2[503] state is predicted at slightly too low an energy, but all the state energies are reproduced at better than 250 keV.

In the second part of the table, the measured nuclear moments of ^{193}Hg, $^{179-195}$Pt, and ^{189}Os are compared with the predicted ones for prolate shape and β values close to the $\langle\beta^2\rangle^{1/2}$ extracted from the IS measurements. We must note that the $3/2^-$ ground states of the odd-A $^{187–193}$Hg and $^{187–191}$Pt nuclei, identified as 3/2, 1/2[510] states, have μ values close to that of the known 3/2, 1/2 [510] state of ^{189}Os [12]. These measured μ values slowly decrease with A, whereas the calculated μ and Q_s values vary rapidly because of admixture changes in the 3/2, 1/2[510] wave function. The admixture in the wave function is due to the fact that the 3/2[512] and 1/2[510] quasiparticle states are found at very close energies in the CHF + BCS calculations. The Coriolis effect becomes especially large when the 3/2[512] state is located above the 1/2[510] state. The 3/2[512] state is found at 20 keV below the 1/2[510] state in the ^{192}Hg core, whereas it is at 15 keV above it in the ^{188}Pt core. This explains why the nuclear moments are perfectly reproduced for ^{193}Hg, while their predictions are too large for the Os and Pt nuclei. Therefore, for the 3/2, 1/2[510] state, the admixtures are overestimated for the Os and Pt nuclei. For the $9/2^+$ ground state of ^{185}Pt, the calculated μ and Q_s values are slightly too small. For the $7/2^-$ isomeric state of ^{183}Pt, the calculated μ value is slightly too large, whereas the predicted and measured Q_s values are in a perfect agreement. At last, for the 1/2 ground states of $^{179-183}$Pt and the 1/2 isomeric state of ^{185}Pt, the measured μ values are perfectly reproduced by the calculations for the 1/2[521] configuration. In Fig. 7, the energies of the coupled quasiparticle states calculated using the prolate Pt cores from $A = 180$ to 198 are compared with the energies of the single-particle states observed in the $^{181-191}$Pt. The positive-parity states are linked with full lines, and the negative-parity states with dotted lines. One can note that numerous states cross each other between the mass numbers 184 and 186. The energies of the low-lying states for $A < 186$ increase with A, while the energies of the low-lying states for $A > 186$ increase when A decreases. For $A < 186$, all the levels observed below 650 keV and previously identified [12] as single-particle states are found in the calculations. However, the 5/2[512] state is calculated at slightly too low an energy, and the 9/2[624], 1/2[510], 3/2[512], and 7/2[503], states have energies that increase as observed, but the slope is too steep. Nevertheless, most of the state energies

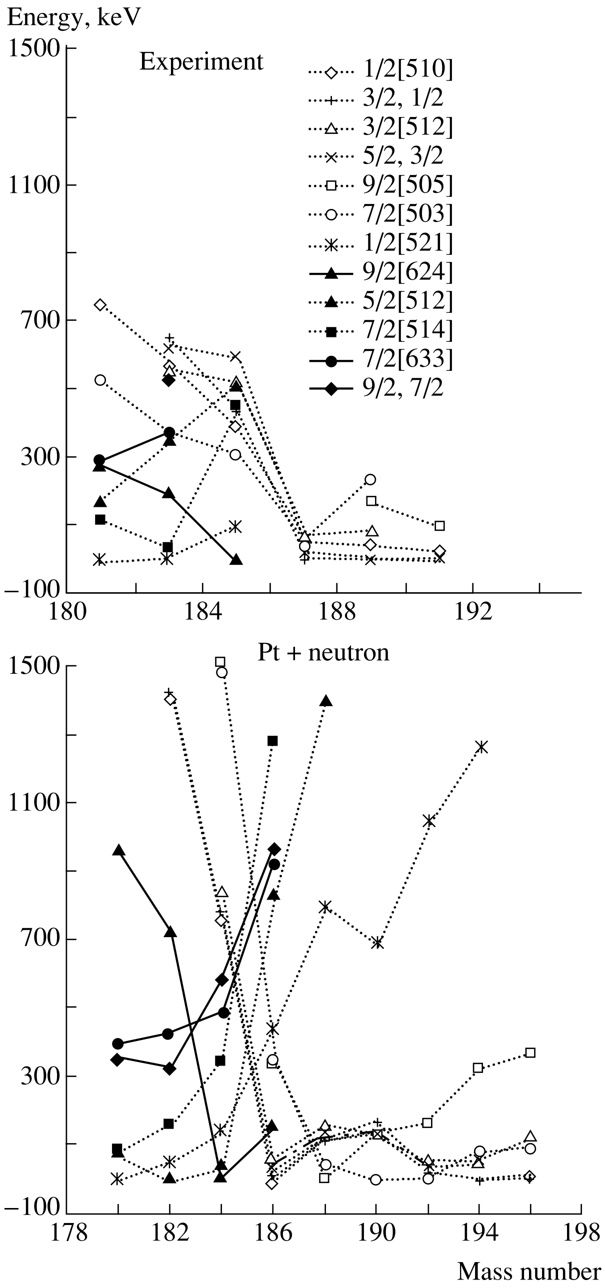

Fig. 7. Comparison of the observed and predicted single-particle spectra of the odd-A Pt isotopes.

are reproduced at better than 500 keV. For $A > 186$, the first levels are identified as prolate states, as suggested by the results presented in the table and in Figs. 4 and 6. For $^{187\text{–}191}$Pt, a satisfactory agreement is found between the measured and predicted energies for the first levels. However, all the levels could not be clearly identified. To go further, it would be interesting to calculate the reduced transition probabilities $B(M1)$ and $B(E2)$.

5. CONCLUSION

We have shown that the model used can reproduce the results satisfactorily for the odd-A $^{181\text{–}185}$Pt that clearly have a prolate shape: the energies of most of the low-lying levels are reproduced within 500 keV, and the nuclear moments are well predicted. Furthermore, the comparison of the measured and calculated results strongly suggests a prolate shape for the $^{187\text{–}193}$Hg and $^{187\text{–}191}$Pt nuclei: the existence at low energy of the 7/2 and 9/2 single-particle states and the negative μ and Q_s values of the 3/2 ground states could be reproduced only in the prolate calculations. It is worth noting that the β values extracted from the IS results and the signs of the nuclear moments played a decisive role in this work.

Finally, the odd-A neutron-deficient Pt and Hg isotopes more likely have a prolate shape while the even ones have a triaxial shape, which indicates that the coupling of a neutron to the core highly influences the mean field producing a nucleon rearrangement.

REFERENCES

1. K. Heyde *et al.*, Phys. Rep. **102**, 291 (1983).
2. G. Ulm *et al.*, Z. Phys. A **325**, 247 (1986).
3. M. G. Porquet *et al.*, Nucl. Phys. A **451**, 365 (1986).
4. Th. Hilberath *et al.*, Z. Phys. A **342**, 1 (1992).
5. G. Passler *et al.*, Nucl. Phys. A **580**, 173 (1994).
6. M. K. Harder *et al.*, Phys. Lett. B **405**, 25 (1997).
7. J. P. Delaroche *et al.*, Phys. Rev. C **50**, 2332 (1994).
8. R. Bengtsson *et al.*, Phys. Lett. B **183**, 1 (1987).
9. M. Meyer *et al.*, Nucl. Phys. A **316**, 93 (1979).
10. J. Libert *et al.*, Phys. Rev. C **25**, 586 (1982).
11. J. Libert *et al.*, Phys. Lett. B **95**, 175 (1980).
12. R. B. Firestone, *Table of Isotopes*, 8th ed. (John Wiley & Sons, New York, 1996), Vol. II.
13. N. V. Zamfir and R. F. Casten, Phys. Lett. B **260**, 265 (1991).
14. H. T. Duong *et al.*, Phys. Lett. B **217**, 401 (1989).
15. F. Le Blanc *et al.*, Phys. Rev. C **60**, 054310 (1999).
16. W. Wallmeroth *et al.*, Nucl. Phys. A **493**, 224 (1989).
17. G. Savard *et al.*, Nucl. Phys. A **512**, 241 (1990).
18. U. Kronert *et al.*, Z. Phys. A **331**, 521 (1988).
19. F. Le Blanc *et al.*, Phys. Rev. Lett. **79**, 2213 (1997).
20. D. Verney *et al.*, in *Proceedings of the International Conference on Experimental Nuclear Physics in Europe Facing the Next Millennium, Sevilla, 1999*; AIP Conf. Proc. **495**, 117 (1999).
21. B. Roussière *et al.*, Nucl. Phys. A **485**, 111 (1988).
22. E. van Walle *et al.*, Hyperfine Interactions **22**, 507 (1985).
23. B. Roussière *et al.*, Nucl. Phys. A **504**, 511 (1989).
24. J. Sauvage *et al.*, Nucl. Phys. A **540**, 83 (1992).
25. J. Nyberg *et al.*, Nucl. Phys. A **511**, 92 (1990).
26. M. J. A. de Voigt *et al.*, Nucl. Phys. A **507**, 447 (1990).

Physics of Atomic Nuclei, Vol. 64, No. 6, 2001, pp. 1141–1146. From Yadernaya Fizika, Vol. 64, No. 6, 2001, pp. 1217–1222.
Original English Text Copyright © 2001 by Kohstall, Belic, von Brentano, Fransen, Herzberg, Jolie, Kneissl, Lehmann, Linnemann, Matschinsky, Nord, Pietralla, Pitz, Scheck, Stedile, Werner, Yates.

Low-Lying Dipole Excitations in the Stable Cd Isotopes: A Systematics*

C. Kohstall, D. Belic, P. von Brentano[1)], C. Fransen[1)], R.-D. Herzberg[1), ***], J. Jolie[2)], U. Kneissl, H. Lehmann[2)], A. Linnemann[1)], P. Matschinsky[1)], A. Nord, N. Pietralla[1), ****], H. H. Pitz, M. Scheck, F. Stedile, V. Werner[1)], and S. W. Yates[3)]**

Institut für Strahlenphysik, Universität Stuttgart, Germany

Received October 25, 2000

Abstract—Low-lying dipole excitations in the medium-weight vibrational nuclei of the Cd isotopic chain were investigated by means of nuclear resonance fluorescence experiments performed at the bremsstrahlung beam of the Stuttgart Dynamitron accelerator (endpoint energy 4.1 MeV). Detailed information has been obtained on excitation energies, spins, decay widths, and transition probabilities of numerous excited states in $^{110–114,116}$Cd. Additionally, the use of two Compton polarimeters enabled model-independent parity assignments for excitations in the even–even isotopes. Strongly excited $J^\pi = 1^-$ states are found in all even–even Cd nuclei at excitation energies near the sum of the energies of the first 2^+ and 3^- states. These excitations are interpreted as the 1^- member of the quadrupole–octupole coupled quintuplet $(2^+ \otimes 3^-)$. The fragmented strength observed in the odd isotopes ^{111,113}Cd is compared with the strength distributions in the neighboring even–even Cd isotopes. © *2001 MAIK "Nauka/Interperiodica"*.

1. MOTIVATION

Low-lying dipole excitations in heavy nuclei are an interesting and important field in modern nuclear structure physics. An outstanding example was the prediction [1] and the subsequent discovery [2] of the orbital $M1$ Scissors Mode in deformed nuclei in 1984, stimulating a large number of both experimental and theoretical works (for references see, e.g., recent reviews [3, 4]). On the other hand, also enhanced electric dipole excitations ($E1$) were expected and observed in heavy nuclei [3, 5]. In semimagic nuclei like the $N = 82$ isotones (see [6–12] and references therein) or the even–even Sn isotopes [13, 14], the corresponding 1^- states were interpreted as the spin 1 member of the $1^-, 2^-, \ldots, 5^-$ quintuplet due to a two-phonon coupling of the quadrupole and octupole phonons. So far, all these enhanced $E1$ excitations were mainly investigated in even–even nuclei. A topic of current interest is also the study of the fragmentation of these dipole modes in the neighboring odd-mass nuclei [15–18]. The coupling of an unpaired nucleon or hole to the even–even core should lead to a splitting of the dipole strength in odd-A nuclei.

In this contribution, we want to focus on strong $E1$ excitations in the medium-weight, spherical nuclei of the Cd isotopic chain ($Z = 48$), which are known as vibrational nuclei. The present systematic nuclear resonance fluorescence (NRF) experiments represent an ideal completion of extensive particle-induced reaction studies [19, 20] and our previous photon scattering experiments [21, 22] performed in the last years.

2. EXPERIMENTAL TECHNIQUES

2.1. Nuclear Resonance Fluorescence Method

Nuclear resonance fluorescence, photon scattering off bound nuclear states, has proven to be an outstanding tool to investigate low-lying dipole excitations in heavy nuclei and to provide detailed spectroscopic information. The low transfer of momentum of real photons gives rise to a high selectivity in exciting low-spin states (dipole transitions). The use of continuous bremsstrahlung radiation enables all states with $\Delta J = 0, \pm 1$ and with sufficient ground-state decay widths to be excited simultaneously.

The following quantities can be extracted in a completely model-independent way [3, 23]:

1. The excitation energies ($\Delta E \leq 1$ keV).

2. The ratio Γ_0^2/Γ (Γ_0 and Γ: ground-state and total decay widths, respectively). Reduced transition

---

[*] This article was submitted by the authors in English.

[1)] Institut für Kernphysik, Universität zu Köln, Germany.

[2)] Institut de Physique, Université de Fribourg, Switzerland.

[3)] Department of Chemistry, University of Kentucky, Lexington, USA.

[**] e-mail: `kohstall@ifs.physik.uni-stuttgart.de`

[***] Present address: Department of Physics, University of Liverpool, UK.

[****] Present address: WNSL, Yale University, New Haven, USA.

1063-7788/01/6406-1141$21.00 © 2001 MAIK "Nauka/Interperiodica"

probabilities $B(M1)\uparrow$ and $B(E1)\uparrow$, respectively, can be deduced if parities are known.

3. The spins J of the excited states (for even–even nuclei).

4. The branching ratios for the decay to lower lying excited states.

5. The parities of the excited states (for even–even nuclei).

The formalism describing NRF experiments is summarized in previous reviews (e.g., [3, 23]). From experiments using continuous electron bremsstrahlung as a photon source, the total scattering cross section $I_{s,f}$, integrated over one resonance and the full solid angle, can be extracted:

$$I_{s,f} = g\left(\pi\frac{\hbar c}{E_\gamma}\right)^2 \frac{\Gamma_0\Gamma_f}{\Gamma}. \quad (1)$$

Here, Γ_0, Γ_f, and Γ are the decay widths of the photoexcited state with spin J to the ground state, to a final lower lying state, and its total width, respectively. The statistical factor $g = (2J+1)/(2J_0+1)$ is called "spin factor." In the case of elastic scattering ($\Gamma_0 = \Gamma_f$), the scattering cross section is proportional to Γ_0^2/Γ. If the decay to other states can be observed or is known, the ground-state width Γ_0 and the total width Γ can be determined. Γ is connected to the lifetime τ of the excited level via the uncertainty relation: $\Gamma = \hbar/\tau$. The product $g\Gamma_0$, which can be directly extracted from the measured scattering intensities, is proportional to the reduced excitation probabilities $B(E1)\uparrow$ or $B(M1)\uparrow$:

$$B(\Pi 1)\uparrow = g\,B(\Pi 1)\downarrow = \frac{9}{16\pi}\left(\frac{\hbar c}{E_\gamma}\right)^3 (g\Gamma_0) \quad (2)$$

and in numerical form:

$$B(E1)\uparrow = 0.955\,\frac{g\Gamma_0}{E_\gamma^3}\,[10^{-3}e^2\,\mathrm{fm}^2], \quad (3)$$

$$B(M1)\uparrow = 0.0864\,\frac{g\Gamma_0}{E_\gamma^3}\,[\mu_N^2].$$

Here, the excitation energies E_x are in MeV and the ground-state transition widths Γ_0 in meV.

Unfortunately, in the case of odd-mass target nuclei, the angular distributions of the scattered photons are rather isotropic. Therefore, in general no unambiguous spin assignments to the photoexcited states are possible, and hence the spin factor g is not known. For the comparison with the strengths in even–even nuclei, one introduces the quantity $g\Gamma_0^{\mathrm{red}}$:

$$g\Gamma_0^{\mathrm{red}} = g\frac{\Gamma_0}{E_\gamma^3}, \quad (4)$$

which is proportional to the reduced dipole excitation probabilities [see (3)].

The spins of the excited states can be easily determined from the measured angular distributions in the case of even–even nuclei. Parities can be assigned model-independently from photon scattering experiments by measuring the linear polarization of the scattered photons using Compton polarimeters [3, 24] or by using linearly polarized bremsstrahlung [3, 23]. In the Stuttgart experiments, sectored single-crystal Ge Compton polarimeters have successfully operated for many years [24]. The parity information is obtained from the measured azimuthal asymmetry ε:

$$\varepsilon(E_\gamma) = \frac{N_\perp - N_\parallel}{N_\perp + N_\parallel} = P_\gamma Q(E_\gamma), \quad (5)$$

where $N_\perp$ and $N_\parallel$ represent the rates of Compton scattering events perpendicular and parallel to the NRF scattering plane defined by the directions of the photon beam and the scattered photons, respectively. The sign of the asymmetry ε, given by the product of the degree of polarization P_γ and the polarization sensitivity Q of the polarimeter device, determines the parity. The polarization sensitivity $Q(E_\gamma)$ of the Compton polarimeter arrangements (including its apparative asymmetries) can be determined experimentally using γ–γ cascades with known spins and mixing ratios or using photons of known linear polarization from appropriate $(p, p'\vec{\gamma})$ reactions [24]. For the Stuttgart polarimeters, the polarization sensitivity amounts to about 20% at a photon energy of about 0.5 MeV and decreases to about 10% at 4 MeV.

2.2. Experimental Setups at the Stuttgart Dynamitron

The NRF measurements reported on have been performed at the well-established bremsstrahlung facility of the Stuttgart Dynamitron accelerator [3], shown schematically in Fig. 1. The high-current DC electron beam (maximum current 4 mA; typical current 0.8 mA) with a maximum energy of 4.3 MeV is bent by 120° and focused on the bremsstrahlung radiator target. The excellent quality of the bremsstrahlung beam and the high flux of typically some 10^6 photons per keV per second for 3 MeV photons enable one to run NRF experiments at two different setups simultaneously. At the first NRF site, the scattered photons were detected now by three carefully shielded HPGe-γ spectrometers (efficiencies of 100% relative to a $3'' \times 3''$ NaI(Tl) detector) placed at scattering angles of about 90°, 127°, and 150° with respect to the incident beam. At the second site, two sectored single-crystal Ge-Compton polarimeters [24] are installed at slightly backward angles of $\approx 95°$ with respect to the photon beam measuring the linear polarization of the resonantly scattered photons. The sensitivity of the polarimeters could be increased considerably in the past by improving the response functions using a BGO anti-Compton shield [25]. An additional Ge-γ detector of modest relative efficiency ($\approx$40%) allows the measurement of angular distributions at this second site too and hence the simultaneous investigation of a second isotope. The NRF targets in the present experiments consisted of discs of highly enriched Cd material in quantities of some grams sandwiched by plates of aluminum allowing an absolute calibration of the incoming photon flux (see [26]).

3. RESULTS AND DISCUSSION

3.1. E1 Two-Phonon Excitations in the Even–Even Cd Isotopes

In Fig. 2, the very clean (γ, γ') spectra for ^{110,116}Cd are depicted in comparison with previously taken data for ^{112,114}Cd [21, 22]. The strong peaks marked by "^{27}Al" correspond to transitions in ^{27}Al used as photon flux standards. The lines at 2.614 MeV labeled with "^{208}Pb" are due to natural background radiation. The spectra look quite similar and are dominated by the marked strong $E1$ two-phonon excitations at excitation energies around 2.5 MeV.

The measured angular distributions clearly identified the strong excitations in all isotopes as dipole transitions. For two of the two-phonon excitations (in ^{110,116}Cd), the negative parity could be established by the present linear polarization measurements using the Compton polarimeters. This is shown in Fig. 3, where the azimuthal asymmetries ε of the transitions in ^{110}Cd are plotted versus the excitation energy. The result for the two-phonon excitation at 2.650 MeV is in excellent agreement with the negative value of ε as expected for $E1$ transitions (lower dashed line) and is more than six standard deviations off from the $M1$ expectation (positive ε values). The asymmetries for the nearly unpolarized ^{27}Al transitions agree with zero within two standard deviations, demonstrating the nearly perfect symmetry of the polarimeter. Negative parities for the candidates of the two-phonon excitations in ^{112,114}Cd are known from the literature and are or will be checked in polarization measurements at Stuttgart.

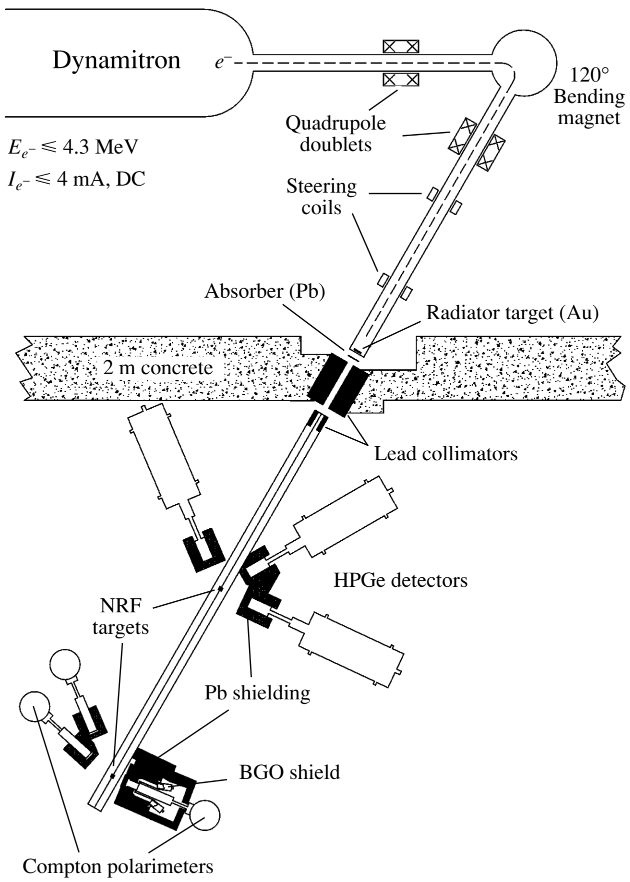

Fig. 1. Sketch of the bremsstrahlung facility and the photon scattering setups installed at the Stuttgart 4 MV Dynamitron accelerator.

Figure 4 summarizes the results for the two-phonon excitations in the even–even Cd isotopes obtained in the Stuttgart NRF experiments. For all investigated isotopes, all quantities are remarkably constant: the energies of the one-phonon excitations $E_x(2^+)$ and $E_x(3^-)$, of the two-phonon excitations $E_x(1^-)$, and the absolute excitation strengths $B(E1, 0^+ \to 1^-)$. Such a behavior, as expected for collective modes in nuclei of an isotopic chain without changes of the nuclear shapes, is reminiscent of the situation in the semimagic Sn isotopes [14].

The observed excitation energies $E_x(1^-)$ are very close to the sum $\sum$ of the one-phonon excitation energies $E_x(2^+)$ and $E_x(3^-)$ corresponding to a nearly completely harmonic coupling of the quadrupole and octupole vibrations. This nearly perfect agreement between the one-phonon sum energies $\sum$ and the two-phonon energies $E_x(1^-)$ is demonstrated in the upper panel of Fig. 4. The two-phonon anharmonicities are small and result in a minor lowering of the 1^- two-phonon states. The measured $B(E1)\!\uparrow$ values

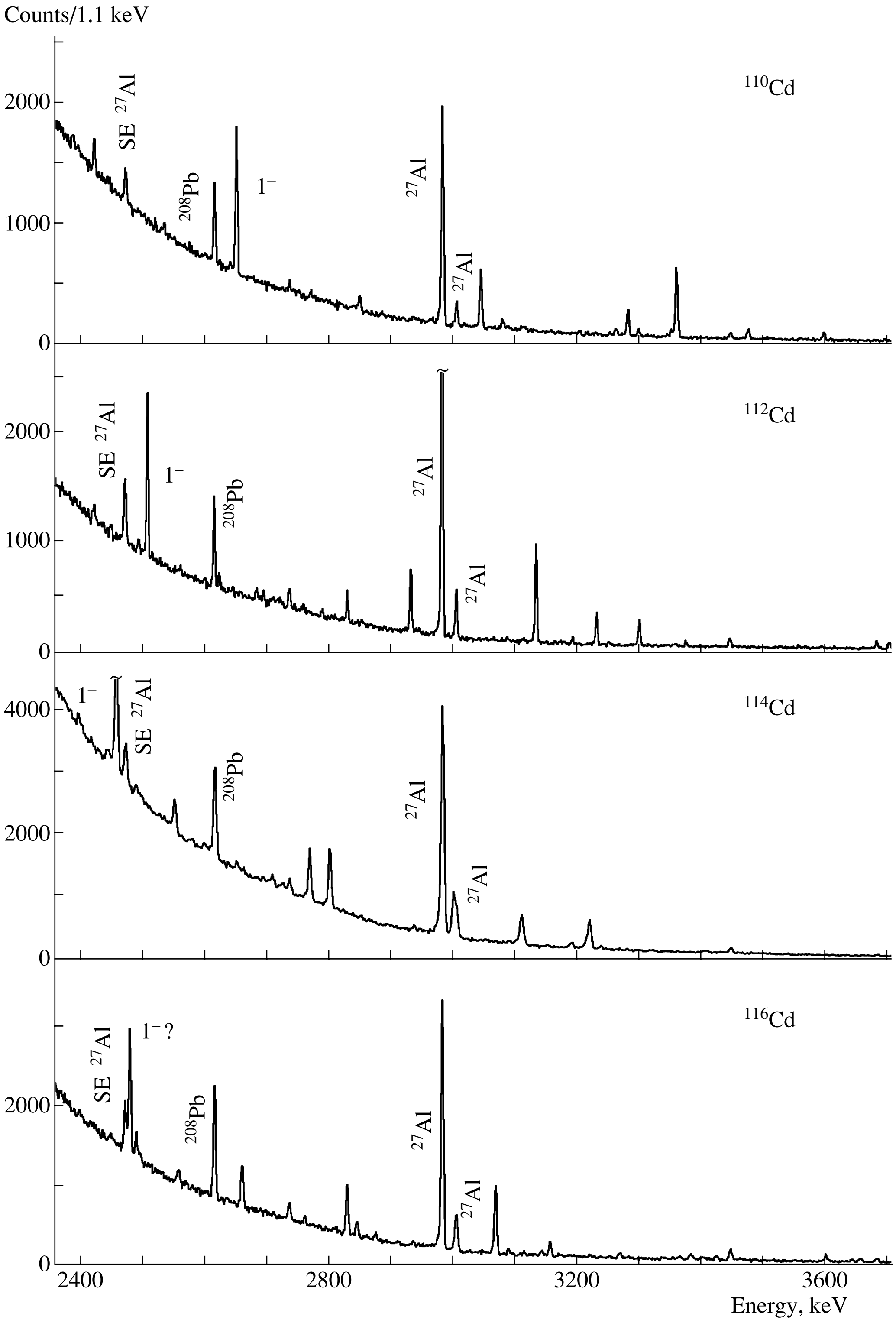

Fig. 2. NRF spectra for the even–even Cd isotopes ^{110,112,114,116}Cd measured in recent NRF studies at Stuttgart.

(see lower panel of Fig. 4; the analysis for ^{116}Cd is not yet completed) are also nearly constant. The absolute values of about $2\times10^{-3}\,e^2\,\mathrm{fm}^2$ are at least one order of magnitude larger than for other $E1$ transitions in neighboring nuclei. However, they are about a factor of three lower than those observed in the semimagic Sn isotopes [14].

So far, there is a lack of detailed calculations for these excitations in the Cd isotopes. Only for ^{112}Cd are calculations available performed in the framework

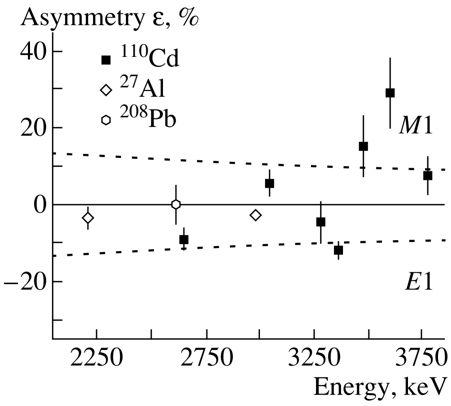

Fig. 3. Azimuthal asymmetries ε measured by the Compton polarimeter. Closed square symbols correspond to excitations in ^{110}Cd, and open symbols correspond to the nearly unpolarized transitions in ^{27}Al, which are used in addition for the absolute photon flux calibration [26].

of the *sdpf*-IBM model by Lehmann *et al.* [22]. They succeeded in reproducing quite well the excitation energies and transition strengths of the first four 1^- states in ^{112}Cd (see [22]).

3.2. Fragmentation of the Dipole Strength in the Odd-Mass Isotopes ^{111,113}Cd

In Fig. 5, the spectra for the odd-mass isotopes ^{111,113}Cd are compared with the spectrum for ^{112}Cd. Obviously, the strengths are strongly fragmented in the odd-mass isotopes as compared to the strength distribution in the even–even neighbor isotope ^{112}Cd.

A more quantitative comparison should be done in terms of reduced transition probabilities, as shown in Fig. 6. As can be seen, the dipole responses of the even–even Cd isotopes ^{112,114}Cd are rather similar, with respect to both the strength distributions and the total strengths. Also, in the odd nucleus ^{113}Cd, the strength seems to be concentrated in two bumps with a somewhat stronger fragmentation as is expected for an odd-mass nucleus. Furthermore, the two groups of excitations are shifted to lower energies. However, the experimentally detected total strength in ^{113}Cd ($\sum g\Gamma_0^{\text{red}} = 8.5 \pm 1.7$ meV/MeV^3) is reduced by a factor of roughly 1.5 as compared to the strengths observed in the neighboring even isotopes (^{112}Cd: 11.8 ± 0.8 meV/MeV^3; ^{114}Cd: 13.4 ± 2.0 meV/MeV^3). This reduction factor is less than that observed in deformed even–even and odd-mass Dy and Gd nuclei [27, 28]. For the deformed odd-mass rare earth nuclei, a recent statistical fluctuation analysis [29, 30] of the corresponding NRF spectra demonstrated that a considerable part of the total dipole strengths in these odd-mass nuclei, the missing strengths as compared to the even–even

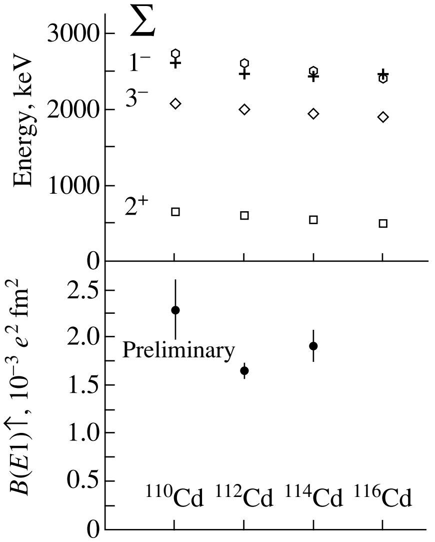

Fig. 4. Upper part: Energies of the 2_1^+ (open squares) and 3_1^- (open diamonds) one-phonon states and the 1^- (crosses) two-phonon states in ^{110,112,114,116}Cd compared to the expected sum energies $\sum = E_{2^+} + E_{3^-}$ (open hexagons). Lower part: Preliminary $B(E1)\uparrow$ values for the two-phonon excitations.

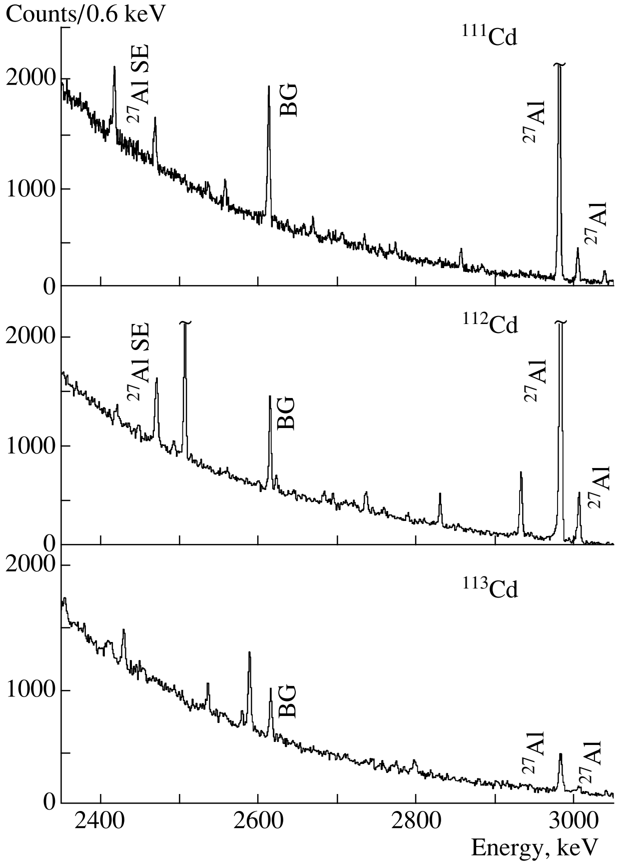

Fig. 5. Comparison of (γ,γ') spectra for even- and odd-mass Cd isotopes.

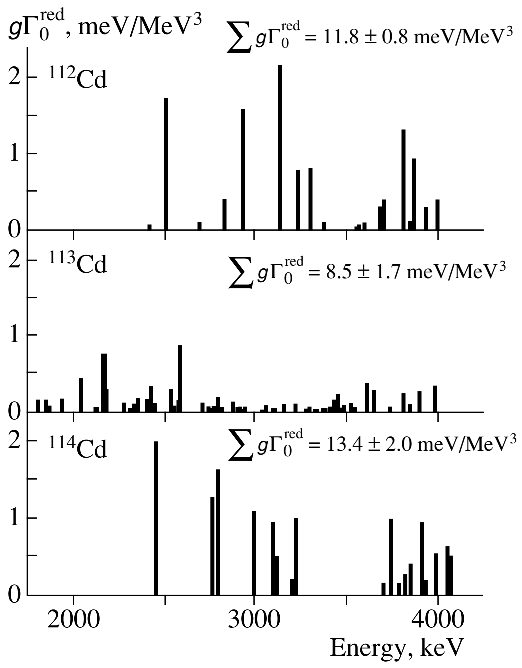

Fig. 6. Comparison between the dipole transition strengths for the even- and odd-mass Cd isotopes ^{112,113,114}Cd. Plotted are the products of the spin factor g and the reduced ground-state transition widths Γ_0^{red} as a function of the excitation energy [22].

neighboring isotopes, is hidden in the continuous background due to a strong fragmentation. The reason for this fragmentation is the diverse coupling possibilities of the single unpaired nucleon to the collective excitations the even–even cores.

ACKNOWLEDGMENTS

Thanks are due to L.E. Kazakov for providing the enriched Cd samples. The support by the Deutsche Forschungsgemeinschaft under contracts Kn 154/30 and Br 799/6 is gratefully acknowledged.

REFERENCES

1. N. Lo Iudice *et al.,* Phys. Rev. Lett. **41**, 1532 (1978).
2. D. Bohle *et al.,* Phys. Lett. B **137**, 27 (1984).
3. U. Kneissl *et al.,* Prog. Part. Nucl. Phys. **37**, 349 (1996).
4. A. Richter, Prog. Part. Nucl. Phys. **34**, 261 (1995).
5. C. Fransen *et al.,* Phys. Rev. C **57**, 129 (1998).
6. F. R. Metzger, Phys. Rev. C **14**, 543 (1976).
7. F. R. Metzger, Phys. Rev. C **18**, 1603 (1978).
8. R.-D. Herzberg *et al.,* Nucl. Phys. A **592**, 211 (1995).
9. T. Belgya *et al.,* Phys. Rev. C **52**, R2314 (1995).
10. M. Wilhelm *et al.,* Phys. Rev. C **54**, R449 (1996).
11. M. Grinberg *et al.,* Nucl. Phys. A **573**, 231 (1994).
12. K. Heyde *et al.,* Phys. Lett. B **393**, 7 (1997).
13. K. Govaert *et al.,* Phys. Lett. B **335**, 113 (1994).
14. J. Bryssinck *et al.,* Phys. Rev. C **59**, 1930 (1999).
15. A. Zilges *et al.,* Phys. Rev. Lett. **70**, 2880 (1993).
16. R.-D. Herzberg *et al.,* Phys. Rev. C **51**, 1226 (1995).
17. V. Yu. Ponomarev *et al.,* Phys. Rev. Lett. **83**, 4029 (1999).
18. J. Bryssinck *et al.,* Phys. Rev. C **62**, 014309 (2000).
19. M. Déléze *et al.,* Nucl. Phys. A **554**, 1 (1993).
20. S. E. Drissi *et al.,* Nucl. Phys. A **614**, 137 (1997).
21. W. Geiger *et al.,* Nucl. Phys. A **580**, 263 (1994).
22. H. Lehmann *et al.,* Phys. Rev. C **60**, 024308 (1999).
23. U. E. P. Berg *et al.,* Annu. Rev. Nucl. Part. Sci. **37**, 33 (1987).
24. B. Schlitt *et al.,* Nucl. Instrum. Methods Phys. Res. A **337**, 416 (1994).
25. H. Maser *et al.,* Phys. Rev. C **53**, 2749 (1996).
26. N. Pietralla *et al.,* Phys. Rev. C **51**, 1021 (1995).
27. J. Margraf *et al.,* Phys. Rev. C **52**, 2429 (1995).
28. A. Nord *et al.,* Phys. Rev. C **54**, 2287 (1996).
29. J. Enders *et al.,* Phys. Rev. Lett. **79**, 2010 (1997).
30. J. Enders *et al.,* Phys. Rev. C **57**, 996 (1998).

Physics of Atomic Nuclei, Vol. 64, No. 6, 2001, pp. 1147–1151. From Yadernaya Fizika, Vol. 64, No. 6, 2001, pp. 1223–1227.
Original English Text Copyright © 2001 by Stoyanov, Lo Iudice, Tsoneva, Grinberg.

Properties of the Low-Lying Excited States in Even–Even Nuclei around the Closed Shell $N = 82$*

Ch. Stoyanov**, **N. Lo Iudice**[1)], **N. Tsoneva**, and **M. Grinberg**

Institute for Nuclear Research and Nuclear Energy, Sofia, Bulgaria

Received October 25, 2000

Abstract—The properties of low-lying states in ^{136}Ba and ^{144}Nd are calculated within the quasiparticle phonon model. It is shown that the strong quadrupole interaction in the particle–particle channel leads to the appearance of low-lying isovector excitations. Due to this reason, there are two branches in the low-lying part of the spectrum, an isoscalar and an isovector one. Both branches show peculiar regularities of $E2$ and $M1$ transitions. © *2001 MAIK "Nauka/Interperiodica"*.

The nuclei around closed shell $N = 82$ have been an object of intensive study in recent years. In this region, the collectivity and the energy of the low-lying excitations change considerably with A. This permits one to establish a close correlation of the simple modes (collective and noncollective) with the detailed structure of the low-lying excited states. By means of photon scattering experiments, a large body of experimental information about low-lying dipole transitions ($E1$ and $M1$) in nuclei around $N = 82$ has been collected [1, 2]. It has been shown that the first 1^- state in even–even nuclei is predominantly a two-phonon member of a quadrupole–octupole multiplet. The excitation energy of the 1^- state and the corresponding $B(E1)$ value are described quite well within the quasiparticle–phonon model (QPM) [3, 4]. The experimental information about the structure of the low-lying states is completed by means of $(n, n'\gamma)$ reaction [5] and lifetime measurements [6]. The structure of low-lying 1^+ states is of great interest since the $M1$ transitions reveal the isovector character of the low-lying states. They appear as a scissors mode in deformed nuclei [7] and are classified as mixed-symmetry states within the neutron–proton version of the interacting boson model (IBM-2) [8, 9]. The structure of the 1^+ states in ^{94}Mo is calculated within the QPM, and the results are presented in [10]. It is shown that the 1^+_1 is a two-phonon state, where the isoscalar 2^+ phonon is coupled with the isovector one. In [10], it is also found that the same component dominates in the structure of the 3^+ and some 2^+ excited states. In the low-lying spectrum of ^{94}Mo, there are two branches. The isoscalar branch includes one- and two-phonon states constructed by the isoscalar 2^+ phonon. Another branch is based on the isovector 2^+ phonon. The strong $E2$ transitions connect the states within each branch, while the strong $M1$ transitions connect the states belonging to different branches.

In the present study, we have used the QPM to calculate the properties of the low-lying states around the closed shell $N = 82$. The structure of the excited states in $N = 80$ (^{136}Ba) and $N = 84$ (^{144}Nd) nuclei and $E2$ and $M1$ transition probabilities have been calculated. The available experimental information has been analyzed, and the properties of the low-lying isovector quadrupole excitations have been discussed.

The most general form of the QPM Hamiltonian is [11]

$$H = H_{\rm av} + H_{\rm pair} + H_M^{\rm ph} + H_{\rm SM}^{\rm ph} + H_M^{\rm pp}. \quad (1)$$

The term $H_{\rm av}$ is the Woods–Saxon potential, $H_{\rm pair}$ represents the monopole pairing interaction, $H_M^{\rm ph}$ stands for the separable multipole–multipole interaction in the particle–hole channel, $H_{\rm SM}^{\rm ph}$ is the separable spin–multipole interaction in the particle–hole channel, and $H_M^{\rm pp}$ stands for the residual interaction in the particle–particle channel.

The first step in QPM is to construct the phonon basis and to express the Hamiltonian (1) in terms of phonons. The phonon operator has the form

$$Q^+_{\lambda\mu i} = \frac{1}{2}\sum_{jj'}\Big\{\psi^{\lambda i}_{jj'}A^+(jj';\lambda\mu) - (-1)^{\lambda-\mu}\phi^{\lambda i}_{jj'}A(jj';\lambda-\mu)\Big\}, \quad (2)$$

---

*This article was submitted by the authors in English.

[1)] Dipartimento di Scienze Fisiche, Università di Napoli Federico II, and INFN, Sezione di Napoli, Italia.

**e-mail: `stoyanov@inrne.bas.bg`

where $A^+(jj';\lambda\mu)$ and $A(jj';\lambda-\mu)$ are two-quasiparticle creation and annihilation operators, respectively, coupled to momentum λ. The energy of the phonons and the amplitudes ψ and ϕ are found by solving the RPA equations.

The Hamiltonian (1) is diagonalized in the model space, where the model wave function of an excited state in even-even nuclei with angular momentum J and projection M includes one-, two-, and three-phonon components. It reads

$$\Psi_\nu(JM) = \Bigg\{\sum_i R_i(J\nu)Q^+_{JMi} + \sum_{\lambda_1 i_1\lambda_2 i_2} P^{\lambda_1 i_1}_{\lambda_2 i_2}(J\nu)\left[Q^+_{\lambda_1\mu_1 i_1}Q^+_{\lambda_2\mu_2 i_2}\right]_{JM} \tag{3}$$

$$+ \sum_{\lambda_1 i_1\lambda_2 i_2\lambda_3 i_3 I} T^{\lambda_1 i_1\,\lambda_2 i_2}_{I\quad\;\lambda_3 i_3}(J\nu)\left[\left[Q^+_{\lambda_1\mu_1 i_1}Q^+_{\lambda_2\mu_2 i_2}\right]_{Ik}Q^+_{\lambda_3\mu_3 i_3}\right]_{JM}\Bigg\}\Psi_0,$$

where $[\ldots]_{JM}$ stands for angular momentum coupling, Ψ_0 represents the phonon vacuum state, and R, P, and T are unknown amplitudes. To ensure a proper antisymmetrization, the norm of the wave function and the necessary matrix elements are calculated using the exact commutation relations of the phonons taking into account their fermion structure [11]. The wave function (3) has been successfully used to calculate the structure of the excited states in the $N = 82$, 84 even–even nuclei [3, 4, 12].

In the present calculations the parameters of the Woods–Saxon potential are taken from [13, 14]. The corresponding single-particle spectra for the $A = 140$ region can be found in [15]. The radial component of the multipole field entering into the particle–hole and particle–particle separable interaction is $f(r) = dU(r)/dr$, where $U(r)$ is the central part of the Woods–Saxon potential. The strengths $\kappa^{(2)}$ and $\kappa^{(3)}$ of the quadrupole–quadrupole and octupole–octupole particle–hole interaction were fixed by a fit to the energies of the first 2^+ and 3^- states. The strengths $\kappa^{(\lambda)}$ of the other multipole terms are adjusted according to the prescription of [11]. The interaction in the particle–particle channel is important only in the quadrupole term. We have used as strength parameter in this channel $G^{(2)} = G^{(2)}_{nn} = G^{(2)}_{pp}$ and $G^{(2)}_{np} = 0$. The value of $G^{(2)}$ will be discussed below. The phonons with multipolarity $1^\pm, 2^+, 3^-, 4^+, 5^-$ are used in the calculations.

The most important states in the RPA basis are the first and second 2^+ states. The first $[2^+]_{\mathrm{RPA}}$ state is an isoscalar one. The properties of the state depend mainly on the value of $\kappa_0^{(2)}$, the isoscalar quadrupole strength parameter. The properties of the second $[2^+]_{\mathrm{RPA}}$ state are very sensitive to the ratio $G^{(2)}/\kappa_0^{(2)}$. The increase in this ratio enhances the collectivity of the $[2_2^+]_{\mathrm{RPA}}$ and changes the nature of the state from isoscalar to isovector. It is shown in [16] that the relevant quantity for checking the nature of an RPA phonon is the ratio

$$B(2_i^+) = \frac{|\langle 2_i^+\|\sum_k^p r_k^2 Y_{2\mu}(\Omega k) - \sum_k^n r_k^2 Y_{2\mu}(\Omega k)\|\mathrm{g.s.}\rangle|^2}{|\langle 2_i^+\|\sum_k^p r_k^2 Y_{2\mu}(\Omega k) + \sum_k^n r_k^2 Y_{2\mu}(\Omega k)\|\mathrm{g.s.}\rangle|^2}. \tag{4}$$

If $B(2_i^+) > 1$, the 2^+ state under consideration is an isovector state, otherwise it is isoscalar.

The dependence of the properties of $[2_2^+]_{\mathrm{RPA}}$ on the ratio $G^{(2)}/\kappa_0^{(2)}$ is shown in Table 1. It is seen that when the ratio $G^{(2)}/\kappa_0^{(2)}$ increases the $B(E2;\mathrm{g.s.}\to[2_2^+]_{\mathrm{RPA}})$ increases too, i.e., the collectivity of $[2_2^+]_{\mathrm{RPA}}$ becomes larger. Also, the $M1$ transition strength between the $[2_2^+]_{\mathrm{RPA}}$ and the $[2_1^+]_{\mathrm{RPA}}$ states increases. The value of $B(2_i^+)$, (4), changes dramatically, indicating that the nature of the $[2_2^+]_{\mathrm{RPA}}$ varies from isoscalar to isovector. Another quantitative check of the nature of $[2_i^+]_{\mathrm{RPA}}$ states is the relative signs of the neutron and proton amplitudes ψ (2). The structure of the first two $[2^+]_{\mathrm{RPA}}$ phonons is shown in Table 2 for ^{136}Ba. It is seen that, while in the case of $[2_1^+]_{\mathrm{RPA}}$ the main components are in phase, in $[2_2^+]_{\mathrm{RPA}}$ the relative sign of the main components has changed and the amplitudes ψ are in opposition of phases. Table 2 illustrates that at an appropriate value of the ratio $G^{(2)}/\kappa_0^{(2)}$ the RPA basis

Table 1. The dependence of $M1$ and $E2$ transitions on the ratio $G^{(2)}/\kappa_0^{(2)}$ in ^{136}Ba

$G^{(2)}/\kappa_0^{(2)}$	$B(E2;\,0_1^+ \to 2_2^+)_{\rm RPA}$, $e^2\,{\rm b}^2$	$B(M1;\,2_2^+ \to 2_1^+)_{\rm RPA}$, μ_N^2	$B(2_2^+)$
0	0.0009	0.042	0.73
0.779	0.010	0.208	14.57
0.847	0.011	0.223	16.42

Table 2. Structure of the first RPA phonons (only the largest components are given) and values of $B(2_i^+)$ [see (4)] for ^{136}Ba

λ_i^π	$w_{\lambda_i^\pi}$, MeV	Structure	$B(E2)\uparrow$, $e^2\,{\rm b}^2$	$B(2_i^+)$
2_1^+	0.940	$0.76(1h_{11/2})_n^2 + 0.68(2g_{7/2})_p^2$ $0.24(3s_{1/2}2d_{3/2})_n + 0.43(2d_{5/2})_p^2$ $0.31(2d_{3/2})_n^2 + 0.39(1g_{7/2}2d_{3/2})_p^2$	0.370	0.00003
2_2^+	1.997	$0.88(1h_{11/2})_n^2 - 0.92(1g_{7/2})_p^2$ $0.38(2d_{3/2})_n^2 - 0.24(2d_{5/2})_p^2$ $0.22(3s_{1/2}2d_{3/2})_n - 0.14(1h_{11/2})_p^2$	0.011	16.4

used contains a collective isoscalar $[2_1^+]_{\rm RPA}$ and a slightly collective isovector $[2_2^+]_{\rm RPA}$ state. The states are connected with a relatively large $M1$ transition. This property of the basis is in agreement with the IBM-2. In this model, the first $[2_1^+]_{\rm RPA}$ is symmetric with respect to the exchange of protons and neutrons, i.e., F spin symmetric. The second $[2_2^+]_{\rm RPA}$ is a mixed symmetry state according to F spin. The required property of the RPA basis determines the value of $G^{(2)} = (0.8\text{–}0.9)\kappa_0^{(2)}$.

To proceed with the QPM eigenvalue problem, the Hamiltonian (1) is diagonalized in the multiphonon basis (3).

The energy and the structure of several 1^+ and 2^+ states are given in Table 3 for ^{136}Ba and Table 4 for ^{144}Nd. Well-pronounced components dominate in the structure of the states. Except for a few states, the main component exhausts more than 80% of the norm of the wave function. Due to the dominance of the main component, the states could be separated into two branches. In ^{136}Ba, the first and second 2^+ states are members of the isoscalar branch, while the 2_3^+, 1^+, and 2_9^+ states are members of the branch based on the isovector $[2_2^+]_{\rm RPA}$ phonon-isovector branch [10]. In ^{144}Nd, the $[2_2^+]_{\rm RPA}$ component and the two-phonon $[2_1^+ \otimes 2_1^+]_{\rm RPA}$ are fragmented over the 2_2^+ and 2_3^+ states. These therefore qualify as mixed (isoscalar and isovector) states, while the 2_1^+ state appears as fully symmetric (isoscalar).

The reduced transition probabilities are shown in Tables 5 and 6. Large $E2$ transitions connect members of the isoscalar branch (g.s. $\to 2_1^+$) and ($2_2^+ \to 2_1^+$). The calculated $B(E2;\,{\rm g.s.} \to 2_2^+)$ value is close to the experimental value in ^{144}Nd, while it is much larger than the experimental one in ^{136}Ba. The reason is that the anharmonicity in ^{136}Ba is larger and the contribution of the $[2_1^+]_{\rm RPA}$ component in the structure of the 2_2^+ state is too large (more than 10%). The value of $B(E2;\,2_2^+ \to 2_1^+)$ in ^{136}Ba agrees with the experimental one, which implies that the

Table 3. Structure and energy of several low-lying states in ^{136}Ba (only the main component is given)

State	Energy, keV		Structure
	Exp.	QPM	
1_1^+	2694	2772	81.7% $[2_1^+ \otimes 2_2^+]_{\rm RPA}$
2_1^+	813	727	80.4% $[2_1^+]_{\rm RPA}$
2_2^+	1551	1653	54.2% $[2_1^+ \otimes 2_1^+]_{\rm RPA}$
2_3^+	2129	1951	88.2% $[2_2^+]_{\rm RPA}$
2_9^+	–	3007	57.7% $[2_1^+ \otimes 2_2^+]_{\rm RPA}$

Table 4. Structure and energy of several low-lying states in ^{144}Nd (only the main components are given)

State	Energy, keV		Structure
	exp.	QPM	
1_1^+	2656	2895	$99\%[2_1^+ \otimes 2_2^+]_{\text{RPA}}$
2_1^+	678	744	$92\%[2_1^+]_{\text{RPA}}$
2_2^+	1561	1674	$69\%[2_1^+ \otimes 2_1^+]_{\text{RPA}}$
2_3^+	2073	1948	$69\%[2_2^+]_{\text{RPA}}$
2_8^+	–	2936	$46\%\ [2_1^+ \otimes 2_2^+]_{\text{RPA}}$

54% contribution of the component $[2_1^+ \otimes 2_1^+]_{\text{RPA}}$ to the norm of the 2_2^+ state (see Table 3) is a realistic one. Another set of large $B(E2)$ values is between the members of the isovector branch—$B(E2;\ 1_1^+ \to 2_3^+)$; $B(E2;\ 2_9^+ \to 2_3^+)$(^{136}Ba); $B(E2;\ 2_8^+ \to 2_3^+)$(^{144}Nd). It is seen from Table 5 that the $E2$ transitions connecting members of different branches are small—$B(E2;\ 1_1^+ \to 2_1^+)$; $B(E2;\ 1_1^+ \to 2_2^+)$; $B(E2;\ 2_3^+ \to 2_1^+)$.

The $M1$ transitions are shown in Table 6. Following the foregoing discussion, one has to expect large $M1$ transition between members of different branches, while inside each branch the $M1$ transitions are small. The results presented in Table 6 confirm such a statement. The values $B(M1;\text{g.s.} \to 1_1^+)$, $B(M1;\ 2_3^+ \to 2_1^+)$, $B(M1;\ 1_1^+ \to 2_2^+)$, etc., are large, while the value $B(M1;\ 1_1^+ \to 2_3^+)$ is small in ^{136}Ba. In ^{144}Nd, because of the fragmentation of the two-phonon and isovector $[2_2^+]_{\text{RPA}}$ components, the $M1$ transition strength connecting $[2_1^+]_{\text{RPA}}$ and $[2_2^+]_{\text{RPA}}$ states is shared between two transitions $2_2^+ \to 2_1^+$ and $2_3^+ \to 2_1^+$. This is confirmed by the experiment [17]. For the same reason, the value $B(M1; 1_1^+ \to 2_3^+)$ is large in ^{144}Nd. The $B(M1)$ values are calculated using the quenching factor $g_s = 0.7$. The contribution of the orbital part in $B(M1)$ value is estimated to be more than 70% for ^{144}Nd.

Table 5. $B(E2)$ values calculated in QPM for ^{136}Ba and ^{144}Nd. (The experimental data are taken from [1, 2, 5, 6, 17]. The notation $2^+_{[2_1^+ \otimes 2_2^+]}$ means 2_9^+ state in ^{136}Ba and 2_8^+ state in ^{144}Nd)

Transition $[e^2\ \text{b}^2]$	Mult.	^{136}Ba		^{144}Nd	
		exp.	QPM	exp.	QPM
$1_1^+ \to 2_1^+$	$E2$	–	0.0015	–	0.0043
$1_1^+ \to 2_2^+$	$E2$	–	0.0008	–	0.021
$1_1^+ \to 2_3^+$	$E2$	–	0.097	–	0.061
$0_1^+ \to 2_1^+$	$E2$	0.400(5)	0.428	0.540	0.413
$0_1^+ \to 2_2^+$	$E2$	0.016(4)	0.09	0.005(1)	0.0045
$0_1^+ \to 2_3^+$	$E2$	0.045(5)	0.017	0.023	0.035
$2_2^+ \to 2_1^+$	$E2$	0.09(4)	0.083	0.095(21)	0.15
$2_3^+ \to 2_1^+$	$E2$	–	0.0055	0.02(1)	0.04
$2^+_{[2_1^+ \otimes 2_2^+]} \to 2_1^+$	$E2$	–	0.0002	–	0.004
$2^+_{[2_1^+ \otimes 2_2^+]} \to 2_3^+$	$E2$	–	0.04	–	0.057

The strength of the component $[[2_1^+ \otimes 2_2^+]_{2^+}]_{\text{RPA}}$, member of the isovector branch, is distributed over several 2^+ states. Its maximal value is around 50% in the 2_9^+ state in ^{136}Ba (Table 3) and 2_8^+ state in ^{144}Nd (Table 4). It means that even in the schematic calculations presented in the paper the quadrupole part of the scissors branch is strongly hindered. For example, the value of $M1$ transition connecting 2_9^+ and 2_2^+ states in ^{136}Ba is much less than the value of $B(M1;\ 1_1^+ \to 2_2^+)$. The same result is found in ^{144}Nd (see Table 6). Because of that, it seems difficult to detect experimentally this branch of the scissors mode.

The calculation of the structure of low-lying states in $N = 80$ ^{136}Ba and $N = 84$ ^{144}Nd reveals that there are two simple modes in the quadrupole excitations, an isoscalar and an isovector one. The properties of these two modes are very close to the ones proposed as symmetric and mixed-symmetry states in IBM-2. The coupling of isoscalar and isovector states leads to a variety of excited states connected by specific values

Table 6. $B(M1)$ values calculated in QPM for ^{136}Ba and ^{144}Nd with $g_s = 0.7$. (The experimental data are taken from [1, 2, 5, 6, 17]. The notation $2^+_{[2_1^+ \otimes 2_2^+]}$ means 2_9^+ state in ^{136}Ba and 2_8^+ state in ^{144}Nd)

Transition $[\mu_N^2]$	Mult.	^{136}Ba		^{144}Nd	
		exp.	QPM	exp.	QPM
$2_2^+ \to 2_1^+$	$M1$	–	0.007	0.11	0.10
$2_3^+ \to 2_1^+$	$M1$	0.26(3)	0.24	0.14(0.04)	0.39
$0_1^+ \to 1_1^+$	$M1$	0.13(2)	0.17	–	0.24
$1_1^+ \to 2_2^+$	$M1$	0.6(1)	0.20	–	0.52
$1_1^+ \to 2_3^+$	$M1$	–	0.01	–	0.18
$2^+_{[2_1^+ \otimes 2_2^+]} \to 2_1^+$	$M1$	–	0.013	–	0.004
$2^+_{[2_1^+ \otimes 2_2^+]} \to 2_2^+$	$M1$	–	0.081	–	0.125
$2^+_{[2_1^+ \otimes 2_2^+]} \to 2_3^+$	$M1$	–	0.001	–	0.047

of $M1$ and $E2$ transitions. We have calculated only the properties of 2^+ and 1^+ states. It is interesting to complete the study by calculating the structure of 3^+ and 4^+excited states and the corresponding $E2$ and $M1$ transitions.

ACKNOWLEDGMENTS

The present work was supported in part by the Bulgarian Science Foundation (contract Ph. 801).

REFERENCES

1. M. Kneissl, H. H. Pitz, and H. Zilges, Prog. Part. Nucl. Phys. **37**, 349 (1996).
2. N. Pietralla *et al.*, Phys. Rev. C **58**, 796 (1998).
3. M. Grinberg and Ch. Stoyanov, Nucl. Phys. A **573**, 231 (1994).
4. V. Yu. Ponomarev, Ch. Stoyanov, N. Tsoneva, and M. Grinberg, Nucl. Phys. A **635**, 470 (1998).
5. S. F. Hicks, C. M. Davoren, W. M. Faulkner, and J. R. Vanhoy, Phys. Rev. C **57**, 2264 (1998).
6. S. J. Robinson, M. M. Hindi, H. G. Borner, *et al.*, Phys. Lett. B **465**, 61 (1999).
7. N. Lo Iudice and F. Palumbo, Phys. Rev. Lett. **41**, 1532 (1978).
8. T. Otsuka, A. Arima, and F. Iachello, Nucl. Phys. A **309**, 1 (1978).
9. F. Iachello, Phys. Rev. Lett. **53**, 1427 (1984).
10. N. Lo Iudice and Ch. Stoyanov, Phys. Rev. C **62**, 047302 (2000).
11. V. G. Soloviev, *Theory of Atomic Nuclei: Quasiparticles and Phonons* (Institute of Physics Publ., Bristol, 1992).
12. Thai Khac Dinh, M. Grinberg, and Ch. Stoyanov, J. Phys. G **18**, 329 (1992).
13. V. A. Chepurnov, Yad. Fiz. **6**, 955 (1967).
14. K. Takeuchi and P. A. Moldauer, Phys. Lett. B **28**, 384 (1969).
15. S. Galès, Ch. Stoyanov, and A. I. Vdovin, Phys. Rep. **166**, 127 (1988).
16. R. Nikolaeva, Ch. Stoyanov, and A. I. Vdovin, Europhys. Lett. **8**, 117 (1989).
17. J. Copnell, S. Robinson, *et al.*, Phys. Lett. B **222**, 1 (1989).

Physics of Atomic Nuclei, Vol. 64, No. 6, 2001, pp. 1152–1156. From Yadernaya Fizika, Vol. 64, No. 6, 2001, pp. 1228–1232.
Original English Text Copyright © 2001 by Majling, Batusov.

Spectroscopy of the Λ Hypernuclei: New Problems and Prospects[*]

L. Majling[**] and **Yu. A. Batusov**[1)]

Nuclear Physics Institute, Academy of Sciences of the Czech Republic

Received October 25, 2000

Abstract—Nonmesonic weak decays of hypernuclei are analyzed. One peculiar case—decay of $A = 10$ hypernuclei—which can resolve the puzzle of the ratio Γ_n/Γ_p (neutron stimulated to proton stimulated rates) is discussed. *© 2001 MAIK "Nauka/Interperiodica".*

1. INTRODUCTION

We dedicate this contribution to the memory of V.G. Soloviev, the leader of the nuclear structure department of BLTP, where our international group (R. Eramzhyan, V. Fetisov, M. Gmitro, M. Kirchbach, R. Mach, L. Majling, R. Wünsch, and J. Žofka) was formed to solve the problems of interactions of μ, π, and K mesons with light nuclei. It was quite natural that, as soon as the brilliant idea of Podgoretsky [1] was confirmed at CERN [2] and physics of hypernuclei was transformed into a fundamental area of intermediate-energy nuclear physics [3], it attracted our interest as well [4].

The study of hypernuclei presents many facets of interest: production of hypernuclei in various reactions [the strangeness exchange $n(K^-, \pi^-)\Lambda$ or associative $n(\pi^+, K^+)\Lambda$]; baryonic decay (production of hyperfragments); emission of γ rays. The purpose of our contribution is to analyze the characteristics of hyperon weak decay in a nuclear medium [5, 6].

2. WEAK DECAYS OF HYPERNUCLEI: EFFECTIVE INTERACTION

Hypernuclei are a convenient laboratory to study the baryon—baryon weak interaction and an associated effective weak Hamiltonian. The strangeness-changing process in which a Λ hyperon converts to a neutron with the release of up to 176 MeV provides a clear signal for the conversion of an s quark to an u or d quark. The effective operator generally employed to analyze $\Delta S = 1$ nonleptonic interactions has the form [7]

$$H_{\Delta S=1} = \frac{1}{2} G_{\mathrm{F}} \sin\theta_w \cos\theta_w \sum_i^6 c_i O_i, \qquad (1)$$

where θ_w is the weak angle, and O_i are the four-quark operators describing lowest order W-boson-exchange diagrams, gluon radiative correction, and also "penguin" diagrams. The coefficients c_i are obtained as solutions of renormalization group equations.

Two experimental features of baryonic $|\Delta S = 1|$ decays are noteworthy:

(i) The empirical $\Delta I = 1/2$ rule: amplitude $(\Delta I = 1/2) \simeq 20$ amplitude $(\Delta I = 3/2)$;

(ii) Γ(nonleptonic) $\simeq 400\,\Gamma$ (semileptonic).

The weak interaction at the quark level is short-ranged, involving W, Z exchange. However, because of the core repulsion, the baryon—baryon effects are modeled in terms of one-meson-exchange interaction, all pseudoscalar (π, η, K) and vector (ρ, ω, K^*) meson exchanges included. The evaluation of the weak baryon—baryon—meson vertices is quark-model-based, but presented in terms of the symmetry $SU(6)_w$ [8, 9].

The properties of the free Λ hyperon are familiar [10]: it decays nearly 100% via the nonleptonic mode $\Lambda \to N + \pi$:

$$\tau = 1/\Gamma_\Lambda = 2.63 \times 10^{-10}\ \mathrm{s};$$
$$\Gamma^{\pi^-}/\Gamma_\Lambda = 0.639, \qquad (2)$$
$$\Gamma^{\pi^0}/\Gamma_\Lambda = 0.358.$$

Table 1. Momentum and kinetic energy of the final nucleon in various modes

Γ^i		Q, MeV	p, MeV/c	T_N, MeV
Γ^{π^-}	$\Lambda \to p + \pi^-$	$38 - (B_\Lambda - B_p)$	$\simeq$100	$\simeq$5
Γ^{π^0}	$\Lambda \to n + \pi^0$	$41 - (B_\Lambda - B_n)$	$\simeq$100	$\simeq$5
Γ^p	$\Lambda + p \to n + p$	$177 - (B_\Lambda + B_p)$	$\simeq$400	$\simeq$88
Γ^n	$\Lambda + n \to n + n$	$177 - (B_\Lambda + B_n)$	$\simeq$400	$\simeq$88

---

[*] This article was submitted by the authors in English.

[1)] Laboratory of Nuclear Problems, JINR, Dubna, Russia.

[**] e-mail: `majling@ujf.cas.cz`

1063-7788/01/6406-1152$21.00 © 2001 MAIK "Nauka/Interperiodica"

Table 2. Summary of the hypernuclear lifetimes

${}^{A}_{\Lambda}Z$	Measured			Calculated τ, ps		
	Ref.	production	τ, ps	[13]	[14]	[15]
Λ	[10]		263			
${}^{3}_{\Lambda}$H	[16]	Rel. ion	240^{+170}_{-100}			
${}^{4}_{\Lambda}$H	[17]	Rel. ion	220^{+50}_{-40}			
	[18]	(K^-, π)	194^{+24}_{-26}			
${}^{4}_{\Lambda}$He	[19]	(K^-, π)	256 ± 27			
	[12]	(K^-, π)	246 ± 27			
${}^{5}_{\Lambda}$He	[20]	(K^-, π)	256 ± 21	263		
(${}^{9}_{\Lambda}$Be)	[21]	(K^-, π)	201 ± 30			
${}^{11}_{\Lambda}$B	[21]	(K^-, π)	192 ± 22			
${}^{12}_{\Lambda}$C	[21]	(K^-, π)	211 ± 31	206	129	214
	[11]	(π^+, K^+)	231 ± 15			
(${}^{16}_{\Lambda}$O)	[22]	Rel. ion	86^{+33}_{-26}		127	
${}^{28}_{\Lambda}$Si	[11]	(π^+, K^+)	206 ± 12	165		202
${}_{\Lambda}$Fe	[11]	(π^+, K^+)	215 ± 14	139	122	195
(${}^{209}_{\Lambda}$Bi)	[23]	$\overline{p}$, fission	250^{+250}_{-100}			
	[24]	e^-, fission	2700 ± 500			
	[25]	e^-, fission	1500 ± 400			
	[25]		80 ± 15			
	[26]	$\overline{p}$, fission	180 ± 40		118	188
	[27]	p , fission	161 ± 21			
(${}^{238}_{\Lambda}$U)	[28]	$\overline{p}$, fission	$100^{+100}_{-\ 50}$			
	[26]	$\overline{p}$, fission	125 ± 15			
	[29]	p , fission	240 ± 60			

Table 3. Survey of measured partial rates

${}^{A}_{\Lambda}Z$ / Γ^i	${}^{4}_{\Lambda}$He	${}^{5}_{\Lambda}$He	${}^{11}_{\Lambda}$B	${}^{12}_{\Lambda}$C
Γ^{π^-}	0.26 ± 0.03 [12] 0.33 ± 0.05 [19]	0.44 ± 0.11 [20] 0.34 ± 0.06 [30]	0.23 ± 0.09 [31]	0.14 ± 0.10 [31] 0.113 ± 0.042 [33]
Γ^{π^0}	0.61 ± 0.08 [12]	0.18 ± 0.20 [20] 0.53 ± 0.03 [19]	0.192 ± 0.090 [32]	0.217 ± 0.084 [32]
Γ^{p}	0.16 ± 0.02 [12] 0.16 ± 0.02 [19]	0.21 ± 0.07 [20] 0.17 ± 0.04 [30]	$0.30^{+0.15}_{-0.11}$ [31]	$0.31^{+0.18}_{-0.11}$ [31]
Γ^{n}	0.04 ± 0.02 [12] $0.01^{+0.04}_{-0.01}$ [19]	0.20 ± 0.11 [20]	0.65 ± 0.17 [31]	0.58 ± 0.18 [31]
Γ^{n}/Γ^{p}	0.25 ± 0.13 [12] $0.06^{+0.28}_{-0.06}$ [19]	0.93 ± 0.55 [20] 1.97 ± 0.67 [30]	$1.04^{+0.59}_{-0.48}$ [20] $2.16^{+1.03}_{-1.53}$ [31]	$1.33^{+1.12}_{-0.81}$ [20] $1.87^{+0.91}_{-1.59}$ [31]

The dominant mechanism of hypernuclear weak decay is not the pionic mode favored by a free Λ but the far more complex $\Lambda + N \to N + N$ process. The total decay width of a hypernucleus, Γ_{tot}, is defined in terms of its mesonic and nonmesonic decay modes [5, 6]

$$\tau^{-1} = \Gamma_{\text{tot}}$$

$$= \underbrace{\Gamma_{\text{mesonic}}}_{\Gamma^{\pi^-} + \Gamma^{\pi^0} + (\Gamma^{\pi^+})} + \underbrace{\Gamma_{\text{nonmesonic}}}_{\Gamma^{p} + \Gamma^{n} + (\Gamma^{\text{mb}})};$$

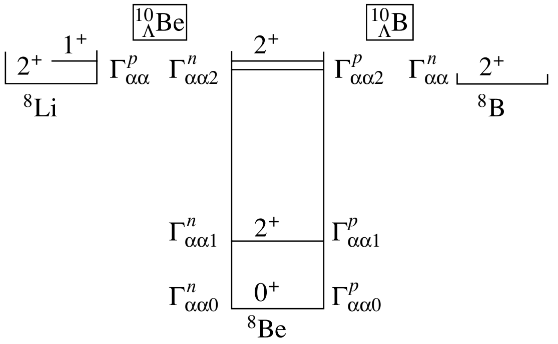

Figure.

Γ^{mb} and Γ^{π^+} are the possible many-body decay modes and are ignored in our discussion. In Table 1, the relevant momentum p and kinetic energy T_N of the final nucleon are displayed. The main observables which can be measured experimentally and should be confronted with theoretical predictions include

(a) the hypernuclear lifetime;

(b) the partial widths Γ^{π^-}, Γ^{π^0}, Γ^p, and Γ^n;

(c) the ratio of parity-violating to parity-conserving decay, which is measured via the proton asymmetry in polarized hypernuclear decay.

Recently, a further step was completed: hadronic weak matrix elements of the form $\langle B'M|H_w|B\rangle$ were implanted into the nucleus with usual many-body shell model wave functions [9]. Spectroscopic factors are utilized to describe the initial hypernuclear and final nuclear structure. A convenient compact expression for the potential is given by

$$V(r) = \sum_i \sum_\alpha V^{(i)}_\alpha(r) O_\alpha I^{(i)}_\alpha(r),$$

where the index i runs over the different mesons exchanged, and α over the different spin operators. The isospin operator $I^{(i)}_\alpha(r)$ depends on the meson.

Table 4. Survey of calculated partial rates

Method		${}^4_\Lambda$He	${}^5_\Lambda$He	${}^{11}_\Lambda$B	${}^{12}_\Lambda$C
		Γ^n/Γ^p			
OPE	[8]		0.05		0.20
	[9]		0.07		0.10
OME	[8]		0.48		0.83
	[9]		0.07		0.07
DQ + OPE	[34]	0.178	0.489		
DQ + OME	[35]	0.024	0.195		
		Γ^p/Γ_Λ			
OPE	[9]		0.43	0.64	0.80
OME	[9]		0.386	0.563	0.705

3. WEAK DECAYS OF HYPERNUCLEI: EXPERIMENTAL SITUATION

The field of weak decay of Λ hypernuclei has experienced impressive progress in the last decade [6]. Among weak decay observables, the lifetime can be measured most accurately [11]. The results from different experiments are listed in Table 2 along with the calculated values. Note that figures in the last column were obtained very recently and some model parameters were corrected in order to achieve agreement with experimental data.

At present, there are four hypernuclei for which the complete set of partial rates has been measured [12]. The results are displayed in Table 3 together with the Γ^n/Γ^p ratio.

The results of the calculation of this ratio in various approaches (One-Pion Exchange, One-Meson Exchange, Direct Quark mechanism) are given in Table 4. The substantial increase in this ratio in the OME model [8] was not confirmed by [9]. The difference between two similar approaches is disturbing [6]. The lower part of Table 4 gives some clue to this puzzle. It appears that calculation leads to a significant overestimation of Γ^p. So, to improve our understanding of the weak baryon–baryon interaction, we need precise measurements of Γ^p and/or Γ^n.

4. NONMESONIC DECAY OF ${}^{10}_{\Lambda}$Be AND ${}^{10}_{\Lambda}$B

In general, the identification of the final nuclear states ${}^{A-2}Z_f$ is not possible with present detectors. Bressani [36] has shown that resolutions planned for the FINUDA spectrometer may allow an exclusive measurement for ^{6}Li as a stopping target and in this case the final state of the residual nucleus could be determined.

The specific properties of the host nuclei ^{9}Be and ^{9}B of the hypernuclei ${}^{10}_{\Lambda}$Be and ${}^{10}_{\Lambda}$B could be very useful in the process of selection of the spin-dependent part of the weak interaction matrix element

$$w^{SJ}_{\ell\tau} = |\langle l_1 l_2 : L'S'JT|V_w|\tau\ell s_\Lambda : L = \ell SJ\rangle|^2.$$

It is well known that removing one nucleon from ^{9}Be or ^{9}B results in ^{8}Be*:

$${}^9\mathrm{B} \to n + ({}^8\mathrm{B} \xrightarrow{\beta^+} {}^8\mathrm{Be}^*),$$

$${}^9\mathrm{B} \to p + {}^8\mathrm{Be}^*,$$

$${}^9\mathrm{Be} \to n + {}^8\mathrm{Be}^*,$$

$${}^9\mathrm{Be} \to p + ({}^8\mathrm{Li} \xrightarrow{\beta^-} {}^8\mathrm{Be}^*).$$

The prevailing part of the final states of the residual nuclei (more than 75% according to Table 5) ultimately decay in the $\alpha\alpha$ channel, and through this unique process it would be possible to identify these

Table 5. Energy levels of ^{8}Be and coefficients of fractional parentage

Experiment Ajzenberg-Selove [37]					Model: $s^4p^4\ E_c\ J_c^+\ T_c$			
					[38]		[39]	
E_c, MeV	J_c^π	T_c	Γ, keV	decay	E_c, MeV	g_c^2	E_c, MeV	g_c^2
0.00	0^+	0	6.8 eV	α	0.00	0.110	0.00	0.112
3.04	2^+	0	1500	α	3.09	0.151	3.41	0.144
11.4	4^+	0	≃3500	α	10.30	–	11.29	–
16.63	2^+	1(+0)	108	γ, α	16.76	0.303	15.81	0.308
16.92	2^+	0(+1)	74	γ, α	16.89	0.086	14.44	0.095
17.64	1^+	1	11	γ, p	17.59	0.134	16.89	0.104

final states. These events are easily recognized as "hammer tracks" in the emulsion.

In Table 5, energy levels of ^{8}Be and coefficients of fractional parentage

$$g_c^2 = \sum_j |\langle p^5 E_{\rm gs} \frac{3}{2}^- \frac{1}{2}\{|p^4 E_c J_c T_c; p_j\rangle|^2$$

are displayed.

In the figure, the relevant states of $A = 8$ isotopes are displayed and the notation of the "partial widths" $\Gamma^\tau_{\alpha\alpha i}$ is explained.

Table 6 demonstrates that these partial widths are various combinations of the four matrix elements (eight for different τ). We see that in principle their study offers a unique possibility to determine all needed matrix elements of the weak interaction [9] and can resolve the puzzle of neutron- to proton-induced decay rates Γ^n/Γ^p [6].

Table 6. Partial nucleon decay widths $\Gamma^\tau_{\alpha\alpha i}$

Proton	w^{01}_{1p}	w^{10}_{1p}	w^{11}_{1p}	w^{12}_{1p}
$\Gamma^p_{\alpha\alpha}$ ($^{10}_{\Lambda}$Be)	0.441	0.157	0.491	0.548
$\Gamma^p_{\alpha\alpha2}$ ($^{10}_{\Lambda}$B)	0.096		0.520	0.439
$\Gamma^p_{\alpha\alpha1}$ ($^{10}_{\Lambda}$B)	0.388		0.051	0.408
$\Gamma^p_{\alpha\alpha0}$ ($^{10}_{\Lambda}$B)	0.412		0.206	
Neutron	w^{01}_{1n}	w^{10}_{1n}	w^{11}_{1n}	w^{12}_{1n}
$\Gamma^n_{\alpha\alpha2}$ ($^{10}_{\Lambda}$Be)	0.096		0.520	0.439
$\Gamma^n_{\alpha\alpha1}$ ($^{10}_{\Lambda}$Be)	0.388		0.051	0.408
$\Gamma^n_{\alpha\alpha0}$ ($^{10}_{\Lambda}$Be)	0.412		0.206	
$\Gamma^n_{\alpha\alpha}$ ($^{10}_{\Lambda}$B)	0.141		0.489	0.505

ACKNOWLEDGMENTS

This work was supported in part by the Grant Agency of the Czech Academy of Sciences, grant no. 1048703.

REFERENCES

1. M. I. Podgoretsky, Zh. Éksp. Teor. Fiz. **44**, 695 (1963) [Sov. Phys. JETP **17**, 470 (1963)].
2. B. Povh, Annu. Rev. Nucl. Part. Sci. **28**, 1 (1978).
3. V. V. Balashov, in *Proceedings of the Seminar on the Kaon–Nucleus Interaction and Hypernuclei, Zvenigorod, 1977* (Nauka, Moscow, 1979), p. 338.
4. J. Žofka *et al.,* Fiz. Élem. Chastits At. Yadra **22**, 1292 (1991) [Sov. J. Part. Nucl. **22**, 628 (1991)]; L. Majling *et al.,* Fiz. Élem. Chastits At. Yadra **28**, 253 (1997) [J. Part. Nucl. **28**, 101 (1997)].
5. J. Cohen, Prog. Part. Nucl. Phys. **25**, 139 (1990).
6. E. Oset and A. Ramos, Prog. Part. Nucl. Phys. **41**, 191 (1998).
7. B. L. Okun', *Leptons and Quarks* (Nauka, Moscow, 1982; North Holland, Amsterdam, 1984); J. F. Donoghue *et al.,* Phys. Rep. **131**, 319 (1986); A. I. Vainshtein *et al.,* Zh. Eksp. Teor. Fiz. **72**, 1275 (1977) [Sov. Phys. JETP **45**, 670 (1977)].
8. J. F. Dubach *et al.,* Ann. Phys. (N.Y.) **249**, 148 (1996); B. F. Gibson, Nuovo Cimento A **102**, 367 (1989).
9. A. Parreno *et al.,* Phys. Rev. C **56**, 339 (1997).
10. Particle Data Group, Eur. J. Phys. C **3**, 1 (1998).
11. H. Bhang *et al.,* Phys. Rev. Lett. **81**, 4321 (1998).
12. V. Zeps, Nucl. Phys. A **639**, 261c (1998).
13. K. Itonaga *et al.,* Nucl. Phys. A **639**, 329c (1998).
14. A. Ramos *et al.,* Phys. Rev. C **50**, 2314 (1994).
15. W. M. Alberico *et al.,* Phys. Rev. C **61**, 044314 (2000).
16. S. Avramenko *et al.,* Nucl. Phys. A **547**, 95c (1992).
17. A. Abdurakhimov *et al.,* Nuovo Cimento A **102**, 645 (1989).
18. H. Outa *et al.,* Nucl. Phys. A **547**, 109c (1992).
19. H. Outa *et al.,* Nucl. Phys. A **639**, 251c (1998).

20. J. Szymanski *et al.,* Phys. Rev. C **43**, 849 (1991).
21. R. Grace *et al.,* Phys. Rev. Lett. **55**, 1055 (1985).
22. K. Nield *et al.,* Phys. Rev. C **13**, 1263 (1976).
23. J. Bocquet *et al.,* Phys. Lett. B **192**, 312 (1987).
24. V. Noga *et al.,* Yad. Fiz. **46**, 1313 (1987) [Sov. J. Nucl. Phys. **46**, 769 (1987)].
25. V. Noga *et al.,* Ukr. Fiz. Zh. **35**, 171 (1990).
26. T. Armstrong *et al.,* Phys. Rev. C **47**, 1957 (1993).
27. P. Kulessa *et al.,* Phys. Lett. B **427**, 403 (1998).
28. J. Bocquet *et al.,* Phys. Lett. B **182**, 146 (1986).
29. H. Ohm *et al.,* Phys. Rev. C **55**, 3062 (1997).
30. H. Noumi *et al.,* in *Proceedings of IV International Symposium on Weak and Elecromagnetic Interactions in Nuclei* (World Sci., Singapore, 1995), p. 550.
31. H. Noumi *et al.,* Phys. Rev. C **52**, 2936 (1995).
32. A. Sakaguchi *et al.,* Phys. Rev. C **43**, 73 (1991).
33. Y. Sato *et al.,* Nucl. Phys. A **639**, 279c (1998).
34. T. Inoue *et al.,* Nucl. Phys. A **633**, 312 (1998).
35. K. Sasaki *et al.,* Nucl. Phys. A **669**, 331 (2000).
36. T. Bressani, Nuovo Cimento A **108**, 649 (1995).
37. F. Ajzenberg-Selove, Nucl. Phys. A **490**, 1 (1988).
38. F. C. Barker, Nucl. Phys. **83**, 418 (1966).
39. S. Cohen and D. Kurath, Nucl. Phys. A **101**, 1 (1967).